



Max-Planck-Institut für Intelligente Systeme
(ehemals Max-Planck-Institut für Metallforschung)
Stuttgart

Correlation between the Microstructure of Porous Materials and the Adsorption Properties of H₂ and D₂

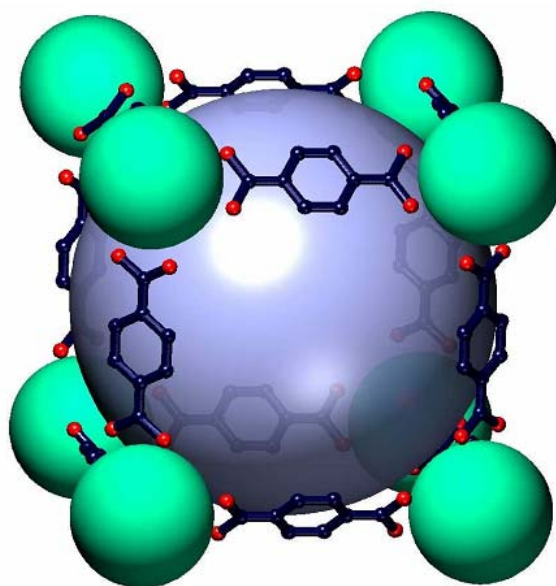
Ivana Krkljuš

Dissertation
an der
Universität Stuttgart

Bericht Nr. 235
Juni 2011

Ivana Biljana Krkljuš

CORRELATION BETWEEN THE
MICROSTRUCTURE OF POROUS MATERIALS AND THE
ADSORPTION PROPERTIES
OF H₂ AND D₂



Max-Planck-Institut für Intelligente Systeme (MPI-IS)

Stuttgart 2011

Correlation between the Microstructure of Porous Materials and the Adsorption Properties of H₂ and D₂

Von der Fakultät Chemie der Universität Stuttgart zur
Erlangung der Würde eines Doktors der Naturwissenschaften
(Dr. rer. nat.) genehmigte Abhandlung

vorgelegt von

Ivana Krkljuš

aus Belgrad, Serbien

Hauptberichter:	Prof. Dr. Emil Roduner
Mitberichter:	Prof. Dr. Gisela Schütz
Vorsitzender des Prüfungsausschusses:	Prof. Dr.–Ing. Elias Klemm
Tag der Einreichung:	28.02.2011
Tag der mündlichen Prüfung:	07.06.2011

Max–Planck–Institut für Intelligente Systeme, Stuttgart
Institut für Physikalische Chemie der Universität Stuttgart

*Мојим најсјајнијим звездама у најтамнијој ноћи.
Хвала што обасјасте ми путе.*

Eidesstattliche Erklärung

Ich versichere, dass ich diese Dissertation selbstständig verfasst und nur die angegebenen Quellen und Hilfsmittel verwendet habe.

Ivana Krkljuš

Stuttgart, den 16.02.2011.

Ivana Krkljuš

CONTENTS

Chapter 1	INTRODUCTION	
1.1	Hydrogen – Clean and Safe Fuel of the Future.....	1
1.2	On–Board Vehicular Hydrogen Storage.....	2
1.3	Scope of the Present Work.....	3
Chapter 2	FUNDAMENTAL ASPECTS	
2.1	Principles of Physisorption.....	5
2.2	Thermal Desorption Spectroscopy (TDS).....	11
2.3	Methods for Measuring the Hydrogen Storage Capacity.....	15
2.4	Quantum Effects.....	17
	2.4.1 Zero–point Energy Effects.....	17
	2.4.2 Tunneling.....	18
2.5	Porous Adsorbents.....	19
	2.5.1 Nanoporous Carbon.....	19
	Activated Carbon.....	19
	Carbon Molecular Sieves.....	21
	2.5.2 Metal–Organic Frameworks.....	23
Chapter 3	EXPERIMENTAL METHOD	
	Thermal Desorption Spectroscopy (TDS).....	26
3.1	The Fundamental and Experimental Advantages of the TDS Technique.....	26
3.2	The Design of the Experimental Apparatus.....	27
3.3	The Principle of the Measurement.....	29
3.4	Calibration with Pd.....	30

Chapter 4	Results with CARBON MOLECULAR SIEVES	
4.1	Investigated CMS Samples.....	32
4.2	Sample Characterisation.....	33
	4.2.1 Adsorption Studies.....	33
	4.2.2 Thermal Desorption Studies	33
4.3	Results.....	34
	4.3.1 Pore Structure Characterization.....	34
	4.3.2 Hydrogen Adsorption	37
	4.3.3 Hydrogen/Deuterium Desorption	37
4.4	Discussion.....	48
4.5	Summary.....	51
Chapter 5	Results with METAL–ORGANIC FRAMEWORKS	
5.1	The Design, Synthesis, and Properties of Crystalline MOFs...	53
5.2	Thermal Desorption Spectroscopy of H ₂ , HD, and D ₂	68
	5.2.1 Results.....	68
	Cu–BTC.....	69
	Fe–BTC.....	73
	Mg–formate(1).....	76
	Mg–formate(2).....	76
	MOF–177.....	83
	MFU–4.....	85
	MFU–4 <i>l</i>	88
	Al(OH)(ndc).....	91
	Al(OH)(bpdc)	91
	MIL–100(Al).....	92
	MIL–100(V).....	94
	MIL–100(Cr).....	94
	MIL–100(Fe).....	97
	5.2.2 Discussion.....	102
	5.2.3 Summary.....	116

Chapter 6	TAILORING the H₂-MOF INTERACTION	
6.1	An Overview.....	119
6.2	The Pore Size Optimization.....	120
6.2.1	Functionalization of the Pore Size and the Pore Volume by Ligand Modification.....	123
6.2.2	Catenane Formation.....	129
6.2.3	Impregnation.....	130
6.3	Influence of Coordinatively Unsaturated Metal Centers on the Strength of H ₂ -MOF Interaction.....	131
Chapter 7	QUANTUM EFFECTS	
7.1	Preferential adsorption of the heavier isotope.....	137
7.2	The difference in the total amount of gas desorbed.....	148
7.3	The difference in the activation energy for desorption.....	150
7.4	A shift in the position of the desorption maxima.....	151
7.5	Quantum effect-induced kinetic molecular sieving.....	153
Chapter 8	CONCLUSIONS	159
APPENDICES		164
THE REFERENCE LIST		183
ACKNOWLEDGEMENTS		196
REFEREED PUBLICATIONS		198
CURRICULUM VITAE		199

ZUSAMMENFASSUNG

Die Speicherung von Wasserstoff spielt bei der Realisierung eines wasserstoffbasierten Energiekreislaufs eine entscheidende Rolle für mobile Anwendungen. Bisher wurden die drei wichtigsten Techniken zur Speicherung von Wasserstoff untersucht: die Speicherung in gasförmigem, flüssigem oder chemisch gebundenem Zustand. Eine erst vor kurzem erforschte Alternative ist die Speicherung des Wasserstoffs in porösen Materialien unter kryogenen Bedingungen. Die physikalische Adsorption von H_2 in poröse Materialien hat besondere Vorteile, nämlich vollständige Reversibilität, schnelle Adsorptions- und Desorptionskinetik, schnelle Beladungszeit, geringe Wärmeentwicklung und vor allem verbesserte Sicherheit.

Die Art der Interaktion zwischen Wasserstoff, Deuterium und Gasgemischen in porösen Materialien wurde durch thermische Desorptionsspektroskopie (TDS) bei tiefen Temperaturen untersucht. Durch diese empfindliche Methode zur Messung der Desorption von adsorbiertem Gas kann es gelingen, die unterschiedlichen Adsorptionszentren, die je nach Stärke der Wechselwirkung unterschiedliche Desorptionstemperaturen für H_2 aufweisen, nachzuweisen. Nach einer geeigneten Kalibrierung der Anlage wurde die Menge an desorbiertem Wasserstoff/Deuterium quantitativ bestimmt. Um weiteren Aufschluss über die Eigenschaften der Adsorptionszentren zu erhalten, wurden thermische Desorptionsspektren nach Abkühlen der Probe auf 20 K in Gasatmosphäre (1–700 mbar) mit unterschiedlichen Temperatureinstellungen gemessen.

Verschiedene Klassen von porösen Materialien, Kohlenstoffmaterialien und kristalline metallorganische Gerüste mit unterschiedlicher Struktur und Textur wurden für die Physisorption von Wasserstoff/Deuterium untersucht. In Bezug auf Kohlenstoffmaterialien wurde für kleinere Porendurchmesser eine Zunahme der Interaktionen mit Wasserstoff/eine Erhöhung der Affinitäten zu Wasserstoff beobachtet. In diesem Fall sind die Van-der-Waals-Kräfte mit dem Adsorbat maximiert, und es herrschen ungeachtet der Geometrie optimale Wechselwirkungen mit allen umgebenden Wänden der Poren.

Metall–organische Gerüste sind poröse Materialien mit wohlgeordneter kristalliner Struktur. Sie bestehen aus Komplexen mit Übergangsmetallen als „Knoten“ und organischen Molekülen (Liganden) als Verbindung zwischen den Knoten. Durch Verwendung geeigneter Knoten und Linker können die MOF für die Wasserstoffspeicherung optimiert werden. Metall–organische Gerüste sind wegen ihrer hohen Porosität, ihrer hohen Speicherkapazität bei tiefer Temperatur und der ausgezeichneten Reversibilitätskinetik interessant als mögliche Feststoffmaterialien zur Wasserstoffspeicherung. Diese neue Klasse von porösen Materialien wurde umfassend im Rahmen dieser Arbeit untersucht.

Entscheidend für die Entwicklung von porösen Materialien ist die Verstärkung der Wechselwirkung mit H_2 , um die Adsorption näher an Raumtemperaturbedingungen zu bringen. Die Strategien zur Verbesserung der H_2 –MOF Bindung wurden sorgfältig untersucht. Diese Ansätze umfassen den Einbau von koordinativ ungesättigten Metallzentren und die Optimierung der Porengröße und Adsorptionsenergien durch Modifizierung von Linkern.

Wasserstoffspeicherung in mikroporösen Metall–organischen Gerüsten mit koordinativ ungesättigten Metallzentren wurde besonders untersucht ebenso wie die Herstellung von Gerüsten mit koordinativ ungesättigten Metallzentren durch die Entfernung metallgebundener flüchtiger Spezies.

Bei Kohlenstoff–Materialien ist das Interaktionspotential des H_2 –MOF in Materialien mit einer Porengröße, die dem kinetischen Durchmesser eines Wasserstoffmoleküls entspricht, besonders erhöht. Solche Effekte könnten aus der Überlappung des Potentialfeldes resultieren, und zwar wegen der Nähe zur Porenwand, welche die Interaktion mit dem Adsorbat verstärkt.

Allerdings verhindern kleinere Poren die Be– und Entladungsprozesse des Wasserstoffs (das Eindringen des Wasserstoffs) drastisch und beschränken die Diffusion. Des Weiteren kann die Geschwindigkeit der Wasserstoffaufnahme und –abgabe des Wasserstoffträgermaterials bei niedrigen Temperaturen durch Quanteneffekte wesentlich beeinflusst sein.

Diese Arbeit ist wie folgt gegliedert:

In Kapitel 1 wird die einzigartige Anwendung von Wasserstoffspeicherung an porösen Materialien zum Zweck der Energienutzung vorgestellt. Das Kapitel gibt einen kurzen Überblick über die Probleme der Wasserstoffspeicherung, sowie den Aufbau der Arbeit.

Eine theoretische Behandlung der grundlegenden Aspekte der Adsorptionsphänomene und die Thermodesorptionsspektroskopie–Technik, die in Kapitel 2 eingeführt wird, ist die Grundlage für die Diskussion, die in den Kapiteln 4, 5 und 6 geführt wird. Die in dieser Studie untersuchten porösen Adsorbentien werden ebenfalls vorgestellt. Darüber hinaus wird der theoretische Ansatz

zur Erklärung der Theorie der Quanteneffekte, die für die Erklärung und die Diskussion der Ergebnisse in Kapitel 7 notwendig sind, dargestellt.

Kapitel 3 stellt ein neu entwickeltes Gerät zur Thermodesorptionspektroskopie (TDS) vor. Der Funktionsplan der Versuchsanordnung wird detailliert dargestellt und das Messprinzip erläutert. Weiterhin wird das Kalibrierungsprinzip mit den anderen in Kapitel 2 dargestellten experimentellen Techniken verglichen.

Kapitel 4 befasst sich hauptsächlich mit dem Adsorptions- und Desorptionsmechanismen bei Kohlenstoffmolekularsieben. Die Sorptionseigenschaften sowie die poröse Struktur der untersuchten Proben, die durch volumetrische Niederdruck-Adsorptionsmessungen nachgewiesen wurden, werden vorgestellt. Die Porengrößenverteilung ermittelt durch Grand Canonical Monte Carlo Simulationen wird mit den Desorptionsmessungen in Beziehung gesetzt.

Kapitel 5 ist den aktuellen Verbindungen aus den Metall-organischen Gerüsten gewidmet. Die Oberflächeneigenschaften und die Porenstruktur der untersuchten Adsorbentien sind im Detail angegeben. Die Wasserstoff-Deuterium-Desorptionsspektren werden vorgestellt und diskutiert.

Das sechste Kapitel versucht die grundlegenden Strategien zu erklären, die im letzten Jahrzehnt erforscht wurden und die darauf abzielen, die Stärke der H₂-Interaktion mit den Metall-organischen Gerüsten zu verbessern. Diese Diskussion wird auf die Analyse der prominenten Ergebnisse aus der Literatur ausgedehnt.

Die Wechselwirkung der Adsorption und Separation von Isotopen unter kryogenen Bedingungen und die langsame Gasdiffusion in engen Poren führt zu komplexen, aber interessanten Fragestellungen, die in Kapitel 7 diskutiert werden. Die zum ersten Mal im Rahmen dieser Arbeit experimentell beobachteten und diskutierten Quanteneffekte bei der Desorption werden mit den experimentellen Daten zu Quanteneffekten bei der Adsorption und etwas ausgedehnteren Simulationenstudien in der Literatur in Verbindung gesetzt.

Kapitel 8 fasst die wichtigsten experimentellen Befunde dieser Arbeit zusammen.

SYNOPSIS

One of the most challenging tasks toward the full implementation of the hydrogen based economy is the reversible storage of hydrogen for portable applications. Three main approaches have been investigated to store the hydrogen, storage as a compressed gas or a liquid, or through a direct chemical bond between the hydrogen atom and the material. The alternative approach, the most recently investigated, is the storage of hydrogen at cryogenic conditions. Storage by physisorption within porous adsorbents has particular advantages of complete reversibility, the fast refueling time, the low heat evolution, and above all increased safety.

The nature of interaction of hydrogen, deuterium, and gas mixtures with porous adsorbents was exploited by performing thermal desorption spectroscopy (TDS) measurements. This sensitive experimental technique gives qualitative information about the different adsorption sites, which show different desorption temperatures depending on the interaction energy. After an appropriate calibration the amount of gas desorbed may be quantified. To gain a more fundamental insight into the available adsorption sites multiple TDS spectra were recorded, corresponding to different surface coverages (in the pressure range of 1 to 700 mbar), and different heating regimes.

Different kind of porous adsorbents, conventional carbon-based materials and novel Metal Organic Framework Materials (MOFs) were used to investigate the hydrogen/deuterium physisorption mechanism. For carbon materials an increase in the hydrogen interaction potential was observed for adsorbents with narrow pore size. The confined geometry, where hydrogen simultaneously interacts with all the surrounding adsorbent walls, strengthens the interaction potential with the adsorbate molecule, thus, maximizing the total van der Waals force on the adsorbate.

Crystalline MOFs are a new class of porous materials assembled from discrete metal centers, which act as framework nodes, and organic ligands, employed as linkers. The material properties can be optimized by changing these two main components. Owing to their high porosity, high storage capacity at low temperature, and excellent reversibility kinetics, MOFs have attracted a

considerable attention as potential solid–state hydrogen storage materials. This novel class of porous adsorbents has been extensively investigated within this thesis.

The greatest challenge for porous adsorbents is to increase the strength of the H₂ binding interaction, and bring adsorption closer to RT conditions. Several strategies, aimed at improving hydrogen adsorption potential in MOFs are closely investigated. These strategies comprise the inclusion of open metal sites and the optimization of the pore size and, thus, the adsorption energy by ligand modification.

The influence of the coordinatively unsaturated metal centers, liberated by the removal of metal–bound volatile species, has been particularly investigated.

As for carbon materials, the H₂–MOF interaction potential is especially enhanced in materials with the pore size comparable to the kinetic diameter of the hydrogen molecule. Such effects may result from the overlap of the potential field due to the proximity of the pore wall, which strengthen the interaction potential with the adsorbate molecule. However, smaller pores prevent hydrogen penetration and induce diffusion limitations. Furthermore, the molecular transport in confined pores at low temperatures may be significantly affected by quantum effects.

This thesis is organized in the following manner:

In Chapter 1, a unique application of hydrogen adsorption on porous adsorbents for energy utilization purposes is introduced. The chapter gives a brief overview of the hydrogen storage problem and the scope of the presents work.

A theoretical treatment of the fundamental aspects of adsorption phenomena and the Thermal Desorption Spectroscopy Technique, introduced in Chapter 2, can be used to understand the discussion which follows in the Chapter 4, –5, and –6. Porous adsorbents investigated in this study are also introduced. In addition, the theoretical treatment of quantum effects necessary for the explanation and the discussion of the results given in Chapter 7 are addressed.

Chapter 3 introduces a newly developed set–up for Thermal Desorption Spectroscopy (TDS). The design of the experimental apparatus is given in details, and the measuring principle explained. A comparison is given to the other experimental techniques referred to in the Chapter 2, and the calibration principle addressed.

Chapter 4 deals mainly with the adsorption/desorption mechanism on Carbon Molecular Sieves. Sorption properties, as well as the porous structure of investigated samples, probed by volumetric low pressure adsorption measurements, are introduced. The pore size distribution resolved from the Grand Canonical Monte Carlo (GCMC) simulations is coupled with the desorption measurements.

Chapter 5 is devoted to topical compounds from the MOF family. The surface characteristics and the pore structure of the investigated adsorbents are given in details. The hydrogen/deuterium desorption spectra are presented and discussed.

The Chapter 6 attempts to define the fundamental strategies investigated during the last decade, aimed to improve the strength of the H₂-MOF interaction. The discussion is extended to the analysis of the prominent results from the literature.

The coupling effect of isotope adsorption and separation at cryogenic conditions, and the slow gas diffusion in confined pores brings about complex, but interesting problem discussed in Chapter 7. Quantum effects in desorption, experimentally observed and discussed for the first time within this thesis, are coupled with the humble experimental data on quantum effects in adsorption and somewhat extended simulations studies from the literature.

Chapter 8 summarized the main experimental findings of this work.

Chapter 1

INTRODUCTION

1.1 Hydrogen – Clean and Safe Fuel of the Future

Hydrogen – the lightest, the simplest, and the most abundant element in the universe has been envisaged as the ultimate solution for the future energy economy. Hydrogen produced from renewable energy sources is regarded as the advanced energy carrier, compared to the energy sources being used traditionally, oil and natural gas. It is non-toxic, and the only sole by-product of its combustion, in the generation of energy, is water. Hydrogen has the highest gravimetric energy density among all fuels. It contains more energy per kilogram (120 MJ kg^{-1}) than either gasoline (44.5 MJ kg^{-1}) or natural gas (50 MJ kg^{-1}) [1]. The energy content of 0.33 kg of hydrogen corresponds to the energy content of 1 kg of oil.

The combustion of hydrogen in a cylinder had been suggested as an alternative to the steam engine as early as 1820 by W. Cecil [2]. However, there are three major technological obstacles toward full implementation of hydrogen based economy. First hydrogen is not an energy source but a carrier of energy. And although it is the most abundant element in the universe it has to be produced from primary energy sources. In order to retain the environmental benefits hydrogen should be generated from renewable sources. By far, the bulk of hydrogen production still relies upon fossil fuels, a by-product of which is CO_2 . Due to its low molecular weight hydrogen seems to be an ideal fuel. Its volumetric density is low, 0.08 kg m^{-3} at ambient temperature and pressure. Furthermore, hydrogen has the second lowest boiling point of all known substances, and is a gas at room temperature (RT). At standard conditions (1 bar and 298 K) five kilograms of hydrogen require a volume of nearly 54 m^3 . To approach the targeted guidelines for hydrogen storage it is ultimately required that the

density of the adsorbed hydrogen surpasses that of its liquid state (70.8 kg m^{-3} at 20.27 K), which is one tenth of that of gasoline ($\sim 700 \text{ kg m}^{-3}$ at RT) [1].

1.2 On-Board Vehicular Hydrogen Storage

While hydrogen production is already technologically feasible its distribution and storage are more challenging than for most fuels. Due to the possible hydrogen embrittlement in steel existing natural gas transmission systems may be unsuitable for the transportation of pure hydrogen gas. Storing hydrogen on-board a vehicle – a car, an aircraft or a ship – in a safe and environmentally friendly way is crucial for the realization of hydrogen based economy. The terms of volumetric ($45 \text{ g L}^{-1} \text{ H}_2$ by 2010 or $81 \text{ g L}^{-1} \text{ H}_2$ by 2015) and gravimetric (6 wt.% by 2010 or 9 wt.% by 2015) density for hydrogen storage system at close to ambient conditions (-20 to $50 \text{ }^\circ\text{C}$) and pressures below 100 bar, designated by the U.S. Department of Energy (DoE) within the framework of its FreedomCAR program for the years 2007, 2010 and 2015¹, are based on the need to store a minimum of 5–6 kg of hydrogen in a passenger car, to provide a driving range of about 300–350 miles, with the refueling rate comparable to conventional ICE vehicles. All targets are application driven and not based upon a particular method or technology for storing hydrogen. The performance of fuel cell powered vehicles must be comparable or superior to the conventional internal combustion engine (ICE) counterparts, in order to achieve a widespread commercial application.

On-board hydrogen storage options so far considered can be generalized into three principle approaches: (1) compressed hydrogen, (2) liquefied hydrogen, and (3) solid state storage. Each storage option has particular advantages and shortcomings [3]. Conventional and rather established methods of hydrogen storage, high pressure storage in carbon-fiber reinforced polymers and cryogenically stored liquid hydrogen have several limitations [4], the most important of which is their energy intensive character associated with the amount of energy spent to compress and liquefy the gas, and significant energy loss due to evaporation. Although compressed hydrogen gas and cryogenically stored liquid hydrogen are already utilized in the prototype fuel cell powered vehicles, large storage volume and cost preclude their commercialization into daily use. Additionally, these tanks pose a risk of explosion when positioned on-board of a moving vehicle. Apart from being stored in gaseous or liquid form, by modifying its physically state conditions (temperature, pressure, and phase) hydrogen can be stored physico-chemically in various solid and liquid compounds. The important criterion of a hydrogen storage system is the reversibility of the hydrogen uptake and

¹ DoE Office of Energy Efficiency and Renewable Energy Hydrogen, Fuel Cells and Infrastructure Technologies Program: Multi-Year Research, Development, and Demonstration Plan, available at: <http://www.eere.energy.gov/hydrogenandfuelcells/mypp>.

release, which excludes all covalent hydrogen carbon compounds as hydrogen storage materials. Proposed alternatives for hydrogen storage and energy transfer include: (1) reversible hydrogen uptake in various metal-based compounds including hydrides (MgH_2 , NaAlH_4), nitrides, and imides (LiNH_2); (2) chemical storage in irreversible hydrogen carriers such as methanol, ammonia, etc.; and (3) physisorption of hydrogen molecules on porous sorbents.

Storing of hydrogen in solid medium is compact and safe. Metal hydrides which reversibly desorb large amounts of hydrogen were among the first materials considered for storage due to the high volumetric density of stored hydrogen at temperatures and pressures close to ambient conditions, and relatively low cost. However, low weight capacities, essentially due to the high molar mass of heavy metals such as lanthanides and zirconium, unfavorable kinetics requiring heating cycles to recover hydrogen, slow refueling kinetics, and susceptibility to contamination by impurities are primary concerns [5]. During the last decade considerable international effort was concentrated in the field of nanoporous materials considered as adsorbents for physical hydrogen storage regarding pronounced advantages of fast kinetics of hydrogen desorption at operating temperatures of a Polymer Electrolyte Membrane (PEM) fuel cell (80 – 120 °C), complete reversibility and fast refueling time, low heat evolution, and above all increased safety. The forces of attraction between hydrogen and the host material originate mainly from the weak van der Waals interactions. Thereby, significant hydrogen adsorption is achieved at low temperature, typically that of liquid nitrogen and/or at very high pressures. Activated Carbons (AC) and Metal-Organic Frameworks (MOFs) are the most closely investigated porous adsorbents for hydrogen storage via physisorption.

1.3 Scope of the Thesis

Physical adsorption is accompanied by low heats of adsorption, with no violent or disruptive structural changes occurring at the adsorbent surface. It is fully reversible, enabling both the adsorption and desorption processes to be studied. A more close insight into the adsorption mechanism, qualitative and quantitative understanding of hydrogen adsorption energy, and what determines preferred adsorption sites is scarce. The nature of interaction of hydrogen and, for the first time, deuterium and hydrogen deuteride with porous adsorbents – subject to this thesis – was extensively exploited by performing Thermal Desorption Spectroscopy (TDS) measurements, extended to temperatures as low as 20 K, suitable for observation of physisorption phenomena. This sensitive experimental technique gives qualitative information about the number, distribution, and the strength of different adsorption sites, as well as, after an appropriate calibration, about the quantity of gas stored.

Different kind of porous adsorbents, from conventional carbon-based materials and microporous inorganic solids to novel Metal Organic Framework Materials (MOFs) were chosen to represent a large variation in surface areas and the pore size distribution, to assess the impact of these factors on hydrogen adsorption. To gain a more fundamental insight into the available adsorption sites multiple TDS spectra were recorded, corresponding to different heating rates, different surface coverages, and by applying interrupted desorption experiments. Distinct adsorption sites were identified and correlated to the material structure.

Results obtained by TDS measurements are shown to yield additional information that support findings obtained by other experimental techniques.

Chapter 2

FUNDAMENTAL ASPECTS

2.1 Principles of Physisorption

Due to unsaturated and unbalanced molecular forces acting on the surface of the solid, the forces not coordinated by surrounding atoms such as those in the bulk of the solid, the surface has a tendency to attract (adsorb), and retain molecules on its surface. The spontaneity of adsorption requires that the overall Gibbs free energy, ΔG_{ads} , must be a negative quantity. Adsorbed molecules lose at least one degree of freedom (of translation), therefore, the entropy change, ΔS_{ads} , of the adsorbate is necessarily negative. Based upon the entropy and free energy changes, the enthalpy change, ΔH_{ads} , accompanying adsorption is always negative, indicating that adsorption must be an exothermic process, Eq. (2.1):

$$\Delta G_{ads} = \Delta H_{ads} - T\Delta S_{ads} \quad (2.1)$$

Physical adsorption of gases on porous adsorbents is one such instance. The released energy is partly absorbed by the solid adsorbent, and partly dissipated to the surrounding. The portion absorbed by the solid increases the particle temperature, and it is this rise in temperature that slows down the adsorption kinetics. The isosteric heat of adsorption, ΔH_{ads} , and the activation energy of desorption, E_d , are related by Eq. (2.2), where E_a is the activation energy of adsorption [6].

$$E_d = \Delta H_{ads} + E_a \quad (2.2)$$

Commonly, adsorption is an unactivated process and $E_a = 0$.

The isosteric heat is a measure of the net attractive force between the solid surface, and an adsorbed molecule. The heats of adsorption, ΔH_{ads} , for gases onto a given solid can, in principle, be measured in a variety of ways and will, in reversible systems, adhere to the Clausius–Clapeyron equation, Eq. (2.3).

$$\left(\frac{\partial \ln p}{\partial T} \right)_V = - \frac{\Delta H_{ads}}{RT^2} \quad (2.3)$$

Depending upon the nature of interaction of adsorbate molecules with the surface, two types of adsorption can be distinguished: physical or van der Waals adsorption, and chemisorption. Physical adsorption is usually considered to arise from the presence of van der Waals forces [7]. These forces appear when the equilibrium distribution of electrons in the molecule and the solid are such that there is no sharing or transfer of electrons between molecule and the solid, and the electrons in the interacting species maintain their respective association as the molecule approaches the surface. The physical and chemical properties of the molecule and the surface are modified, but not drastically altered. Van der Waals forces between a molecule and a solid surface arise chiefly from London–type dispersion interactions [8]. The dispersion interaction is defined between two neutral, separated particles with nonoverlapping charge densities and without a permanent dipole moment. The dispersion energy depends on the distance between the particles, r , the polarisabilities, α_1' , and, α_2' , and the ionization energies of the interacting particles, I_1 , and, I_2 , Eq. (2.4):

$$U_{London} \approx - \frac{3}{2} \left(\frac{I_1 I_2}{I_1 + I_2} \right) \alpha_1' \alpha_2' \frac{1}{r^6} \quad (2.4)$$

Under mutual interaction an asymmetric polarization of electron charge is induced in molecules, that create temporarily dipole moments, and atoms or molecules become attracted by electrostatic forces. The dispersion interaction between nonpolar molecules is always attractive, with a potential inversely proportional to the sixth power of the separation distance between the particles (r^{-6}). It is several orders of magnitude weaker than the typical covalent or ionic interactions, and is a factor of 10 smaller than the hydrogen bond. When molecules approach each other on the distance smaller than the sum of their radii (so-called *van der Waals radii*) the atoms are repulsed rapidly and proportionally to the twelfth power of the separation distance (r^{-12}). The “ r^{-6} ” potential for dispersion interactions was first proposed in 1930 by F. London [8], and the overall “6–12” potential for dispersive van der Waals interaction is known as Lennard–Jones (LJ) potential, Eq. (2.5):

$$V_{LJ} = \varepsilon \left[\left(\frac{r_0}{r} \right)^{12} - \left(\frac{r_0}{r} \right)^6 \right] \quad (2.5)$$

where ε is the energy of attraction between atoms, r_0 is the equilibrium distance at which the dispersive (attractive), and the repulsive forces balance, and the system achieves its minimum energy at the minimum of the potential curve $V(r_0)$. Dispersion forces are always present between adjacent molecules, but they are usually rendered insignificant by strong chemical bonds.

The energetic relationship between the physisorption (P) and chemisorptions (C) can be illustrated by analysis of the schematic energy diagrams shown in Fig. 2.1. At large distances there is essentially no attraction between the surface and the molecule for physical adsorption. As the molecule approaches the surface an attraction due to van der Waals interactions is developed, leading to an energy minimum representing the heat of physical adsorption, ΔH_{ads} . At some distance, in this case the molecular radius of the vapor, an overlap between the electron clouds begins to develop, leading to the development of a repulsive interaction. The energy minimum for chemisorption, ΔH_{chem} , is much deeper than ΔH_{ads} , and will occur at shorter distances.

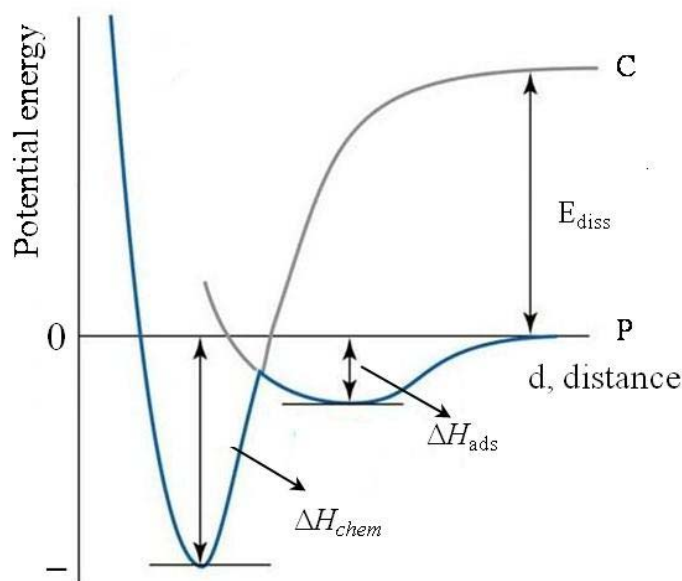


Fig. 2.1 Schematic diagram of the potential energy curves for physical (P) and chemical (C) adsorption of a molecule, and its constituents as a function of distance from the surface.

Chemisorptions occurs when the overlap between the molecular orbitals of the adsorbed particle and the surface atoms permit the formation of chemical bonds, which are characterized by dissociation energies, E_{diss} , typically exceeding 40 kJ mol^{-1} . The most common difference between the two kinds of adsorption is the magnitude of the heat of adsorption. In the case of physical

adsorption the heat of adsorption is of the same order of magnitude as the heat of condensation, and usually does not exceed 10 to 20 kJ mol⁻¹. Although energetically quite different, the stronger chemisorption phenomenon must be preceded by a physical adsorption process.

For a given adsorbate–adsorbent system, the equilibrium amount of gas (volume, V) adsorbed by a solid at a constant temperature, T , and as a function of the gas pressure, P , is defined by its adsorption isotherm. Six characteristic shapes of physisorption isotherms (Fig. 2.2) are identified in the IUPAC classification [9], which is an extension of a classification originally proposed by Brunauer et al. [10]. All isotherms tend to be linear in the low–pressure region of the adsorption isotherm, referred to as the *Henry's law* region, where the amount of gas adsorbed is proportional to the pressure, p .

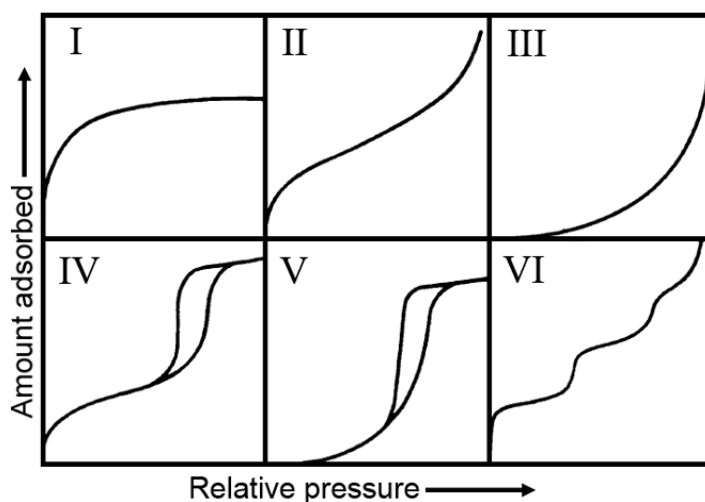


Fig. 2.2 Classification of gas adsorption isotherms after ref. [9].

Each of physisorption isotherms is observed in practice, but by far the most common are types I, II, and IV. Classical microporous materials commonly show isotherms of type I, usually termed the *Langmuir type*. These isotherms exhibit prominent adsorption at low relative pressures, p/p_0 , until a limiting quantity is asymptotically approached, usually identified with the attainment of complete monolayer coverage. *Type I isotherms* are common to chemisorption, although encountered as well for physical adsorption in fine micropores whose pore dimensions does not exceed a few molecular diameters. Complete filling of these narrow pores at quite a low relative vapor pressure corresponds to the completion of a molecular monolayer.

Type II isotherms are most frequently encountered when adsorption occurs on nonporous solids, or on adsorbents with a wide distribution of pore sizes. In contrast to the type I isotherm, the adsorbate molecules exhibit relatively strong mutual interaction which leads to the tendency for multilayer formation. The inflection point of the isotherm, termed *Point B* by Emmett and Brunauer [11],

usually occurs near the completion of the first adsorbed monolayer, and proceeds with a rather long linear portion upon increasing relative pressure. Multilayer formation then begins, which may lead to surface condensation.

Stepwise *Type IV isotherm* is a special case of layer-by-layer adsorption on a uniform surface for solids containing pores in the mesopore range. The shape of the Type IV isotherm follows the same path as the Type II at lower relative pressures, until its slope starts decreasing at higher pressures. At the saturation vapor pressure, the isotherm levels off to a constant value of adsorption. Characteristic feature of Type IV isotherms is the final saturation plateau and, in many cases, adsorption–desorption hysteresis loop, attributed to capillary condensation in the mesopores. These adsorption isotherms have led to the development of the theory of capillary condensation, first propounded by Zsigmondy [12], on the principles earlier established by Lord Kelvin (earlier name Thomson) [13].

The first theoretical equation which has described the relationship between the amounts of gas adsorbed, and the equilibrium gas pressure at constant temperature, was advanced by Langmuir [14]. Apart from restricting adsorption to formation of a monolayer, the Langmuir model is based on the following assumptions: (1) the surface is homogeneous, i.e., the adsorption energy of each and every molecule of a given adsorbate is the same, the heat of adsorption is constant over the surface, and independent of the surface coverage, (2) adsorption on the surface is localized, i.e., adsorbed atoms (and/or molecules) are adsorbed at fixed sites, and do not migrate over the surface, (3) each site can accommodate only one molecule or atom, and there are no interactions between adjacent molecules on the surface.

The Langmuir theory is based on a kinetic approach in which the rate of adsorption (rate constant k_a) is assumed to be proportional to the adsorbate partial pressure, p , and to the fraction of surface that remains uncovered by the adsorbate ($1-\theta$), where 1 corresponds to the complete saturation of a monolayer, and θ is the fractional surface coverage. At the same time while molecules get adsorbed, the other molecules are desorbed when they attain sufficient activation energy for desorption. At a fixed temperature, the rate of desorption from the surface (rate constant k_d) is directly proportional to the number of sites occupied by the adsorbate, θ . At equilibrium, the rates of adsorption and desorption are equal and a dynamic equilibrium is attained, Eq. (2.6):

$$k_a p(1 - \theta) = k_d \theta \quad (2.6)$$

The more usual form of the Eq. (2.6), for first-order desorption, is written as follows, Eq. (2.7):

$$\theta = \frac{q}{q_m} = \frac{bp}{1+bp} \quad (2.7)$$

where b corresponds to k_a/k_d , and q_m is the quantity of adsorbate adsorbed in a single monolayer. The ratio q/q_m can be measured, and expressed in different ways.

A major assumption of the Langmuir isotherm model is that adsorption stops at monolayer coverage. Consequently, only adsorbate molecules that impinge on a bare surface have a certain probability of being adsorbed, while those impinging on a site already occupied by an adsorbed molecule would be immediately reevaporated back into the gas phase. However, physical adsorption involves long range van der Waals forces leading to multilayer adsorption, the upper limit of which is condensation of the adsorbate. Brunauer, Emmett, and Teller [15] are the first to develop a theory, based on their earlier work [11, 16], to account for this multilayer adsorption, hereinafter referred to as BET. The basic assumption of the *BET theory* is that molecules in the first layer can act as adsorption sites for molecules in the following layer, and it is not necessary for an early layer to be completed before the next layer starts to form. The adsorption and/or desorption takes place at the top–most layer. Adsorption of the first monolayer has a characteristic heat of adsorption, ΔH_A , while all succeeding layers are controlled by the heat of condensation of the pure bulk adsorbate in question, ΔH_L . The BET isotherm gives a Type II (S–shape) isotherm, and may be represented in the simple or infinity form, Eq. (2.8):

$$V = \frac{V_m cp}{(p_0 - p)[1 + (c-1)p / p_0]} \quad (2.8)$$

where V is the volume of the adsorbed vapor at STP, V_m is the volume of gas required to form a monolayer, p is the adsorbate partial pressure, p_0 is the adsorbate saturation vapor pressure, and c is a dimensionless empirical constant related exponentially to the net molar energy of adsorption [17], Eq. (2.9) [18]:

$$c \approx \exp \frac{(\Delta H_A - \Delta H_L)}{RT} \quad (2.9)$$

where R is the universal gas constant, and T is the absolute temperature. The larger the value of c is, the sooner will the multilayer be formed, and the isotherm convexities will increase toward the low pressure region.

The BET equation may be transformed into the two–parameter BET equation, written in the linear form, Eq. (2.10):

$$\frac{p}{V(p_0 - p)} = \frac{1}{V_m c} + \frac{(c-1)}{V_m c} \frac{p}{p_0} \quad (2.10)$$

A plot of $[p/V(p_0 - p)]$ vs. p/p_0 gives a straight line, with the intercept $I = 1/(V_m c)$, and the slope equal to $S = (c-1)/(V_m c)$. Since c , in general, is large for physisorption, the slope is close to $1/V_m$. Derived constants, $V_m = I/(S+I)$ and c , are used to calculate the specific surface area (SSA) of adsorbent material, based on the following Eq. (2.11):

$$S_{BET} = \frac{a_m N_a V_m}{m_{sample} M_v} \quad (2.11)$$

where a_m is the area per molecule of the adsorbed gas, N_a is Avogadro's number, m_{sample} is the sample mass, and M_v is the gram molecular volume of gas (22.400 L at STP). The SSA of the adsorbent is usually measured by adsorption of nitrogen at 77 K, whereas nitrogen is generally considered to be the most suitable adsorbate for surface area determination [9]. Based on the adsorption of nitrogen, at its normal boiling point, on a wide range of porous solids, the classification of the pores by their sizes has been made into three main categories: (1) the *macropores*, having average diameter greater than 50 nm, (2) the *mesopores*, with diameters between 2 and 50 nm, and (3) the *micropores*, having average diameter less than 2 nm. The micropores are further divided into *supermicropores* (0.7–2.0 nm), and *ultramicro pores* (diameter less than 0.7 nm). Each of these groups of pores plays a specific role in the adsorption process. Argon sorption at 87 K, and carbon dioxide sorption at 273 K are commonly used to determine the volume due to narrow micropores [19, 20], and are complementary to nitrogen adsorption [20–22]. Water vapor is also employed for sorption measurements [23, 24].

2.2 Thermal Desorption Spectroscopy (TDS)

The Temperature-Programmed Desorption (TPD), or Thermal Desorption Spectroscopy (TDS) technique was described for the first time in 1963 by Amenomiya and Cvetanović [25], as a useful tool for the investigation of highly temperature dependent phenomena on powdered solids. The same experimental principle was previously applied for studying desorbed gases from heated metallic filaments in high vacuum (HV), the so-called flash filament method, described by Apker in the late 1940's [26]. Excellent reviews on the theoretical background and applications of the TDS technique were given in the following years by Cvetanović and Amenomiya [27, 28], King [29], Falconer and Schwarz [30], Sklyarov [31], and Bhatia et al. [32]. Basic equations describing thermal desorption from an energetically homogeneous surface were given by Smith and Aranoff

[33], and have been subsequently discussed and extended by several other researchers, Redhead [34], Carter [35, 36], Ehrlich [37], and Yakerson [38].

Desorption processes on solid surfaces can be described using a general rate equation that accounts for the dependence of the desorption rate constant on temperature, Eq. (2.12):

$$r_{des} = -\frac{d\theta}{dt} = \kappa_d(\theta)\theta^n \quad (2.12)$$

where r_{des} is the desorption rate, θ is the relative surface coverage (the saturation coverage corresponds to $\theta = 1$), t is the time, κ_d is the rate constant for the desorption process, and n denotes the order of desorption (typically 0, 1 or 2). The rate of desorption, in general, follows an Arrhenius-type behavior, Eq. (2.13):

$$\kappa_d(\theta) = A \exp\left[-\frac{E_a^{des}(\theta)}{RT}\right] \quad (2.13)$$

where A is the pre-exponential factor, $E_a^{des}(\theta)$ is the activation energy of desorption, R is the universal gas constant, and T is the temperature. In the particular case of simple molecular adsorption, studied within the field of physisorption, the pre-exponential factor may be equated with the frequency of vibration, $\nu(\theta)$. Each time when the bond between the molecule and the substrate is stretched, during the course of vibration, can be considered as an attempt to break the bond, and hence an attempt at overcoming the barrier to desorption. The resulting rate law is usually referred to as the Polanyi-Wigner equation [39], Eq. (2.14):

$$r_{des}(\theta) = -\frac{d\theta}{dt} = \nu(\theta)\theta^n \exp\left[-\frac{E_a^{des}(\theta)}{RT}\right] \quad (2.14)$$

where n is the order of desorption. In cases where readsorption is significant, an extra term must be added to Eq. (2.14) [40], resulting in Eq. (2.15):

$$\frac{d\theta}{dt} = k_a(\theta)p(1-\theta)^n \exp\left[-\frac{E_a^{des}(\theta)}{RT}\right] - \nu(\theta)\theta^n \exp\left[-\frac{E_a^{des}(\theta)}{RT}\right] \quad (2.15)$$

where subscripts a and d refer to adsorption and desorption, respectively, and p is the pressure in the gas phase. In the TDS experiment temperature and time are interrelated by the heating rate β , $dT/dt = \beta$, which enables two reaction variables to be studied at the same time. If the sample is heated in a linear manner the following expression can be written, Eq. (2.16):

$$T = T_0 + \frac{dT}{dt} t = T_0 + \beta t \quad (2.16)$$

where T is the temperature at any time t , T_0 is the initial temperature, and β is the heating rate.

If the pumping speed is high enough, so that no readsorption takes place during the experiment, the intensity of the mass spectrometer signal is proportional to the desorption rate r_{des} , and the total area under the desorption curve corresponds to the amount of gas originally adsorbed. According to Eq. (2.14) and Eq. (2.16), the following expression can be rewritten, Eq. (2.17), as a differential equation with respect to the temperature:

$$I(T) \propto \frac{\nu(\theta)\theta^n}{\beta} \exp\left[-\frac{E_a^{des}(\theta)}{RT}\right] \quad (2.17)$$

In general, rate parameters depend on the surface coverage, temperature, adsorbent SSA, and on the adsorbate volume. Since the last two quantities are generally fixed for given desorption systems, the dependence of the rate parameters on these variables is usually neglected. At low temperatures the exponential term (Eq. 2.17) is vanishingly small ($E_a^{des} \gg RT$). The surface just starts to become depleted of adsorbate, and the intensity of the desorption signal is negligible, $I(T) \sim 0$. While increasing the temperature the exponential energy term rapidly increases, most notably when the value of RT approaches that of the activation energy for desorption, E_a^{des} . The intensity of the desorption signal is significant, $I(T) > 0$, goes through the maximum, and then drops back to zero (if the temperature is raised to a sufficiently high value to remove all adsorbed molecules).

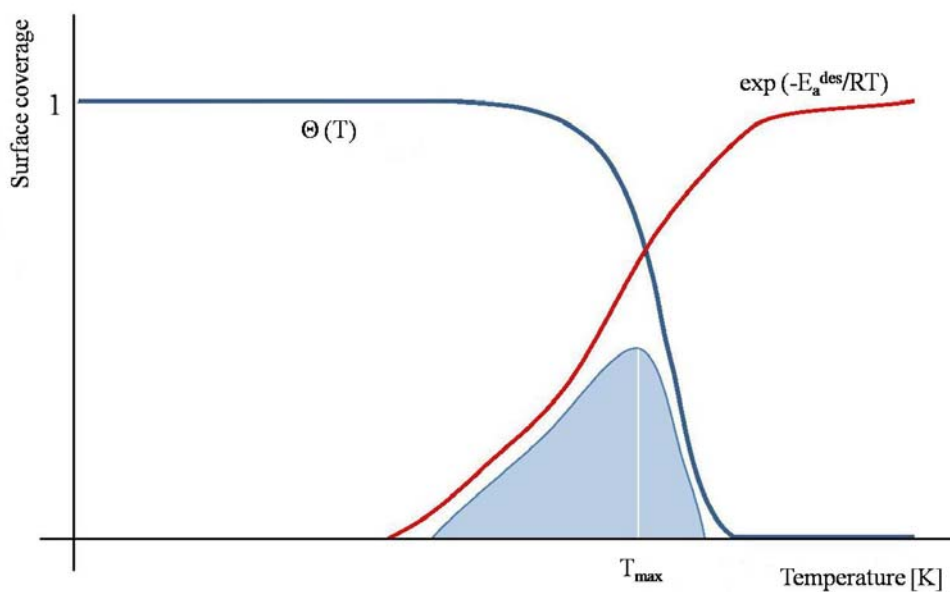


Fig. 2.3 The variation of the pre-exponential term, and the exponential term as a function of temperature. The shaded area represents the desorption spectrum.

The coverage dependence of the rate parameters, unlike the temperature dependence, cannot be neglected, since it is an important variable that may affect kinetic parameters. Both the activation energy of desorption, and the pre-exponential frequency factor depend on the surface coverage, regarding the adsorbate-adsorbate interactions. The shaded area in Fig. 2.3 is an approximate representation of the product of these two functions, and, hence, also an approximate representation of the desorption signal itself.

The shape of the desorption peaks, the position of the peak maximum on the temperature scale, and how both these change with surface coverage are related in a fundamental way, to the desorption process through the order of desorption, and, therefore, provide information on the manner in which the gas is adsorbed. *First-order desorption* kinetics, Eq. (2.18), refers to atomic or non-dissociative molecular desorption, as in the case of physisorption. Eventual interactions with other molecules do not control the rate of desorption.

$$n = 1 \Rightarrow r_{des}(\theta) = -\frac{d\theta}{dt} = \nu(\theta)\theta \exp\left[-\frac{E_a^{des}(\theta)}{RT}\right] \quad (2.18)$$

For the first-order desorption kinetics the following applies²: (1) depending on the value of E_a^{des} the peak maximum temperature also varies – the higher the value of E_a^{des} , the higher will be the peak temperature T_{max} , (2) the desorption peak will show a balance of θ and $\exp(-E_a^{des}/RT)$ terms, (3) the desorption rate is proportional to the instantaneous coverage, (4) the temperature at which the maximum rate of desorption occurs is not dependent upon, and consequently does not change with the initial coverage, (5) the shape of the desorption peak will tend to be asymmetric, with the signal decreasing rapidly after the maximum has been attained.

Several attempts have been made to characterize the asymmetry of a TDS spectrum with one parameter, which then serves as an indicator of the desorption order. This is done by the *Shape Index Analysis* [41] and *skewness parameter analysis*, proposed by Chan, Aris and Weinberg [42]. More commonly, a desorption order is predicted from the shape of the TDS spectra.

Methods of analyzing TDS spectra have been discussed within several publications [30, 31, 42–46]. The simplest method used for acquisition of thermodynamic and kinetic parameters from TDS data is the one described by Redhead [34], *Redhead's desorption peak temperature method*. Using a simple material balance, Redhead showed that the pressure in a high vacuum chamber is proportional to the desorption rate for low-surface-area samples. This method requires a single

² Introduction to Surface Analysis, <http://www.cem.msu.edu>.

desorption spectrum and it is, in principle, valid only for the first-order desorption kinetics, with coverage-independent ν and E_a^{des} . The method can be extended to fractional, or zero-order kinetics if the desorption spectrum corresponds to evaporation from a saturated monolayer [47]. The form of the Redhead equation [48] for the first order desorption kinetics [49] is given by Eq. (2.19):

$$\frac{E_a^{des}}{RT_{max}^2} = \frac{\nu}{\beta} \exp\left(-\frac{E_a^{des}}{RT_{max}}\right) \quad (2.19)$$

which defines the temperature at which the maximum occurs, T_{max} .

Plots of E_a^{des} vs. T_{max} for certain ν and β are almost linear, and are approximated by Eq. (2.20):

$$E_a^{des} = RT_{max} \left[\ln\left(\frac{\nu T_{max}}{\beta}\right) - 3.46 \right] \quad (2.20)$$

An alternative method used for the determination of E_a^{des} , without having to assume a value for the pre-exponential factor, outlined by Redhead [34], and discussed in details by Lord and Kittelberger [50], is the *heating rate variation method*. The method requires a series of TDS spectra at saturation surface coverage for a range of heating rates.

The exact analysis that needs no assumptions, aimed to determination of $E_a^{des}(\theta)$ and $\nu(\theta)$, is called *the complete analysis*, and was first proposed by King [29]. Besides the complete analysis Habenschaden and Küppers [51] have proposed an alternative method, *the threshold or leading edge analysis*, for the direct determination of E_a^{des} and its dependence on the adsorbate coverage.

The TDS technique, in general, has shown to be useful for the determination of the surface area available for reactant adsorption (the active surface area). Examples are found for the oxide-supported metals Pt and Rh, where adsorption occurs on the metal itself, and not on the support [52]. Chemisorptive properties of different catalytic materials and reaction pathways on oxides can be studied, for which purpose the technique was extended to a rather different, but related, experimental technique called temperature-programmed oxidation (TPO). Another related technique is temperature-programmed reduction (TPR), proposed in its present form by Robertson et al. [53]. TPR is used for the observation of mechanistic aspects of reactions under study, the effects of chemical composition, promoter's dispersion, and surface groups on catalyst performance.

2.3 Methods for Measuring the Hydrogen Sorption Capacity

Two primary experimental methods used to measure hydrogen storage capacity of porous adsorbents are (a) the gravimetric method, which provides a direct measurement of the adsorption

capacity, and (b) the volumetric method, which is an indirect method involving the addition of known aliquots of gas to the sample.

In *the gravimetric method (gravimetry)* [54] the hydrogen uptake is directly measured by the mass change of the sample, using a highly-sensitive microbalance, while the apparent weight of the unhydrided sample is used as a counterbalance. The most important correction for gravimetric measurements is the buoyancy correction, the effect of which arises from the displacement of hydrogen gas by the sample and the sample cell, resulting in an upward force on the sample. The degree of the upward force (buoyancy) is proportional to the volume of hydrogen displaced and the density of the surrounding hydrogen at the measurement temperature and pressure [9].

The *Volumetric method (volumetry)*, *i.e.*, manometric method [55] determines the hydrogen uptake by measuring changes in pressure during adsorption and/or desorption within a closed calibrated system at known temperature, following the ideal gas law $PV = nRT$, or ideally the real gas law, $PV = nZRT$, where Z is the hydrogen compressibility at pressure, P , and temperature, T . Any change in pressure beyond the one expected due to the change in volume is attributed to hydrogen adsorption, and used to calculate the number of moles of hydrogen adsorbed by the sample, knowing the pressure, the temperature, and the volume of the gas reservoir and the sample cell. Volumetric measurements assume isothermal conditions, therefore temperature corrections, and the dead space corrections, that account for the volume occupied by the sample itself, have to be made.

A detailed discussion of sources of errors for hydrogen adsorption measurements was given by Broom [56, 57]. Reproducibility studies have been published as well [58, 59].

The hydrogen adsorption capacity can be studied theoretically by the Molecular Simulation methods in which the equations of statistical mechanics are solved numerically for the model of real systems, and the adsorption performance of real or hypothetical materials evaluated based on an atomistic model of its structure using computers. A variety of molecular simulation methods have been used to study adsorption, the Grand Canonical Monte Carlo (GCMC) [60, 61], the Gibbs Ensemble Monte Carlo (GEMC) [60, 62], and the Canonical Ensemble Molecular Dynamics (MD) methods, applied to study gas adsorption in confined and bulk fluids, as a function of pressure and temperature [63]. Simulation methods provide a detailed adsorption mechanism on the molecular scale, which is not easily accessible from experimental methods.

The first reported simulations of gas adsorption in MOF-like materials were published by Kawakami et al. [64]. Ordered, crystalline structure makes MOFs particularly amenable to molecular modeling studies [65, 66].

2.4 Quantum effects

Quantum effects are dynamic effects which occur whenever particles are confined in space [67]. Any spatial constraint by potential walls of sufficient height gives rise to a discrete, mass dependent spectrum of energies. Depending on the shape of the confining potential, the functional dependence on the mass varies. However, the separation between energy levels is larger for the lower mass. If this separation is comparable to, or larger than the thermal energy, then the equilibrium population of the particles over the energy levels has to be evaluated non-classically, and the behavior with temperature of various measurable quantities becomes mass dependent.

The two most important quantum effects are related to zero-point energy, and to tunneling. They are most effectively revealed by isotope effects, that is by variation of properties such as hyperfine coupling constants, diffusion and chemical reaction rates when the mass of the particle changes, and they are particularly important for small masses.

2.4.1 Zero-point energy effects

Particles which are confined in a potential well have zero-point energy, E_0 , which disappears in the classical limit of infinite mass, but it is very significant for hydrogen isotopes confined in regions of space of atomic dimensions. Because of the uncertainty principle, the lowest energy level that a particle can occupy is always above the electronic potential minimum (denoted as the zero-point energy, or the ground-state energy). The smaller the particle, the less well defined its location and the higher its zero-point energy.

If we consider a single structureless particle of a mass m , which moves without friction and in the absence of external forces along the x -axis only, in a one-dimensional square well of length l , the eigenenergies are quantized and determined by the value of n , Eq. (2.21):

$$E_n = \frac{h^2 n^2}{8ma^2} \quad (2.21)$$

where h is Planck's constant, and n is a non-zero integer quantum number ($n = 1, 2, 3, \dots$). For the particle in a one-dimensional square well the least energy value E_0 is that for the quantum number $n = 1$, Eq. (2.22):

$$E_0 = \frac{h^2}{8ma^2} = \frac{5.49 \cdot 10^{-68} \text{ J}^2 \text{ s}^2}{ma^2} \quad (2.22)$$

Apart from the ground state of the system the zero-point energy affects also transition states. If a transition state is a bottle neck, for example when a diffusing atom has to squeeze through the lattice from one interstitial state to the next, the zero-point energy effect in the transition state is dominant, and diffusion of a lighter particle has higher activation energy.

2.4.2 Tunneling

A potential well that rises abruptly to infinity suppresses the wave function of a particle inside the wall to zero. However, infinite barriers do not occur in the real world, and thus the wave functions ψ adopt a non-zero value inside the wall, Fig. 2.4.

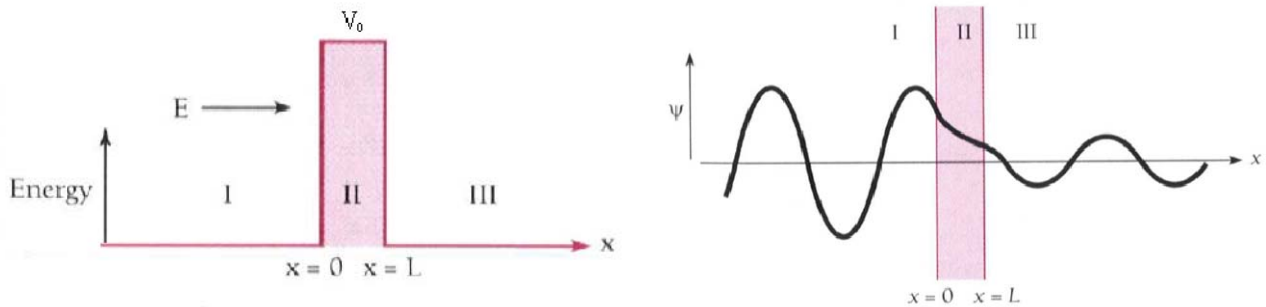


Fig. 2.4 Rectangular potential barrier (left) and a depiction of the particle wave function (right), for a quantum particle which tunnels through a barrier.

According to the Born interpretation $\psi^*(r)\psi(r)$ represents the probability density of finding the particle at a position r in space. Thus, a non-zero value of ψ inside the barrier of height V_0 represents a finite probability of finding the particle of energy $0 < E < V_0$ inside the barrier, with negative kinetic energy. This passage into a classically forbidden region is called tunneling. If the barrier is not infinitely wide the particle can tunnel through the barrier. The transmission coefficient T gives the probability that a particle colliding with the barrier at kinetic energy E is found on the other side of the barrier. For a particle which tunnels through a 1D rectangular barrier of height V_0 and width L , the transmission coefficient T is given by Eq. (2.23) for $x > 1$, and by Eq. (2.24) for $x < 1$ [67]:

$$T = \frac{4(1-x)}{4(1-x) + \sin^2 y} \quad (2.23)$$

$$T = \frac{4(1-x)}{4(1-x) + \sinh^2 y} \quad (2.24)$$

with the relative energy

$$x = \frac{E}{V_0} \quad (2.25)$$

and

$$y = \frac{L}{\hbar} \sqrt{2mV_0 |1-x|} \quad (2.26)$$

The transmission coefficient has a strong dependence on the width of the barrier, and on the mass of the tunneling particle.

Classically, T equals unity for $E > V_0$. Quantum mechanically this is not the case. There are very pronounced oscillations with T , significantly below unity at certain energies, in particular for the heavier particle.

Transmission for $E < V_0$ ($x < 1$) is generally referred to as tunneling since it is classically forbidden. The lighter isotope is favored by several orders of magnitude at low energies, but the selectivity decreases rapidly to unity as the energy approaches V_0 . As a consequence of oscillations in T , the heavier isotope is favored over the lighter one at energies just above the barrier. The high transmission ratio for lighter isotope at low energies dominates the effect even at temperatures which correspond to average energies $E > V_0$.

2.5 Porous Adsorbents

2.5.1 Nanoporous Carbons

Activated Carbon

The term Activated Carbon (AC) is used to describe a wide variety of carbonaceous adsorbents manufactured to exhibit a high degree of porosity. AC is produced by the thermal decomposition of different carbonaceous materials, followed by an activation process. Nearly all carbon-containing organic materials, mainly coals (lignites, bituminous coals, and mineral coals – anthracites), waste wooden materials, and agricultural by-products can be used as AC precursors. Two types of manufacturing processes are employed for AC production, physical (thermal) activation, and chemical treatment. In *physical activation* material is carbonized at 400 to 500 °C, usually in an oxygen-lean environment, which keeps the material from burning, and eliminates most of the noncarbon elements as volatile gaseous species. The residual elementary carbon atoms group themselves into stacks of aromatic sheets, cross-linked in a random manner. The interstices formed

between these aromatic sheets give rise to pores, further developed, and enhanced during the activation process. The carbonized materials react with water steam (+130 °C), blown in at coal temperature of approximately 800 to 1000 °C, to form carbon monoxide and hydrogen which exit as gases, leaving behind a highly porous structure. A second commercial route for producing ACs is by *chemical activation*. It is carried out in a single stage, i.e., carbonization and activation occurs simultaneously. A young carbonaceous material, usually sawdust, is mixed with concentrated solution of a dehydrating agent, mainly phosphoric acid, zinc chloride, or potassium hydroxide. The resultant mixture is heated at relatively low temperature, usually less than 600 °C, under inert atmosphere. The resultant micropores are larger, compared to the ones developed by physical adsorption. The amorphous interspace between graphitic units forms the pore network with size usually in the range of meso- and macroporosity.

Nongraphitizable carbons, such as ACs, have a disordered structure whose essential feature is a twisted network of several parallel carbon layer planes, cross-linked by an extended network of aliphatic bridging groups. The deviations present, such as the interlayer spacing, and the orientation of the layers, serves to break the local symmetry that would lead to elongated, straight domains of actual nanoscale graphite [68]. The layers are composed of condensed regular hexagonal rings, and occur singly or in small stacks of two, three, or four [69, 70], Fig. 2.5. The result is a twisted network, i.e., *turbostratic structure* – the term proposed by Biscoe and Warren [71], coined to describe translation of loosely bonded layer planes along the a-axis, and rotation of layer planes about the c-axis, which is where the term turbo (means: rotation) comes from.

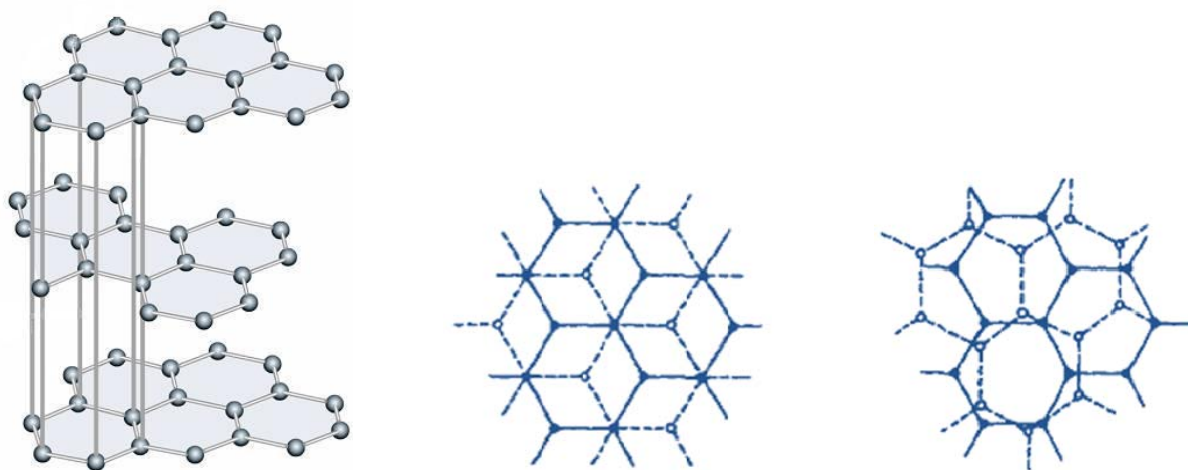


Fig. 2.5 Graphite stacking and pore wall configuration, pointing to 3D hexagonal unit (left). Comparison of 3D crystal lattice of graphite (middle), and the *turbostratic structure* (right) after [72].

ACs are unique and versatile adsorbents. Adsorption by porous carbons dates back to 3750 BC when Egyptians and Sumerians used charcoal for the reduction of copper, zinc, and tin ores in the manufacture of bronze. The first record of the medicinal use of charcoal was found in Thebes (Greece) around 460 BC by Hippocrates and Pliny the Elder, to treat epilepsy, chlorosis, and anthrax. The first application of adsorbent carbons in industry took place in England, in 1794, when the wood charcoal was successfully used to decolorize sugar syrups. The major development took place during the World War I, when adsorbent carbons found its use in the military respirators for protection against hazardous gases and vapors. In 1930's activated carbon material, as known in its present form, was discovered by R. von Ostrejko. Nowadays, about 80% (~300,000 tons/yr) of the total ACs production is used for liquid-phase applications – odor, color, and taste removal, and for removal of organic and inorganic impurities from domestic and industrial waste water (sewage treatment). The remainder is used for gas-phase applications – purification of air in inhabited places (restaurants), and in respirators for work under hostile environments (mining). AC is also used in medicine to combat certain types of bacterial ailments, for adsorptive removal of certain toxins and poisons, and purifications of blood.

Carbon Molecular Sieves

Carbon Molecular Sieves (CMSs) are a specialized class of AC, designed to contain primarily narrow micropores on the order of molecular dimensions. The size of the micropores, with effective micropore diameters ranging from about 4 to 9 Å [73], is optimized to admit small molecules, and exclude large ones. The most suitable natural precursors are cellulosic and animal materials, anthracite-, bituminous-, and brown coal, lignocellulosic materials (macadamia nut shells [74, 75], and walnut shells [76]), coconut shell char, pitch, wood charcoal, bones, and coke. The inherent pore structure of the precursor is set into a suitable pore range by controlled thermal treatment. When natural precursors are used controlled activation by oxidation is required as well [77]. Irrespective of the source of the CMSs, the final tailoring of the pore apertures is performed by coating the pore opening either by chemical vapor infiltration (CVI) with hydrocarbon gas, or by impregnation with the thermosetting polymers. The deposition of carbon has to be carefully controlled so as to deposit carbon on the pore entrance itself, and reduce the micropore opening without decreasing the pore volume (Fig. 2.6). Partially blocked pores can be subsequently and selectively gasified in carbon dioxide, to open the micropore to appropriate size.

Most of the early work in the CMSs field was promoted by the results of Walker's group [78–80], using polymers as precursors. The basis for the commercial production of CMSs were developed from the Bergbau Forschung Institute for coal research in Germany, by Jüntgen and co-workers

[81–83], using bituminous coal and anthracite, Fig. 2.7. The Takeda Chemical Company (Japan) and Bergbau Forschung (Germany) are the leading manufacturers of CMSs used all over the world, accompanied by the MAST (UK), and the Carbon Membranes (Israel).

The most important large-scale application of CMSs is for the separation of nitrogen from air by a pressure-swing adsorption (PSA) process [84].

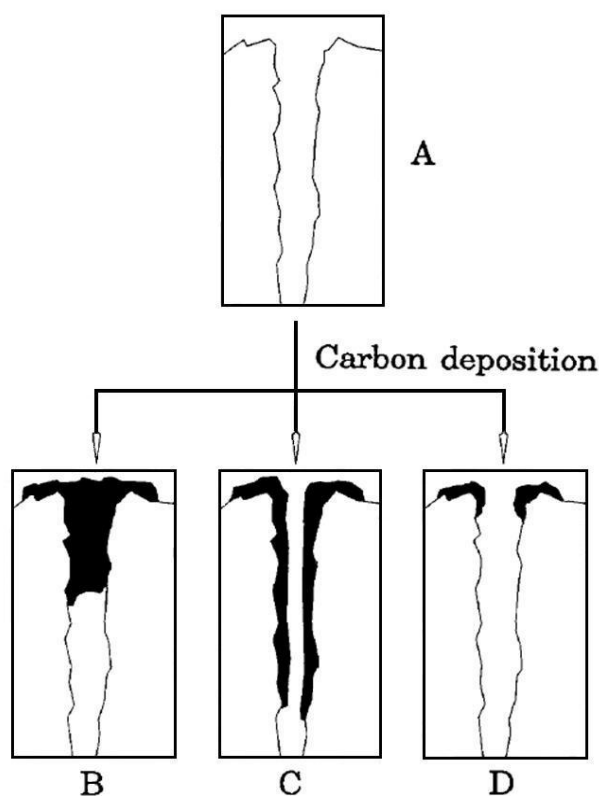


Fig. 2.6 Schematic representation of carbon deposition onto/into a pore via pyrolysis, comprising uncoated micropores (A), deposition of carbon resulting in blockage of the pore (B), deposition of carbon on the pore walls (C), deposition of carbon on the pore openings (D), redrawn from [73].

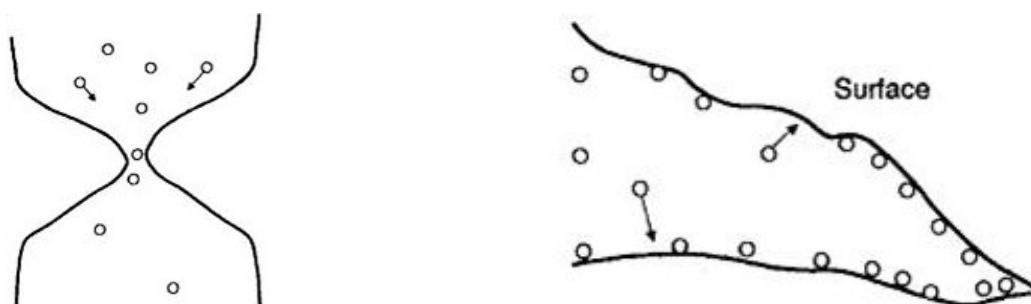


Fig. 2.7 Molecular sieve carbons made by the Bergbau-Forschung: type CMS N₂ with bottlenecks near 0.5 nm formed by the coke deposition at the pore mouth (a), and type CMS H₂ formed by the steam activation (b). Redrawn from the reference [83].

2.5.2 Metal–Organic Frameworks

Metal Organic Frameworks (MOFs), also known as porous coordination polymers or supramolecular structures, are the subgroup of inorganic–organic hybrid materials constructed by self-assembling of metal ions with polyfunctional organic ligands via coordination bonds, designed to form a rigid and stable 3D network.

The phrase *Coordination Polymers* appeared in the early 1960s [85], the area was first reviewed in 1964, when the first synthesis and publication on novel materials which, nowadays, might be addressed as MOFs was reported by Tomic in 1965 [86].

In the past these materials suffered the lack of framework stability, and although several prominent examples were identified, many structures did not retain the porosity after treatment under mild conditions in vacuum, i.e., after removing the solvent molecules. MOFs reported by the group of Robson in the early 1990s [87, 88] had little or no practical applicability. Nevertheless, this group of researchers should be recognized for contemplating a concept of postsynthetic functionalisation of MOFs for the first time [89], an approach widely exploited in the MOF chemistry today. The pioneering work of O. Yaghi [90] and S. Kitagawa [91] led to the successful synthesis of MOFs which exhibited permanent porosity, and turned out to be a breakthrough in the MOF chemistry. The term MOFs, itself, was coined by Yaghi [92, 93]. To date, there are tens of thousands of MOFs catalogued in the Cambridge Structural Database (CSD) [94]. A system of nomenclature for common nets, and some of their properties has been developed, and can be accessed through a web-based database known as the Reticular Chemistry Structure Resource (RCSR) [95]. Differences in the MOF nomenclature itself do exist, and merely reflect the type of the framework, and individual research group (institution) who conducted the synthesis.

Infinite, crystalline 1D–3D MOF architectures are designed from the assembly of discrete metal centers, or small metal–containing polynuclear subunits (clusters, chains, or layers), which act as the nodes of the framework, and multidentate organic bridging ligands employed as linkers.

Usually divalent (Zn^{2+} , Cu^{2+}), or trivalent cations (Cr^{3+} , Al^{3+}) are used, and mainly carboxylate-based ligands, containing N- or/and O-donor atoms. The framework structure and chemical functionality are governed by the properties of these main two components. Coordination numbers can range from 2 to 7, giving rise to various geometries – linear, T- or Y-shaped, tetrahedral, square-planar, square-pyramidal, trigonal-bipyramidal, octahedral, trigonal-prismatic [96], and pentagonal-bipyramidal [97]. The resulting structures possess tunnels or cavities with pore sizes between 3 and 34 Å [98], giving rise to 1D- (chain), 2D- (layer), or 3D- networks [99]. Some MOFs are known to exhibit high framework flexibility, and shrinkage/expansion due to inclusion/exclusion of guest molecules, leading to breathing effects [97, 100], Fig. 2.8.

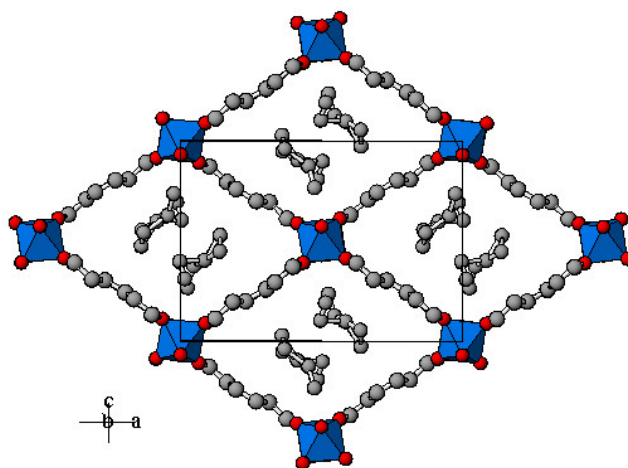


Fig. 2.8 Views of the 3D structure of $\text{Al}(\text{OH})[\text{O}_2\text{C}-\text{C}_6\text{H}_4-\text{CO}_2][\text{HO}_2\text{C}-\text{C}_6\text{H}_4-\text{CO}_2\text{H}]_{0.70}$ or MIL-53, a MOF with flexible spatial structure, showing the channel system.

MOFs can be engineered to have high skeletal density. The total lack of non-accessible bulk volume gives them, on a weight-specific basis, the highest porosities and exceptionally high surface area for crystalline materials [98, 101], a record unprecedented in zeolite chemistry. Remarkable values for surface areas, exceeding $5000 \text{ m}^2 \text{ g}^{-1}$, were reported for MOF structures MIL-101 [98], UMCM-1 [102], and UMCM-2 [103]. The highest surface area reported to date is claimed for MOF-210, with the BET surface area of $6240 \text{ m}^2 \text{ g}^{-1}$ and Langmuir surface area of $10.400 \text{ m}^2 \text{ g}^{-1}$ [104], which is considerably greater than crystalline zeolites with the highest surface area of $904 \text{ m}^2 \text{ g}^{-1}$ [105], and also higher than the theoretical maximum value obtained for carbon adsorbents ($2630 \text{ m}^2 \text{ g}^{-1}$ based on the coverage of the two sides of a graphene sheet [106]). These outstanding values for surface area give to MOFs the ability to behave as hosts for certain molecules, while the large surface area is considered to be a prerequisite for large adsorption capacity.

In 1997 the group of Prof. Kitagawa first reported gas adsorption on MOFs [91], while the first report of MOFs as potential hydrogen storage adsorbents was published by Prof. Yaghi and co-workers in 2003 [107]. MOF-5, a zinc-terephthalate with a cubic framework structure, demonstrated an uptake of 4.5 wt.% of hydrogen at 77 K, and 1 wt.% at RT and 20 bar. Since then, at least 150 unique MOFs have been evaluated for their ability to store hydrogen. Among thousands of reported structures, for many years, the benchmark for H_2 adsorption in MOFs was 7.5 wt.% and 32 g L^{-1} at 77 K and 70 bar for MOF-177 [59]. Only recently, a new record was published by Yaghi which reports surface excess hydrogen uptake in MOF-210 of 8.6 wt.% [104], higher than the one in MOF-177.

Holistic and systematic approaches are shown to be necessary to understand the mechanism, structure, and thermodynamics of storage materials. Coupled with measurements of porosity, many methods have been developed to obtain a detailed understanding of the localizations of hydrogen within the porous sorbents, especially MOFs. Radiation scattering techniques provide extensive information about the microstructure of porous materials, and about the state of molecules adsorbed at surfaces, and within the pores. The crystalline nature of MOFs allows a high degree of structural characterization to be achieved through X-ray diffraction methods, used as well for direct observation of hydrogen in the pores [108, 109].

The most reliable experimental method for obtaining a molecular level understanding of hydrogen adsorption in nanoporous adsorbents, especially in the crystal lattice of the MOFs, is neutron powder diffraction. Neutron diffraction yields a structure that is representative of bulk specimens, and enables *in situ* measurements using special sample containers. Because of the large incoherent cross section of H₂ the neutron diffraction data are collected on deuterated-MOF samples. Inelastic neutron scattering has been used to explore the site-specific interactions of hydrogen with MOF framework, and the energies of those binding events [110]. Light scattering techniques, IR spectroscopy [111], and Raman spectroscopy [112, 113], were also applied to gain additional information on the binding sites of H₂. Density functional theory (DFT) calculations were employed as well to calculate the equilibrium density profile for all H₂ locations in simple pore geometries such as slits [114], or cylindrical capillaries [115].

MOFs, an emerging new class of porous solids, have found promising applications for the storage of small molecules (H₂, CH₄, CO₂, etc.) [116–118], catalysis [119, 120], selective gas adsorption, and separation [121, 122], drug delivery [123], etc.

Chapter 3

EXPERIMENTAL METHOD

Thermal Desorption Spectroscopy (TDS)

3.1 The Fundamental and Experimental Advantages of the TDS Technique

Characterization of porous adsorbents by gas adsorption was conducted by performing Thermal Desorption Spectroscopy (TDS) measurements with a special experimental set-up, suitable for cryo-adsorption. Compared to the other experimental methods, commonly applied for the characterization of porous adsorbents, i.e., the volumetric and gravimetric methods (Chapter 2.3), the TDS method has several prominent advantages. The particular advantage of TDS, especially when carried out with quadrupole mass spectrometer (QMS), is that apart from the atoms/molecules expected to desorb from the surface other evolved species can be identified as well, whereas the other two methods are non-selective. While the gas delivery system itself contains a certain amount of water, usually on the order of several *ppm*, small sample quantities and prolonged exposure to the hydrogen stream may lead to significant water adsorption. The water contamination may be misinterpreted as hydrogen adsorption, especially when the gravimetric method is applied. Since the weight of a H₂O molecule is equal to the weight of nine H₂ molecules, 0.5 wt.% of H₂O adsorbed can be regarded as 4.5 wt.% of H₂ capacity. The volumetric method, on the other hand, can quantify the change in a measurable property (pressure) to indirectly calculate hydrogen concentration, and rely on the assumption that the change in the direct variable used for correlation during adsorption/desorption is due to hydrogen gas alone.

The TDS method is quick, compared to the time-consuming experimental studies of adsorption equilibria, and determination of the static sorption isotherms. Moreover, there is a fundamental

theoretical reason why the amount that desorbs is much more sensitive to temperature changes, used in TDS studies, than to the changes of pressure, commonly used in the isothermal studies of adsorption equilibrium. Temperature appears in the exponential terms of the appropriate thermodynamic expressions, whereas pressure is essentially a multiplying factor in these expressions. Thus, for both experimental and theoretical reasons, studies of thermodesorption kinetics are more suitable to obtain qualitative and quantitative information about the surface heterogeneity of solid surfaces [124].

The application of theoretical methods (Chapter 2.3) for the characterization of crystalline adsorbents is straightforward, because the structural model can be obtained from crystal structure data. However, it is often necessary to “idealize” the structure by removing remanent solvent molecules, and signs of structural disorder.

3.2 The Design of the Experimental Apparatus

The TDS experiments were carried out using an in-house designed and built experimental set-up. The instrument has been rebuilt, and the completely novel experimental chamber constructed. This includes advances in the especially designed sample cell, which enables tight connection with the copper block, improvements in the furnace and insulation design, using ceramic tubes of better dimensions and insulating capability, the usage of new temperature sensors, positioned closer to the sample cell, optimization of the heating parameters, so as to obtain a linear heating ramp, and small incremental improvements which accumulated to improve the desorption measurements.

The set-up consists of three main compartments – the sample chamber compartment as the central part, the flowing helium cryostat as the lower part, and the upper part comprising the QMS, intended for detection, Fig. 3.1. The stainless steel chamber is connected to a couple of heating elements, and a flowing helium cryostat. The sample cell, made out of copper, is positioned in the lower, central part of the chamber, and screened by the copper block, used as a shielding to diminish temperature oscillations of the flowing helium cryostat. A resistive heater, controlled by the proportional–integral–derivative temperature programmer allows the temperature to be ramped up and down with a chosen heating rate, or work in isothermal conditions in the temperature range between 20 and 500 K.

The heating rate can be varied over one order of magnitude, in the range of 0.10 to 0.01 K s⁻¹. A Platinum resistor (Pt103) is used to measure the temperature. For a reference, additional thermo element (NiCr–Ni) is used for monitoring the temperature throughout the experiment. The temperature in the cryostat itself is monitored in two steps – with the Pt100 resistor, and with an AuFe512 thermocouple.

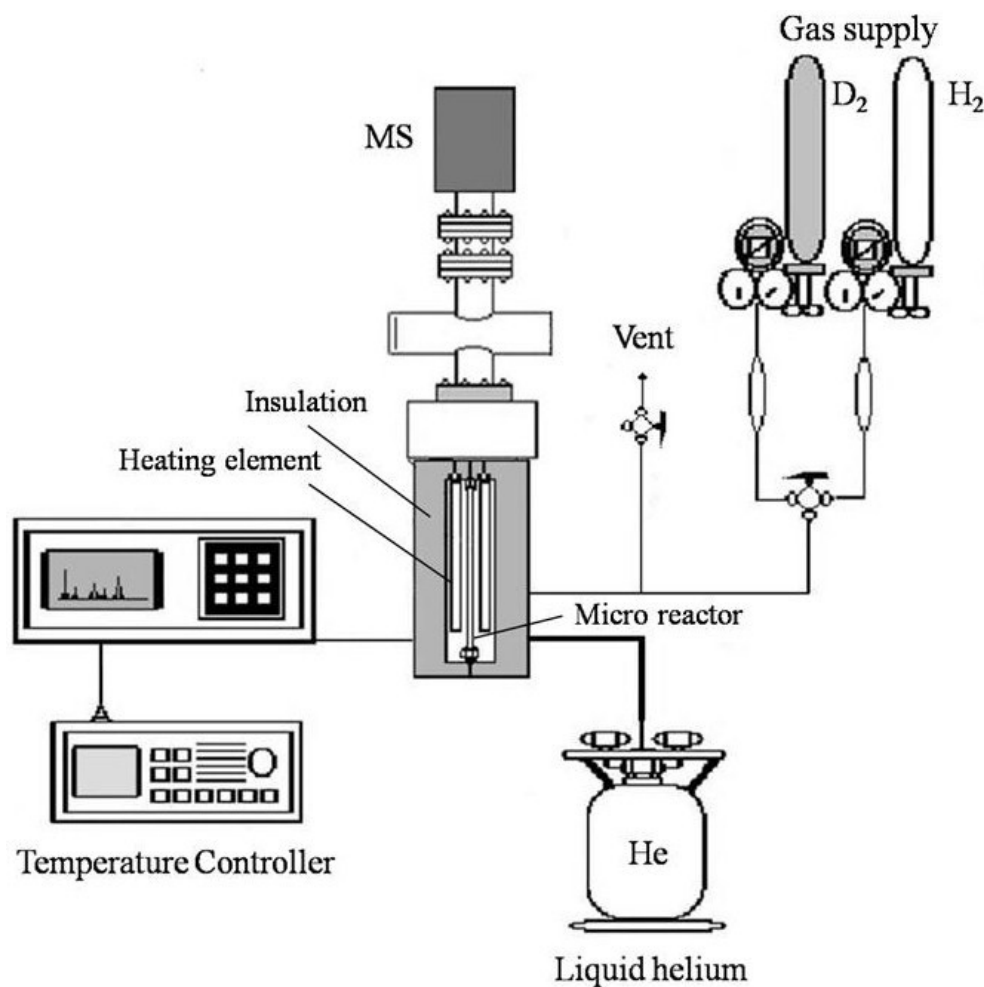


Fig. 3.1 Detailed flow diagram of the low-temperature TDS apparatus design with main components indicated in the picture.

The equipment comprises a low-pressure gas handling panel, designed to allow two different gases, or mixtures thereof to be loaded. Valves are disposed in a way that dead volumes are minimized and easily vented. The gas pressure, in an mbar pressure range, is adjusted manually by a needle valve. Basic evacuation of the sample chamber is carried out with a 56 l s^{-1} turbo molecular pump (PFEIFFER BALZERS TPH 062), backed with the fore pump. Desorption products leaving the chamber are closely monitored by an on-line QMS, supplied by the Spectra Satellite 100 D-HP. The spectrometer is placed right above the sample chamber, in a small ultra high vacuum (UHV) chamber pumped by the turbo molecular pump Varian (TURBO V-70 C.U.). It is held at a temperature between 32 and 35 °C. Whilst heating the sample in a controlled manner, desorption of species with a mass to charge ratio of up to 100 amu can be monitored. The temperature-time profile is recorded throughout the experiment, and data stored in the computer memory (RGA for Windows-Software), so that the TDS curves for several fixed masses can subsequently be constructed.

3.3 The Principle of the Measurement

The complete measuring procedure has been optimized and further improved to increase the sensitivity of measurements.

Before any adsorption measurements are undertaken, the adsorbent is pretreated under HV-conditions to remove all physisorbed molecules residing on the adsorbent surface (moisture or any impurity adsorbed from the air), and in the pores (molecules captured after synthesis). Out-gassing is carried out using a constant heating rate of 1 K s^{-1} up to a specified temperature plateau, for the duration of several hours. The out-gassing procedure is repeated prior to each new experimental run by heating the sample at elevated temperature under HV for more than 1 h, to provide a reproducible state of the adsorbent surface.

Furthermore, after every change of the sample, the experimental equipment was completely backed out, to avoid extended water and air contributions to the background spectrum. Depending on the state of the mass spectrometer used, the filament itself can be partially oxidized and hydrogen can reduce the filament to create water, unless a complete back out of system is regularly performed.

The quantity of the sample employed for TDS measurement (ordinarily 3 to 5 mg) is kept sufficiently small to enable good correspondence to the sensitivity of the mass spectrometer ($2 \cdot 10^{-11}$ mbar), i.e., to detain evolution of gas molecules in the range of linear operation of the mass spectrometer.

A well-known quantity of gas, in the range of 1 to 700 mbar, is introduced at RT, and the sample cooled down to about 20 K under the gas atmosphere. During adsorption the sample chamber is isolated from the excess of gas coming from the gas inlet. When adsorption equilibrium is attained, the chamber is evacuated to remove residual gases and re-attain HV conditions. Before starting the measurement the pressure changes are monitored mass spectrometrically for about 15 min., until a good signal-to-noise ratio is attained. Then the sample is subjected to a heating regime in a controlled manner, so as to give a linear temperature ramp. All desorption products liberated from the sample are continuously monitored, and the intensity variation of each recorded mass fragment is measured as a function of time and temperature.

During desorption the m/Z signals of 1 amu (corresponding to atomic hydrogen), 2 amu (corresponding to molecular hydrogen, atomic deuterium), and 18 amu (corresponding to water) are recorded. In the case of measurements with deuterium additionally the m/Z signals of 3 amu (corresponding to hydrogen deuteride), and 4 amu (corresponding to deuterium) are recorded. No desorption of any water was observed in the temperature range where H_2/D_2 desorption is pronounced, most commonly from 17 to 120 K. In addition, blank experiments, with the empty

sample cell were performed, to investigate possible contributions to the measured spectrum. The amount of gas stored within the sample cell is found to be negligible.

3.4 Calibration with Pd

In order to achieve accurate data acquisition and quantify the amount of gas desorbed, the output of the mass spectrometer was calibrated with a well known standard, Pd powder (PD-1010, ABCR Karlsruhe), with a mean particle size of 60 μm , for both hydrogen and deuterium gas. Prior to measurements Pd powder was out-gassed at 500 K under HV. It was hydrided/deuterated by loading 700 mbar of H_2/D_2 at RT, and the experiment performed following the procedure previously described. The TDS spectrum, Fig. 3.2, is recorded with a constant heating rate of 0.10 K s^{-1} , in the range of 20 to 370 K.

Because of the HV condition practiced the mass spectrometer signal is directly proportional to the desorption rate (Chapter 2.2), while the area under the desorption curve is directly proportional to the total amount of hydrogen/deuterium desorbed. Upon hydriding/deuterating Pd with 700 mbar of gas there is a co-existence of β - and $\alpha+\beta$ -phase. The relationship between the pressure and concentration in the β phase can be described by the phenomenological Eq. (3.1) [125]:

$$\ln\left(\frac{p_{\text{H}_2}}{p_{\text{D}_2}}\right) = -A(T) + B(T)\left(\frac{x}{Pd}\right) \quad (3.1)$$

where x represents the H/Pd (D/Pd) atomic ratio, p is the H_2 (D_2) pressure, and A and B are temperature dependent constants. The values for A and B decrease with increasing temperature, and are calculated according to ref. [125].

The gas desorption starts around 200 K, the spectra develop a sharp desorption maximum at around 310 K, which can be correlated to the $\alpha+\beta$ region of the PdH_x phase diagram [126], accompanied by a broad desorption shoulder at about 250 K into the β region, Fig. 3.2. Under stated experimental conditions the corresponding deuterium content (D/Pd ~ 0.67) is slightly lower than the corresponding hydrogen content (H/Pd ~ 0.70). This yields a storage capacity of 0.66 wt.%, and 1.23 wt.% for hydrogen and deuterium, respectively [125]

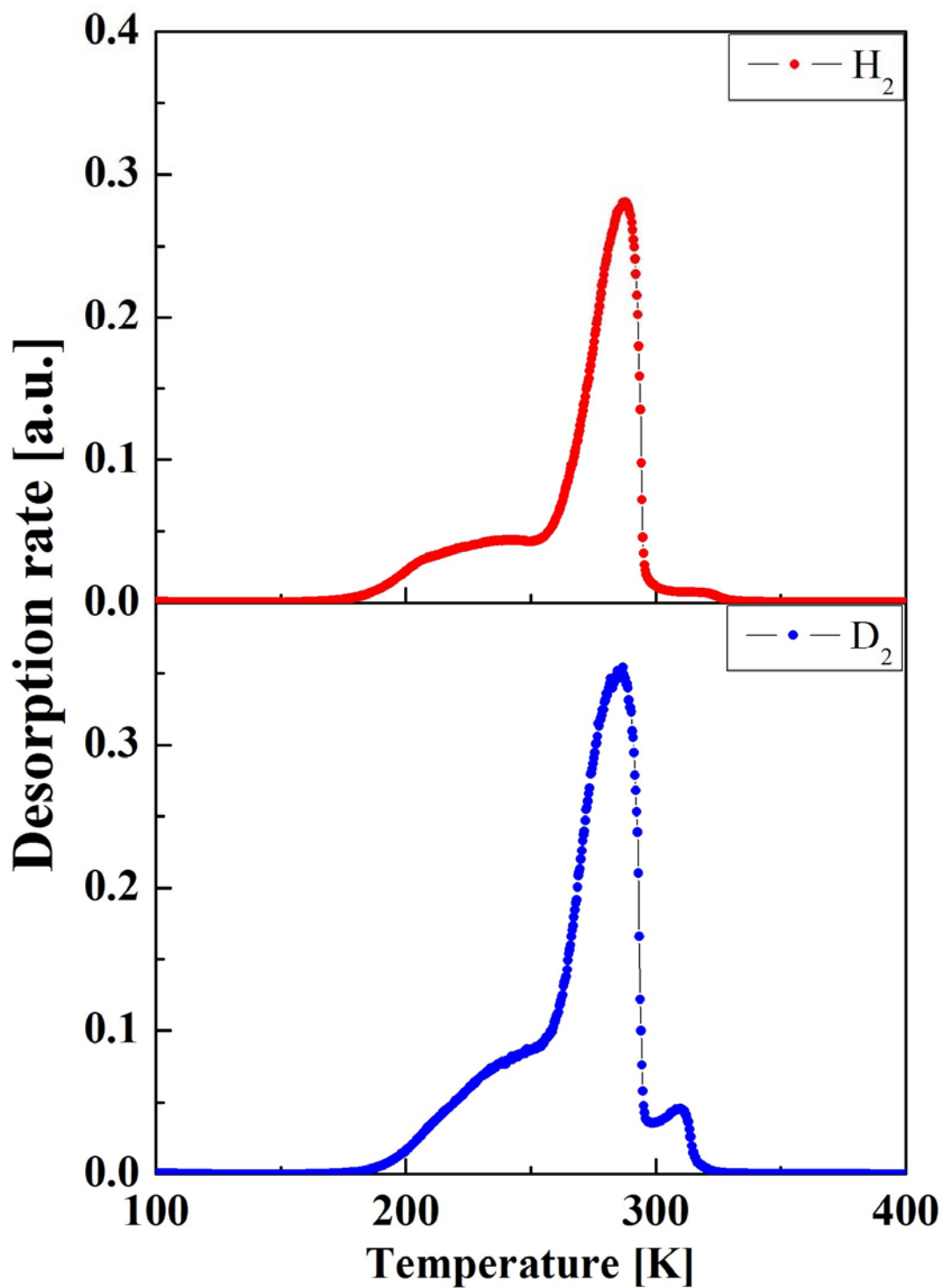


Fig. 3.2 The TDS spectra of hydrogen/deuterium in Pd recorded with the heating rate of 0.10 K s^{-1} . The spectra are presented in the temperature range from 100 to 400 K.

Chapter 4

CARBON MOLECULAR SIEVES

4.1 Investigated samples

Commercially available CMSs, Takeda 3A, -4A, and -5A (hereafter denoted as T3A, T4A, and T5A, respectively) have been obtained from Takeda Chemical Industries Ltd. Japan (commercial code names: SHIRASAGI MSC-3K-Type 172 for T3A, SHIRASAGI MSC-4A for T4A, and SHIRASAGI XZM-4/6 for T5A), in the form of pelletized extrudates of cylindrical shape (approximate diameter: 1.9, 2.2, and 3.5 mm for T3A, T4A, and T5A, respectively).

T3A is produced by carbon deposition on a microporous substrate resulting from the carbonization of a coconut shell [127]. Due to a considerable amount of potassium that mineral matter of coconut shells contains, ACs based on coconut shell has a high density, extraordinary hardness, and high and narrow micropore distribution. T4A consists of microparticles with a radius of the order of several microns [128], and it does not show an ordered hierarchical pore structure [129], due to the pelletization procedure commonly employed in the production of commercial CMS materials [130]. The micropores of T4A have slit-like openings, located between the two graphitized carbon layer planes [128]. T5A is a coconut shell based molecular sieve used in pressure swing adsorption (PSA) gas separation processes (N_2 from air, CH_4 from CH_4/CO_2 mixture, C_2H_4 from mixtures of gases), first described by Jüntgen and co-workers at the Bergbau-Forschungs-Institute for Coal Research [83]. The pellets are formed by agglomeration of discrete microparticles of the order of a micron, where the interstitial voids and microparticle porosity give the pellet its porous structure [131].

4.2 Sample Characterization

4.2.1 Adsorption Studies

The sorption properties, as well as the porous structure of the three carbon materials were probed by N₂ (77 K), CO₂ (273 K), and H₂ (77 K) low pressure (up to 1 bar) adsorption measurements, using an automatic volumetric adsorption system (Autosorb-1 MP, Quantachrome). In order to minimize any possible diffusion limitations T3A was ground with pestle and mortar, and used as a powder, while T4A and T5A were used as received. Prior to all adsorption measurements the samples (typically 50 – 85 mg) were out-gassed at 523 K (for about 12 h) under high vacuum ($<10^{-5}$ mbar). The N₂ data (77 K) were corrected for thermal transpiration effects, while the equilibration time was set to at least 5 min. Longer equilibration (up to 30 min./point) was used when slow kinetics were revealed (e.g. for T3A, H₂ adsorption at 77 K). The N₂ (77 K) isotherms were analysed in terms of surface area and pore volumes on the basis of the Brunauer–Emmett–Teller (BET), Dubinin–Radushkevich (DR) and t–method (carbon–black) approximations. Additionally, Grand Canonical Monte Carlo (GCMC) simulated adsorption isotherms in slit pores of varying width [132] were used to derive CO₂ based pore size distributions from the adsorption branches of the isotherms.

4.2.2 Thermal Desorption Studies

The TDS measurements were performed using hydrogen and deuterium as probe molecules, as well as gas mixtures at 20 K. The spectra were initially recorded in the temperature range from 20 to 370 K using two distinct heating rates, 0.10 and 0.01 K s⁻¹. For all measurements the m/Z signal of 18 amu (corresponding to water desorption) was recorded, and found not to influence desorption spectrum in the relevant temperature range. The desorption rate is expressed by the number of molecules per second, per gram of sample, thus, the intensity of desorption can be easily compared for different samples.

The amount of desorbed gas was determined quantitatively using calibration with Pd. All contributions below 27 K for hydrogen, and below 30.3 K for deuterium were subtracted (this region is associated with multilayer formation, typical for the development of a common leading edge in the TDS spectra, especially pronounced for higher coverages).

Due to the limitations of the permissible sample holder opening (1.7 mm), compared to the sizes of the CMS pellets, the samples were grinded in an agate mortar, and smaller pieces were used for measurements. The samples (with mass typically in the range of 3–5 mg) were out-gassed at 523 K for several hours under high vacuum, before the exposure to gas, but also after each desorption measurement for more than 1h, to obtain a reproducible state of the adsorbent surface.

4.3 Results

The presentation of the results within this thesis is organized in the following manner. The important experimental findings are summarized graphically and narratively within the Results section. These data are supported with the additional information given as figures, and/or tables in the Appendix section, identified as A, B, etc. An interpretation of the results of the work is given in the Discussion section, followed by the short Conclusions section at the end of the chapter. The main conclusions of the study are given in the separate, Conclusions chapter, at the end of the manuscript.

4.3.1 Pore Structure Characterisation

The experimental N₂ adsorption isotherms at 77 K for the three CMS samples are presented in Fig. 4.1. Unlike T4A, and T5A, which revealed significant adsorption capacities, T3A adsorbed negligible amounts of N₂ at 77 K. This can be attributed to the very small pore size within T3A (or small pore openings), which strongly hinders N₂ diffusion, making, thus, the pore network practically inaccessible for N₂ molecules (especially at 77 K). However, a measurable amount of gas was adsorbed at high relative pressures ($p/p_0 > 0.9$), implying the existence of macroporosity. The N₂ adsorption isotherms of T4A, and T5A are of type I, i.e., typical for microporous solids, and show a significant uptake (T5A adsorbs more than T4A) at very low relative pressures ($p/p_0 < 0.1$), which levels off to a plateau region. This region is not entirely horizontal, but has a small increasing slope for both samples. The increase can be due to the existence of a small number of mesopores, network alterations upon adsorption (e.g. swelling), or due to a very constricted part of the porous system, where molecules can enter either at high pressures, or after a long time (i.e. the time needed to reach higher relative pressures).

Both T4A and T5A reveal hysteresis. However, T5A has a clear H4 loop which closes at $p/p_0 = 0.45$, while hysteresis persists down to very low relative pressures for T4A. Such low pressure hysteresis is commonly related to structural changes (e.g. opening of confined spaces and molecular entrapment therein). In the present case these changes are consistent with the small upward slope observed in the plateau region.

While it was rather easy to measure adsorption isotherms at very low relative pressures ($p/p_0 < 10^{-6}$) for T5A, it was practically impossible to do so for T4A, due to extremely long equilibration times, combined with small pressure differences recorded. This observation is compatible with very slow N₂ diffusion for T4A (due to pore opening constrictions). Therefore, the very low pressure points of the T4A isotherm might not represent the real equilibrium values.

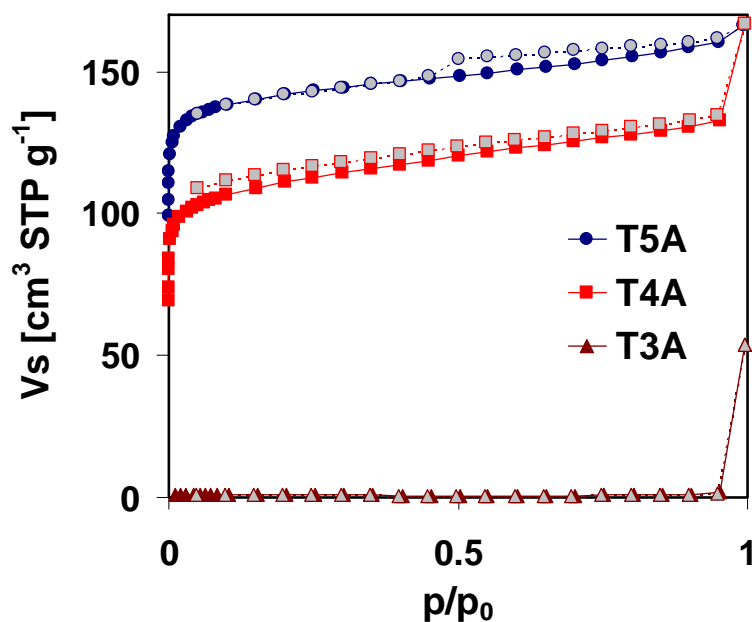


Fig. 4.1 Experimental N_2 adsorption isotherms at 77 K.³

The CO_2 adsorption isotherms at 273 K are presented in Fig. 4.2. Opposite to N_2 adsorption at 77 K, considerable CO_2 adsorption is observed at 273 K, for all three investigated samples. As expected, at such high temperatures diffusion limitations are minimized, and the T3A pore system is fully accessible to CO_2 molecules.

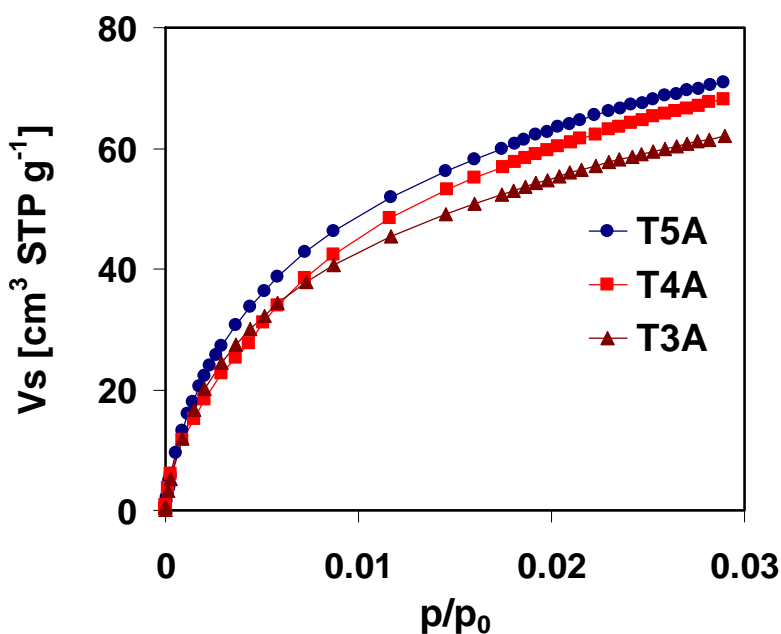


Fig. 4.2 Experimental CO_2 adsorption isotherms at 273K.

³ Adsorption measurements, as well as GCMC simulations courteously by Dr. T. Steriotis and co-workers.

The amounts adsorbed at around 1 bar ($p/p_0 \sim 0.29$) follows the trend $T5A > T4A > T3A$. However, at lower pressures ($p/p_0 < 6 \times 10^{-3}$) a cross-over is observed, revealing higher uptake for T3A, compared to T4A. The latter is compatible with the existence of smaller pore sizes in T3A, compared to T4A. As the pore size decreases, the pore wall potentials overlap, and create deeper energetic minima. Thus, in smaller pores adsorption is stronger. However, due to the limited pore volume, small pores are completely filled at lower relative pressures (compared to larger ones), giving rise to such isothermal curves cross-over. Indeed, after fitting the experimental adsorption isotherms with the aid of a carbon slit/ CO_2 CGMC kernel and, thus, deducing the micropore size distributions (Fig. 4.3), it becomes evident that T3A has the narrowest pores of all the samples (the majority of the effective microporosity is around 0.35 nm). On the other hand, T4A has a similar pore size with T5A (the respective pore size distributions are centered between 0.5 and 0.55 nm), but also contains some very narrow pores (< 0.5 nm). The calculated DR micropore volumes and surface areas, as well as the micropore volumes derived from the GCMC fitting of the isotherms, are listed in Table A-1.

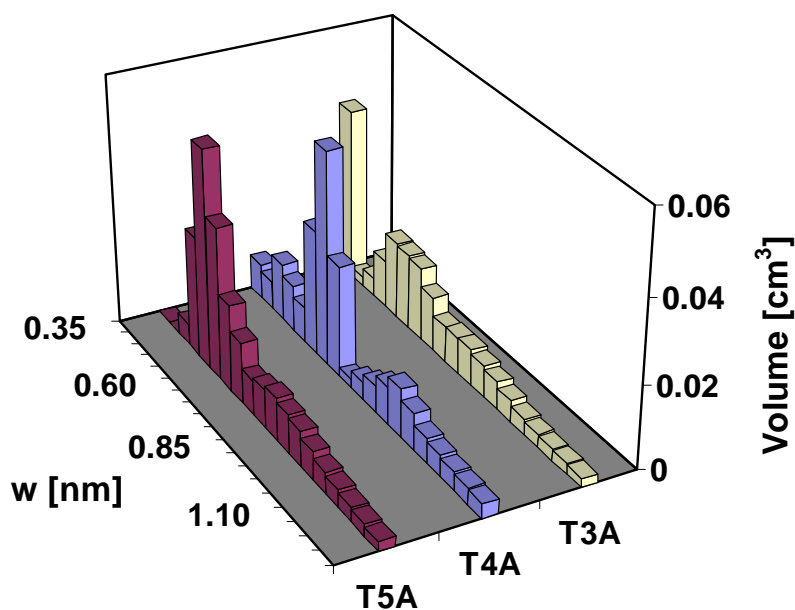


Fig. 4.3 GCMC pore size (width, w) distributions, based on CO_2 adsorption isotherms (273 K).

Unlike zeolites, or MOFs samples, carbon samples may differ in porosity regarding to different sample batches. Therefore, it was necessary to perform independent porosity characterization and base discussion on these findings. Nearly for illustration, available porosity data published in the literature for the three investigated CMS samples are summarized in Table A-2. A fair agreement is found.

4.3.2 Hydrogen Adsorption

The hydrogen adsorption isotherms for all samples are presented in Fig. 4.4. Overall, the T4A and T5A isotherms show very similar behaviour. Subtle differences are observed at low pressures, where a curve crossover is observed, and T4A reveals stronger adsorption than T5A. Both isotherms are fully reversible. T3A, on the other hand, exhibits a hysteretic behaviour even at low pressures, which is attributed to the slow kinetics of hydrogen at 77 K in the narrow sized micropores. A tremendous difference of hydrogen diffusivities between T3A and the other two samples becomes evident when kinetic uptake curves are plotted. A typical example for $p = 1.33$ mbar is presented in Fig. 4.5.

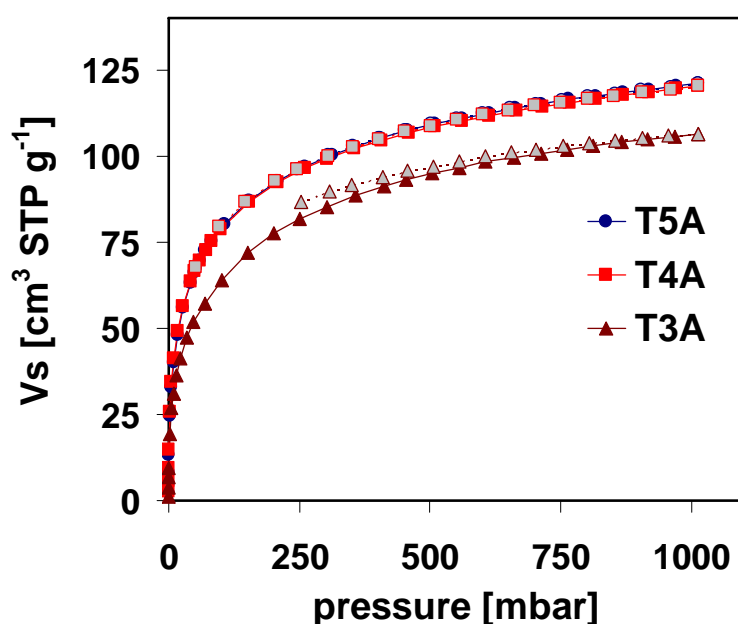


Fig. 4.4 Experimental H₂ adsorption isotherms at 77 K.

4.4.3 Hydrogen/Deuterium Desorption

In Fig. 4.6 a comparison is given for hydrogen and deuterium TDS spectra of T3A. The spectra are obtained for three different initial gas loadings (50, 500, and 700 mbar), and recorded with the heating rate of 0.10 K s^{-1} . The desorption profile has the same shape for both H₂ and D₂, apart from a pronounced difference in the intensity of the desorption spectra. Most interestingly, the T3A desorption spectra clearly show two separate, distinguishable desorption regimes, at low and high temperature. At low temperature a small desorption shoulder is observed at 25 K, while two additional maxima appear at 33 and 44 K (700 mbar hydrogen loading). At high temperature a pronounced, nearly symmetric peak centered at 122 K is observed, while the amount of gas desorbed above 180 K is found to be negligible. Desorption maxima are centered at 35, 45, and 119

K for deuterium desorption (700 mbar gas loading). A slight shift in the position of the desorption maxima toward lower temperature is observed for increased gas loading. The total amount of gas desorbed is calculated to be 0.30 wt.% and 0.97 wt.% for hydrogen and deuterium, respectively (700 mbar gas loading).

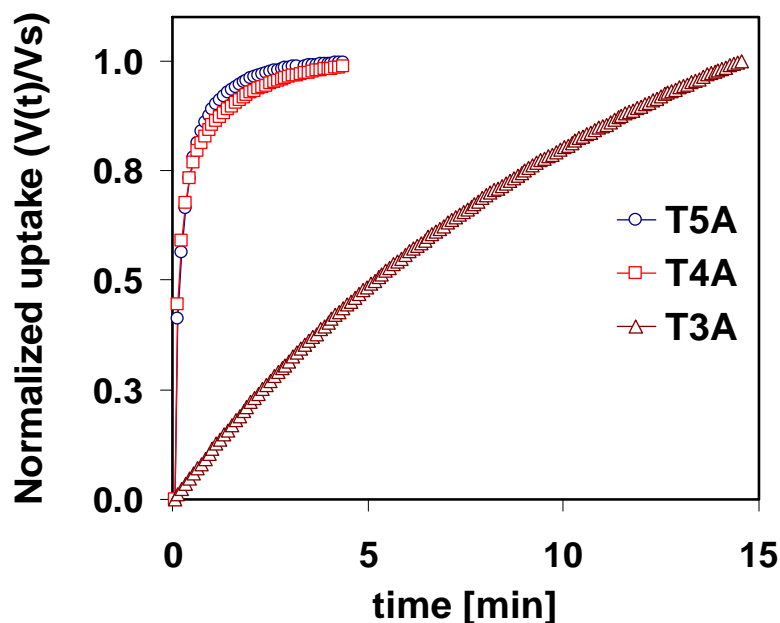


Fig. 4.5 An example for kinetic H₂ uptake at 77 K (final equilibrium at 1.33 mbar).

In Fig. 4.7 hydrogen desorption spectra of T3A, obtained for 25 and 500 mbar gas loading, are presented. Spectra are recorded with two heating rates, 0.10 and 0.01 K s⁻¹. When using a slower heating rate of 0.01 K s⁻¹ the desorption spectra are shifted toward lower temperatures.

Finally, a series of TDS experiments after loading with hydrogen/deuterium mixtures (300 mbar of H₂ and 300 mbar of D₂) were performed on T3A, aiming to investigate the desorption mechanism on an atomic level. The analysis of the desorbing gases showed dominant m/Z signals of 2 amu and 4 amu, corresponding to molecular hydrogen and deuterium, respectively, whereas the desorption traces derived from the m/Z signals of 1 amu (corresponding to atomic hydrogen), and 3 amu (corresponding to hydrogen deuteride) were found to be considerably lower, Fig. 4.8. This is a clear indication that physisorption process mainly occurs. However, there is also a small signal of HD, indicating that some exchange does occur.

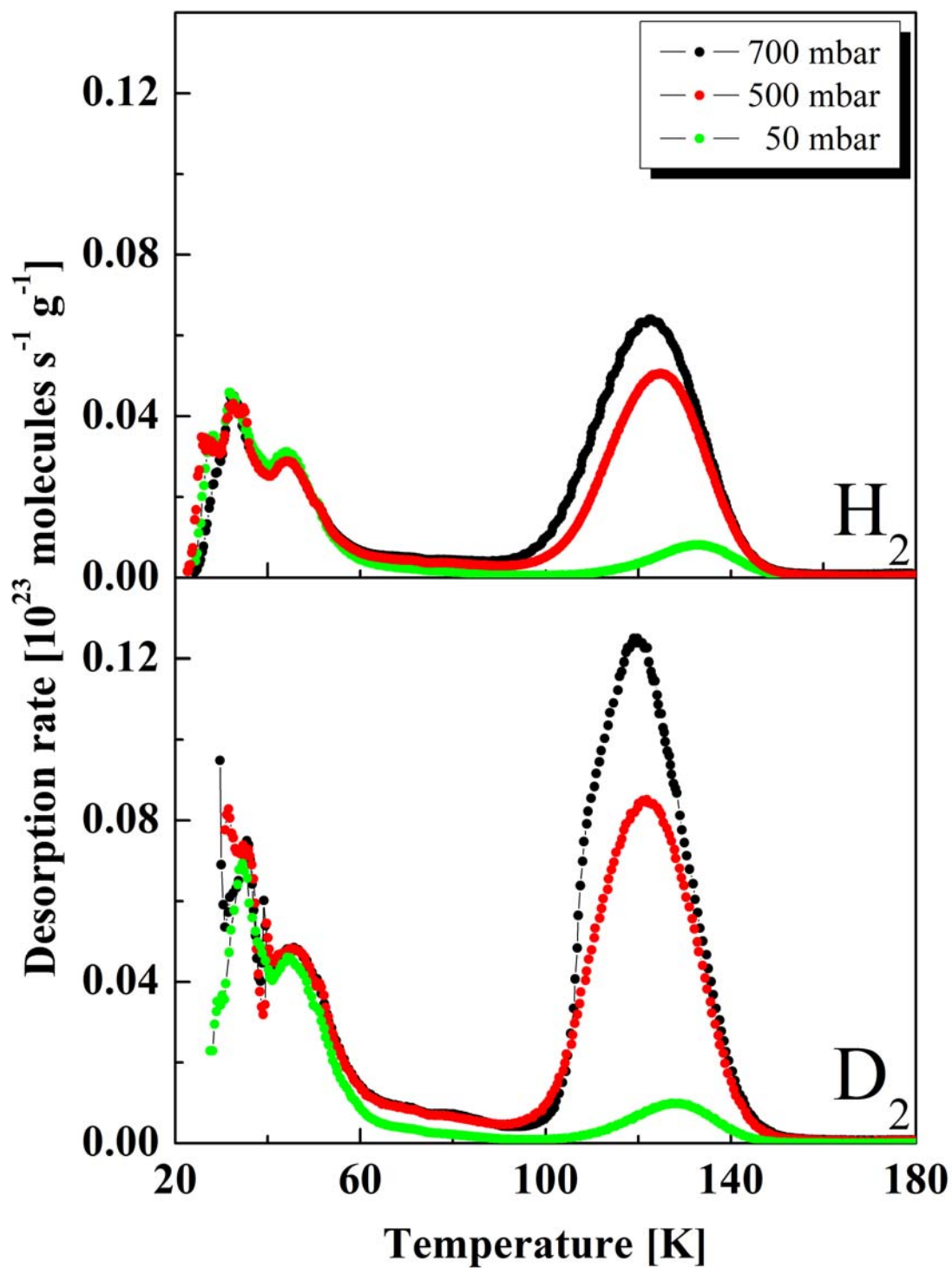


Fig. 4.6 The TDS spectra of H_2 and D_2 desorbed from T3A. The spectra are obtained for different initial gas loadings, and with the heating rate of 0.10 K s^{-1} .

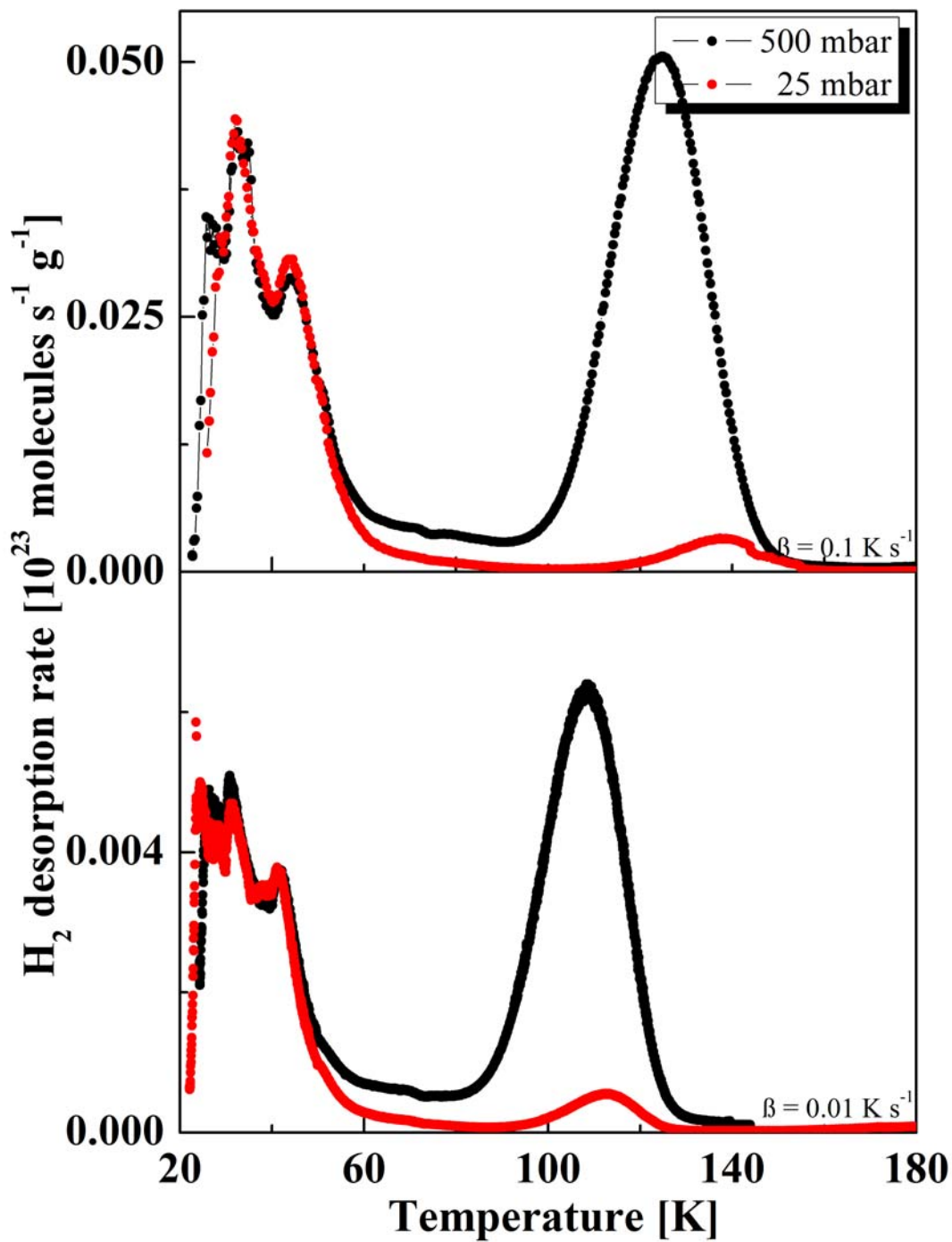


Fig. 4.7 Hydrogen TDS spectra of T3A for 25 and 500 mbar gas loading, recorded with the heating rate of 0.10 and 0.01 K s⁻¹.

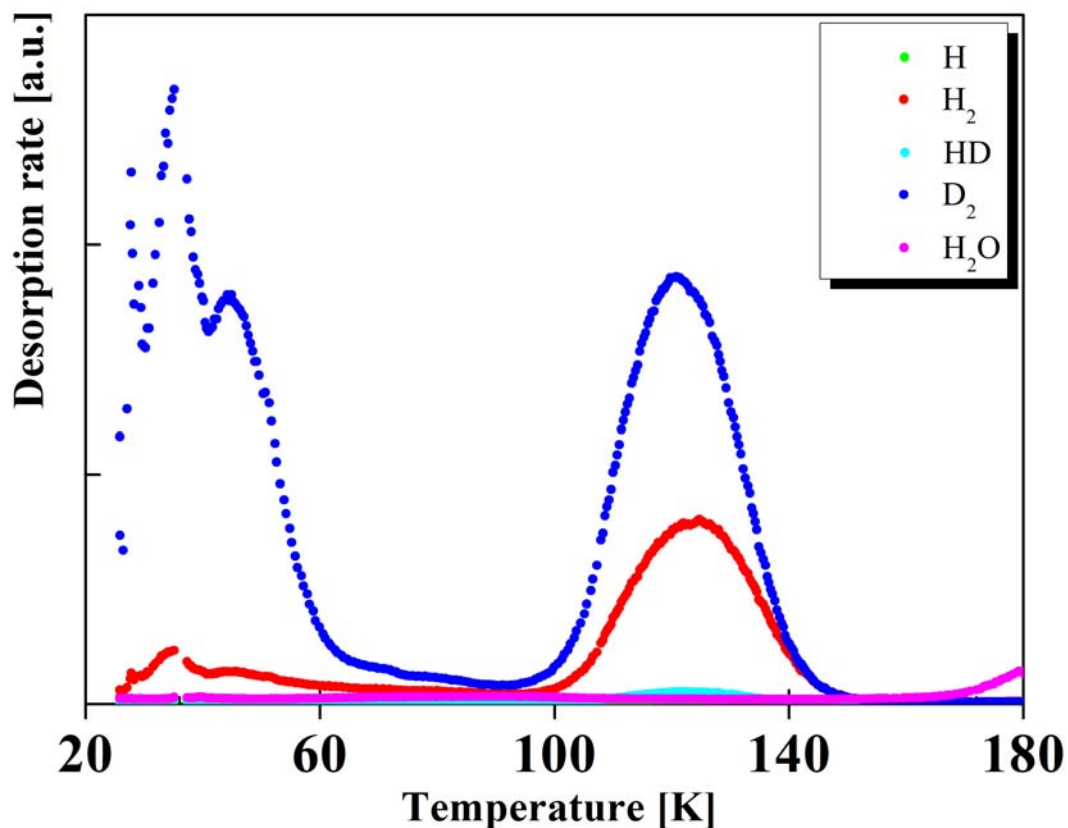


Fig. 4.8 The TDS spectra of T3A with respect to atomic and molecular hydrogen, atomic and molecular deuterium, hydrogen deuteride and water. The spectra are obtained after exposure of the sample to a H_2/D_2 gas mixture, and recorded with the heating rate of 0.10 K s^{-1} .

T4A exhibits entirely different desorption spectra depicting only one, broad desorption peak. In Fig. 4.9 a comparison is given for hydrogen and deuterium desorption. Spectra are obtained for different initial gas loadings, in the range from 1 to 700 mbar. Following the increase in pressure, the intensity of peaks increases as well, and attains saturation for 15 mbar gas loading. Several small, overlapping desorption maxima are also observed. The peak maxima shift slightly toward lower temperatures for increased gas loading, without affecting the shape of the peak. For 700 mbar gas loading another peak is observed, centered around 25 K for hydrogen, and around 27 K for deuterium. The amount of gas desorbed is calculated to be 1.64 wt.% and 4.82 wt.% for hydrogen and deuterium, respectively (700 mbar gas loading).

In Fig. 4.10 a comparison for hydrogen and deuterium TDS spectra of T5A is given. Spectra are obtained for 25 mbar gas loading and recorded with the heating rate of 0.10 and 0.01 K s^{-1} . Apart from the slight difference in the peak intensity both spectra have a similar shape. T5A shows desorption profiles with two distinguishable desorption maxima, at 35 and 44 K, and a small desorption shoulder at about 51 K for hydrogen. For deuterium desorption peaks are centered at 32, 44, and 51 K. Further comparison between hydrogen and deuterium desorption is given in Fig. 4.11,

for 1, 7, and 25 mbar gas loading. Gradual filling of adsorption sites and intensity increase are observed upon increasing the gas loading. For 1 mbar gas loading a nonsaturating hydrogen peak appeared at 66 K for H₂, and 70 K for D₂, followed by a small peak at lower temperature of 45 K for H₂, and 50 K for D₂. Upon increasing gas loading the peak maxima shift toward lower temperature, the peak intensity increases, and the maxima coalesce. The spectra have a common trailing edge, and the majority of gas molecules are desorbed below 80 K. The total amount of gas desorbed is calculated to be 1.74 wt.% and 4.83 wt.% for hydrogen and deuterium, respectively (25 mbar gas loading).

Further comparison between the desorption mechanism of all three investigated samples is given in Fig. 4.12 and 4.13, for hydrogen and deuterium desorption, respectively. The presented spectra show pronounced differences in the desorption temperatures, desorption profiles, and in the magnitude of the signal (desorption area).

The total amount of hydrogen desorbed of all three CMS samples is correlated to the BET SSA calculated from the N₂ adsorption data at 77 K, and CO₂ adsorption at 273 K, Fig. A-1. An almost linear correlation between the total storage capacity and the SSA is obtained. In addition, a good correlation is found between the total amount of hydrogen desorbed and the micropore volume of the CMS samples, Fig. A-2.

The total amount of hydrogen and deuterium desorbed for each gas loading applied for all investigated samples is given in Table A-3 and A-4, respectively.

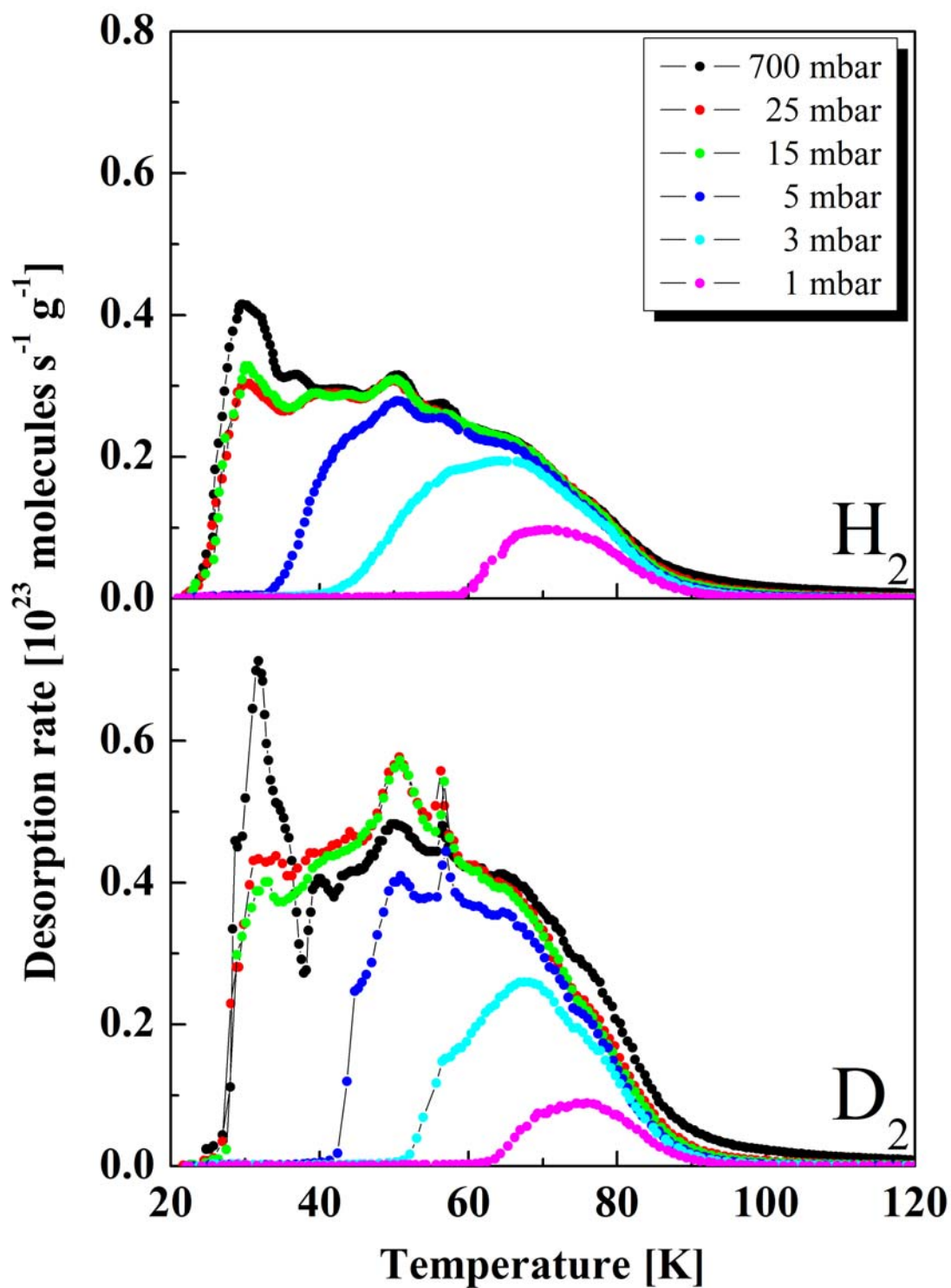


Fig. 4.9 H_2/D_2 desorption spectra of T4A for different initial gas loadings, recorded with the heating rate of 0.10 K s^{-1} .

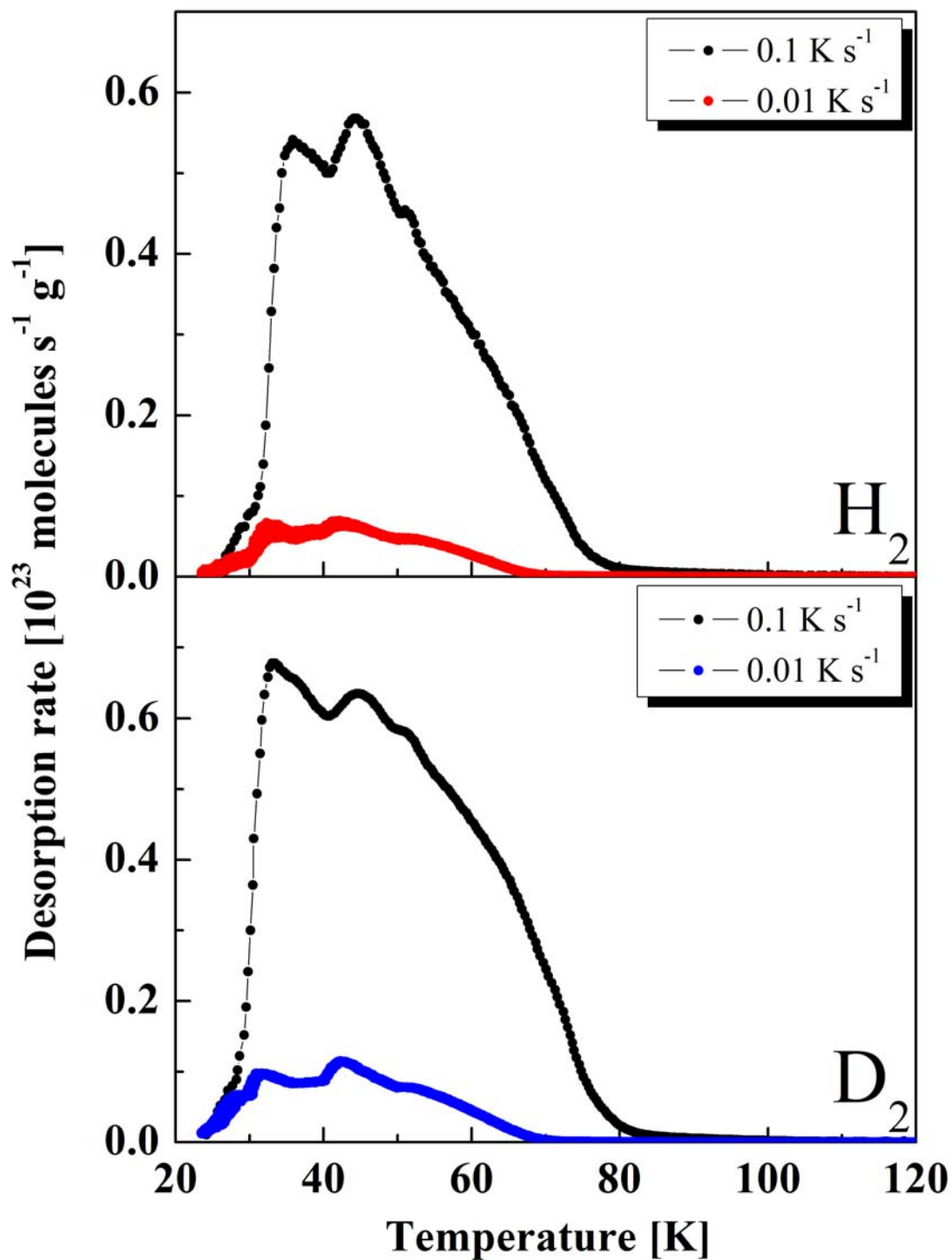


Fig. 4.10 The desorption spectra of hydrogen and deuterium on T5A, loaded at 25 mbar, and recorded with the heating rate of 0.10 and 0.01 K s^{-1} .

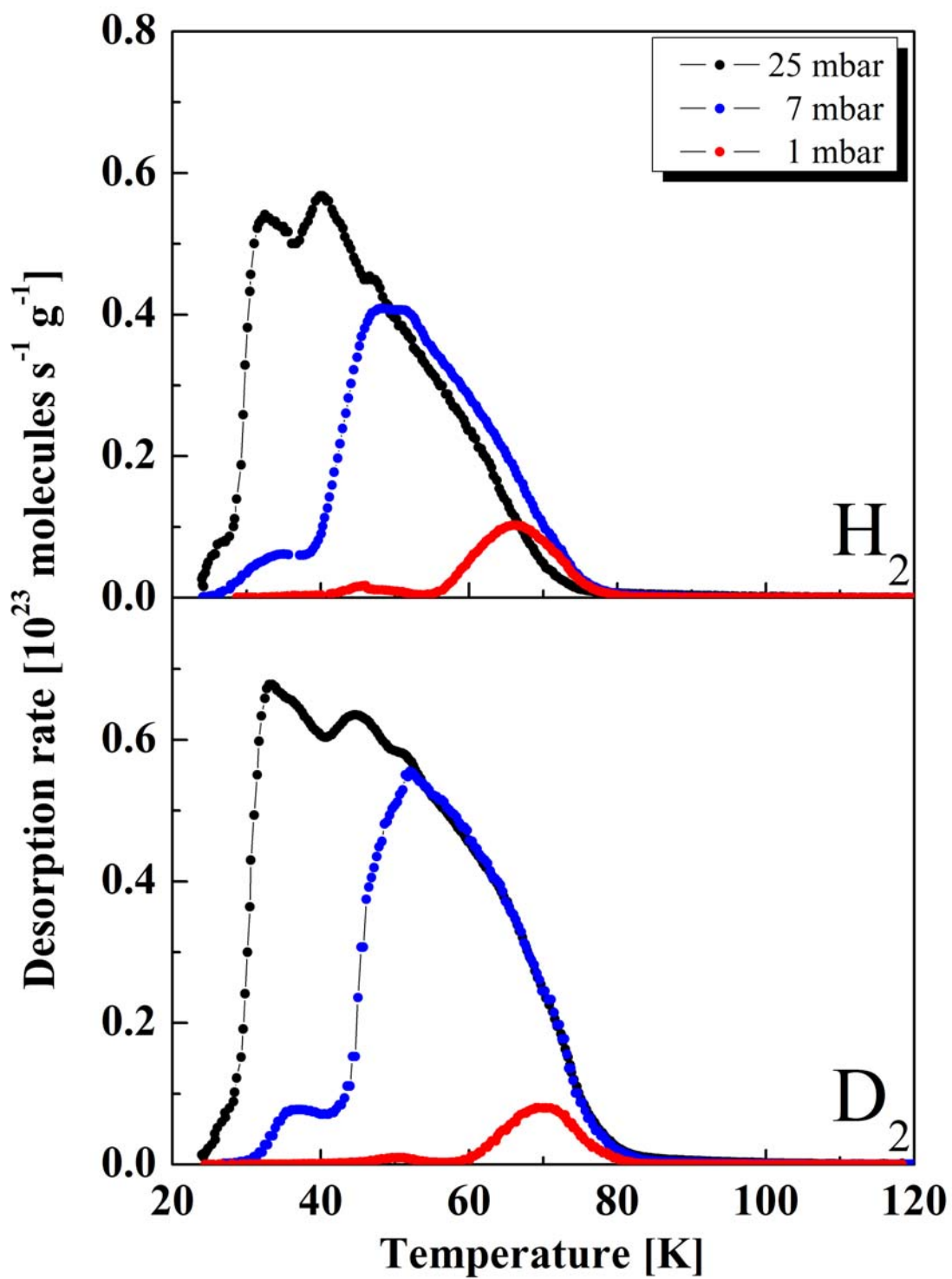


Fig. 4.11 A comparison of H_2 and D_2 desorption spectra of T5A obtained for 1, 7, and 25 mbar gas loading. The spectra are recorded with the heating rate of 0.10 K s^{-1} .

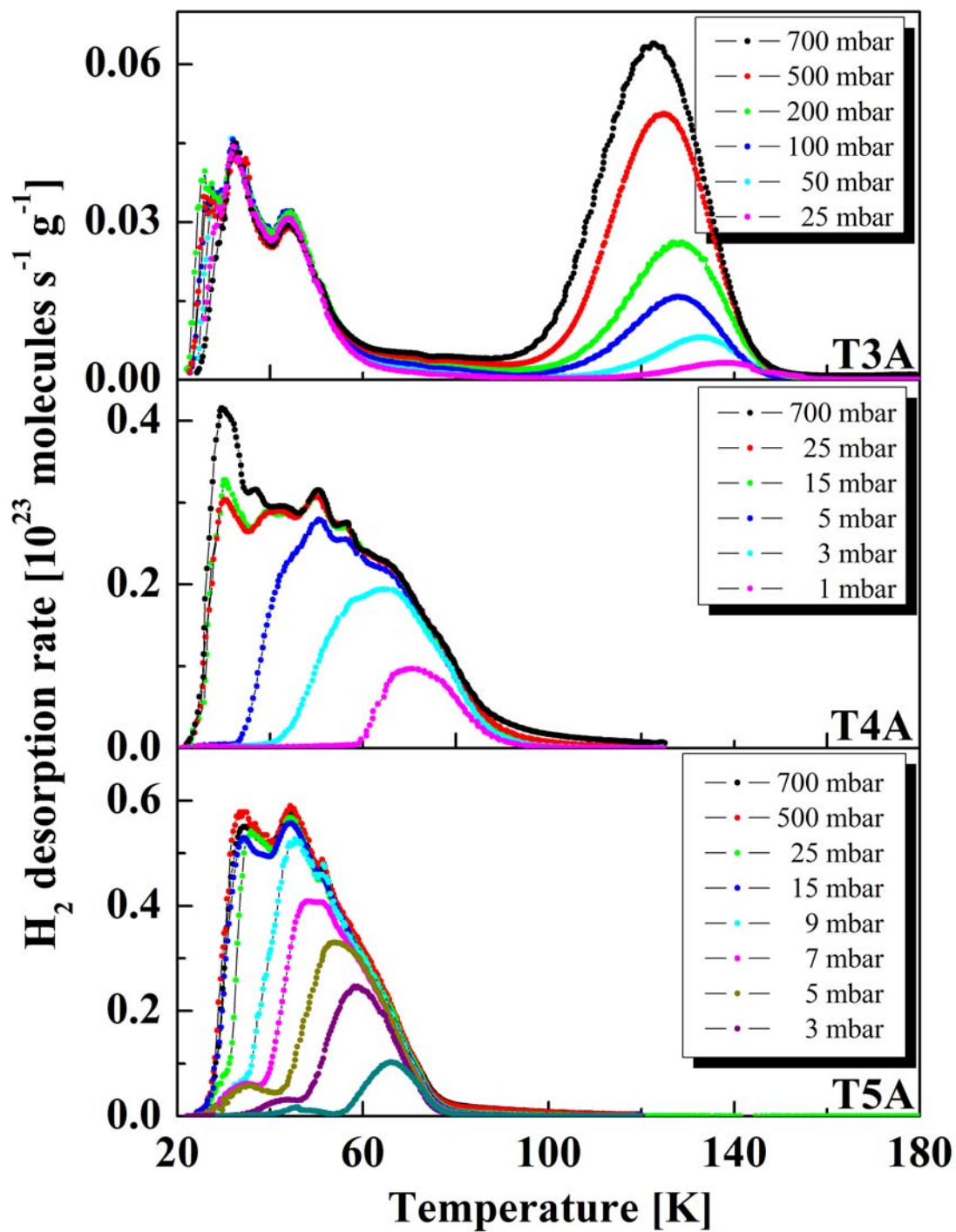


Fig. 4.12 H₂ TDS spectra of T3A, T4A, and T5A obtained for different initial gas loadings, recorded with the heating rate of 0.10 K s⁻¹.

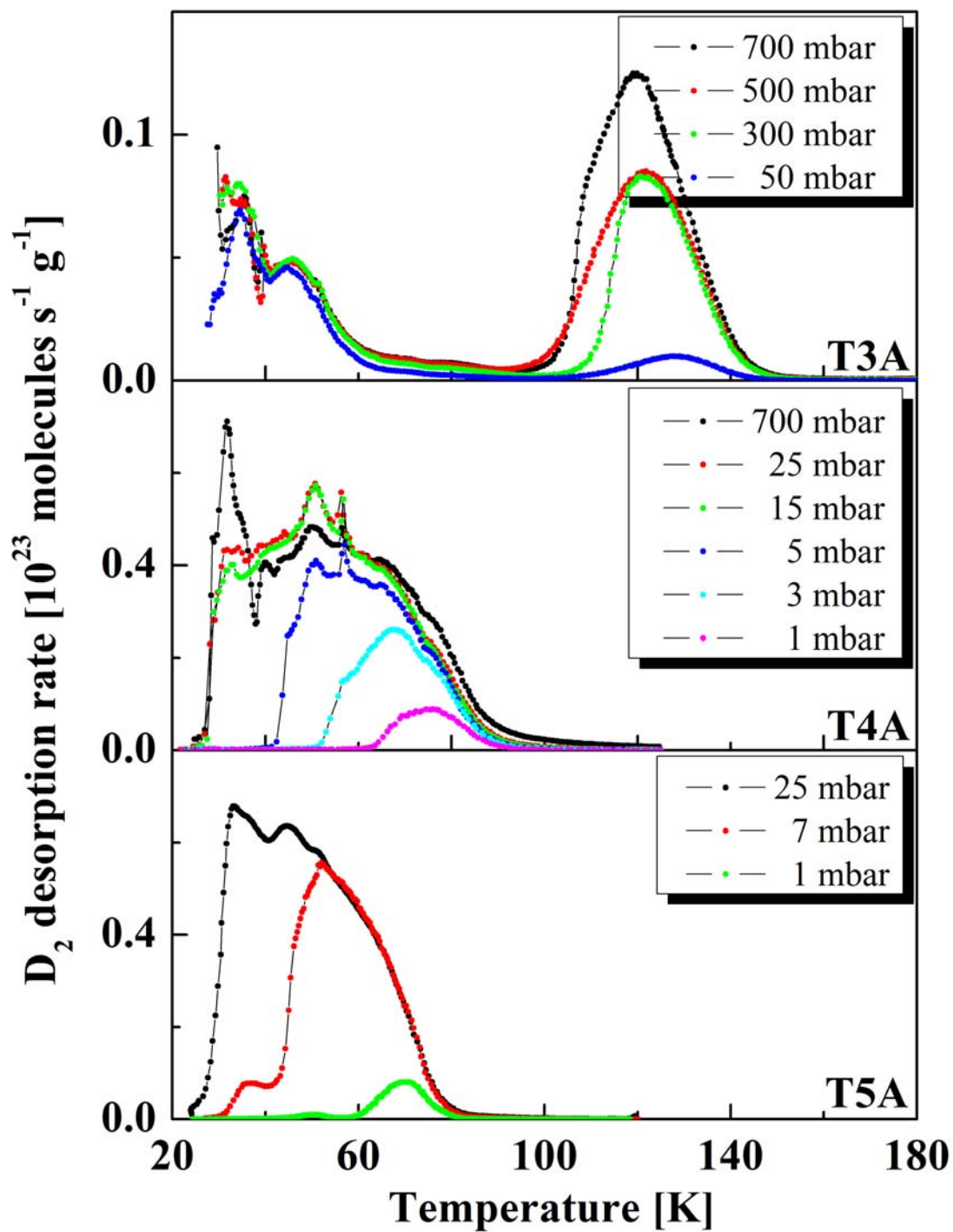


Fig. 4.13 A comparison of D_2 TDS spectra of T3A, T4A, and T5A, recorded with the heating rate of 0.10 K s^{-1} .

4.4 Discussion

The potential utility of carbon as hydrogen adsorbent was extensively investigated in the last decades, and it has been found that the adsorption rate is fast, and the uptake is reversible. However, the values for hydrogen storage capacity, which have been reported in the literature over the years for pure carbon based materials, scatter over several orders of magnitude. Nowadays, the highest reliable weight-based storage capacity under cryogenic conditions has been achieved for lab-made ACs, characterized by a BET surface area of $3220 \text{ m}^2 \text{ g}^{-1}$, and the total hydrogen sorption capacity of 6.0 wt.% at 77 K and 40 bar [133]. At RT the storage capacity is reduced to 0.6 wt.% at 298 K and 50 bar, far from the targets set by the automotive industry. This poor performance is attributed to the weak van der Waals interaction between hydrogen molecules and carbon surface. Physisorption forces may be enhanced in narrow micropores, with a size close to the kinetic diameter of the adsorbate molecules (0.28 nm for H_2), which can be explained in terms of confinement effects [134]. The effect of pore size on the hydrogen-carbon adsorption enthalpy was treated in the literature both theoretically [135], and experimentally [136–138].

The distinctively different hydrogen adsorption/desorption behaviour of the three CMS samples can be clearly related to the respective microstructure variations. In general, the hydrogen sorption capacity of porous carbons scales with the BET specific surface area [139–144]. Indeed, the total amount of hydrogen desorbed from T4A, and T5A (1.64 wt.% and 2.02 wt.%, respectively, at a adsorption pressure of 700 mbar) correlates well with the derived N_2 BET surface area ($428 \text{ m}^2 \text{ g}^{-1}$ for T4A, and $560 \text{ m}^2 \text{ g}^{-1}$ for T5A). However, this approximation does not apply to the desorption behaviour of T3A where the total amount of hydrogen desorbed was 0.3 wt.%, and for which it was not possible to obtain a reliable BET surface area due to its negligible N_2 adsorption at 77 K. A further correlation can be made with the SSA calculated from the CO_2 adsorption data, Table A–1, while T3A is fully accessible to CO_2 molecules. A linear correlation is found between the total amount of hydrogen desorbed and the apparent SSA. As expected, the storage capacity increases with the increase in the SSA, Fig. A–1.

Apart from the nature of the carbon precursor [145], the preparation and activation procedure [146] strongly influence the properties of the final material. The adsorption capacity within porous carbons and the kinetics of adsorption are further influenced by the surface microstructure, particularly SSA, pore volume, and pore size distribution. Macropores are generally thought to arise from the fissures and interstitial spaces present in the original char. They are not of considerable importance in terms of adsorption capacity. The area contributed to the macro- and mesopores is usually very small, compared to the total surface area of carbon. They both act as transport pores, leading adsorbate molecules to the micropore cavity. Micropores, however, constitute about 95% of

the total surface area of porous carbons and, therefore, determine to a considerable extent the adsorption capacity. The graphitic structure provides an interconnected network of slit-shaped pores, formed by spaces between the graphite sheets [70], providing considerable microporosity. Apart from slit-shaped pores [147, 148], various pore shapes (ink-bottle shaped, V-shaped, capillaries open at both ends, or with one end closed, and many more) were found within the AC. CMSs are a special class of porous carbons usually produced on pyrolysis of polymeric precursors [78–80], containing primarily narrow micropores of molecular dimensions (effective diameter between 0.4 and 0.9 nm) [73], which allow the separation of molecular species by size exclusion. The selectivity may occur either because the pore width (or the pore opening) is narrower than the adsorbate molecules, or because the shape of the pores does not allow the adsorbate molecules to penetrate into the micropores. Molecular sieve effects are especially pronounced within T3A, which is why the specific surface area of T3A is not proportional to the adsorption capacity of T3A. Indeed, the best linear correlation has been shown when relating hydrogen adsorption capacity to micropore volume [149]. Almost a linear correlation is found between the total amount of hydrogen desorbed and the micropore volume deduced from the MC approach, Fig. A–2. Even a better correlation was observed after subtracting the amount of gas desorbed below 85 K for T3A, while the main adsorption peak observed at high temperature is attributed to adsorption in the micropores alone.

The main aim of the present work is to provide insight into the critical role of pore size on the adsorption/desorption of hydrogen/deuterium, investigating a series of CMSs. A detailed TDS investigation, made by comparing three narrow sized samples with ultramicropores, showed the salient effect that just a slight change in the pore size (the pore opening diameter) has on the desorption profile, the differences that cannot be observed from the time-consuming experimental studies of adsorption equilibrium, and determination of the static sorption isotherms, nor GCMC runs. Only for T3A two separated desorption regimes, at low and high temperature, are observed, which points to the existence of different adsorption sites and different H₂–carbon interaction. The sites corresponding to the low temperature H₂ desorption maxima observed at 33 and 44 K, get filled immediately, and attain saturation already for 25 mbar hydrogen loading, as shown by the unchanged peak intensity upon gas loading increase (Fig. 4.12, 4.13), indicating that these adsorption sites are easily accessible to hydrogen molecules. As the shape and position of these low temperature peaks are also independent of coverage, they can be attributed to adsorption into the macropores, formed from voids generated from the agglomeration of micrometer sized carbon grains [150]. On the other hand, the high temperature desorption peak observed at 122 K (comprising the highest temperature peak ever measured for TDS of physisorbed hydrogen, not

observed for T4A and T5A spectra), points to a different desorption mechanism. A strong H_2 interaction emanates from narrow microporosity of T3A, bearing the narrowest pores among three investigated samples, and with dimensions comparable to those of the hydrogen molecule, according to the CO_2 adsorption analysis (Fig. 4.3). Such effects may result from the overlap of the potential field due to the proximity of the pore walls, which strengthen the interaction potential with the adsorbate molecule [151].

When increasing the initial gas loading the signal intensity rises, while the peaks expand and broaden toward lower temperature. Prolonged filling of high temperature maxima, without attaining the saturation value, even for 700 mbar gas loading, suggests that a diffusion limited process occurs, possibly hindering the penetration of H_2 into the T3A micropores. Indeed, a tremendous difference of hydrogen diffusivities between T3A and the other two samples was observed by the significantly slower kinetics, recorded during the low pressure/temperature H_2 adsorption measurements of T3A (Fig. 4.5). Possible diffusion limitations due to microporosity are also suggested by the shift of the position of the high temperature desorption maxima by nearly 17 K, when applying a slower heating rate of 0.01 K s^{-1} (Fig. 4.7). Such considerable shift in the peak position of the high temperature maxima within T3A was observed for neither T4A nor T5A, and it is the first experimental observations of that kind made by the TDS measurements on porous adsorbents.

Typically, transport of gas molecules into microporous adsorbents is governed by (a) macropore diffusion, (b) micropore diffusion, and (c) entry into the micropore [130]. T3A is known to have uncommon ink-bottle-shaped micropores [150], consisting of a narrow neck, and a much wider main body. During adsorption in ink-bottle-shaped pores, the restriction at the pore opening imparts diffusion limitations, giving rise to a barrier for gas penetration into the micropore [130]. As such the molecule has to overcome a non-zero activation energy to pass the pore opening [70]. The energy barrier at the pore entrance was previously shown to influence transport of argon and nitrogen molecules into T3A [152]. Indeed, T3A is known to be capable of selectively adsorbing the components of air by distinguishing the 0.2 \AA size difference between nitrogen and oxygen [153], with the exclusion of molecules greater than 4.2 \AA . Selectivity for oxygen over nitrogen adsorption is kinetically based [70, 154]. Both oxygen and nitrogen are nearly equally adsorbed [145], but the smaller oxygen molecule (kinetic diameter 0.346 nm) diffuses two to three orders of magnitude faster than the larger nitrogen molecule (kinetic diameter 0.364 nm). Thus, T3A enables the separation of molecules that have the same equilibrium characteristics. An ideal separation of nitrogen from oxygen, where nitrogen will not be adsorbed at all, is not possible to achieve due to the surface adsorption of nitrogen [70], though several approaches have been proposed in the literature to improve oxygen to nitrogen selectivity [84, 155–159].

On the other hand, T4A contains larger micropores compared to T3A (Fig. 4.3), and exhibits a single, broad H₂ desorption peak with several small overlapping maxima, which suggest desorption from multiple sites with similar binding energy, at comparable rates. Gas penetration is not restricted and desorption maxima are readily filled, as also shown by the reversible H₂ adsorption isotherm (Fig. 4.4), and the respective fast kinetics (Fig. 4.5). T4A mainly contains pores with aperture size of about 0.5 nm, and these are the main sites for accommodation of gas molecules. A sharp maximum observed at 50 K relates to adsorption at slightly narrower pores (< 0.5 nm), while the low temperature region is correlated to weak H₂–carbon interaction, and attributed to adsorption in macropores. The saturation uptake is reached already for 15 mbar gas loading, and further increase in pressure results in adsorption in multilayers and, thus, a low temperature peak at around 29 K (Fig 4.12, 4.13).

In a similar manner, the main sites for accommodation of gas molecules into T5A are also pores with aperture size around 0.5 nm (Fig. 4.3). In such pores the surface adsorption mechanism prevails, and correlates to a desorption peak observed in the low temperature region, related to a rather weak interaction. Nevertheless, the desorption peaks of T5A (Fig. 4.12, 4.13) are clearly positioned to lower temperatures, compared to both T3A and T4A samples, as a result of the absence of narrow micropores, reflected by the respective pore size distributions. Indeed, delicate differences in the pore width were shown to have a pronounced effect on gas mobility through T3A and T5A [130], as well as the sorbate relaxation rates and diffusivities derived for T4A and T5A [160].

4.5 Summary

The porous structure of the three CMS samples was comprehensively characterized by N₂ (77 K), CO₂ (273 K), and H₂ (77 K) adsorption. The TDS measurements were extensively used for probing into details of the hydrogen physisorption mechanism. The copious amounts of data, collected down to very low gas loadings, revealed salient differences among the three investigated samples, and allowed observation of sequential filling of different adsorption sites. The TDS measurements gave a new overview on adsorption/desorption mechanism of Takeda CMSs, the one never accessed, nor possible to do so with the volumetric adsorption measurements.

The slight differences in the pore size of the three carbons influenced not only the shape of the desorption spectra, but more importantly the interaction potential, the height of the response curves, and, therefore, the total gas uptake. A linear correlation has been found between the total amount of hydrogen desorbed, from all three investigated samples, and the apparent specific surface area calculated from the CO₂ adsorption data, and with the micropore volume determined by a MC

approach. Although the maximum H₂ uptake was derived for the case of T5A, the strongest interaction was observed for T3A, bearing the narrowest micropores among all three CMS samples. This finding was based on the measurement of a desorption peak centered at 122 K, the highest desorption maximum ever recorded for physisorbed hydrogen. The confined geometry and narrow sized micropores, where hydrogen simultaneously interacts with multiple pore walls, lead to an enhanced adsorption enthalpy, opposite to the interaction of hydrogen with the wide pores where hydrogen can interact with only one wall at the time. Owing to this different pore structure the hydrogen binding energies in pure carbon materials are found to be in the range from 4 to 15 kJ mol⁻¹ [161].

Furthermore, the TDS measurements on T3A showed the diffusion limited hydrogen adsorption/desorption kinetics, due to the narrow-size pore opening diameter, an observation never made before on porous adsorbents with this experimental technique.

Chapter 5

METAL–ORGANIC FRAMEWORKS

5.1 The design, synthesis, and properties of crystalline MOFs

Cu – BTC

The first MOF with a microporous structure that is reminiscent of the zeolite topology [162], copper(II) benzene–1,3,5–tricarboxylate, hereafter denoted as Cu–BTC, was first reported and described by Chui et al. [163]. It was named HKUST–1 (Hong Kong University of Science and Technology, structure 1). Later, the synthesis conditions were optimized so as to obtain a thermally more robust structure, and improve the product purity; from synthesis under the mild hydrothermal conditions [162, 164], over the novel electrochemical approach proposed by BASF SE [165], toward the synthesis performed under ultrasonic irradiation [166].

Cu–BTC is constructed from $\text{Cu}_2(\text{COO})_4$ paddle–wheel units assembled from two copper atoms forming dimers, where each copper atom is coordinated by four oxygens, coming from the benzene–1,3,5–tricarboxylate (denotes BTC) linkers, and by one water molecule. Each metal atom completes its pseudooctahedral coordination sphere with four oxygen atoms arranged in a square plane, one Cu atom, and an axial aqua ligand on the top of the octahedron. BTC ligand (trimesic acid) has three equally spaced carboxylate groups, which are able to bind in a bidentate fashion to copper ions, and, thus, produce rigid structures. Four BTC groups are arranged in a square, and used to connect the primary building blocks. The choice of the BTC group results in thermally stable and structural rigid face–centered–cubic crystalline structure of $Fm\text{--}3m$ symmetry, which forms a Pt_3O_4 –type network.

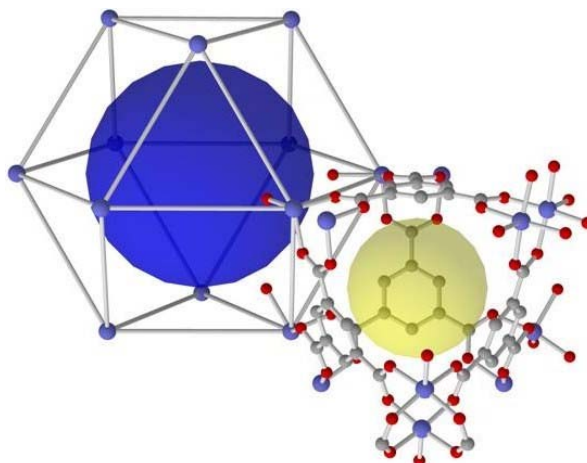


Fig. 5.1 A pictorial representation of the bimodal pore structure in $\text{Cu}_3(\text{BTC})_2$, courteously by Prof. Dr. Stefan Kaskel. The blue and yellow spheres show the location of the large and small pore, respectively. Representation comprises the following atoms: Cu (blue), O (red), and C (grey). H atoms omitted for clarity.

The framework has an open 3D channel system, with a bimodal pore size distribution [167], depicted in Fig. 5.1. The main (hydrophilic) square-shaped pores, of about 9 Å diameter, are formed from 12 $\text{Cu}_2(\text{OOC}^-)_4$ paddle-wheel subunits forming a cuboctahedron (Fig. 5.1, blue sphere). One water molecule is coordinated to the copper center, pointing towards the center of the pore (12 water molecules per pore in total). The oxygen atoms of these water ligands are arranged to form a cuboctahedron (Fig. 5.2.), where the vertical and diagonal O–O distances are 8.24 and 11.67 Å, whereas Cu–Cu internuclear separations across the pore are 11.3 and 16.0 Å, respectively [164].

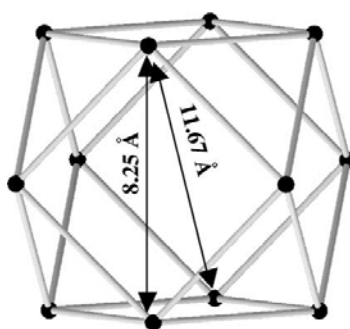


Fig. 5.2 Polyhedral arrangement of the axially bound water molecules inside the pore, reproduced from the ref. [164].

A second pore system of tetrahedron-shaped side pockets (Fig. 5.1, yellow sphere), of about 5 Å diameter, is built up from four benzene rings that constitute the inner surface, with the centers of the rings forming a tetrahedron [168]. The side pockets are accessible from larger pores through

triangular windows of about 3.5 Å diameter, marked by the three Cu^{2+} ions, 8 Å apart from each other [168].

When exposed to water, Cu–BTC forms a crystallohydrate $[\text{Cu}_3(\text{BTC})_2(\text{H}_2\text{O})_3]_n$ of a light cyan color. The dehydration of the compound is accompanied by the color change to blue navy [164], ascribed to the activation of new d–d transitions of Cu^{2+} ions. The water molecules, present in the first coordination sphere of the copper ions, are easily removed by thermally–assisted evacuation, which induces a coordinative vacancy on Cu^{2+} species and change in symmetry around the copper ion, due to the shortening of the Cu–Cu distance and the distortion of the Cu–O bonds. The effect of full dehydration of the compound was extensively investigated by the group of S. Bordiga [169]. The dehydration process makes the framework Cu(II) sites accessible for adsorbate (guest) molecules [163], while the 3D crystalline structure (Fig. 5.3) remains intact.

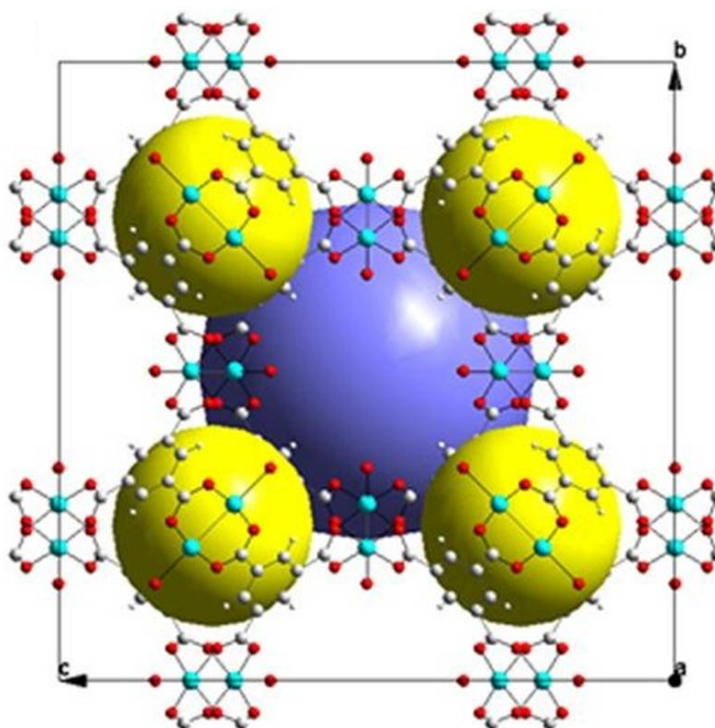


Fig. 5.3 The unit cell crystal structure of Cu–BTC, comprising Cu (turquoise), O (red), and C (white). H atoms omitted for clarity. Blue and yellow spheres indicate large and small pores, respectively. The representation is taken from the ref. [170].

The Cu–BTC unit cell possesses a free volume of 66% [170], and a BET surface area commonly ranging from 1200 to 1500 $\text{m}^2 \text{g}^{-1}$ [162, 167]. The porosity of the material is found to be greatly influenced by the synthesis procedure applied [172].

The Cu–BTC sample, employed for this study, has been produced by the novel electrochemical approach at BASF SE [165], under the sample code Basolite™ C300. A nitrogen adsorption

measurement yielded 1154 and 1958 m² g⁻¹ for BET and Langmuir surface area, respectively. Both the BET and Langmuir model are commonly applied to characterize the SSA of microporous samples. The differences in the apparent values for the SSA arise while both models cannot adequately describe the N₂ adsorption isotherms of a microporous material. In general, Langmuir surface area values are higher than those determined from the BET model. For characterization of MOF samples the BET model is regarded as more suitable while the Langmuir model assumes that a homogenous monolayer of the adsorbate is formed on the walls of the adsorbent, and within MOFs the 3D structure is accessed by the N₂ molecules.⁴ The sample bulk density was determined to be 0.35 g cm⁻³.⁵

Fe–BTC

A commercially available ferric benzene–1,3,5–tricarboxylate, hereafter denoted as Fe–BTC, with the formula unit of C₉H₃FeO₆, has been used for the TDS measurements. The structure of Fe–BTC is built up by the trimers of iron octahedral, sharing a common vertex μ₃–O, linked by the BTC moieties [173]. This leads to the two types of mesoporous cages with internal free diameters of 25 and 29 Å, and pore opening of 5.5 Å and 8.6 Å, respectively. One of the coordination positions of Fe³⁺ ions is occupied by the solvent molecules, which may be removed under the HV, without compromising the stability of the crystal structure.

The sample used for present investigation has been provided by BASF SE, under the sample code Basolite™ F300. This is a hydrophilic MOF with a BET surface area in the range of 1300 to 1600 m² g⁻¹, and the bulk density in the range of 0.16 to 0.35 g cm⁻³. The sample is XRD amorphous.⁴

Mg–formate(1)

A microporous magnesium formate is a light-weight, porous MOF, which crystallizes upon reaction of the metal nitrate with formic acid, using dimethylformamide as solvent media, at elevated temperatures. The material was synthesized for the first time in 2006 by Rood et al. [174]. The structure of the material is given by the formula Mg₃(O₂CH)₆, solved by single-crystal X-ray diffraction [175]. There are four crystallographically independent Mn(II) ions, each of which is octahedrally coordinated by six oxygen atoms of six different formate molecules, Fig. 5.4. All of the formates adopt similar binding modes, with one oxygen connecting to a single metal center, and

⁴ Dr. M. Thommes, oral communication at the 1st International Conference on Metal Organic Frameworks and Open Framework Compounds, 8th – 10th October, 2008, Augsburg, Germany.

⁵ BASF Product Datasheet, BASOLITE MOF Properties – <https://www.sigmaaldrich.com>.

the second oxygen bridging between two other metals. Mn–O distances are in the range of 2.0199(9) – 2.1139(9) Å [174].

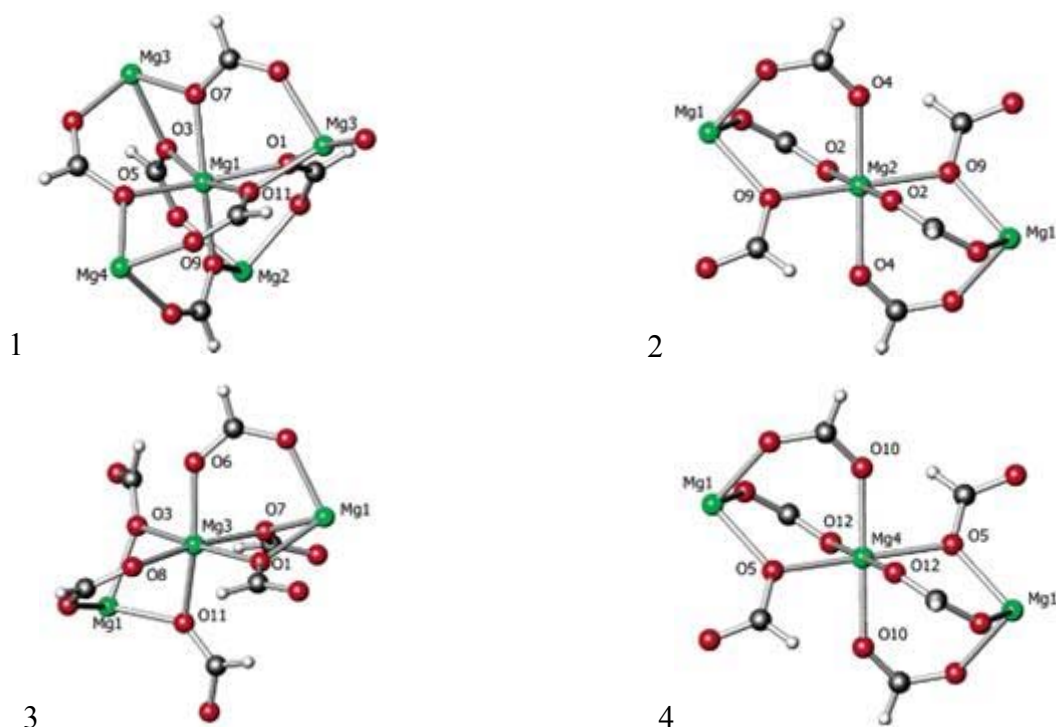


Fig. 5.4 Local geometries surrounding the four independent octahedrally coordinated magnesium centers. Reproduced from the ref. [174].

Looking along the *b*-axis, the cell can be divided into four squares with Mg(2) and Mg(4) located in the corners, coordinating to formate molecules, and giving rise to a 3D network. The 3D network (Fig. 5.5) may be represented with one-dimensional chains, built of edge-shared MgO₆ octahedra, linked by the formate ligands. Among the four independent Mg(II) centers, Mg(1) and Mg(3) are linked together by the vertex-sharing octahedral, in a distorted geometry.

The one-dimensional zig-zag channels, with an internal diameter of 3.4 Å [175], are interlinked via small windows, ca. 4.5 x 5.5 Å² wide [174], to form a channel running along the *b* axis. The assessable void volume of the channels is estimated to be 488 Å³ per unit cell, which is 30.2% of the unit cell (1617 Å³).

The sample employed for this study has been produced at BASF SE [175], by the semitechnical route, and under the sample code Mg-formate LR 0219. Nitrogen adsorption measurements at 77 K yielded 16 and 24 m² g⁻¹ for the BET and Langmuir surface areas, respectively.

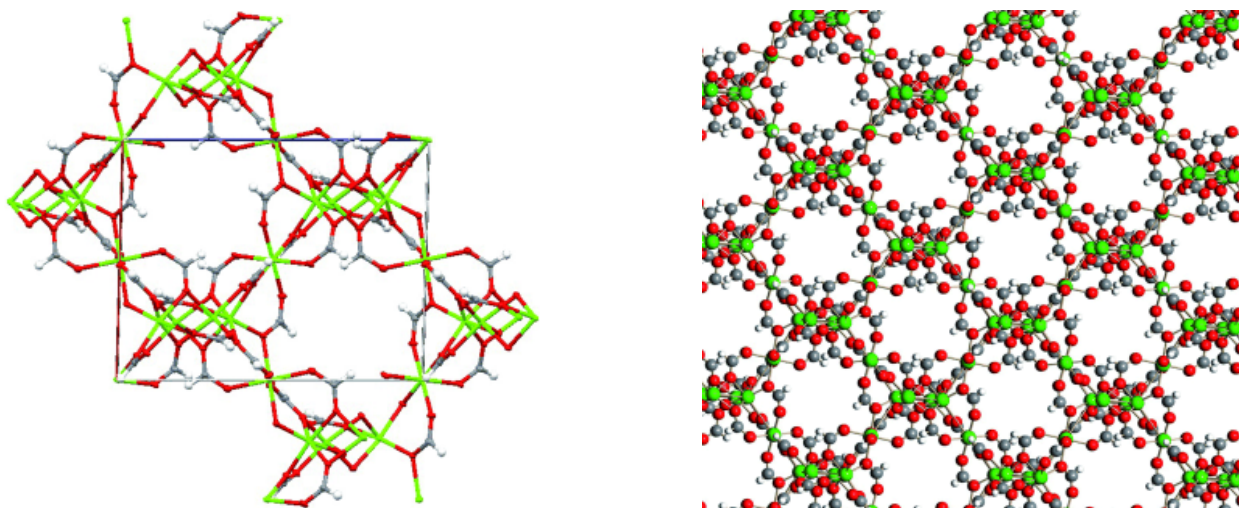


Fig. 5.5 The 3D structure of Mg–formate(1), comprising Mg (green), O (red), C (grey), and H (white) [175].

Mg–formate(2)

Mg–formate(2) has the formula unit of $C_2H_2MgO_4$, and it is isostructural to Mg–formate(1). The sample has been provided by BASF SE, under the sample code BasosivTM M050. The preparation procedure has not been disclosed, except that the synthesis procedure was slightly modified (in particular, a different solvent was employed for the synthesis), which resulted in samples with wider pores. The BET surface area is determined to be in the range of $400 - 600 \text{ m}^2 \text{ g}^{-1}$, with the bulk density of $0.30 - 0.40 \text{ g cm}^{-3}$.⁶

MOF–177

A block-shaped crystal $Zn_4O(BTB)_2 \cdot (DEF)_{15}(H_2O)_3$, named MOF–177, is composed of octahedral zinc(II) clusters (Zn_4O) linked by 1,3,5–tris(4′–carboxyphenyl)benzene (H_3BTB), the largest cross linker used thus far in MOF synthesis. The DEF stands for N,N–diethylformamide. The structure is entirely constructed of six-member C_6H_4 , C_6H_3 , and OZn_2CO_2 rings, giving rise to the six diamond-shaped channels, surrounding a pore containing eclipsed BTB^{3-} moieties. Between the central benzene rings of BTB^{3-} , a large pore with the diameter of 11.17 \AA can be accommodated, while the narrowest pore dimension is estimated to be 10.8 \AA [101]. The underlying topology of MOF–177 is a (6,3)–coordinated net, with the centre of the octahedral $OZn_4(CO_2)_6$ cluster as the site of six-coordination, and the centre of the BTB unit as the site of three coordination. The manner of arranging six-membered (C_6H_4) rings, 1,3,5–linked to a central ring (C_6H_3), and further to Zn clusters, gave rise to an exceptional surface area.

⁶ BASF Product Datasheet, BASOLITE MOF Properties – <https://www.sigmaaldrich.com>.

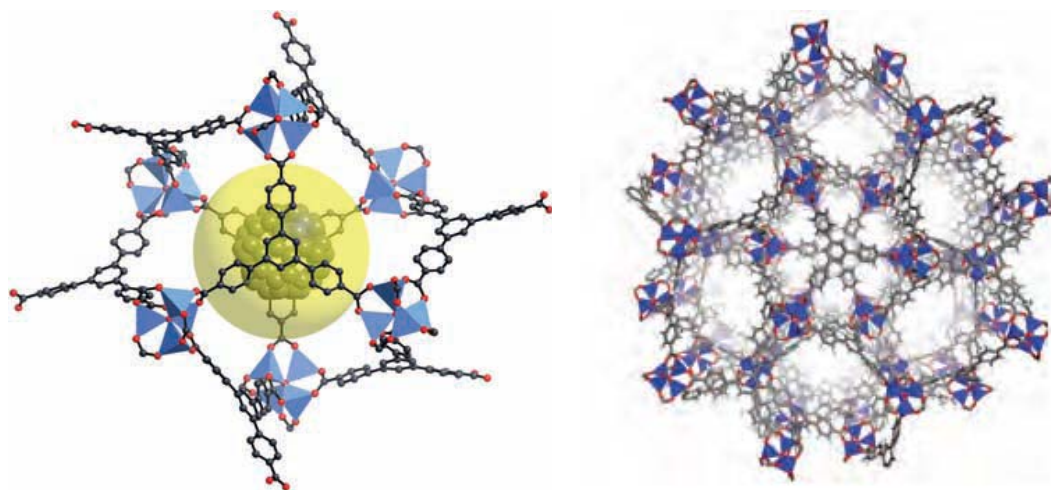


Fig. 5.6 The crystalline structure of MOF-177, reproduced from the ref. [176]. An approximately spherical pore is shown as large yellow sphere. Atom colors: C (grey), O (red), and Zn (blue tetrahedra). H atoms are omitted for clarity.

The investigated sample has been provided by BASF SE, under the sample code Basolite™ Z 377. The sample has 4239 and 5635 m² g⁻¹ for the BET and Langmuir surface areas, respectively.

MFU-4

A novel MOF [Zn₅Cl₄(BBTA)₃]-3DMF, hereafter denoted as MFU-4 (MFU being the acronym for Metal-Organic Framework Ulm University), is constructed from symmetric pentanuclear {Zn₅Cl₄}⁶⁺ secondary building units (SBUs), interconnected with linear dianionic benzobistriazolate (BBTA²⁻) linkers [177], giving rise to a cubic crystal lattice, Fig. 5.7. Zinc ions are present within two different coordination environments, one octahedral and four tetrahedral. Each Zn₅ unit is connected to six BBTA ligands by 18 Zn-N bonds, with each ligand coordinating one central, and two peripheral Zn atoms.

The MFU-4 framework is constructed from smaller and larger cavities, arranged in an alternate fashion (Fig. 5.8 left). The aperture joining two structurally different cavities is built up by 4 Cl atoms, at a distance of 3.01 Å from its geometric centre. The centre of the smaller cavities has a distance of 3.68 Å to each Cl atom, and imaginary sphere with a diameter of 3.87 Å could fit into it. Each of the larger cavities is surrounded by twelve phenyl rings, and an imaginary sphere with a diameter of 11.94 Å would fit into it.

The material has been synthesized under solvothermal conditions, using a mixture of anhydrous ZnCl₂ and H₂-BBTA in DMF (DMF= N,N'-dimethylformamide), and by Microwave Irradiation Method in a microwave synthesizer (CEM, Discover S), Fig. 5.9. Both synthesis methods proved to exhibit the same analytical results [177].

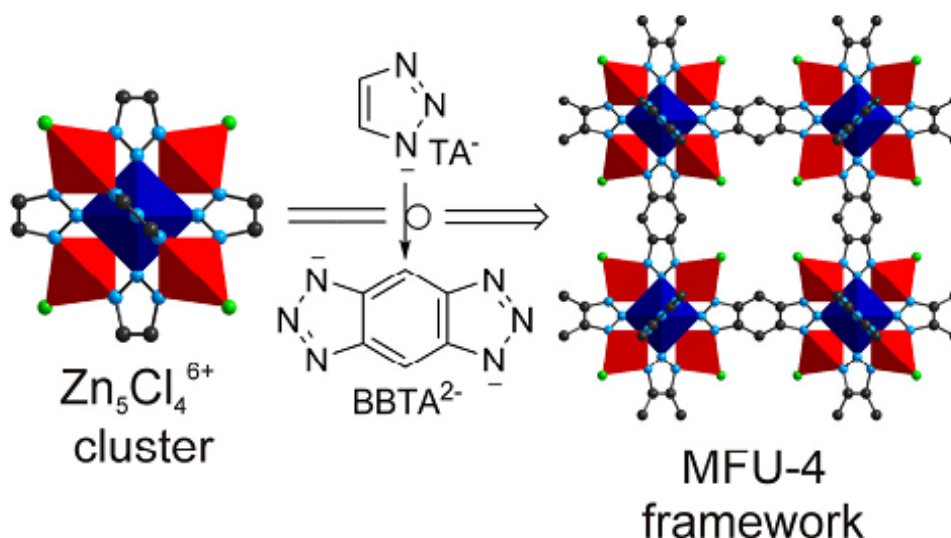


Fig. 5.7 Construction principle of cubic MFU-4 frameworks comprising $Zn_5Cl_4^{6+}$ coordination units and bis-triazolate linkers, courteously by D. Denysenko.

The framework is stable against moisture, and has a specific pore volume of $0.42 \text{ cm}^3 \text{ g}^{-1}$, estimated from the water adsorption isotherm [177]. Nitrogen molecules are occluded from adsorption at 77 K, and pressure up to 1 bar. Therefore, the surface area was calculated from a Monte Carlo integration technique, and determined to be $1611 \text{ m}^2 \text{ g}^{-1}$.

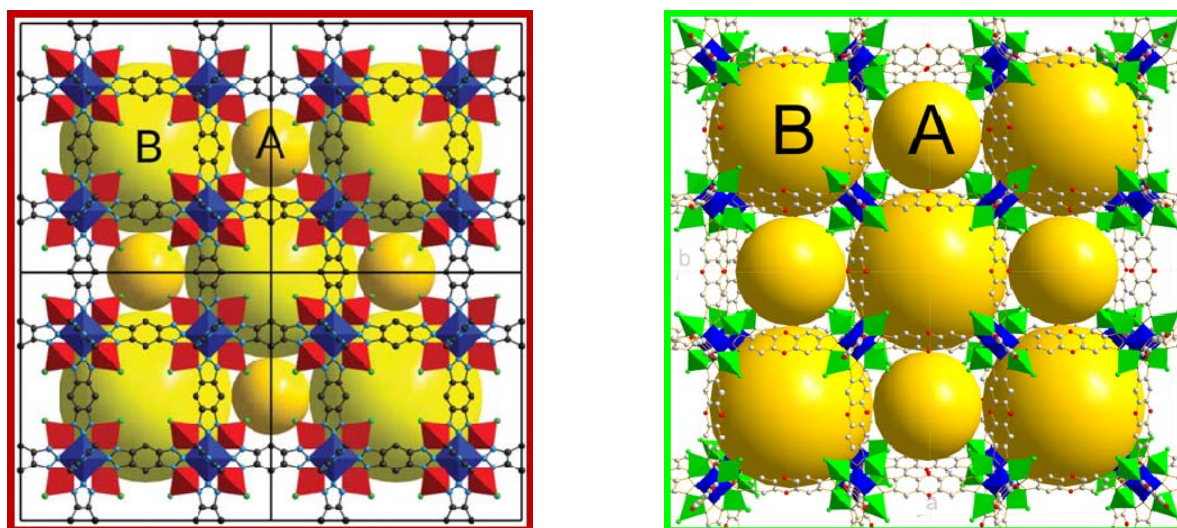


Fig. 5.8 Ball and stick representation of the MFU-4-type framework along the crystallographic a -direction: MFU-4 (left), and MFU-4 l (right). The larger cavity (light yellow sphere) is marked as B-cell, whereas the smaller cavity (dark yellow sphere) as A-cell. Octahedrally coordinated Zn ions are represented with blue octahedra, tetrahedrally coordinated Zn ions with red tetrahedra (MFU-4), and green tetrahedra (MFU-4 l). Atom colors: N (light blue), C (grey), Cl (green), and O (red). H atoms are omitted for clarity. Reproduced from the ref. [177, 178].

MFU-4l(arge)

The crystal structure of $[\text{Zn}_5\text{Cl}_4(\text{BTDD})_3]$, named MFU-4l, another MFU-4-type framework, is cubic six-connected net, similar to that of MFU-4. Cationic pentanuclear $\text{Zn}_5\text{Cl}_4^{6+}$ clusters are interlinked by BTDD^{2-} anions, comprising two types of Zn ions, tetrahedrally and octahedrally coordinated, Fig. 5.8 right.

Analogous to MFU-4, the framework of MFU-4l has two different types of cavities, the smaller, and the larger ones, arranged in an alternating fashion (referred to as A and B cells, respectively). Imaginary spheres with a diameter of 11.97 and 18.56 Å could fit into the A- and B-cells, respectively, while the aperture between the A and B-cells would admit the passage of an imaginary sphere with a diameter of 9.13 Å.

The material was synthesized in a high yield using solvothermal and/or microwave method, and N,N-dimethylformamide (DMF) as a solvent. As a result, a microcrystalline powder with a typical crystal size from 1 to 5 μm was obtained (Fig. 5.9 right). The compound exhibits permanent porosity, and the BET surface area of 2750 m² g⁻¹. The pore volume was determined to be 1.26 cm³ g⁻¹, by argon sorption measurements [178].

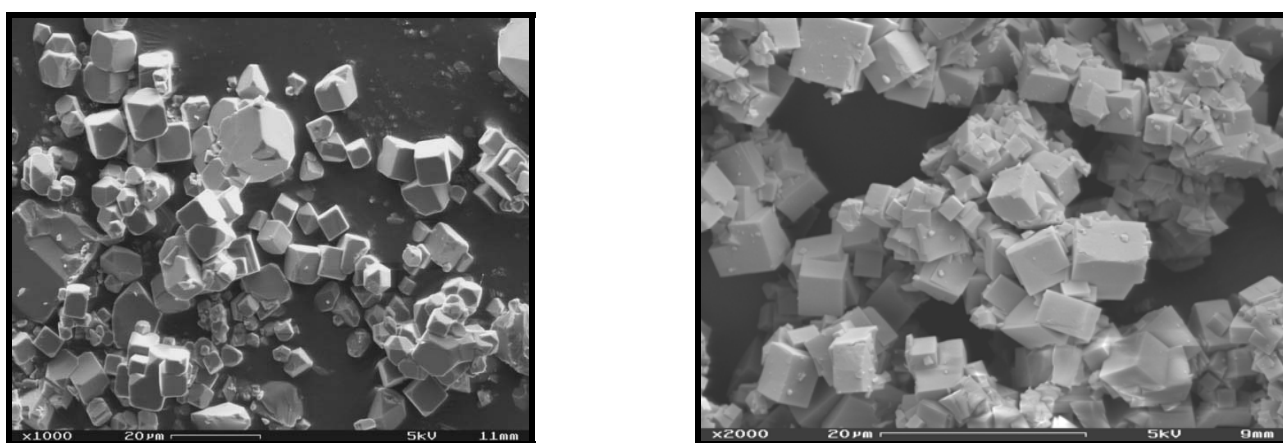


Fig. 5.9 SEM image of MFU-4-type framework synthesized by the solvothermal method, MFU-4 (left) and MFU-4l (right). Reproduced from the ref. [177, 178].

Al(OH)(ndc)

Al-based MOF, $\text{Al}(\text{OH})(\text{ndc})(\text{DMF})_{1.5}(\text{H}_2\text{O})_{1.5}$ named DUT-4 (standing for Dresden University of Technology Structure No. 4) [179], synthesized using N,N-dimethylformamide (DMF) as solvent and structure-directing agent, and 2,6-naphthalene dicarboxylate (ndc) as linker, has been employed for the TDS measurements. In $\text{Al}(\text{OH})(\text{ndc})$ structure aluminum cation is octahedrally coordinated to six oxygen atoms, whereby the octahedron is slightly distorted. The axial positions

of the octahedra are occupied by hydroxyl groups, forming $-\text{Al}-\text{OH}-$ chains. The naphthalate ligands bridge the chains to form a 3D framework (Fig. 5.10), with rectangular channels of about $8.5 \times 8.5 \text{ \AA}^2$ in diameter. The material exhibits the BET and Langmuir surface area of 1308 and $1996 \text{ m}^2 \text{ g}^{-1}$, respectively, estimated by the N_2 adsorption at 77 K and 1 bar. The pore volume is determined to be $0.68 \text{ cm}^3 \text{ g}^{-1}$ [179].

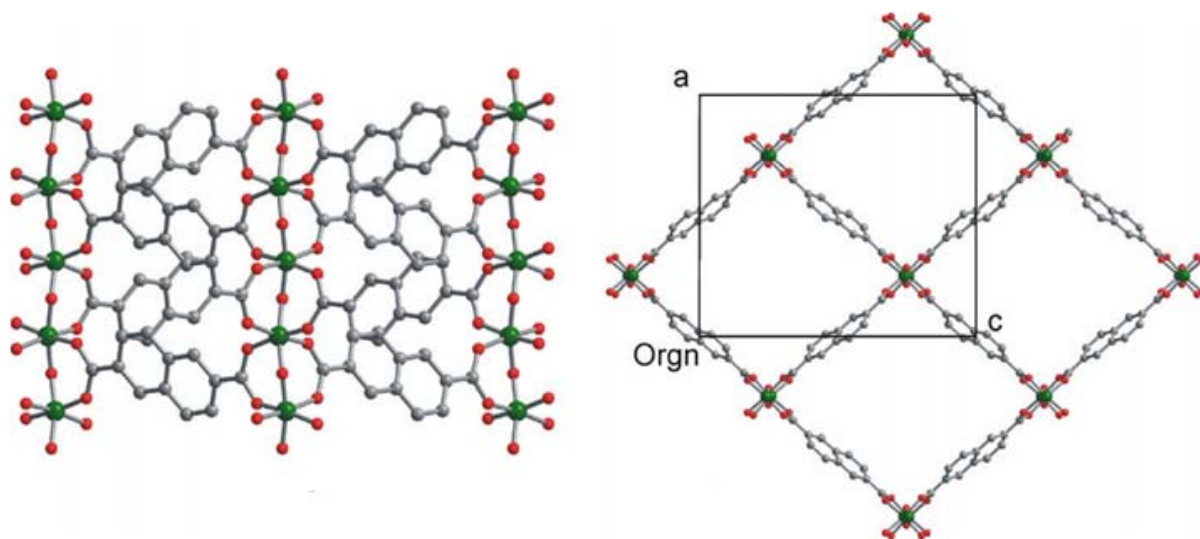


Fig. 5.10 The structure of $\text{Al}(\text{OH})(\text{ndc})$ viewed along the b -axis (left) and along the c -axis (right), comprising the following atoms: Al (green), O (red), and C (grey). H atoms are omitted for clarity. The representation is adopted from the ref. [179].

Al(OH)(bpdc)

The same supramolecular architecture as for $\text{Al}(\text{OH})(\text{ndc})$ was obtained for $\text{Al}(\text{OH})(\text{bpdc})(\text{DMF})_{1.8}(\text{H}_2\text{O})_{3.5}$, using 4,4'-biphenyl dicarboxylate (bpdc) as linker. The material is reported under the sample code is DUT-5 [179]. $\text{Al}(\text{OH})(\text{bpdc})$ has slightly larger pores, compared to $\text{Al}(\text{OH})(\text{ndc})$, about $11.1 \times 11.1 \text{ \AA}^2$ in size (Fig. 5.11). The BET and Langmuir surface areas are calculated to be 1613 and $2335 \text{ m}^2 \text{ g}^{-1}$, respectively, and the pore volume $0.81 \text{ cm}^3 \text{ g}^{-1}$ [179].

MIL-100 series

Four isostructural samples from MIL-100 series, MIL-100(Al, -V, -Cr, and -Fe), kindly provided by the group of Prof. G. Férey, were employed for this study. MIL stands for Matérial Institut Lavoisier.

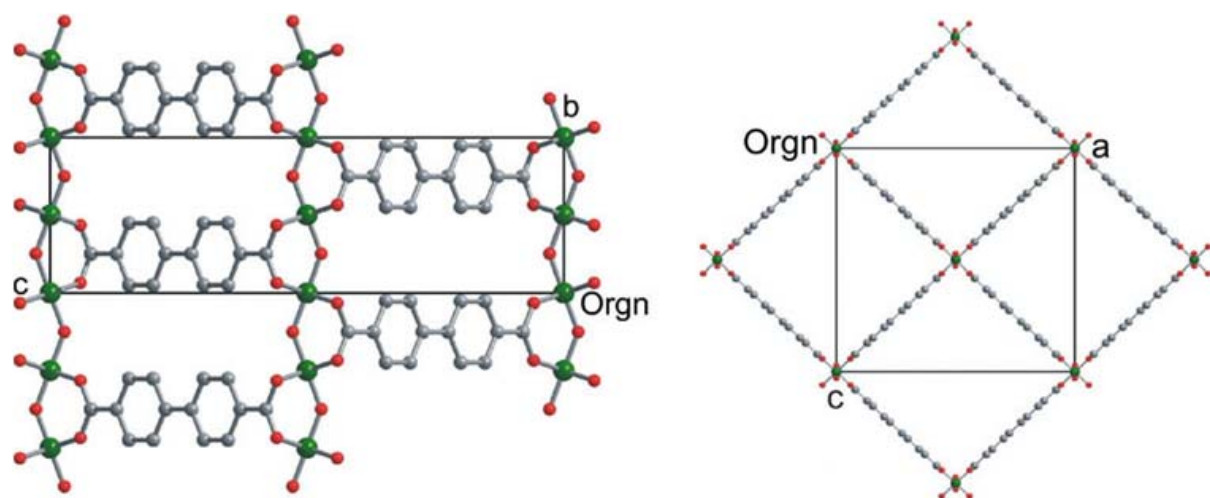


Fig. 5.11 The structure of Al(OH)(bpdc) viewed along a -axis (a), and along b -axis (b), comprising Al (green), O (red), and C (grey). H atoms are omitted for clarity. The representation is adopted from the ref. [179].

MIL-100(Al)

MIL-100(Al) , $\text{Al}_3\text{O(H}_2\text{O)}_2(\text{OH})(\text{BTC})_2 \cdot 24\text{H}_2\text{O}$, is built up from trinuclear, octahedrally coordinated aluminum building units (Al_3O), connected to each other through four trimesate (BTC) ligands, giving rise to a super-tetrahedron [99]. The Al_3O units are located at each corner of the tetrahedron, and the aromatic ring of the BTC ligand at the center of each face of the tetrahedral unit. The corresponding 3D framework is based on MTN topology, related to the high silica zeolite ZSM-39, Fig. 5.12. It exhibits the cubic arrangement of two types of cages closely packed, a small and a large cage, with the window diameter of 5.2 and 8.8 Å, respectively.

The surface area of MIL-100(Al) was measured to be $2152(39) \text{ m}^2 \text{ g}^{-1}$ and $2919(44) \text{ m}^2 \text{ g}^{-1}$ for BET and Langmuir surface area, respectively, while the pore volume is determined to be $0.82 \text{ cm}^3 \text{ g}^{-1}$ [99].

MIL-100(V)

MIL-100(V) is isostructural to the other samples of the MIL-100 series.⁷ The structure remains to be published.

⁷ Personal communication – Prof. Christian Serre.

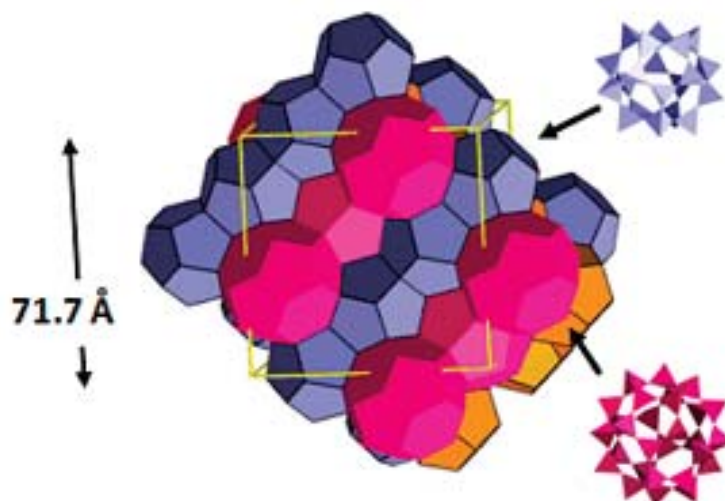


Fig. 5.12 A representation of the zeolite of MTN type topology, showing cubic arrangement of two types of cages, the small (blue) and the large ones (pink). Reproduced from the ref. [99].

MIL-100 (Cr)

MIL-100(Cr) is the first sample synthesized from MIL-100-type framework. The group of Prof. Férey combined targeted chemistry and computational design to create a porous chromium carboxylate with the chemical composition $\text{Cr}_3\text{F}(\text{H}_2\text{O})_3\text{O}[\text{C}_6\text{H}_3-(\text{CO}_2)_3]_2 \cdot n\text{H}_2\text{O}$ ($n \sim 28$). The compound is built up from trimeric chromium(III) octahedral clusters, linked by carboxylate moieties (BTC), which further assemble into microporous super-tetrahedral units, to produce an augmented zeolitic architecture of the MTN type. The trimeric units contain three terminal groups, H_2O , OH , or F .

MIL-100(Cr) is the first example of a porous solid with crystalline walls, and a giant cubic cell, the volume of which is close to $380,000 \text{ \AA}^3$. This crystalline MOF has three types of cages of different dimensions, Fig. 5.13. It comprises both micropores, with a diameter of 6.5 \AA , and two mesoporous cages. The smaller cage is built up from 20 super-tetrahedra, and has an internal diameter of 25 \AA , which is accessible through microporous pentagonal windows of $4.7 \times 5.7 \text{ \AA}^2$. The second, large mesoporous cage is assembled from 28 super-tetrahedral, and has a free aperture close to 29 \AA , accessible through the large hexagonal windows of about $8.6 \times 8.6 \text{ \AA}^2$. In the as-synthesized form these pores are occupied by water molecules, which can be removed by thermally-assisted evacuation. Using the Dubinin-Radushkevich equation a pore volume of around $1.16 \text{ cm}^3 \text{ g}^{-1}$ was determined for MIL-100(Cr). The apparent Langmuir surface area is determined to be $3100(40) \text{ m}^2 \text{ g}^{-1}$ [98, 180].

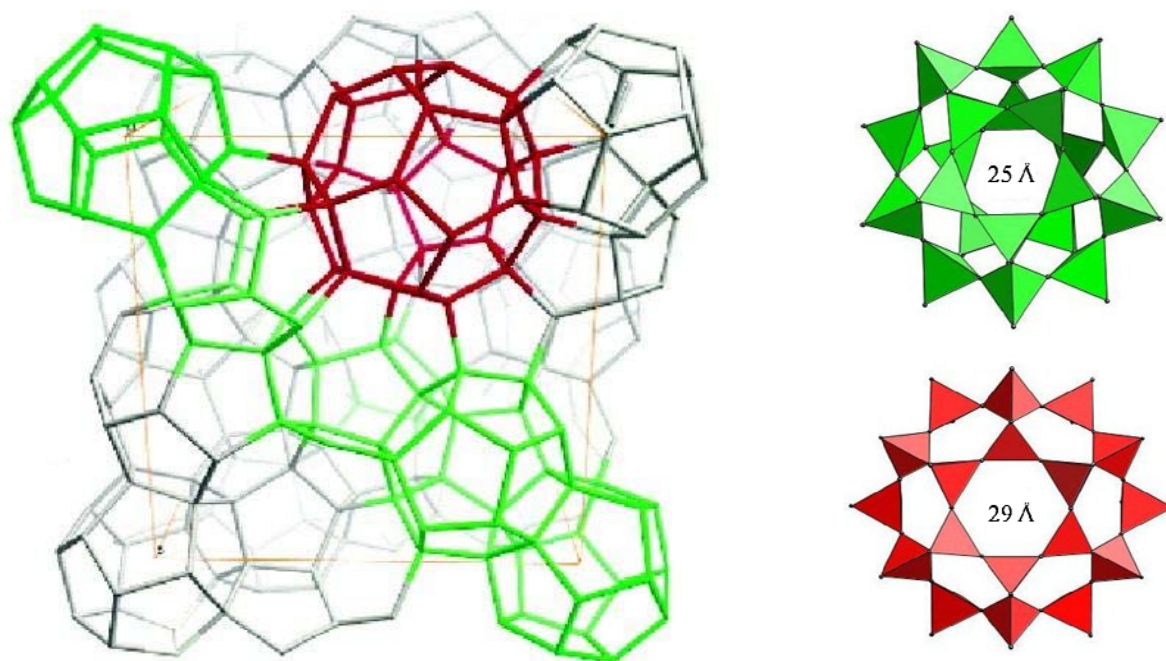


Fig. 5.13 Schematic representation of the 3D zeolitic architecture of MIL-100-type framework. A unit cell is given on the left, and two types of mesoporous cages in polyhedral mode on the right; the medium cage (green), and large cage (red). The medium cages share faces and form interconnected rods, the interstices of which are located in the large cages. Representation is adopted according to the ref. [180].

MIL-100 (Fe)

Another mesoporous MOF from the MIL-100 series, MIL-100(Fe), of chemical composition $\text{Fe}_3\text{F}_3\text{O}[\text{C}_6\text{H}_3-(\text{CO}_2)_2]_3 \cdot n\text{H}_2\text{O}$ ($n \sim 14.5$), has been used for the TDS investigation. The structure is formed by the supertetrahedra as building blocks, constructed of iron(III) trimers linked by the tricarboxylate BTC linkers. The supertetrahedra themselves have a microporous character with a pore size slightly larger than in MIL-100(Cr), 6.6 Å in diameter. Like within MIL-100(Cr), supertetrahedra form two types of mesoporous cages of free apertures of ca. 25 and 29 Å in diameter, accessible through microporous windows of ca. $4.7 \times 5.5 \text{ \AA}^2$ and $8.6 \times 8.6 \text{ \AA}^2$, respectively. Nitrogen physisorption measurements revealed a Langmuir surface area which exceeds $2800(100) \text{ m}^2 \text{ g}^{-1}$ [181].

Table 5.1. summarizes the structural and sorption characteristics of all investigated MOF samples.

TABLE 5.1**The Structural and Sorption Characteristics of Investigated Micro- and Mesoporous MOFs with Conformationally Rigid Structure.**

Sample Code	Sample	Empirical Formula	Central metal ion	Organic linker	Pore and (window opening) diameter [Å]	S _{BET} [m ² g ⁻¹]	S _{Langmuir} [m ² g ⁻¹]
Basolite™ C300	Cu–BTC	C ₁₈ H ₆ Cu ₃ O ₁₂	Cu ²⁺	BTC	9 & 5 (3.5)	1154	1958
Basolite™ F300	Fe–BTC	C ₉ H ₃ FeO ₆	Fe ³⁺	BTC	25 (5.5) & 29 (8.6)	1300–1600	/
LR 0219	Mg–formate(1)	C ₆ H ₆ Mg ₃ O ₁₂	Mg ²⁺	FA	3.4	16	24
Basosiv™ M050	Mg–formate(2)	C ₂ H ₂ MgO ₄	Mg ²⁺	FA	/	400–600	/
Basolite Z377	MOF–177	C ₁₂₉ H ₂₀₁ N ₁₅ O ₃₁ Zn ₄	Zn ⁴⁺	BTB	11.17 (10.8)	4239	5635
/	MFU–4	C ₁₈ Cl ₄ N ₁₈ Zn ₅	Zn ²⁺	BBTA	3.88 & 11.94 (2.52)	1611	/
/	MFU–4l	C ₃₆ C ₁₄ N ₁₈ H ₁₂ O ₆ Zn ₅	Zn ³⁺	BTDD	11.97 & 18.56 (9.13)	2746	/
DUT–4	Al(OH)(ndc)	C ₄₈ H ₂₈ O ₂₀ Al ₄	Al ³⁺	NDC	8.5 x 8.5	1308	1996
DUT–5	Al(OH)(bpdc)	C ₅₆ H ₃₆ O ₂₀ Al ₄	Al ³⁺	BPDC	11.1 x 11.1	1613	2335

/	MIL-100(Al)	$C_{306}H_{102}Al_{51}O_{374}$	Al^{3+}	BTC	25 (5.2) & 29 (8.8)	2152(39)	2919(44)
/	MIL-100(V)	/	V^{3+}	BTC	25 & 29	/	2139
/	MIL-100(Cr)	/	Cr^{3+}	BTC	6.5, 25 (4.7 x 5.7) & 29 (8.6 x 8.6)	/	3100
/	MIL-100(Fe)	/	Fe^{3+}	BTC	6.6, 25 (4.5 x 5.5) & 29 (8.6 x 8.6)	/	2800

Acronyms:

BTC – benzene-1,3,5-tricarboxylate, *FA* – Formic Acid, *BTB* – benzene-1,3,5-tribenzoate, *H₂-BBTA* = 1H,5H-benzo(1,2-d:4,5-d')bistriazole}, *H₂-BTDD* – bis-1H-1,2,3-triazolo-[4,5-b],[4',5'-i]dibenzo-[1,4]-dioxin, *NDC* – naphthalene-2,6-dicarboxylate, *BPDC* – 4,4'-biphenyldicarboxylate.

5.2. Thermal Desorption Spectroscopy of H₂, HD, and D₂

5.2.1 Results

Prior to H₂/HD/D₂ adsorption, all investigated MOF samples have been out-gassed under HV, following the activation procedure prescribed by the sample supplier (to avoid possible changes in the MOF crystal structure, or its total decomposition under the conditions of activation), Table 5.2.

TABLE 5.2

The total amount and the out-gassing procedure of investigated MOF Samples employed for the TDS measurements.

Sample	Sample mass [mg]	T_{act} [K]	t_a [h]
Cu-BTC	3.72	480	8
Fe-BTC	4.16	470	10
Mg-formate(1)	5.04	470	14
Mg-formate(2)	4.30	470	10
MOF-177	3.12	417	15
MFU-4	4.17	500	15
MFU-4l	3.28	430	20
Al(OH)(ndc)	2.16	455	7
Al(OH)(bpdc)	3.18	455	7
MIL-100(Al)	3.43	460	9
MIL-100(V)	4.16	420	8
MIL-100(Cr)	3.36	515	10
MIL-100(Fe)	2.87	470	40

Acronyms: T_{act} – activation temperature, and t_a – time of annealing.

The majority of the TDS spectra are presented with respect to both hydrogen and deuterium desorption, in the same temperature range and for the same intensity range, thus, the relative contribution of different maxima can be directly compared. All spectra are presented in the temperature range, where gas desorption is pronounced, and occurs above the background level. Most commonly, in the temperature range from 17 to 120 K, whereas desorption at higher temperature is found to be negligible.

Initially, a comparison is given for hydrogen and deuterium TDS spectra recorded under the same experimental conditions. The investigated MOF samples were cooled down to about 20 K, under 25 mbar gas atmosphere, and, after evacuating the sample cell at 20 K, the TDS spectra of Cu–BTC (Fig. 5.14), Fe–BTC (Fig. 5.18), Mg–formate(1) (Fig. 5.20), Mg–formate(2) (Fig. 5.23), MFU–4 (Fig. 5.30), MFU–4l (Fig. 5.32), MIL–100(V) (Fig. 5.38), MIL–100(Cr) (Fig. 5.40), and MIL–100(Fe) (Fig. 5.42) have been recorded with two distinct heating rates, 0.10 and 0.01 K s⁻¹.

To get a closer insight into the desorption mechanism, and the number of different adsorption sites, several desorption spectra have been recorded for each sample by changing the initial gas loading. The samples were exposed to gas at RT, and subsequently cooled down to about 20 K. The following samples were recorded by changing the initial gas loading in the pressure range from 1 to 700 mbar: Fe–BTC (Fig. 5.19), Mg–formate(1) (Fig. 5.21), Mg–formate(2) (Fig. 5.24), MOF–177 (Fig. 5.27), MFU–4 (Fig. 5.31), and MFU–4l (Fig. 5.33), while the initial gas loading was varied in the range from 1 to 25 mbar for MIL–100(V) (Fig. 5.39), MIL–100(Cr) (Fig. 5.41), and MIL–100(Fe) (Fig. 5.43). All spectra are recorded with the heating rate of 0.10 K s⁻¹.

Cu – BTC

Fig. 5.14 shows the TDS spectra of hydrogen and deuterium for Cu–BTC, for two distinct heating rates, 0.10 and 0.01 K s⁻¹. Three maxima are observed, and centered at about 31, 35, and 47 K for hydrogen, and at about 32, 38, and 51 K for deuterium (heating rate of 0.01 K s⁻¹). The total gas uptake is determined to be 117 and 197 molecules per unit cell for H₂ and D₂. In this representation 1 wt% of hydrogen storage corresponds to 48 H₂ molecules per unit cell.

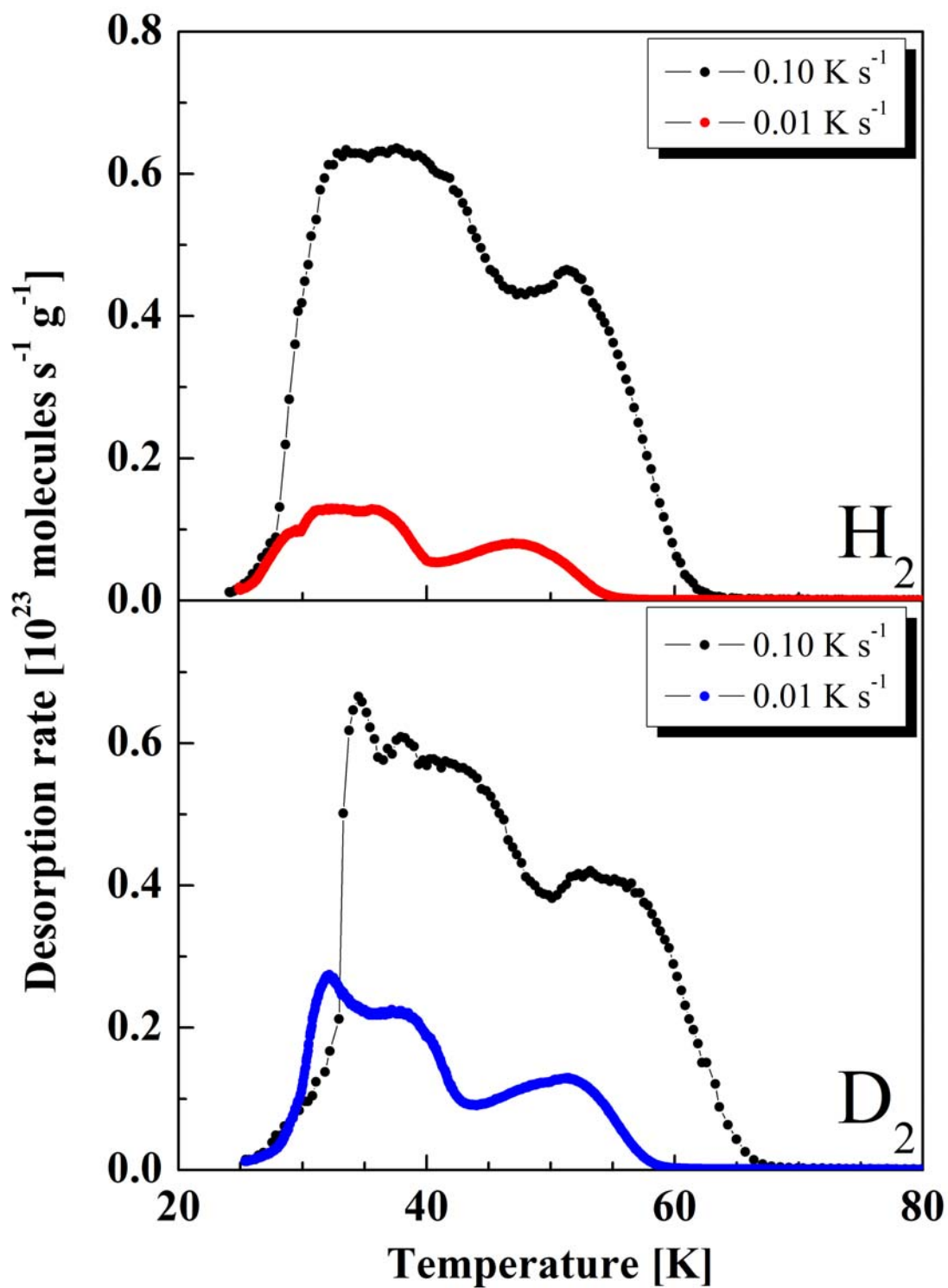


Fig. 5.14 The TDS spectra of hydrogen and deuterium on Cu-BTC, loaded at 25 mbar, and recorded with the heating rate of 0.10 and 0.01 $K s^{-1}$.

In Fig. 5.15 the interrupted desorption spectrum of Cu–BTC is shown. The sample was loaded with 25 mbar of deuterium, and the spectra recorded with the heating rate of 0.01 K s^{-1} . The first heating run was carried out from 24 to 45 K (Fig. 5.15a), and from 24 to 48 K (Fig. 5.15b), and resulted in one desorption peak, followed by an additional shoulder at high temperature. The contribution of different maxima was found to be better separated using 45 K as an inflection point. Therefore, spectra shown in Fig. 5.15a are used for further discussion. The second heating run, applied from 25 to 80 K, showed only one desorption peak, centered at 51 K.

The total amount of deuterium desorbed within the first heating run is 131 D_2 molecules per unit cell. In the second run, the amount of deuterium desorbed corresponds to 61 D_2 molecules per unit cell. Both values are calculated after subtracting the amount of gas desorbed below 30.3 K.

In addition, sequential filling of different adsorption sites was studied by changing the initial gas loading (Fig. 5.16). The sequential filling of the high temperature maximum is shown in Fig. 5.17, in the temperature range from 40 to 65 K. The heating rate was set to 0.01 K s^{-1} , to preserve slow gas desorption, and attain good resolution of overlapping maxima. The shape of the peaks did not change for different gas loadings. The peaks are asymmetric, and for all exposures coincide in the trailing edge of the desorption spectra. In the range of 1 to 6 mbar pronounced filling of the first adsorption site, with the maximum centered at about 53 K, was observed. In this pressure range 7 to 35 D_2 molecules per unit cell were desorbed in total. Increasing the pressure further resulted in increased intensity of the second maximum, centered at about 38 K, where 106 D_2 molecules per unit cell were desorbed. For 25 mbar gas loading filling of the third adsorption site was pronounced, and 197 D_2 molecules per unit cell desorbed in total. Further increase in pressure (200 mbar) increased the total storage capacity to 218 D_2 molecules per unit cell. The amount of gas desorbed within each gas loading is given in Table B–1, expressed both in wt.% D_2 , and by the number of D_2 molecules per unit cell.

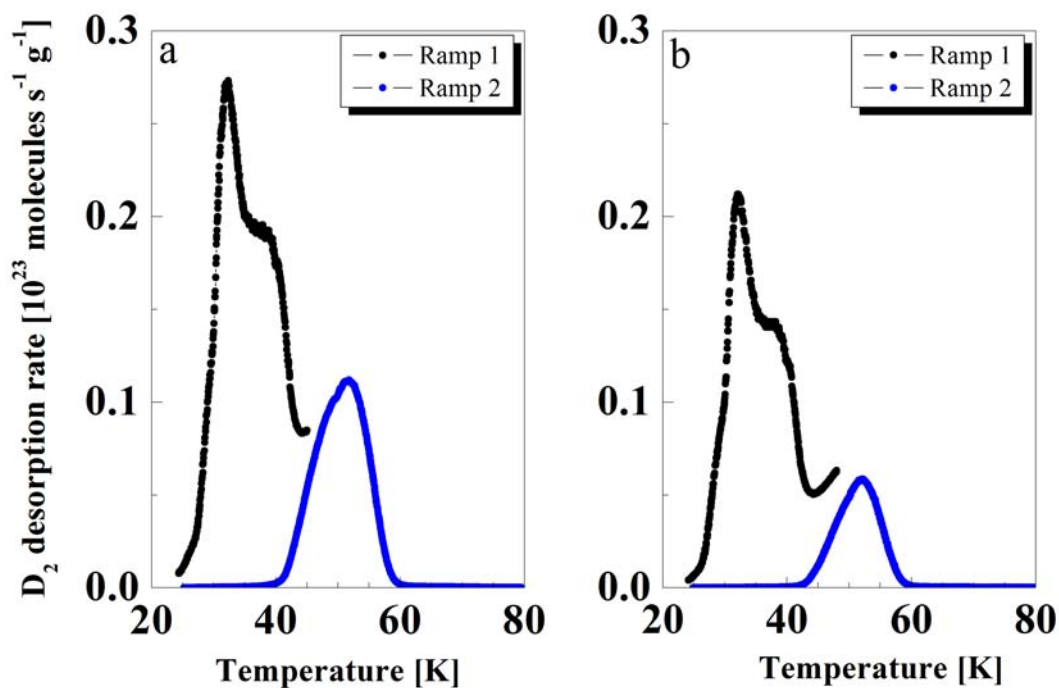


Fig. 5.15 Deuterium desorption spectra on Cu-BTC, obtained upon applying two independent heating regimes, from 24 to 45 K (a), and from 24 to 48 K (b) (denoted as ramp 1), and from 25 to 80 K (denoted as ramp 2).

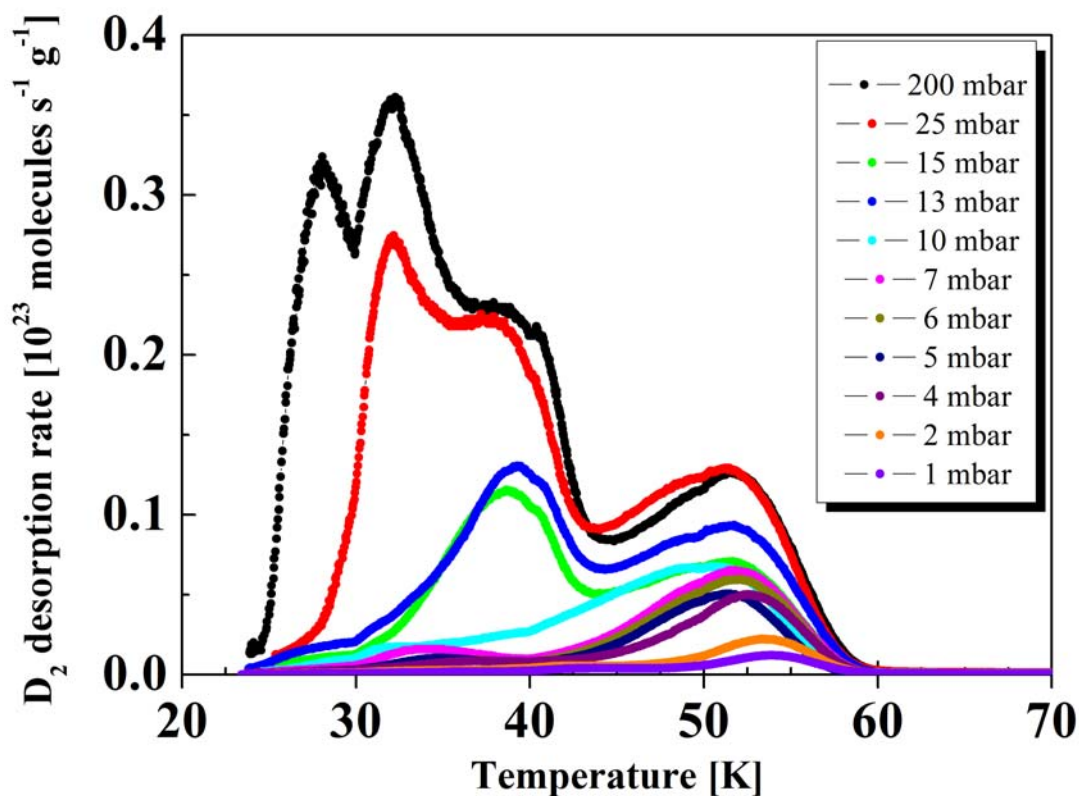


Fig. 5.16 Deuterium desorption spectra obtained by altering initial gas loading on Cu-BTC, in the range from 1 to 200 mbar. The spectra are recorded with the heating rate of 0.01 K s^{-1} .

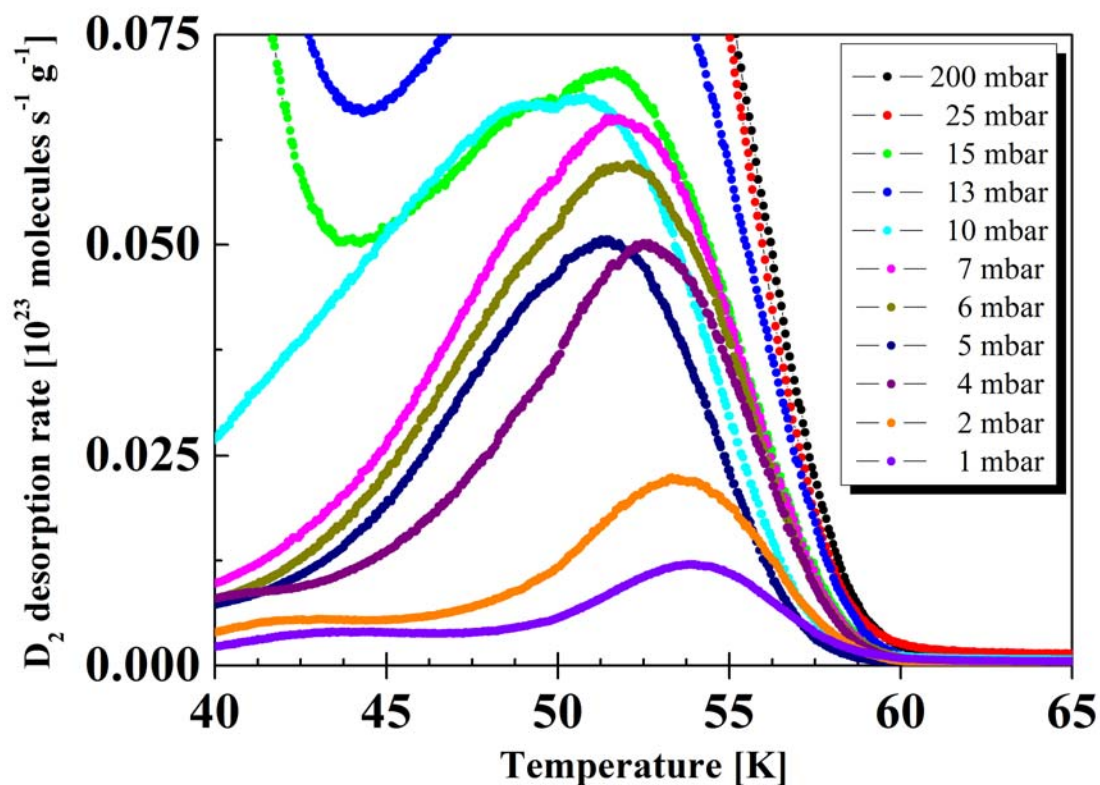


Fig. 5.17 Pronounced filling of the high temperature maximum for Cu-BTC, presented in the temperature range from 40 to 65 K, and recorded with the heating rate of 0.01 K s^{-1} .

Fe – BTC

In Fig. 5.18 the TDS spectra of hydrogen and deuterium for Fe-BTC are shown. The main desorption peak is observed at about 27 and 33 K for hydrogen and deuterium, respectively. Two additional desorption shoulders can be resolved, at 23 and 42 K for hydrogen, and at 27 and 44 K for deuterium.

The total amount of gas desorbed corresponds to 2.02 wt.% H_2 and 3.06 wt.% D_2 .

Furthermore, an additional investigation has been made by partial sample loading. Upon increasing the initial gas loading, the peak intensity increases, Fig. 5.19. The spectra coincide in the trailing edge, and the position of the peak maximum shifts toward lower temperatures for increased gas loading. The total amount of gas desorbed for all partial coverages used is given in Table B-2.

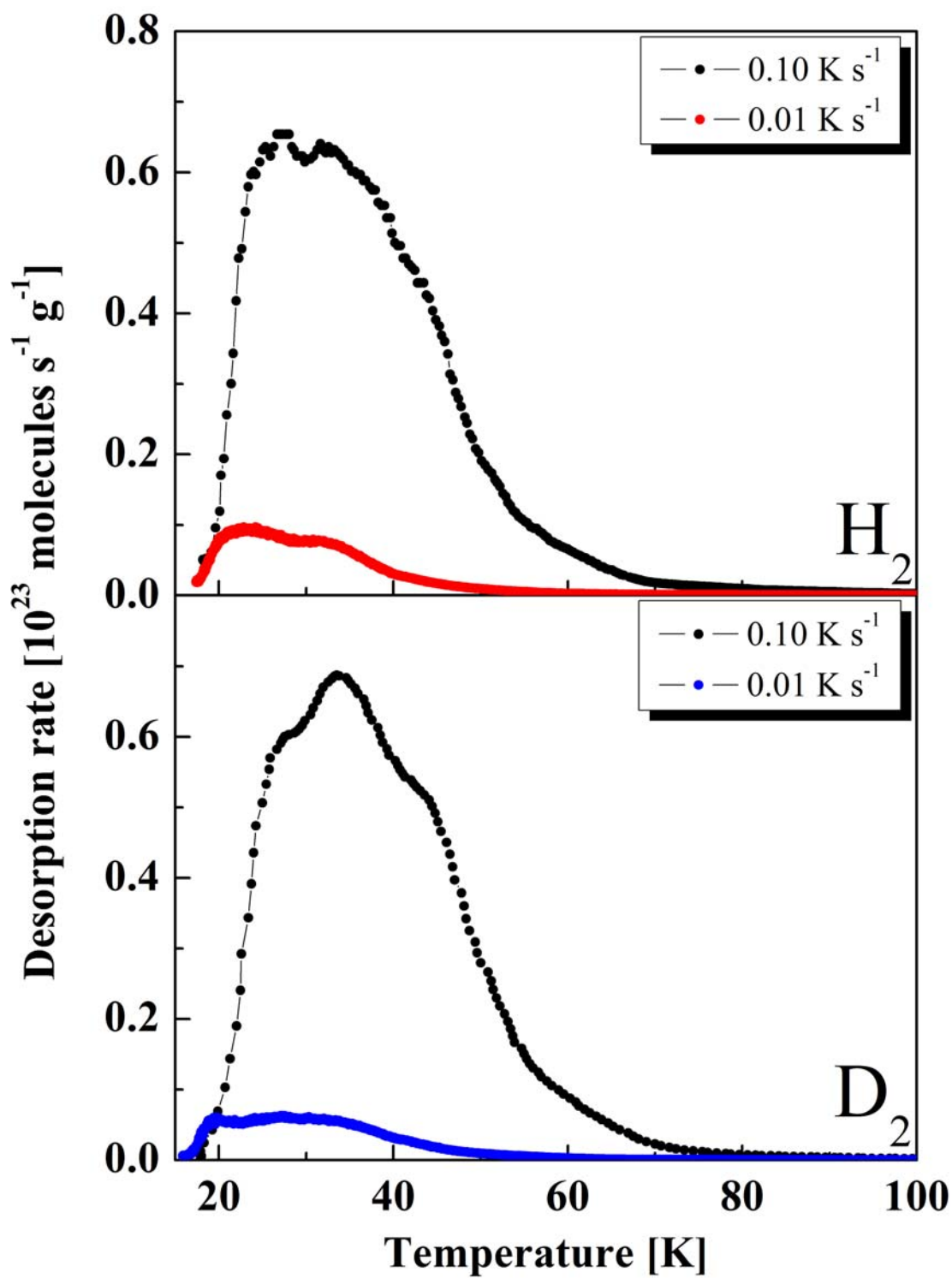


Fig. 5.18 A comparison of the TDS spectra of hydrogen and deuterium for Fe-BTC loaded at 25 mbar, and recorded with the heating rate of 0.10 and 0.01 $K s^{-1}$.

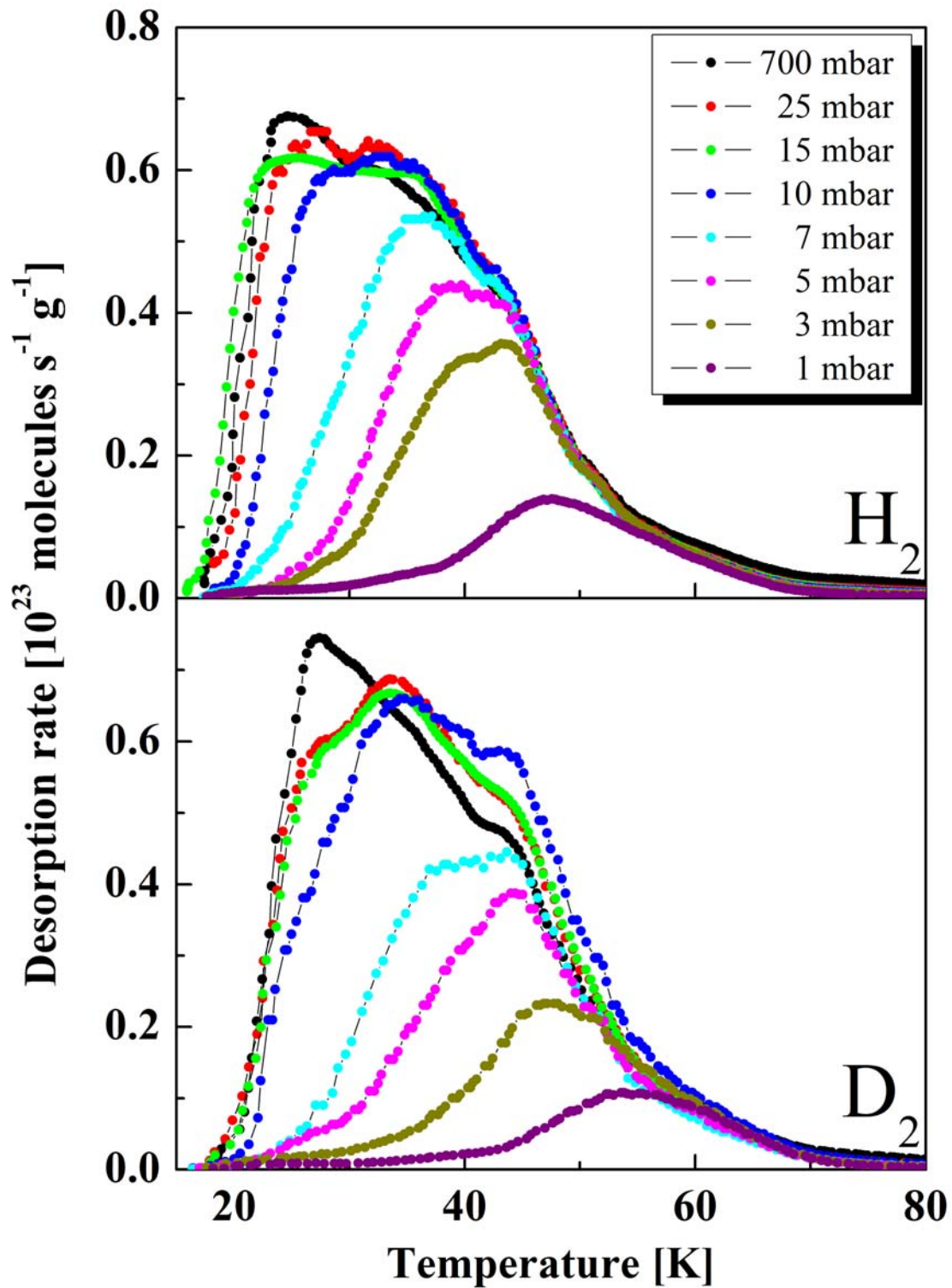


Fig. 5.19 The TDS spectra of hydrogen and deuterium for Fe–BTC, for different initial gas loadings, and recorded with the heating rate of 0.10 K s^{-1} .

Mg-formate(1)

Fig. 5.20 shows hydrogen and deuterium desorption spectra of Mg-formate(1), recorded with two distinct heating rates, 0.10 and 0.01 K s⁻¹. Apart from the low temperature peak centered at 19 K, the hydrogen desorption spectrum shows one broad maximum centered at about 48 K, and an additional maximum centered at about 78 K. For deuterium desorption maxima are centered at 26, 51, and 74 K (heating rate of 0.10 K s⁻¹). The total amount of gas desorbed is calculated to be 0.81 wt.% H₂, and 1.68 wt.% D₂.

The desorption mechanism of Mg-formate(1) was further investigated by partial sample loading, Fig. 5.21. The partial filling of the main desorption peak is observed, with the maximum centered at about 48 and 51 K for hydrogen and deuterium, respectively. For increased gas loading (25, 100, and 700 mbar), filling of the high temperature maximum, centered at about 74 K for hydrogen and 73 K for deuterium, is pronounced (expressed for 700 mbar gas loading). Fig. 5.22 shows the high temperature regime with higher resolution. The total amount of gas desorbed for each applied pressure is given in the Table B-3.

Mg-formate(2)

In Fig. 5.23 the thermal desorption spectra of hydrogen and deuterium for Mg-formate(2) are presented. Two maxima are observed, at 23 and 51 K, and at 27 and 54 K for hydrogen and deuterium, respectively. Additionally, a small desorption shoulder is observed at about 76 and 71 K for hydrogen and deuterium, respectively. The total amount of gas desorbed is calculated to be 1.78 wt.% H₂, and 4.32 wt.% D₂.

Furthermore, the mechanism of gas desorption was investigated by partial loading, Fig. 5.24. For increased gas loading the main desorption peak gets filled. The high temperature regime is further addressed with a higher resolution in Fig. 5.25 for hydrogen, and in Fig. 5.26 for deuterium desorption. The spectra are presented in the narrow temperature range, from 65 to 85 K for hydrogen, and in the range of 65 to 80 K for deuterium, with emphasis on the change in the peak intensity. The total amount of gas desorbed, corresponding to different initial gas loadings, is given in Table B-4.

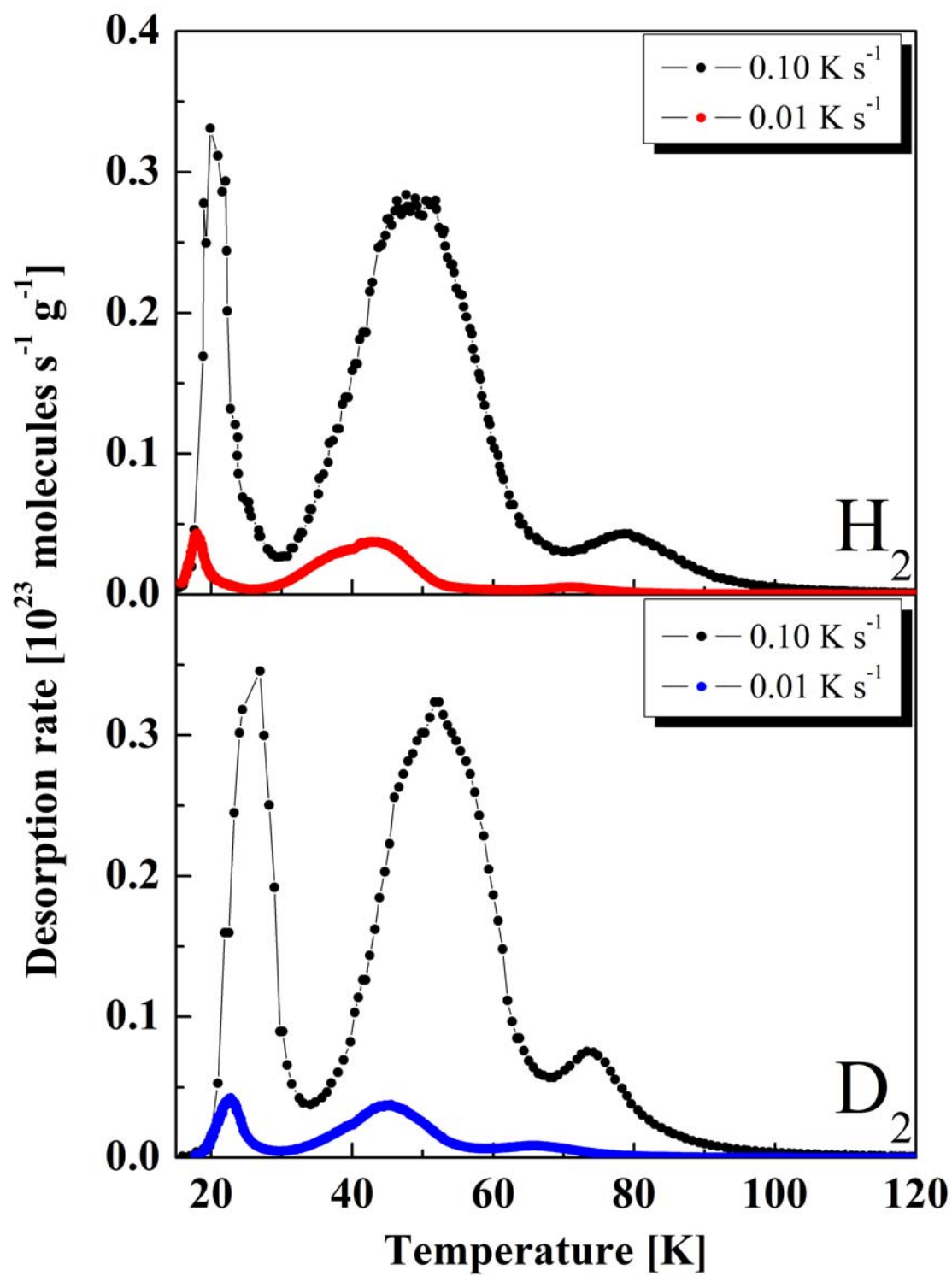


Fig. 5.20 H₂ and D₂ TDS spectra of Mg-formate(1), loaded at 25 mbar, and recorded with the two distinct heating rates, 0.10 and 0.01 K s⁻¹.

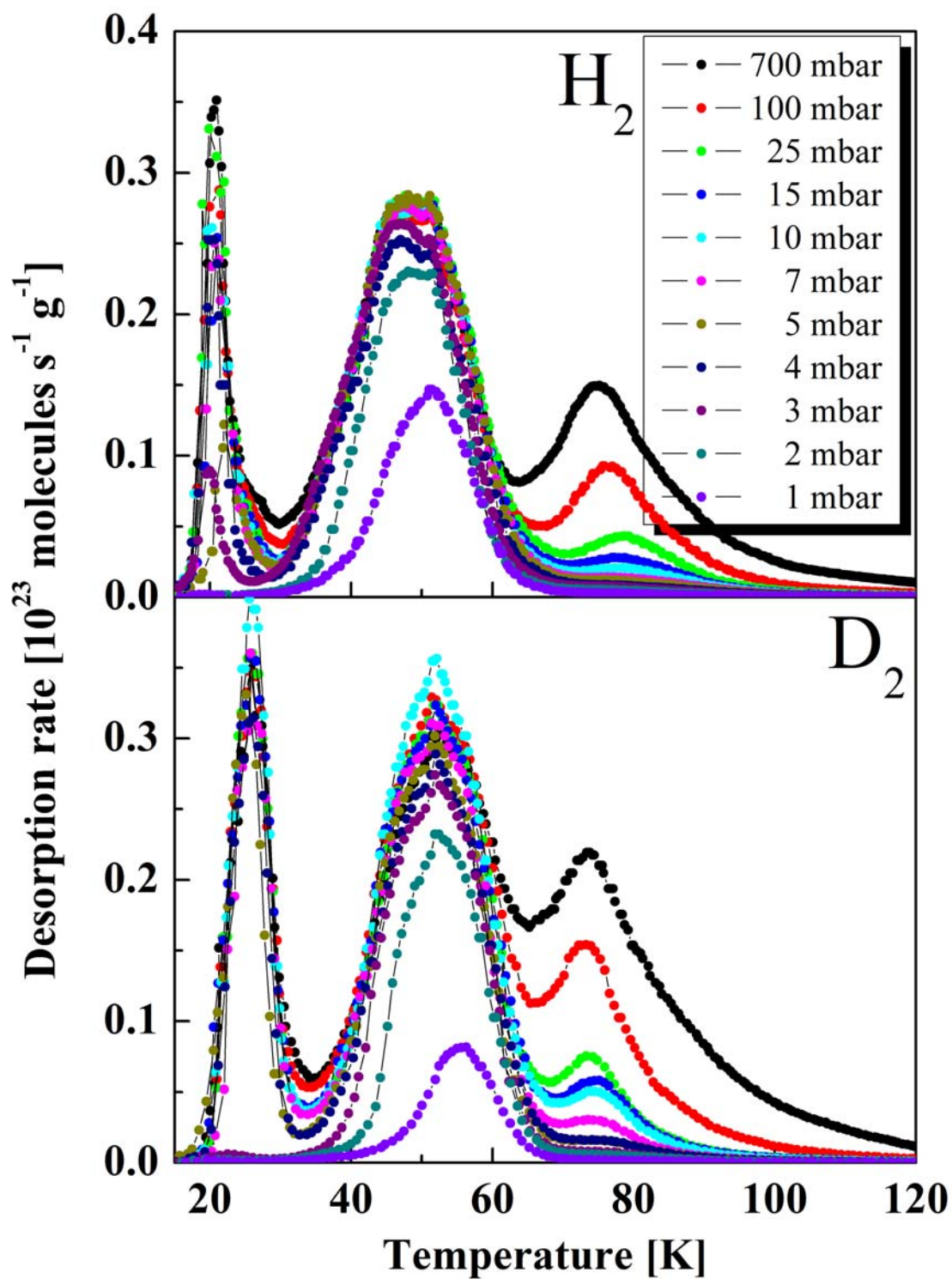


Fig. 5.21 H_2/D_2 desorption spectra of Mg-formate(1) obtained for different initial gas loadings, and recorded with the heating rate of 0.10 K s^{-1} .

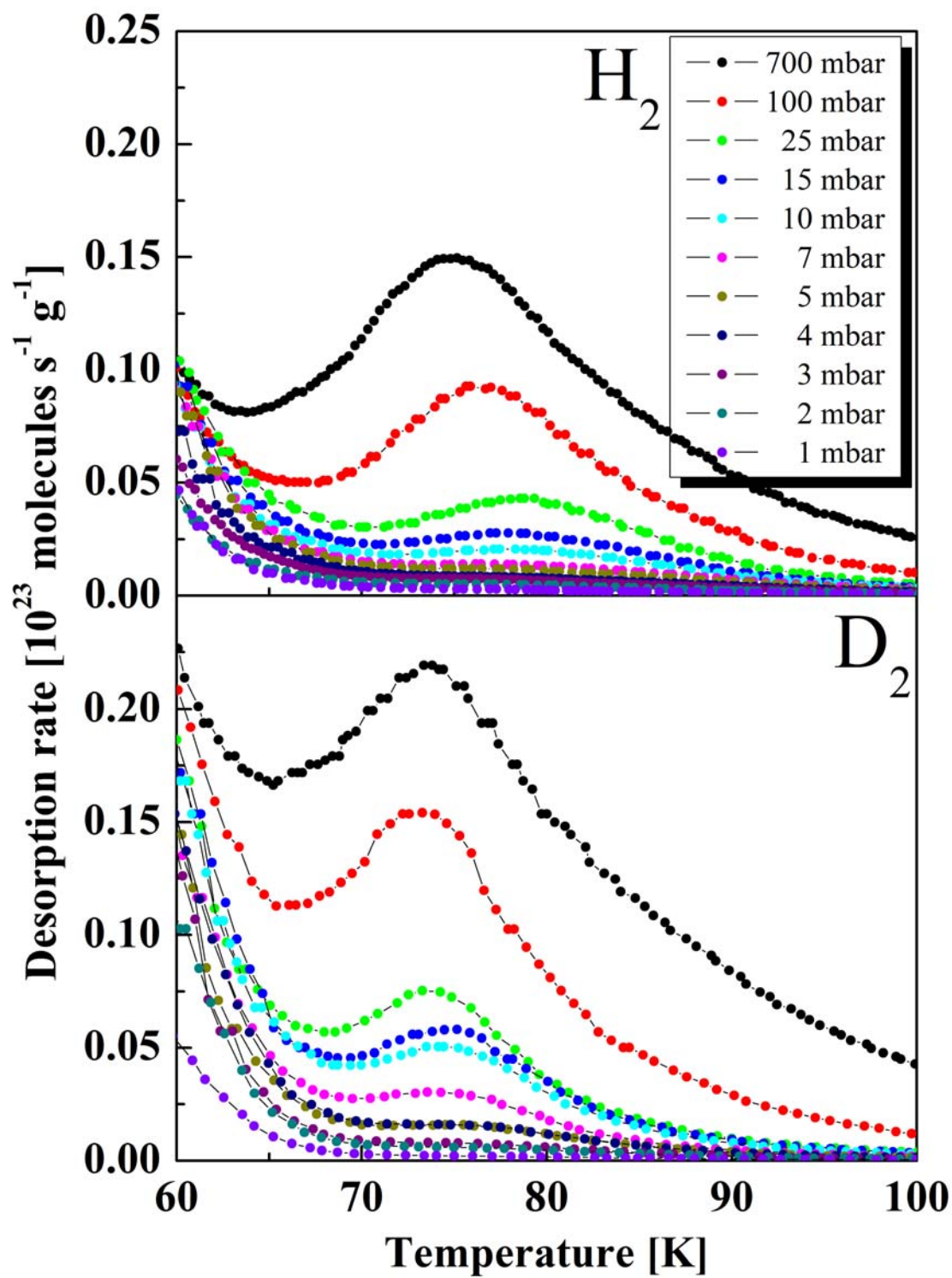


Fig. 5.22 The TDS spectra of Mg-formate(1) with the respect to the high temperature maximum. The spectra are recorded with the heating rate of 0.10 K s^{-1} , and presented in the temperature range from 60 to 100 K.

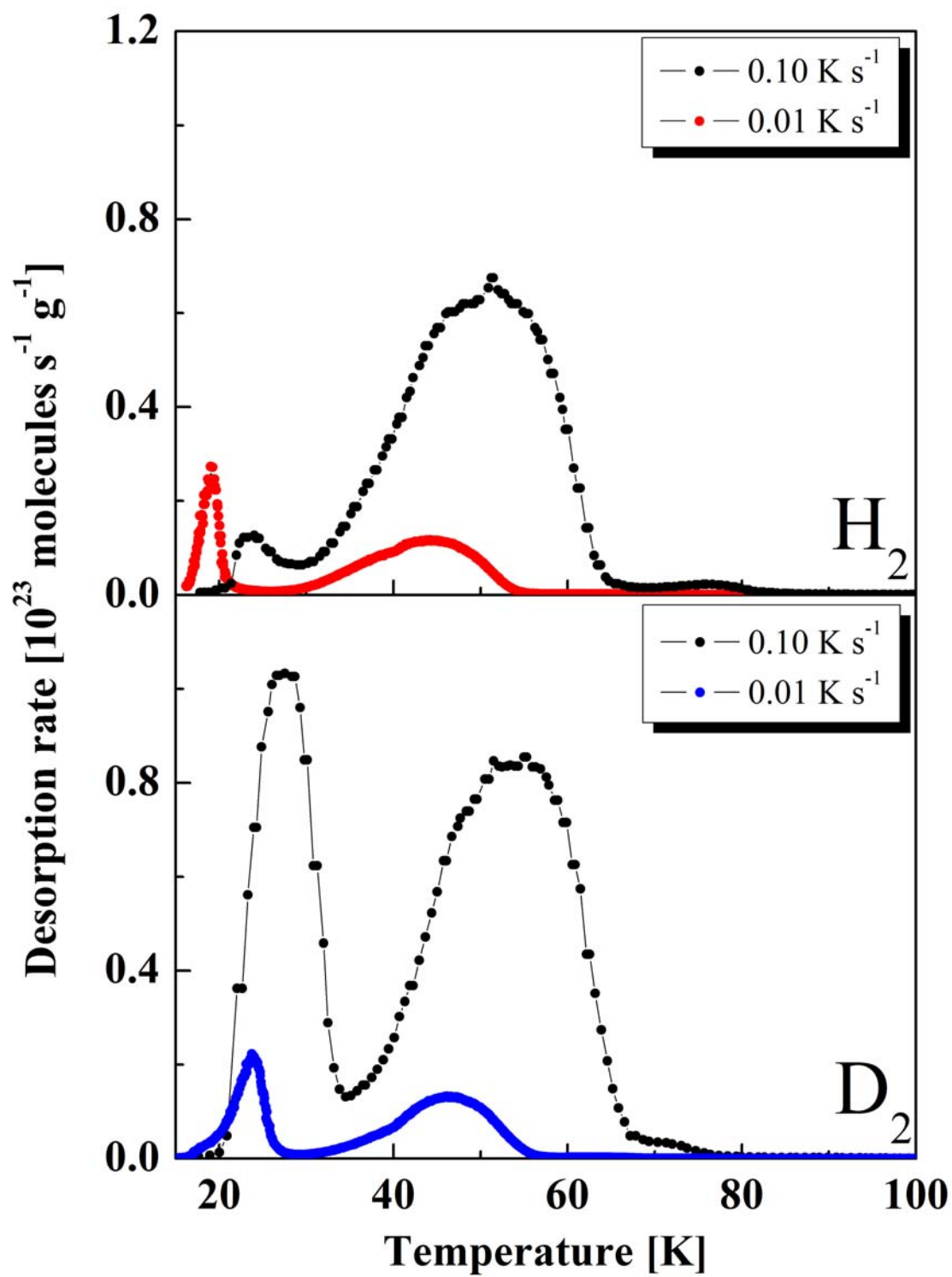


Fig. 5.23 The TDS spectra of hydrogen and deuterium for Mg-formate(2). The spectra are obtained for 25 mbar gas loading, and recorded with the heating rate of 0.10 and 0.01 $K s^{-1}$.

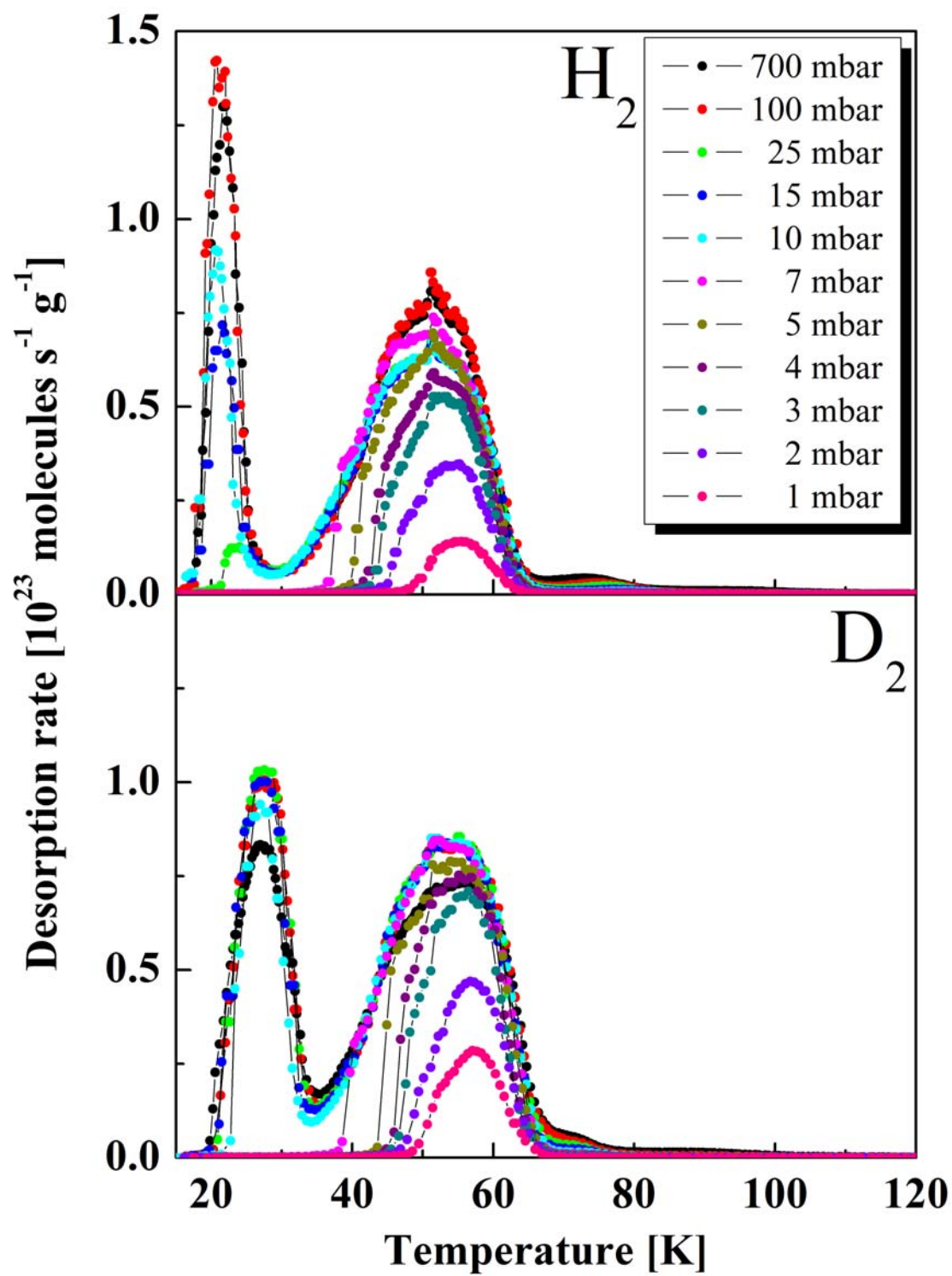


Fig. 5.24 The TDS spectra of hydrogen and deuterium for Mg-formate(2), recorded for different initial gas loadings, and recorded with the heating rate of 0.10 K s^{-1} .

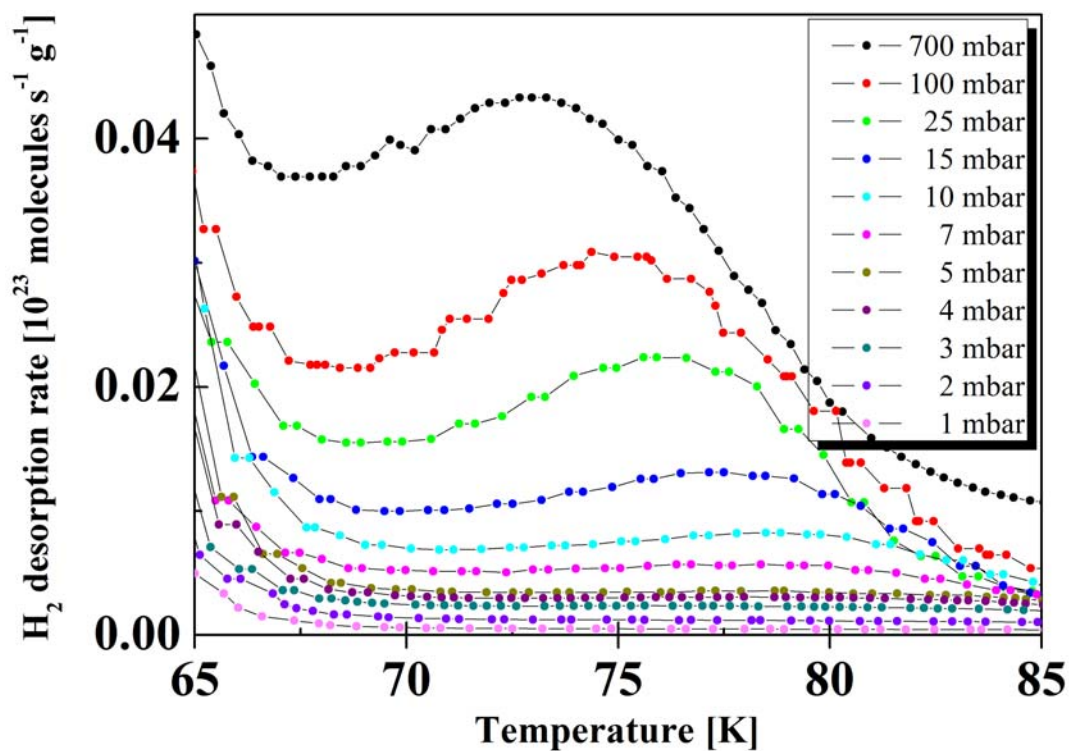


Fig. 5.25 The TDS spectra of hydrogen adsorbed on Mg-formate(2), showing a gradual filling of the high temperature maximum, recorded with the heating rate of 0.10 K s^{-1} .

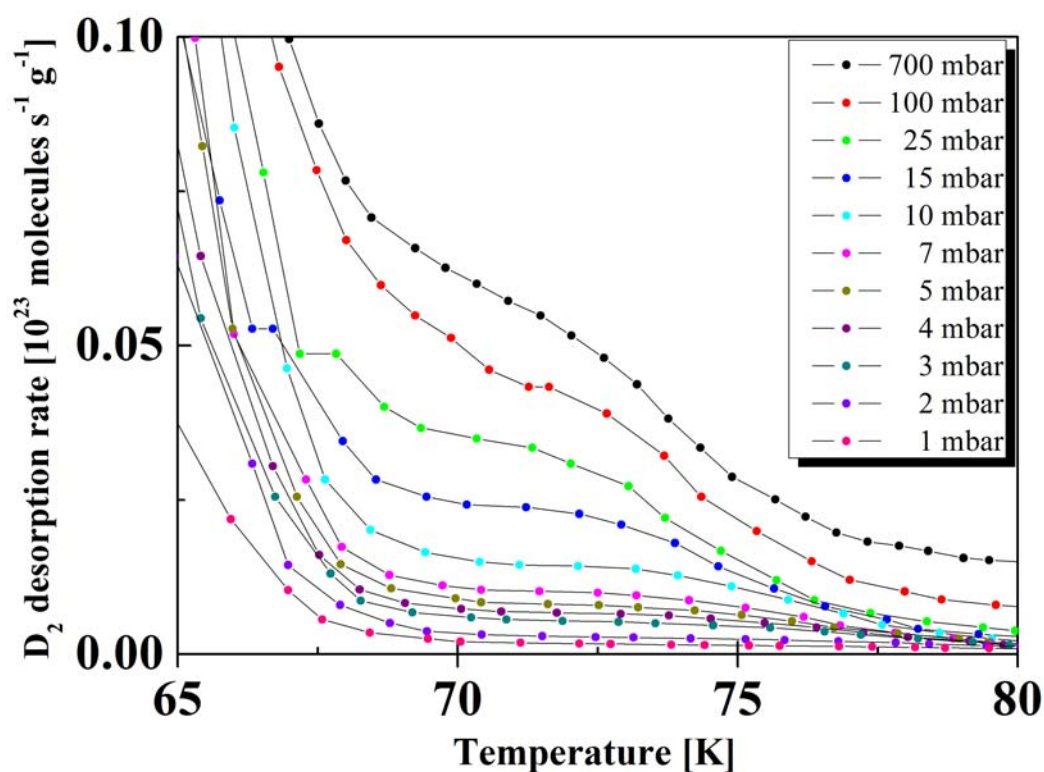


Fig. 5.26 The TDS spectra of deuterium for Mg-formate(2), with respect to the partial loading of the high temperature maximum. The desorption is presented in the temperature range from 65 to 80 K, and spectra recorded with the heating rate of 0.10 K s^{-1} .

MOF-177

In Fig. 5.27 the desorption spectra of MOF-177 are presented, for six different hydrogen loadings. The spectra are presented in the temperature range from 20 to 60 K, whereas the amount of gas desorbed at higher temperatures is found to be negligible. All desorption spectra begin with a long desorption tail at low temperature, below 30 K. In addition, a broad maximum is observed at about 35 K (expressed for 500 mbar gas loading). This maximum has a tendency to shift toward lower temperatures, upon increasing the initial gas loading. For 700 mbar gas loading two maxima are observed, at 32 and 37 K. The total amount of gas desorbed is given in the Table B-5.

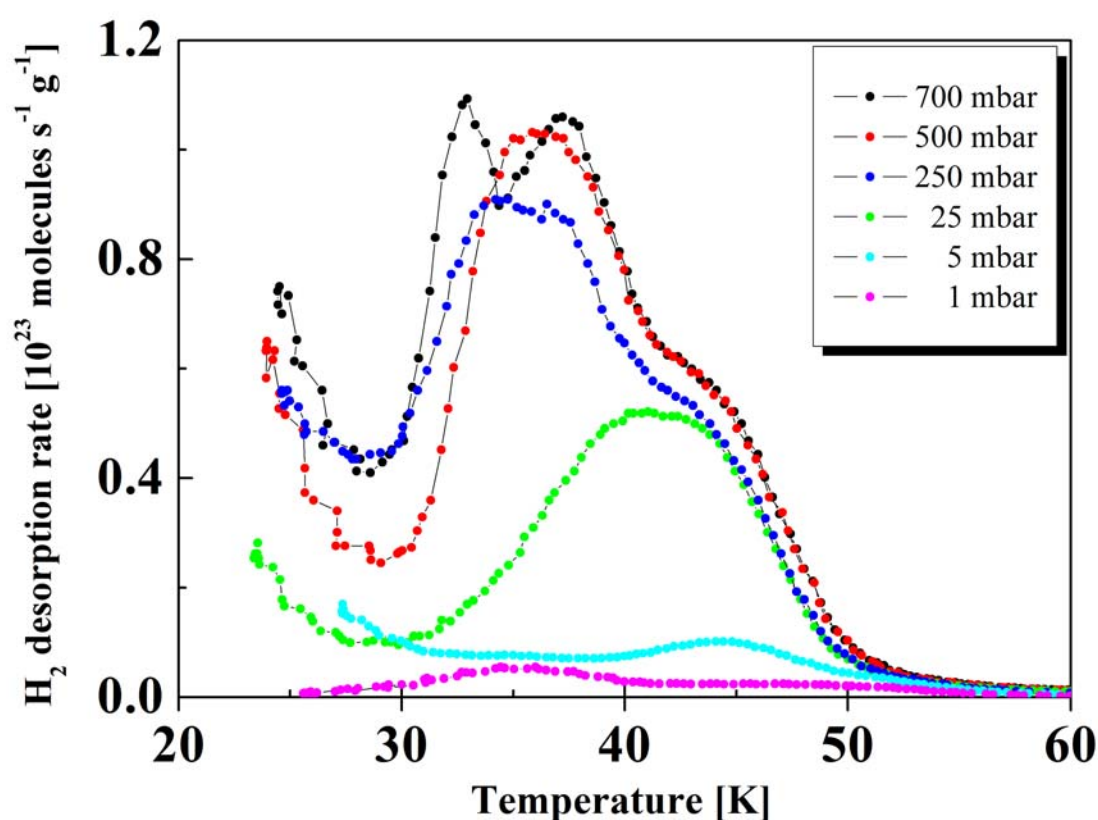


Fig. 5.27 The thermal desorption spectra of hydrogen for MOF-177, obtained for different initial gas loadings, and recorded with the heating rate of 0.10 K s^{-1} .

The desorption mechanism for MOF-177 was further investigated by performing measurements with deuterium. In Fig. 5.28 three desorption spectra are presented, for 25, 700, and 900 mbar gas loading, in the temperature range from 20 to 70 K. Apart from the long desorption tail at low temperature, as in the case of hydrogen desorption, a broad maximum is observed at 40 K, and additional peak at about 32 K (expressed for 700 mbar gas loading).

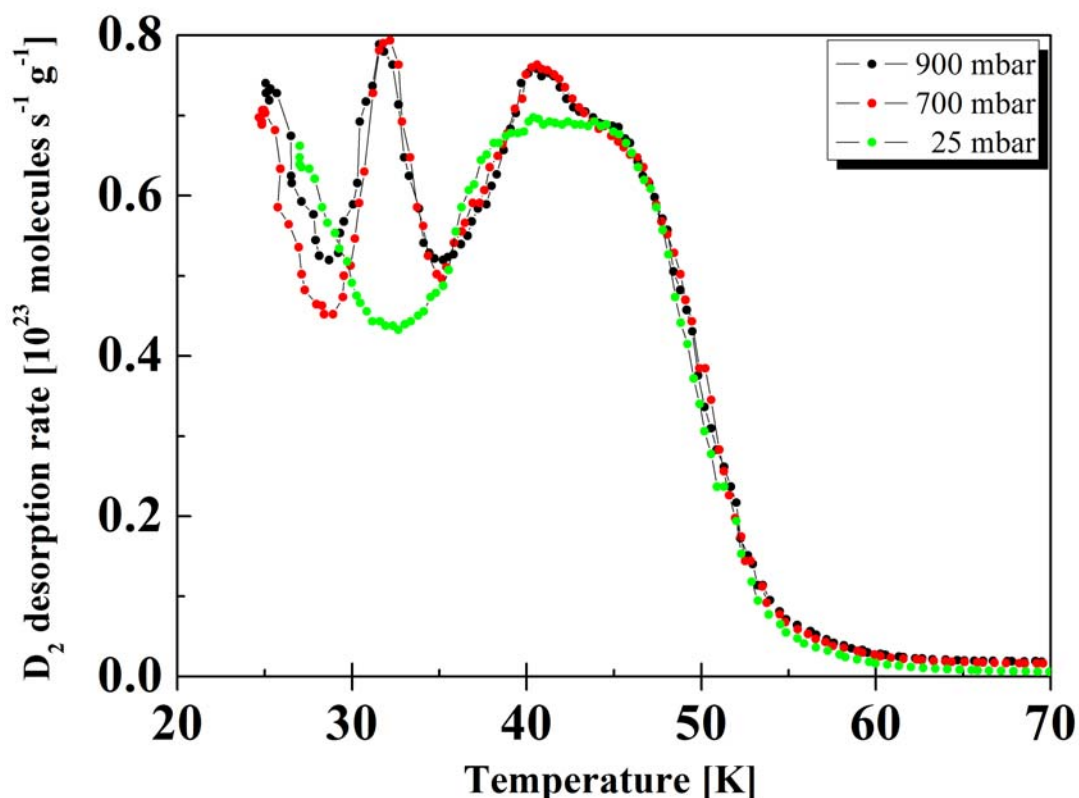


Fig. 5.28 The TDS spectra of deuterium for MOF-177, recorded for different gas loadings, and with the heating rate of 0.10 K s^{-1} .

In addition, gas mixture (300 mbar of H_2 + 300 mbar of D_2) was used for the TDS measurements, to probe possible adsorption on atomic level (Fig. 5.29). The desorption spectra are presented in the temperature range from 20 to 70 K, and recorded with the heating rate of 0.10 K s^{-1} . A broad desorption peak is observed at about 40 K, and relates to deuterium desorption on molecular level. The intensity of the peak for molecular hydrogen desorption was considerably lower, and with the maximum centered at 36 K. Desorption of gases on atomic level was found to be negligible, and in the background level, with the exclusion of HD, where a small contribution may be observed.

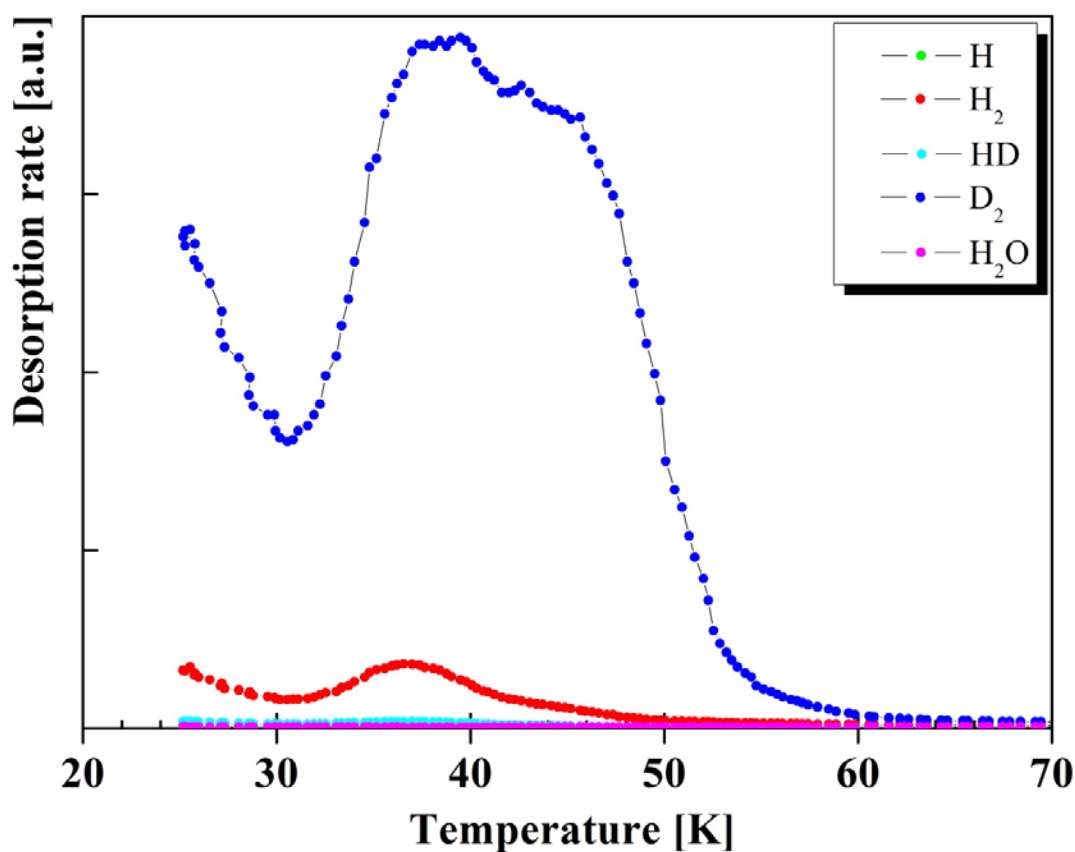


Fig. 5.29 Desorption from MOF-177 surface with respect to atomic and molecular hydrogen, atomic and molecular deuterium, hydrogen deuteride and water. The spectra are recorded after exposing the sample to H_2/D_2 gas mixture, and recorded with heating rate of 0.10 K s^{-1} .

MFU-4

In Fig. 5.30 the thermal desorption spectra of hydrogen and deuterium for MFU-4 are presented. The spectra show a low-temperature peak at about 30 K, and an additional major peak at 74 K for hydrogen, and at 25 and 74 K for deuterium (heating rate of 0.10 K s^{-1}). The total amount of gas desorbed corresponds to 0.23 wt.% H_2 , and 0.36 wt.% D_2 .

Fig. 5.31 shows the thermal desorption spectra of MFU-4 for different initial gas loadings. The spectra coincide, and show common leading-, and a common trailing edge. A small desorption shoulder is observed at very low temperature of about 23 and 25 K for hydrogen and deuterium, respectively.

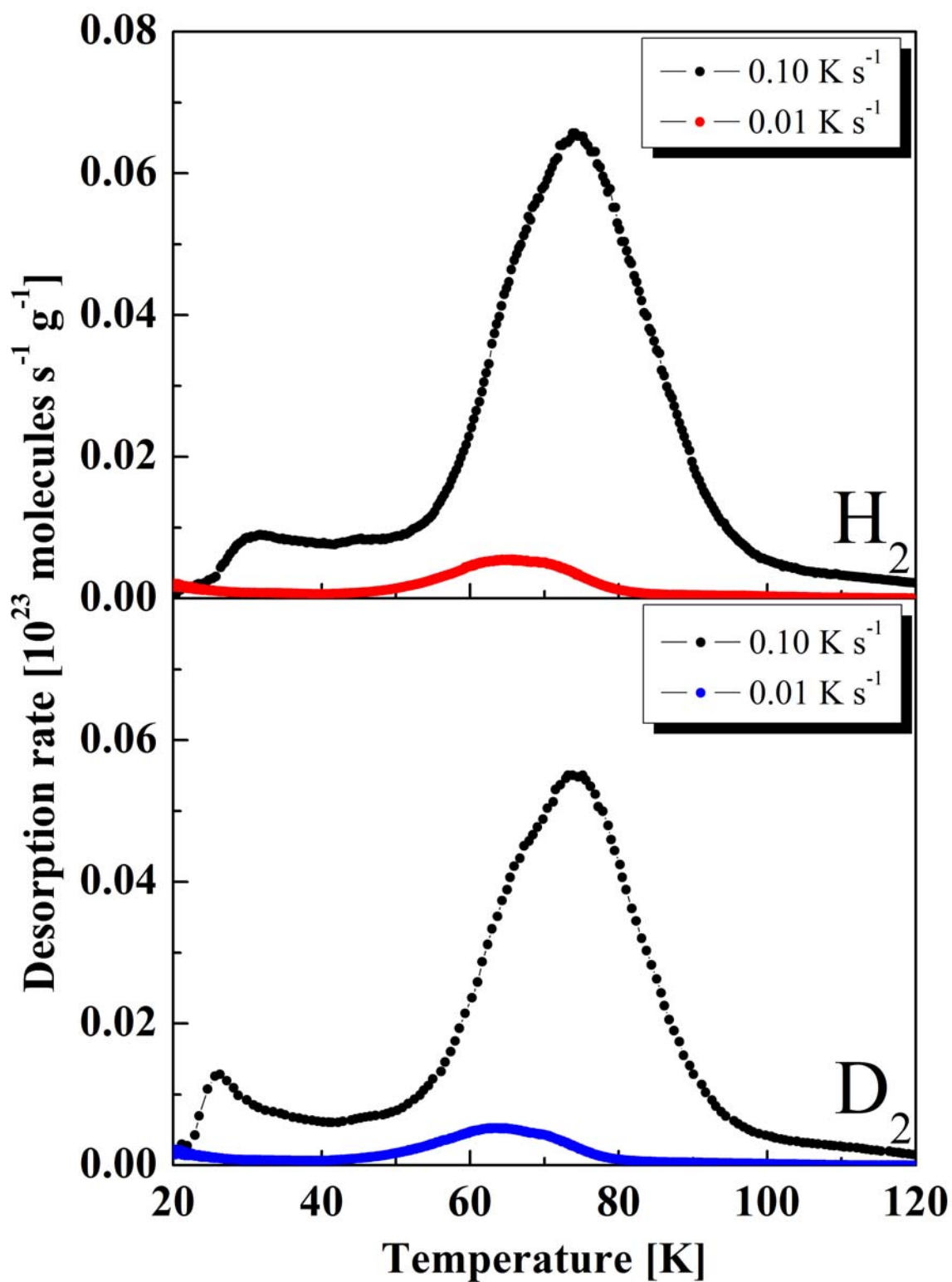


Fig. 5.30 A comparison of hydrogen and deuterium desorption spectra of MFU-4 loaded at 25 mbar, and recorded with two distinct heating rates, 0.10 and 0.01 K s^{-1} .

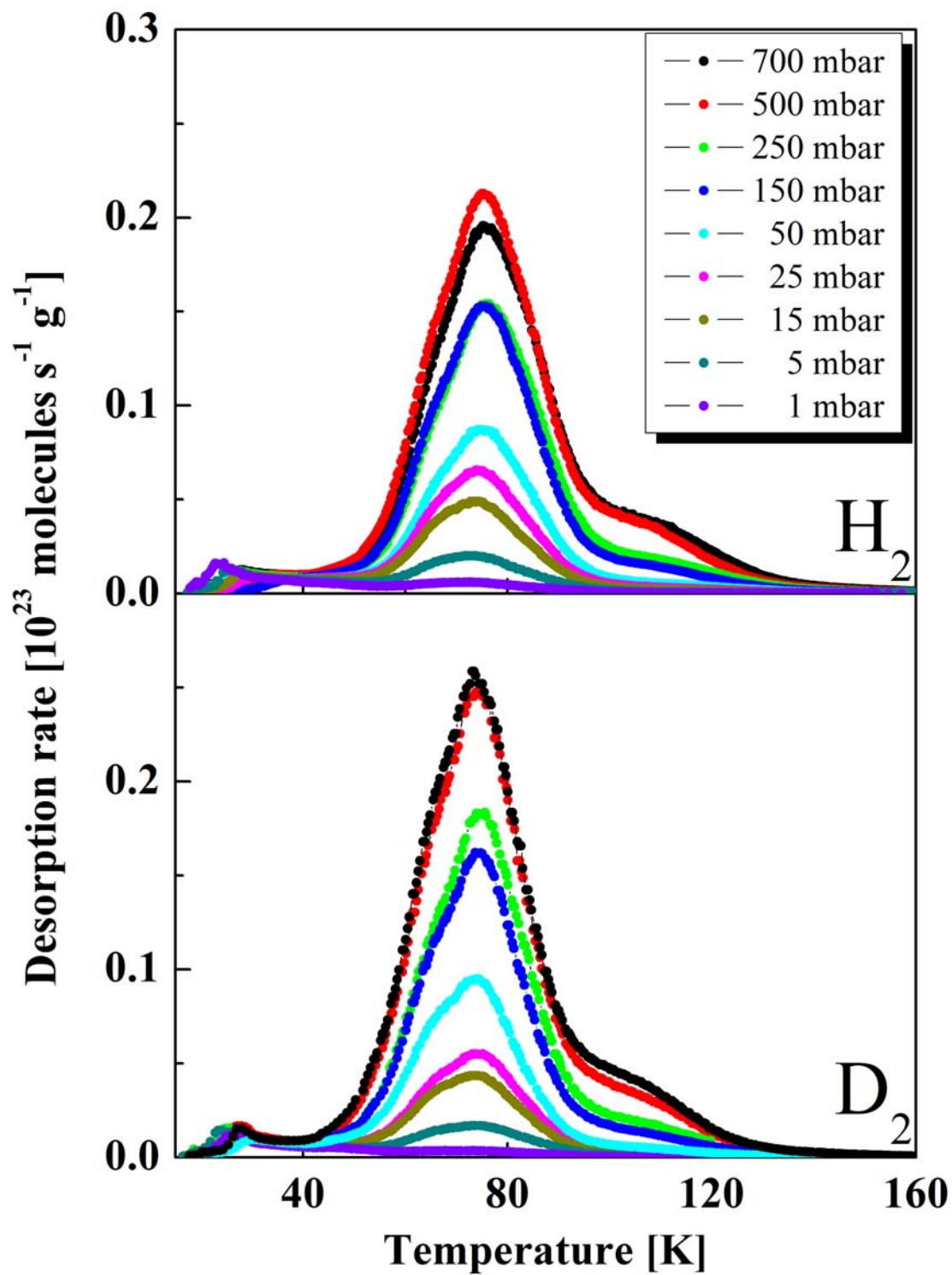


Fig. 5.31 The TDS spectra of MFU-4l obtained for different initial gas loadings, and recorded with the heating rate of 0.10 K s^{-1} .

The desorption spectrum, in addition, shows a major maximum centered at 75 K for hydrogen, i.e., 74 K for deuterium. For higher gas loadings (500 and 700 mbar) another desorption maximum is observed, centered at about 109 and 105 K for hydrogen and deuterium, respectively. Table B-6 summarizes the desorbed amount of gas for all gas exposures applied.

MFU-4l

In Fig. 5.32 the TDS spectra of hydrogen and deuterium for MFU-4l are shown, in the temperature range from 15 to 80 K. The spectra exhibit broad maximum, centered at about 31 and 32 K for hydrogen and deuterium, respectively. Apart from the major maximum, an additional peak is observed at slightly higher temperature, centered at about 51 and 53 K for hydrogen and deuterium, respectively. The total amount of gas desorbed is calculated to 2.29 wt.% H₂, and 4.73 wt.% D₂.

An additional comparison between hydrogen and deuterium desorption is shown in Fig. 5.33. The desorption spectra are recorded for different initial gas loadings, in the pressure range from 1 to 700 mbar. For 1 mbar gas loading a single maximum is observed, centered at 54 and 57 K for hydrogen and deuterium, respectively. For the sample loaded at 5 mbar this maximum reaches the saturation value, and an additional maximum appears at 33 K for hydrogen, and at 36 K for deuterium. An intensity increase and filling of the major adsorption site is observed while increasing the pressure further, and a slight shift in the position of the desorption maxima toward lower temperatures. Somewhat broad desorption maxima are observed at low temperature, for 700 mbar gas loading, in particular for deuterium desorption. Owing to the fact that already for 25 mbar gas loading saturation intensity has been reached, further pressure increase results in adsorption in multilayers. Due to the higher molar density of liquid D₂ (41.9 mol L⁻¹ at 22.24 K) than H₂ (35.12 mol L⁻¹ at 20.2 K) more liquid deuterium is formed, and gives rise to a broader maximum at low temperature. The total amount of gas desorbed for each pressure applied is given in Table B-7.

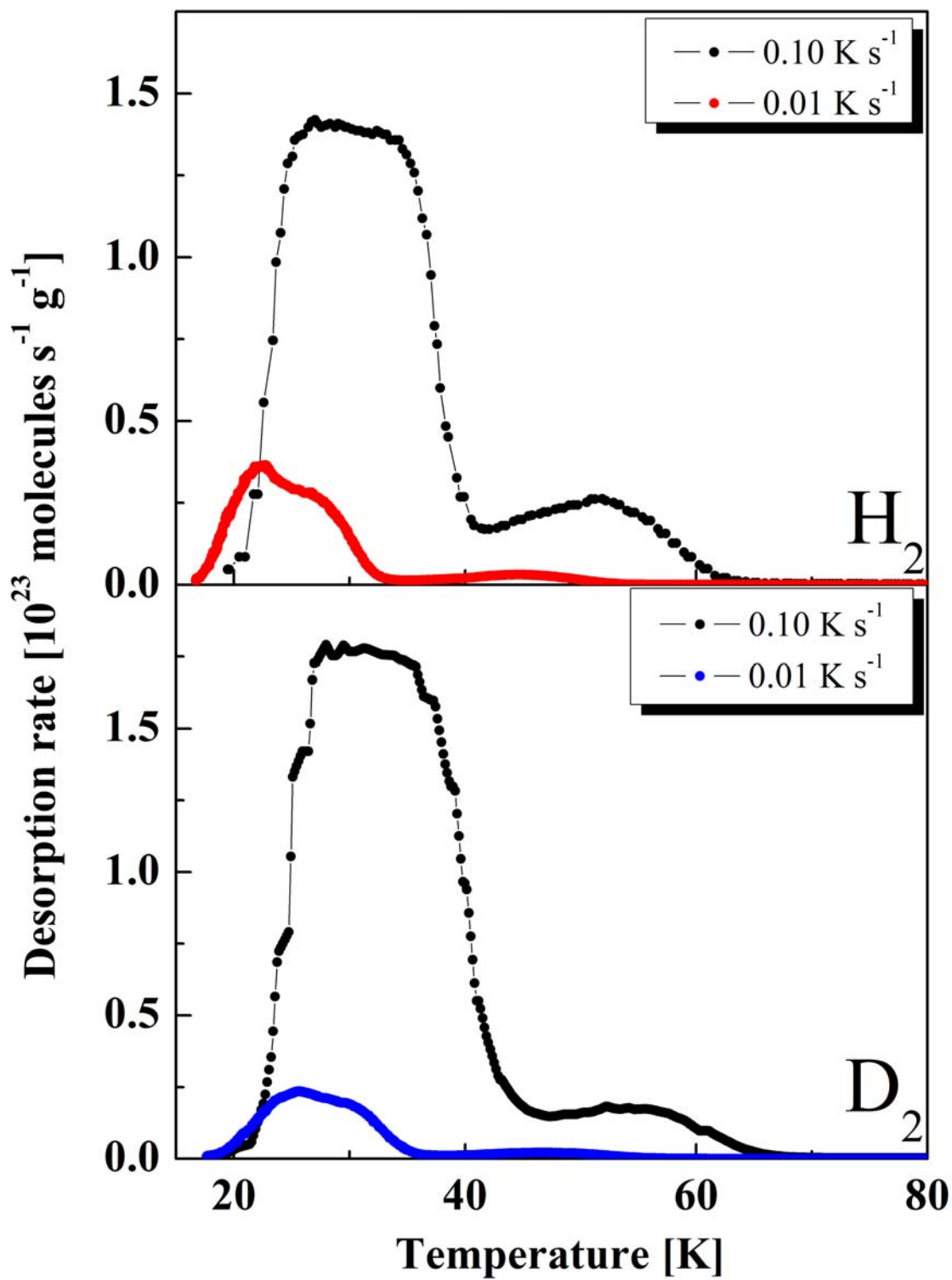


Fig. 5.32 A comparison of the TDS spectra of hydrogen and deuterium for MFU-4l, loaded at 25 mbar, and recorded with the heating rate of 0.10 and 0.01 $K s^{-1}$.

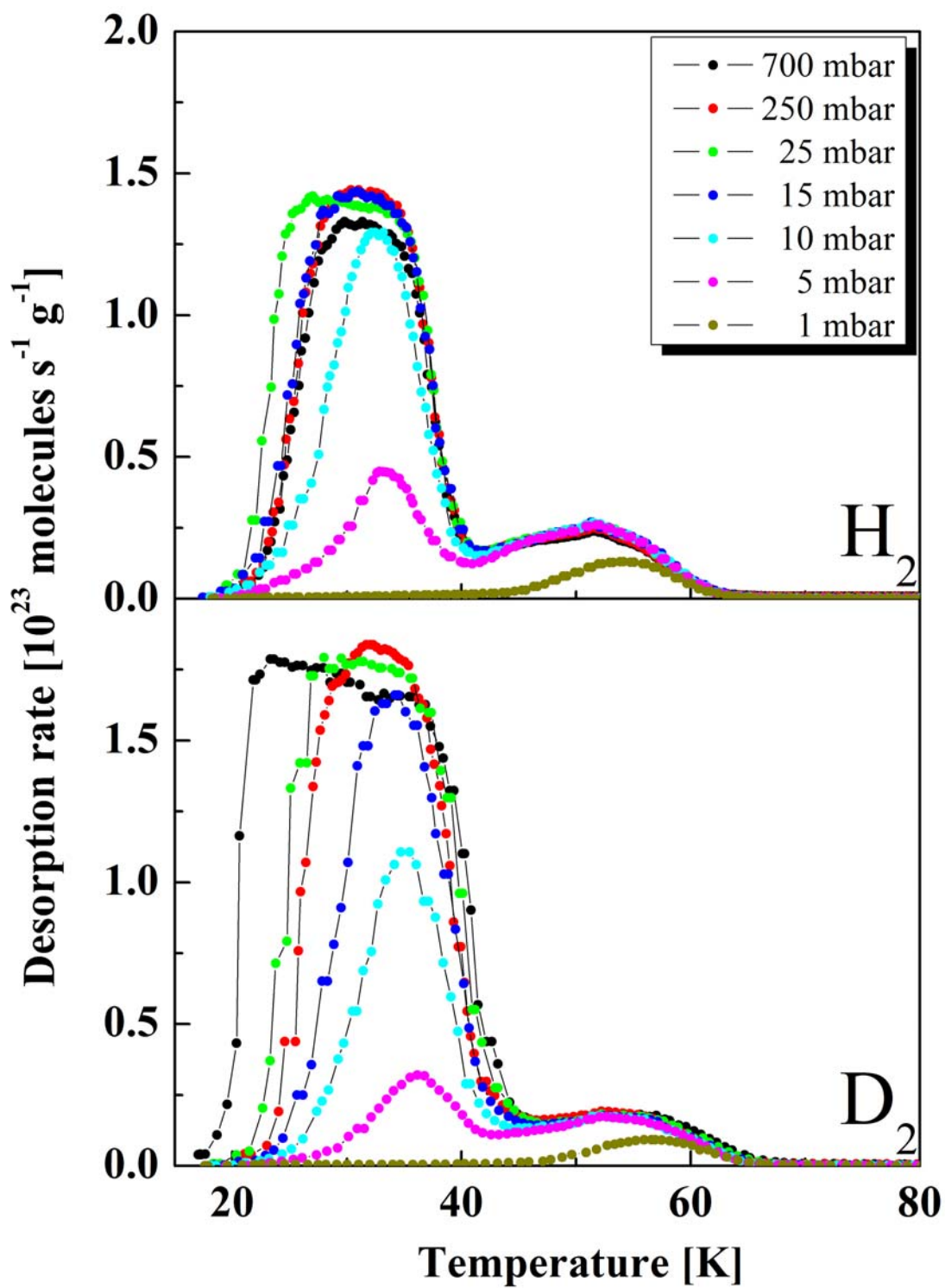


Fig. 5.33 The TDS spectra of hydrogen and deuterium for MFU-4l, recorded for different initial gas loadings, and with the heating rate of $0.10 K s^{-1}$.

Al(OH)(ndc)

In Fig. 5.34 hydrogen desorption spectra for Al(OH)(ndc) are presented, loaded at 15 mbar, and recorded with two heating rates, 0.10 and 0.01 K s⁻¹. The desorption mainly occurs in the temperature range from 20 to 80 K. The spectra exhibit three maxima, at 35 K, at about 43, and 55 K (heating rate of 0.10 K s⁻¹).

The total amount of gas desorbed corresponds to 0.82 wt.% H₂.

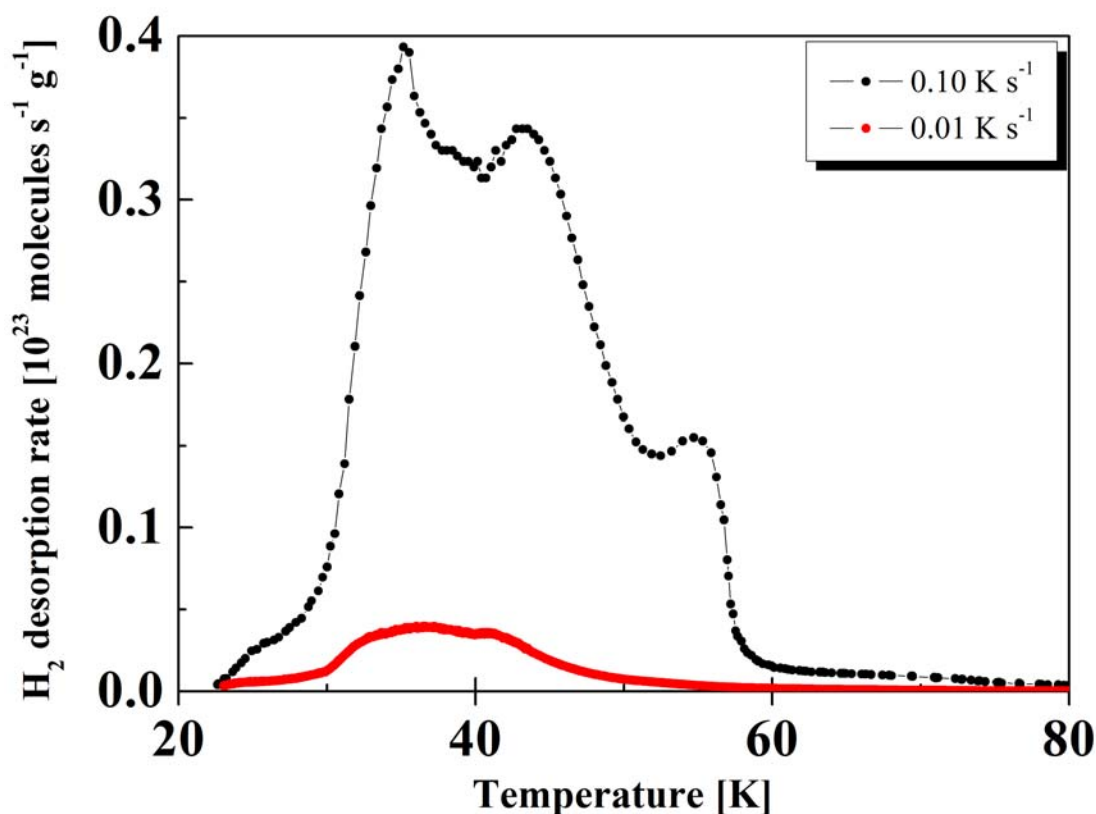


Fig. 5.34 The TDS spectra of Al(OH)(bpdC) loaded at 15 mbar of hydrogen, and recorded with the heating rates of 0.10 and 0.01 K s⁻¹.

Al(OH)(bpdC)

Fig. 5.35 shows hydrogen desorption spectra of Al(OH)(bpdC), loaded at 15 mbar, and recorded with two heating rates, 0.10 and 0.01 K s⁻¹. The spectra are presented in the temperature range from 20 to 80 K. At low temperature desorption shoulder is observed, at about 29 K (heating rate of 0.10 K s⁻¹). In addition, a major maximum at about 33 K, and a small desorption shoulder at 42 K are observed.

The total amount of gas desorbed is calculated to be 2.41 wt.% H₂.

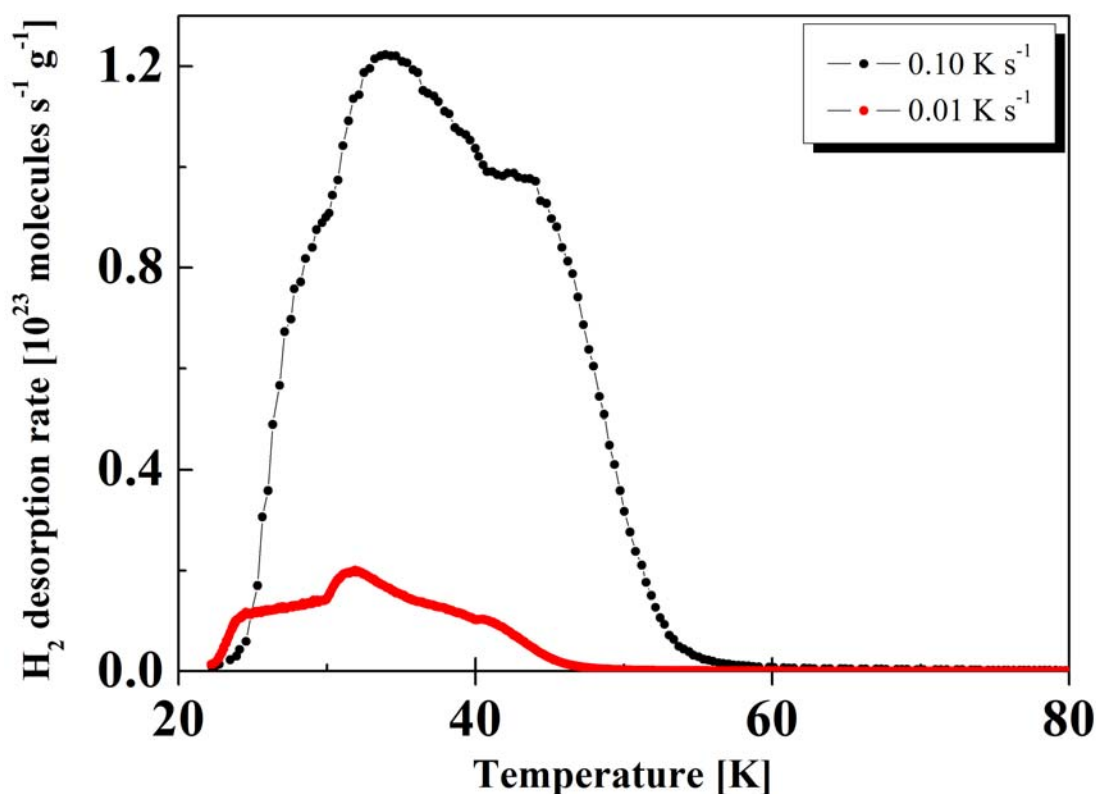


Fig. 5.35 The TDS spectra of Al(OH)(bpdC) loaded at 15 mbar of hydrogen, and recorded with the heating rates of 0.10 and 0.01 K s⁻¹.

MIL-100(Al)

In Fig. 5.36 the TDS spectra of hydrogen for MIL-100(Al) are shown, loading at 15 mbar, and recorded with the heating rate of 0.10 and 0.01 K s⁻¹. The spectra are presented in the temperature range from 20 to 80 K. Two pronounced maxima are observed, a sharp maximum at 24 K, and a broad peak at about 34 K. In addition, a small desorption shoulder is observed at about 41 K (heating rate of 0.10 K s⁻¹).

The total amount of hydrogen desorbed is calculated to be 1.45 wt.%.

Furthermore, the desorption spectra obtained by changing the initial gas loading, in the pressure range from 1 to 15 mbar are given in Fig. 5.37, as determined by deuterium desorption. The spectra are presented in the temperature range from 20 to 60 K, and recorded with the heating rate of 0.01 K s⁻¹. Three maxima are observed, and centered at 23, 34, and 42 K. The total amount of deuterium desorbed for each pressure applied is given in Table B-8.

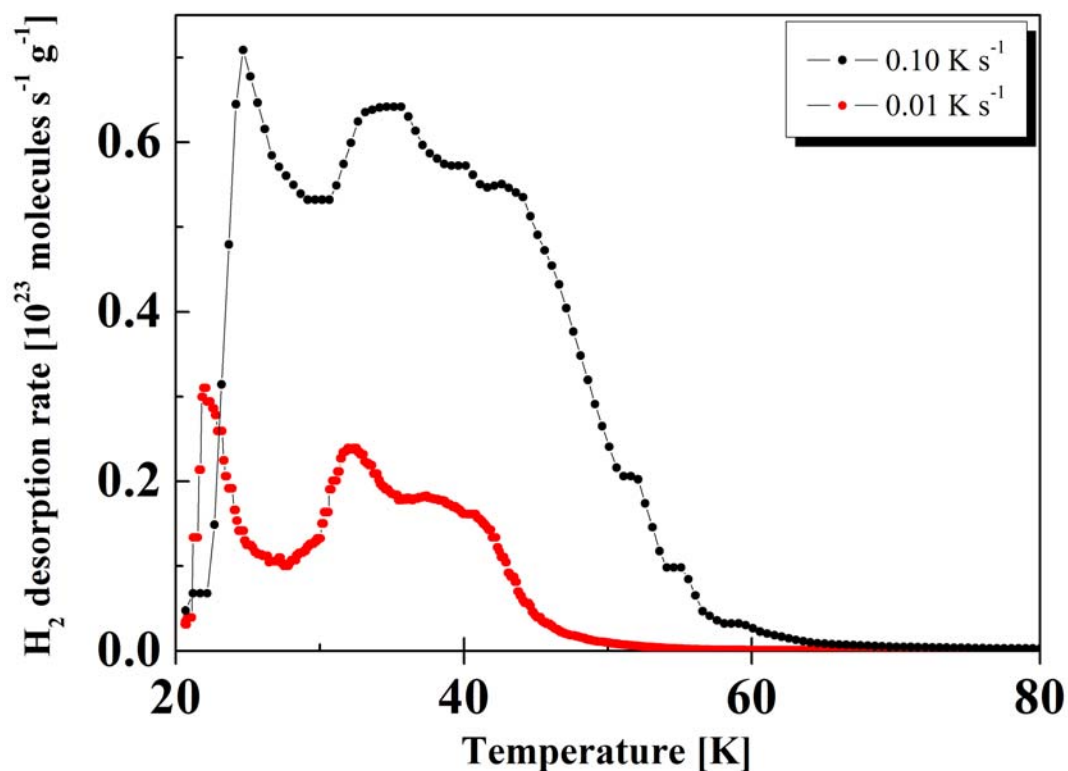


Fig. 5.36 The TDS spectra of MIL-100(Al) loaded at 15 mbar of hydrogen, and recorded with the heating rate of 0.10 and 0.01 K s⁻¹.

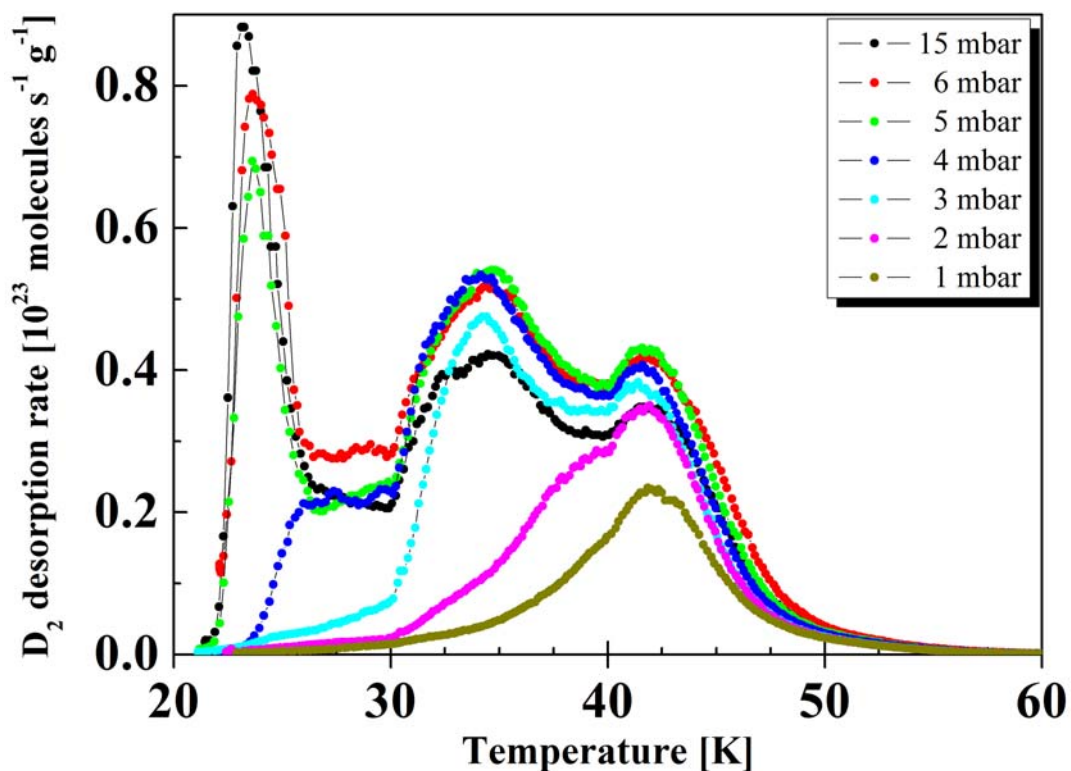


Fig. 5.37 The TDS spectra of deuterium for MIL-100(Al), recorded for different initial gas loadings, and recorded with the heating rate of 0.01 K s⁻¹.

MIL-100(V)

In Fig. 5.38 the TDS spectra of hydrogen and deuterium for MIL-100(V) are presented, in the temperature range from 20 to 120 K. Spectra show pronounced maximum at 36 K for hydrogen, and at about 37 K for deuterium (heating rate of 0.10 K s^{-1}). In addition, at high temperature another shoulder is observed, centered at about 56 and 66 K for hydrogen and deuterium, respectively. The total amount of gas desorbed corresponds to 2.57 wt.% H_2 , and 6.11 wt.% D_2 .

In addition, a comparison between hydrogen and deuterium desorption mechanism is given in Fig. 5.39, for spectra recorded upon partial gas loading. For 1 mbar gas loading a single maximum is observed, centered at 61 and 65 K for hydrogen and deuterium, respectively. For the sample loaded at 3 mbar this maximum reaches the saturation value, and an additional maximum appears at 42 K for hydrogen, and at 47 K for deuterium. For the sample loaded at 5 mbar, in addition, a small shoulder may be observed at lower temperature, centered at 32 K for both hydrogen and deuterium. A further increase in pressure (25 mbar) results in an increased peak intensity, and gives rise to a pronounced desorption maximum centered at 36 K, and 38 K for hydrogen and deuterium, respectively, without attaining the saturation intensity. Upon increasing the initial gas loading, a slight shift in the position of the desorption maxima toward lower temperatures is observed.

MIL-100(Cr)

In Fig. 5.40 the TDS spectra of hydrogen and deuterium for MIL-100(Cr) loaded at 25 mbar are presented, in the temperature range from 20 to 120 K. A small desorption shoulder is observed at low temperature, better resolved for deuterium desorption, and centered at about 28 K (heating rate of 0.10 K s^{-1}). In addition, one major maximum is observed, centered at 33 K for hydrogen, and at 34 K for deuterium, and, at high temperature, a rather broad desorption peak appeared in the temperature range from 60 to 120 K. The total amount of gas desorbed is calculated to be 1.34 wt.% H_2 , and 3.56 wt.% D_2 .

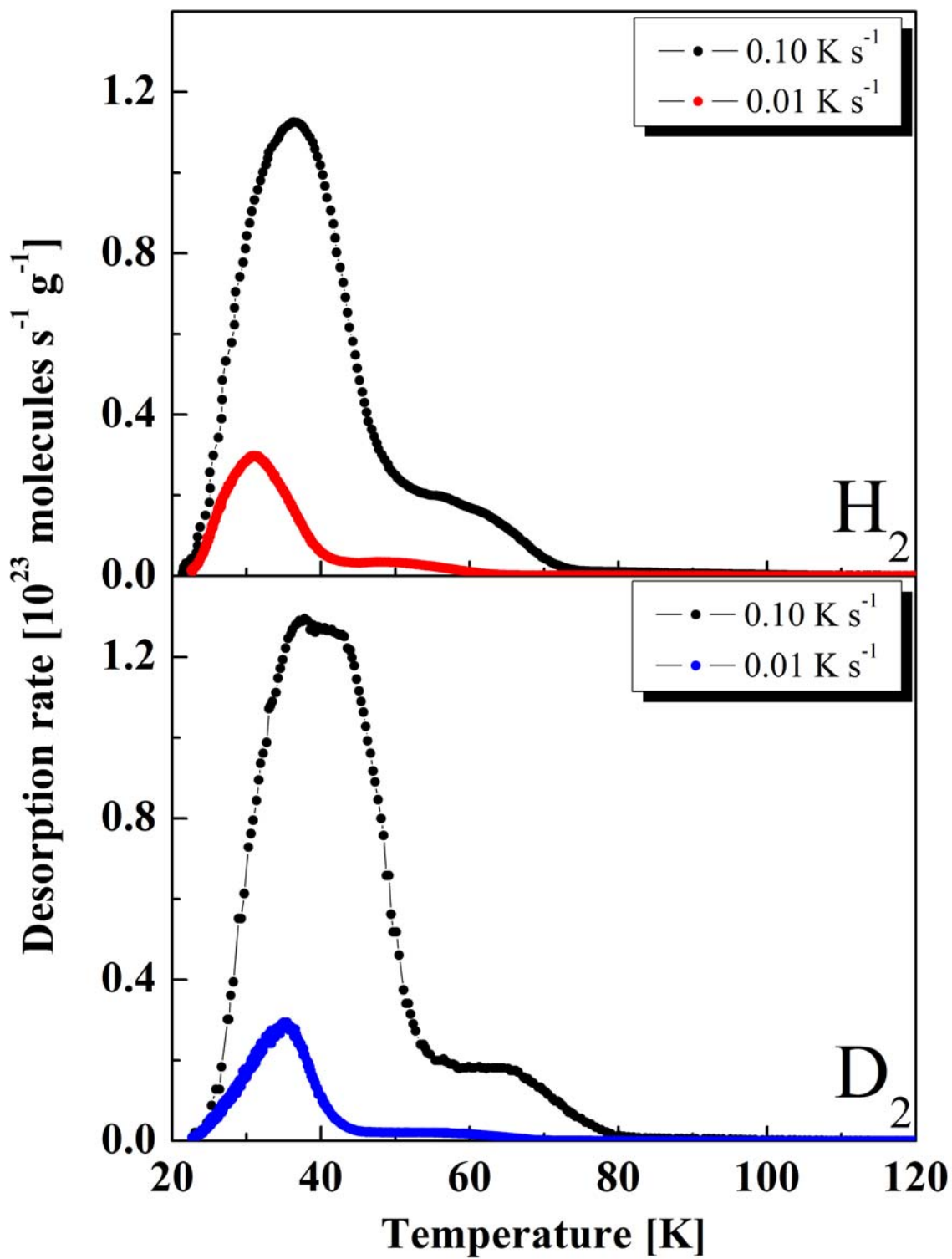


Fig. 5.38 The TDS spectra of hydrogen and deuterium for MIL-100(V) loaded at 25 mbar, and recorded with the heating rate of 0.10 and 0.01 $K s^{-1}$.

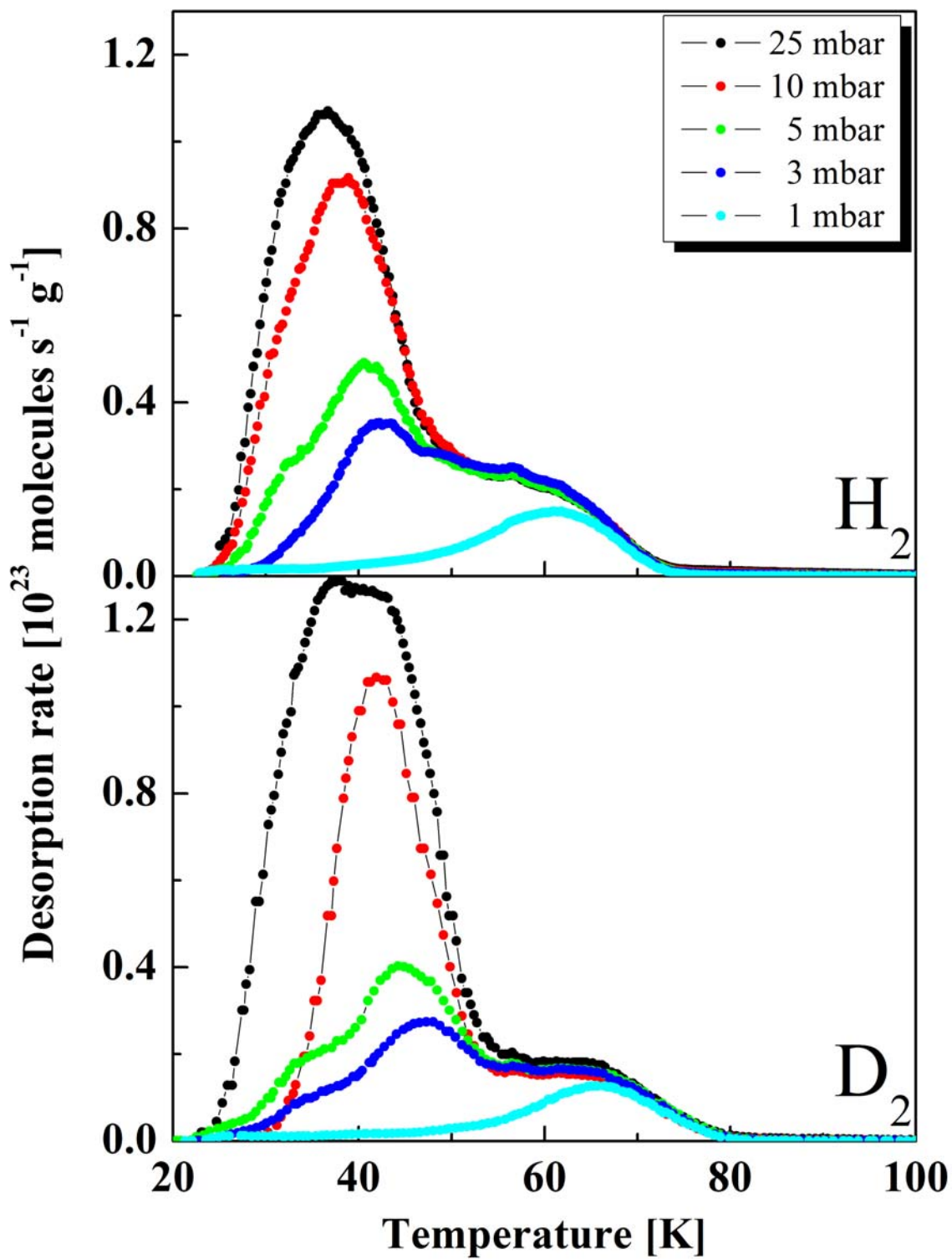


Fig. 5.39 The TDS spectra of hydrogen and deuterium for MIL-100(V), recorded for different initial gas loadings, and with the heating rate of 0.10 K s^{-1} .

The desorption mechanism for MIL-100(Cr) is further investigated by changing the initial gas loading (Fig. 5.41). For the sample loaded at 1 mbar a single maximum is observed, and centered at 81 and 99 K for hydrogen and deuterium, respectively. A further increase in pressure (3 mbar gas loading) shows, in addition, two maxima, at 37 and 47 K (expressed for deuterium desorption, while the peak position is better resolved than for hydrogen). For 5 mbar loading both peaks become more pronounced, and show a slight shift toward lower temperature. A further increase in pressure results in an intensity increase. The first two maxima coalesce, and appear as one broad maximum, centered at 33 and 34 K for hydrogen and deuterium, respectively (25 mbar gas loading). The total amount of hydrogen and deuterium desorbed for each gas loading applied is given in Table B-9 and Table B-10, respectively.

MIL-100(Fe)

In Fig. 5.42 the TDS spectra of hydrogen and deuterium for MIL-100(Fe) loaded at 25 mbar are presented, in the temperature range from 15 to 120 K. The spectra exhibit major maximum centered at 33 and 37 K for hydrogen and deuterium, respectively (heating rate of 0.10 K s^{-1}). In addition, a small desorption shoulder is observed, centered at 43 K for deuterium desorption. At high temperature another desorption peak, rather long, broad, and with the low intensity is observed. The total amount of gas desorbed corresponds to 1.24 wt.% H_2 , and 2.45 wt.% D_2 .

Furthermore, the desorption mechanism for MIL-100(Fe) is investigated upon applying different initial gas loadings (Fig. 5.43). For 1 mbar gas loading a major maximum is observed, centered at 46 and 53 K for hydrogen and deuterium, respectively, and another broad peak at higher temperature. Upon increasing the gas loading further, an intensity increase is observed, while position of the main maximum shifts toward lower temperature. Table B-9 and C-10 summarizes the total amount of gas desorbed from MIL-100(Fe) for hydrogen and deuterium, respectively.

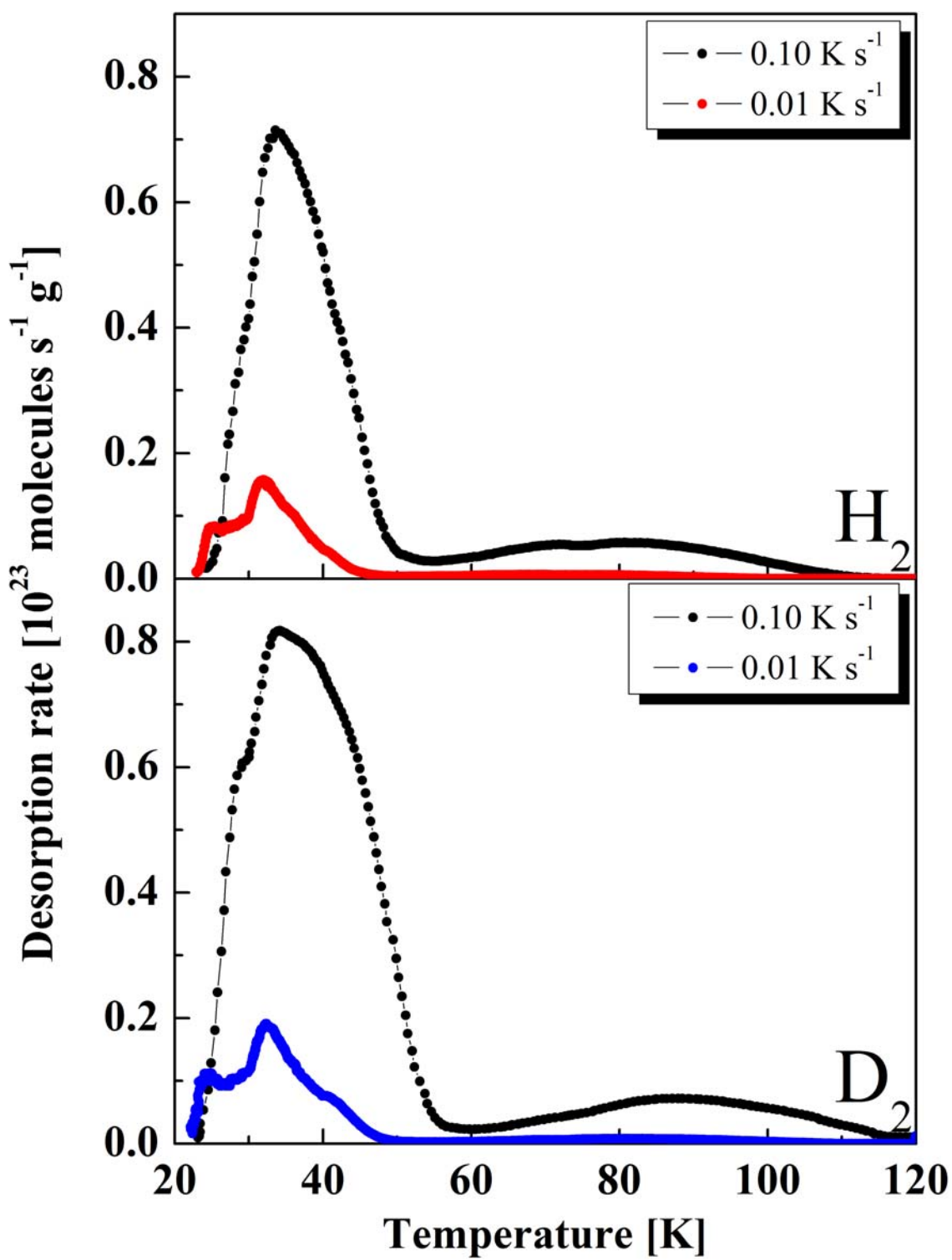


Fig. 5.40 The TDS spectra of H_2 and D_2 for MIL-100(Cr) loaded at 25 mbar, and recorded with the heating rate of 0.10 and $0.01 K s^{-1}$.

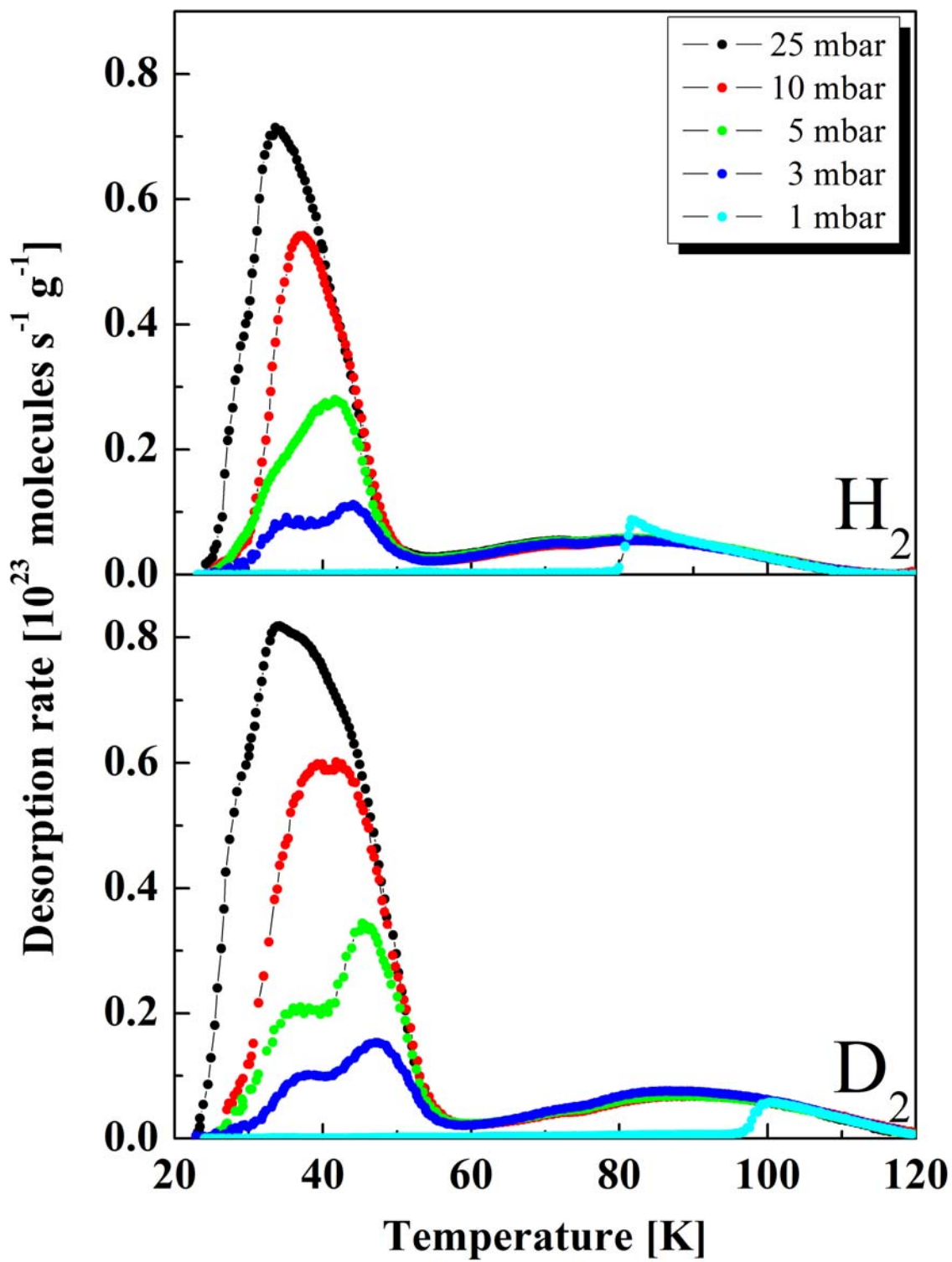


Fig. 5.41 Hydrogen and deuterium desorption spectra for MIL-100(Cr) recorded for different initial gas loadings, and with the heating rate of 0.10 K s^{-1} . The desorption spectra are presented in the temperature range from 15 K to 120 K.

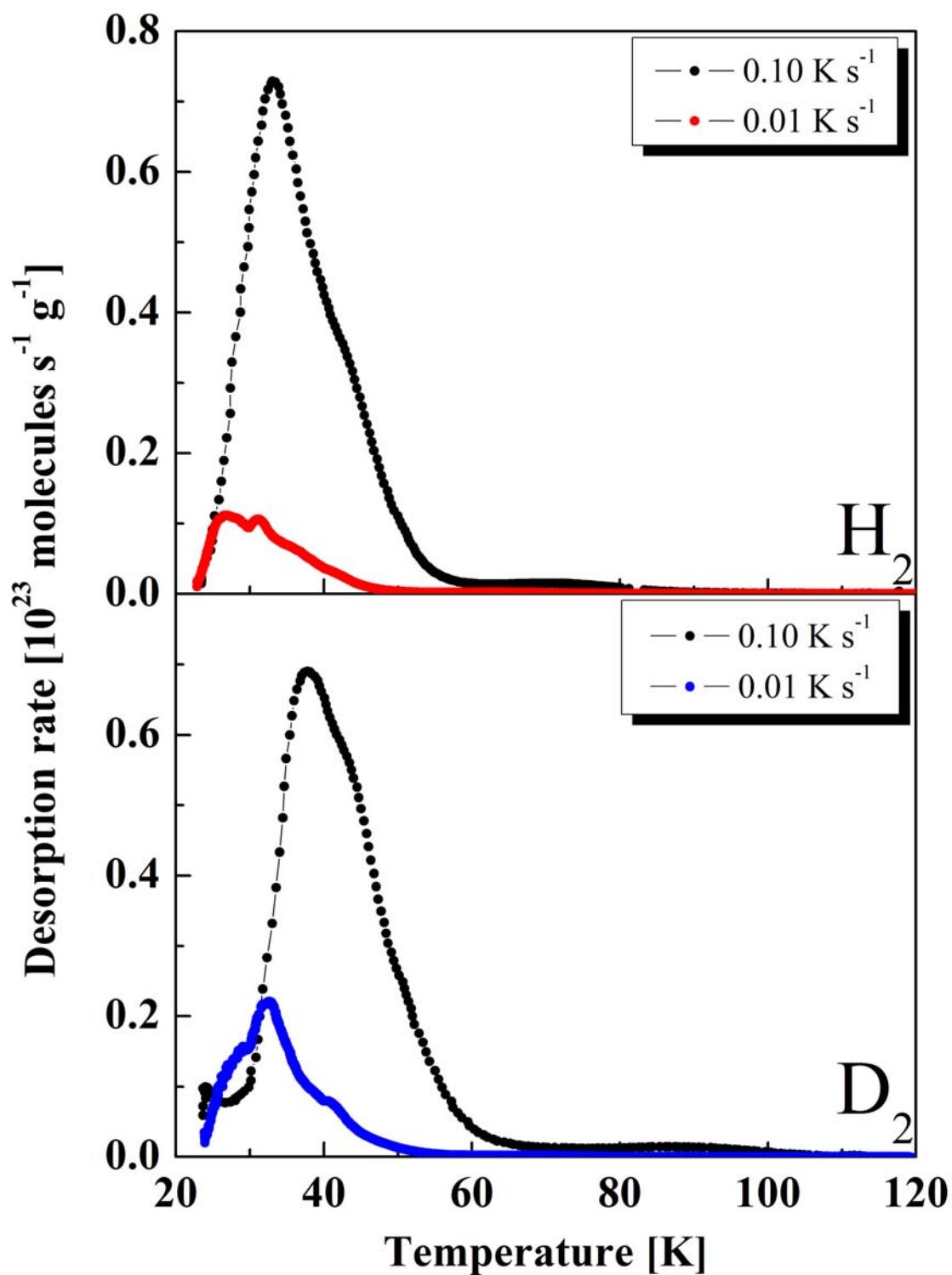


Fig. 5.42 The TDS spectra of hydrogen and deuterium for MIL-100(Fe) loaded at 25 mbar, and recorded with two distinct heating rates, $0.10 K s^{-1}$ and $0.01 K s^{-1}$.

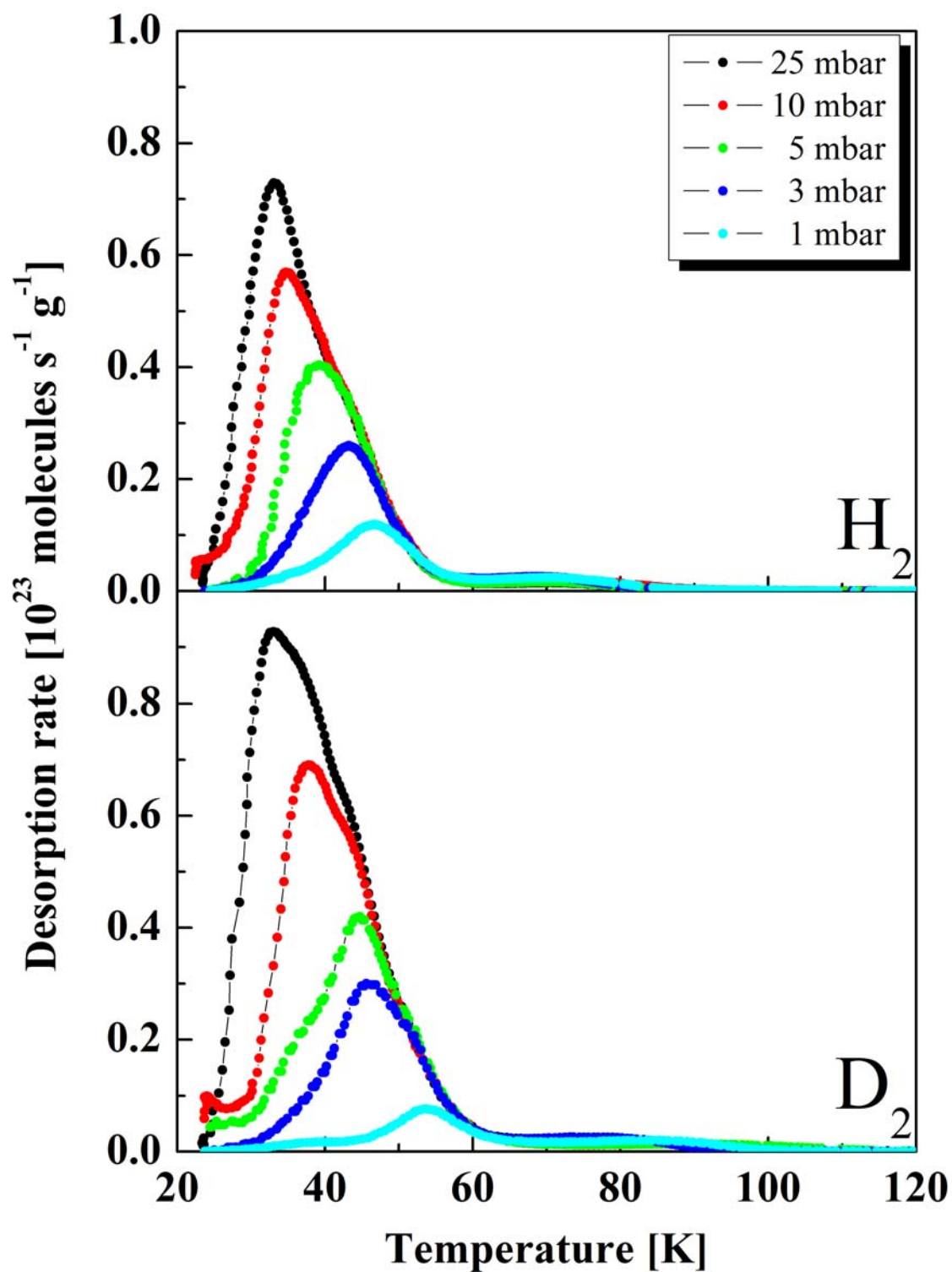


Fig. 5.43 The TDS spectra of hydrogen and deuterium for MIL-100(Fe), recorded for different initial gas loadings, and with the heating rate of 0.10 K s^{-1} .

In Fig. 5.44 a comparison is given for the hydrogen desorption spectra of all four investigated samples from MIL-100 series, MIL-100(Al, -V, -Cr, and -Fe).

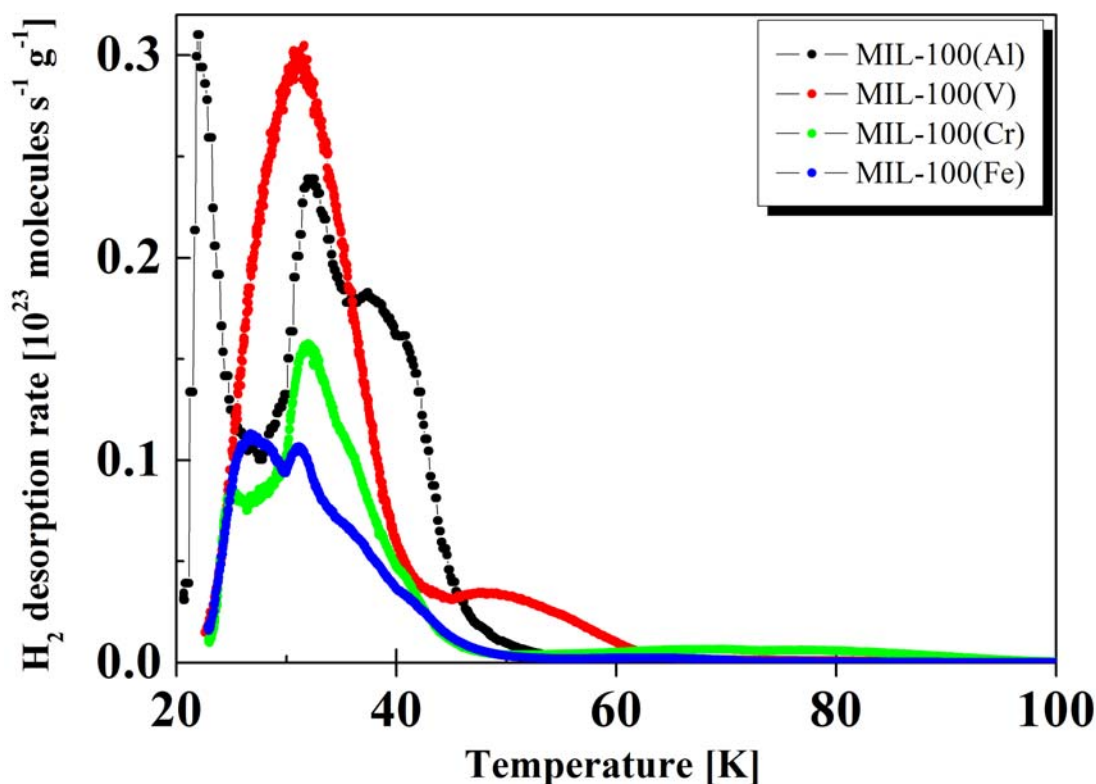


Fig. 5.44 A comparison of hydrogen thermal desorption spectra for MIL-100(Al, -V, -Cr, and -Fe). The spectra are recorded with the heating rate of 0.01 K s^{-1} .

5.2.2 Discussion

Owing to the high sensitivity of the TDS technique only a few mg of sample are needed to obtain a quick overview on the number and strength of energetically different adsorption sites. The sample mass was kept sufficiently small, typically in the range of 3 to 5 mg (Table 6.1), while the small sample quantities are desirable to minimize readsorption, decrease the possibility of intraparticle diffusion limitations, and allow better thermocouple contact [30]. This is an important point since diffusion resistance and readsorption can cause a peak broadening, and a possible shift in the position of the peak maximum [182]. Furthermore, powder samples exhibit a volume-dependent TDS response, owing to interparticle-diffusion [183].

All solids, especially porous adsorbents, have a great affinity to water and adsorb moisture from air. During the TDS experiment several masses were simultaneously measured to ensure that co-desorption of species other than hydrogen/deuterium does not occur. Prior to performing the measurements all investigated samples were out-gassed at elevated temperature under HV (Table

6.1), thus, all TDS results are reported on the bases of activated samples. For convenient data comparison the desorption rate is expressed by the number of hydrogen and deuterium molecules desorbed per gram of sample.

The spectra recorded with two distinct heating rates, 0.10 and 0.01 K s⁻¹, show differences in intensity, and in the position of the peak maximum. For the slower heating rate, the TDS spectra are shifted to lower temperatures. The desorption rate, or equivalently peak intensity, increases with the increase in heating rate, and takes less time to attain the maximum value. In the representations of pressure vs. temperature the area under the curves decreases for slower heating rates. However, the fractional coverage which remains on surface, when peak maximum is attained (the intensity–time area), is equal for both heating rates. The desorption spectra recorded with the heating rate of 0.01 K s⁻¹ are found to be particularly useful in resolving the desorption from multiple adsorption sites with similar energetic barriers to desorption, since the peak separation increases with decreasing the heating rate. The resolution of the overlapping maxima, as a common problem in the analysis of the TDS spectra, and a sequential filling of the different adsorption sites was investigated in details by applying partial gas loading. The shape of the TDS peaks did not change for different initial gas loadings, and the TDS measurements were shown to be both repeatable and reproducible. The only change is the one in intensity, and corresponds to the amount of gas originally adsorbed on a particular adsorption site. Furthermore, by changing the initial gas loading additional information about the saturation coverage is obtained. The saturation of the first monolayer was estimated from the onset of multilayer desorption. With coverages approaching the multilayer regime the desorption spectra broaden toward lower temperatures, and developed a common leading edge. Since the lateral interaction between physisorbed molecules is weaker, compared to binding energy between gas molecules and the adsorbent, the position of peak maximum is on higher temperature for monolayer than for multilayer desorption. The decrease in enthalpy of deuterium adsorption with increasing the amount adsorbed was reported previously for D₂–MOF interaction [184].

To further clarify desorption mechanism from the MOF surface the technique of interrupted desorption was applied. Having first cooled the sample under the gas atmosphere, a linear heating ramp was applied to a specified temperature, then the heating was interrupted, and the sample cooled down again under HV conditions. Afterwards, a second heating run was started, and the TDS spectrum of the remaining gas adsorbed on the sample measured. By varying the interruption temperature, and the heating rate, a series of desorption spectra were recorded to separate the contribution of different maxima.

Commonly, a low temperature peak was observed, typically below 27 K, assigned to liquid hydrogen/deuterium. During cooling under the gas atmosphere a certain amount of gas is liquefied,

or adsorbed in multilayers, giving rise to additional desorption in the low-temperature region. The peak intensity of this peak depends on the experimental conditions applied, in particular on the cooling procedure, on the pore size distribution, and the sample surface area. Therefore, it was not used for correlating with adsorption sites in MOFs, while independent maxima observed on higher temperatures are assigned to different adsorption sites, possessing different desorption energies.

The amount of gas desorbed from the sample was quantified using the calibration with Pd powder. All contributions below 27 K for hydrogen, and below 30.3 K for deuterium were subtracted, while the sample was cooled down below the adsorbate boiling temperature (20.3 K and 23.6 for H₂ and D₂, respectively), and a certain amount of gas most probably liquefied. Due to higher boiling point of D₂, the contribution of evaporating liquefied deuterium is at higher temperature, and overlaps more strongly with the first physisorption peak. Moreover, the same cooling procedure was used for both gases and, therefore, more liquid deuterium may be formed, which leads to higher contribution than in the case of hydrogen.

The shape of the TDS spectra, and the coverage independent position of the desorption maximum at low coverages are indicative of the first-order desorption kinetics (Eq. (2.18), Chapter 2.2), which refers to atomic or non-dissociative molecular desorption, as in the case of physisorption. Eventual interactions with other molecules do not control the rate of desorption.

In general, the TDS experiment can be used for the determination of four important kinetic parameters: the desorption rate constant, k_d , the order of the desorption, n , the pre-exponential frequency factor, ν , and the activation energy for desorption, E_a^{des} . Since both the temperature, and the sample coverage change continuously, and simultaneously, and the kinetic information are available only in the narrow temperature range, the analysis of the TDS data is straightforward. Two unknown, interrelated, and coverage dependent parameters are contained in the Polanyi-Wigner equation, $E_a^{des}(\theta)$ and $\nu(\theta)$, Eq. (2.14). Assessing these values from the TDS spectra is usually model dependent, and requires inclusion of several desorption spectra with change in the heating rate, or initial coverage. Several methods for the determination of kinetic parameters, commonly suggested in the literature, have been discussed in Chapter 2.2. In particular, Redhead's desorption peak temperature method, commonly used for the first-order desorption process, gives only a rough estimation of the activation energy for the desorption, since the value of the pre-exponential frequency factor, and the reaction order are assumed a priori [185]. On the other hand, the heating rate variation method assumes that the fractional coverage left on the surface, when the peak maximum is attained, is the same for all the heating rates. Therefore, to obtain a reliable value of E_a^{des} , the value of β has to be varied by the several orders of magnitude. Regarding the construction principle of the experimental set-up used for the TDS measurements, it was possible to

change the heating rate only by one order of magnitude, in the range $0.01 - 0.10 \text{ K s}^{-1}$, which is why the heating rate variation method could not be applied. Furthermore, the analysis methods commonly suggested in the literature are mostly applicable for the analysis of the TDS spectra corresponding to the processes taking place on a uniform surface. All investigated MOF samples are found to be energetically heterogeneous, due to the nature of the framework, variation in the pore sizes, the presence of unsaturated metal centers, etc. Therefore, a straightforward analysis of kinetic parameters for processes taking place on non-uniform surfaces, with coverage-dependent activation energy, was not possible, and has not been employed.

Cu – BTC

The TDS measurements were employed to study hydrogen/deuterium desorption from the crystalline MOF copper(II) benzene-1,3,5-tricarboxylate, hereafter denoted as Cu-BTC, with a special emphasis to D_2 desorption. A sequential filling of the three different adsorption sites was observed, with the maxima centered at 31, 35, and 47 K, and 32, 38, and 51 K for hydrogen and deuterium, respectively (Fig. 5.14, heating rate of 0.01 K s^{-1}). For convenient data comparison, with the one published in the literature, the total amount of gas desorbed is given by the number of H_2/D_2 molecules per unit cell of Cu-BTC. The dehydrated form of Cu-BTC possesses a unit cell of 624 atoms in total (48 copper, 192 oxygen, 96 hydrogen, and 288 carbon).

In the literature several studies have examined the nature of adsorption sites in Cu-BTC. Combined GCMC simulations, and the high-resolution low-pressure Ar adsorption experiments showed that the tetrahedral side pockets are preferential adsorption sites for Ar molecules, and are filled prior to the large pores. The third adsorption step was attributed to the solidification of argon in the pores [167]. By performing neutron powder diffraction study of D_2 -loaded Cu-BTC [186] the author identified six distinct positions for D_2 adsorption, one site near the metal center, three sites in the side pockets, and two sites in the large pore. Molecules initially bind to the coordinatively unsaturated Cu^{2+} sites, followed by filling of the tetrahedral side pockets, before the Cu^{2+} site is fully saturated [186, 187], and finally the large pore is occupied. A sequential filling of different adsorption sites was observed using four different gas loadings. For loading corresponding to 24 D_2 molecules per unit cell almost all molecules are adsorbed near the coordinatively unsaturated Cu atoms (Fig. 5.45). For the second loading step, corresponding to 47 D_2 molecules per unit cell, again almost all deuterium molecules are adsorbed at the first and the most favorable adsorption site, near the metal centers. Following binding at Cu^{2+} sites, about 10% of the D_2 molecules are adsorbed in the side pockets. For the loading by 91 D_2 molecules per unit cell the amount of molecules adsorbed at the metal centers remains approximately the same, and the side pockets get filled (about

45% at the metal site, and 55% in the side pockets). For the final loadings of 211 D_2 molecules per unit cell the amount of molecules adsorbed on the metal sites remains approximately the same. However, both the side pockets, and the large pore are filled about equally (24% at the metal site, 40% in the side pockets, and 36% in the large pore).

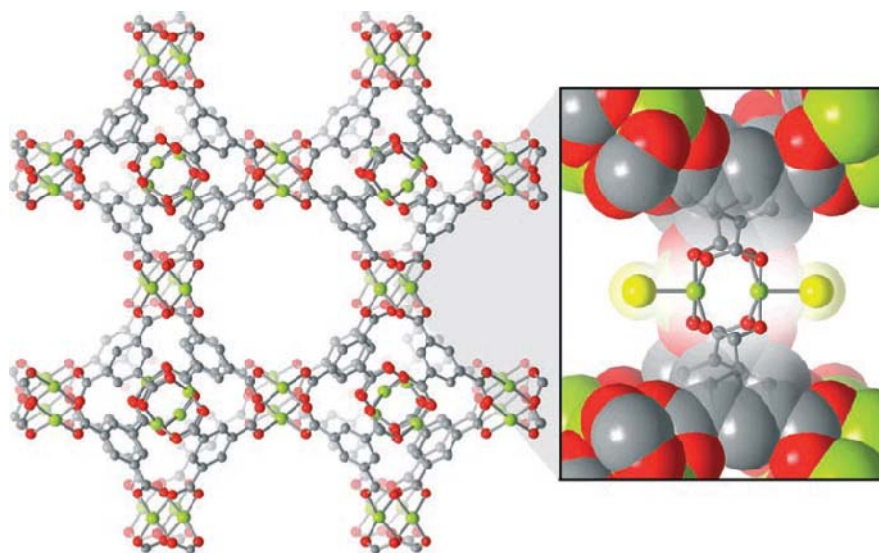


Fig. 5.45 A portion of the crystal structure of Cu-BTC, and the position of the Cu^{2+} -bound D_2 molecules (yellow spheres), as determined by the powder neutron diffraction [186]. Corresponding atoms are represented by Cu (green), O (red), and C (gray). H atoms are omitted for clarity. Graphical representation adopted from ref. [188].

The experimental data by Peterson et al. are used for a comparison with the experimental results obtained by the TDS technique. For the sample loaded at 25 mbar, corresponding to 197 D_2 molecules per unit cell, the three desorption maxima are observed (Fig. 5.14). By interrupted desorption the first two maxima are separated from the third one at higher temperature. In the first heating run 131 D_2 molecules per unit cell are desorbed and 61 D_2 molecules per unit cell desorbed in the second run. If we assign the first and the second maximum to the large pore, and the side pockets, respectively, the third maximum will correspond to the metal site. The amount of deuterium desorbed within the second run is slightly higher than the adsorption at the metal sites observed by Peterson et al., which may be explained by a fraction of deuterium adsorbed in the side pockets. This interpretation is further supported with the spectra obtained by partial loading (Fig. 5.16). Upon increasing the gas loading, the sequential filling of different adsorption sites is observed. The peak intensity should correspond to the amount of gas originally adsorbed on the corresponding site. For 1 mbar pressure loading a sharp desorption peak appeared, with the maximum centered at 53 K, and 7 D_2 molecules per unit cell were desorbed. This maximum, possessing the highest desorption temperature, is attributed to adsorption at the metal sites. The low-temperature infrared spectroscopy measurements, done by the group of S. Bordiga [169],

provided the first experimental evidence for the direct interaction between the unsaturated open metal centers and hydrogen molecules in Cu–BTC. By the variable–temperature infrared spectroscopy measurements, the hydrogen binding energy for unsaturated Cu^{2+} ion was determined to be 10 kJ mol^{-1} [189], which is in a good agreement with the hydrogen adsorption enthalpy at this site ($6\text{--}10 \text{ kJ mol}^{-1}$), estimated from the inelastic neutron scattering (INS) studies [190]. In this pressure regime, in addition, two desorption shoulders are present at lower temperature (Fig. 5.16), with the maxima centered at 43 and 36 K, suggesting successive filling of the pore system, the side pockets, and the large pores, respectively. The four benzene rings of the BTC linker, that constitute the inner surface of the side pockets [168], and an optimal pore diameter of about $6\text{--}7 \text{ \AA}$ [191] strengthen the interaction of D_2 molecules with the pore walls, and get partially filled. At low gas loading most of the adsorption is attributed to the metal sites, while the pore system plays only a secondary role. For 7 mbar D_2 loading the metal sites are still mainly occupied, and 41 D_2 molecules per unit cell desorbed in total. Further, for 10 mbar D_2 loading the total amount of gas desorbed is 53 D_2 molecules per unit cell. The intensity of the high temperature peak remains the same, and two peaks at lower temperature get filled. For an increased deuterium loading (15 mbar), filling of the side pockets is pronounced, with 87 D_2 molecules per unit cell desorbed. Followed by the saturation of the side pockets, for increased gas loading, pronounced filling of the last adsorption site is observed, with the maximum centered at about 32 K. In this pressure regime adsorption in the large pores is pronounced, and the total uptake is determined to be 197 D_2 molecules per unit cell. Different positions of adsorbate molecules, correlated to adsorption sites, are given in Fig. 5.46.

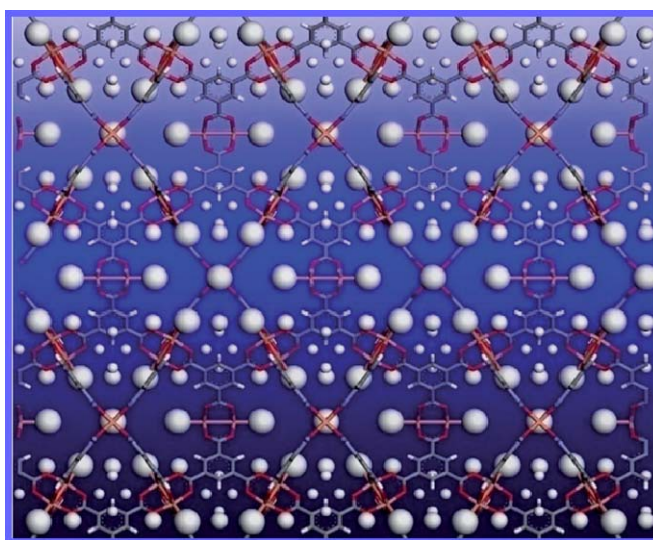


Fig. 5.46 The hydrogen positions in Cu–BTC as determined by powder neutron diffraction [186]. The hydrogen molecules are represented as balls of different sizes according to their adsorption site. Representation is adopted from the ref. [192].

Fe – BTC

The structure of Fe–BTC resembles Cu–BTC in terms of structural parameters, as both possess two different types of pores, and an open metal site. Although the same BTC ligand was used for synthesis of both compounds, the coordination units differ. The BTC ligand acts as a trigonal planar ligand connecting diatomic metal clusters within Cu–BTC, i.e., connects trimers of iron octahedral ($\text{Fe}_3\text{-}\mu_3\text{O}$) within Fe–BTC. The usage of Fe^{3+} , as a metal center, resulted in a structure with considerably larger pores, and rather different pore openings. For low gas loading, in the pressure range from 1 to 5 mbar, one maximum is observed, and can be attributed to adsorption of gas molecules at the Fe^{3+} metal center, Fig. 5.19. This maximum, centered at about 54 K for deuterium (1 mbar pressure loading), is in a good agreement with the maximum observed for D_2 loaded Cu–BTC (Fig. 5.14), centered at about 53 K. Indeed, sample dehydration in vacuum proceeds in a coordinative vacancy on Cu^{2+} sites, which makes them accessible for adsorbate molecules [164, 169]. Likewise, Fe^{3+} is regarded as the active site in Fe–BTC [173]. $\text{Fe}_3\text{-}\mu_3\text{O}$ clusters have one of the positions which are not engaged with the framework carboxylate groups, and are free to coordinate with the solvent, a substrate, or any other ligand. Upon increasing the pressure further (7 mbar), the desorption spectra broaden toward lower temperatures, and the high temperature maximum begins to overlap with the second maximum, centered at 34 K for deuterium (10 mbar pressure loading). It is attributed to adsorption in the small 25 Å pores. A small desorption shoulder, originated from adsorption at $\text{Fe}_3\text{-}\mu_3\text{O}$ metal clusters, is still observable, and with the maxima centered at about 43 K. The maximum gets further filled for 15 and 25 mbar gas loading (Fig. 5.19). Again, for Fe–BTC a correlation can be made to the desorption mechanism observed for the Cu–BTC structure. The desorption from the side pockets for Cu–BTC proceeds in the same temperature range, at about 37 K (Fig. 5.14), while the size of the tetrahedral side pockets within Cu–BTC is comparable to the 5.5 Å pore opening of the small pore within Fe–BTC. The final step in the desorption mechanism is observed for 700 mbar gas loading, when the peak broadens further toward lower temperatures, and shows a single maximum, centered at 24 and 27 K for hydrogen and deuterium, respectively (Fig. 5.19). Here, gas desorption proceeds from the large 29 Å pores. The pore opening of 8.6 Å is again comparable to the diameter of the large 9 Å pore within Cu–BTC. Furthermore, the total amount of gas desorbed (1.62 wt.% H_2 , and 2.97 wt.% D_2) is in excellent agreement with the amount of gas desorbed from Cu–BTC (1.64 wt.% H_2 , and 3.00 wt.% D_2), referring to measurements done under the same experimental conditions (for the sample loaded at 25 mbar), and upon applying the same heating rate of 0.10 K s^{-1} . These values are expected since the BET surface area is comparable as well, $1154 \text{ m}^2 \text{ g}^{-1}$ and $1300 - 1600 \text{ m}^2 \text{ g}^{-1}$ for Cu–BTC and Fe–BTC, respectively.

Mg-formate(1)

The number and the strength of adsorption sites for hydrogen and deuterium was further investigated for Mg-formate(1). Apart from the low temperature peak centered at 21 and 25 K for hydrogen and deuterium, respectively, the desorption spectra of Mg-formate(1) show two additional maxima, centered around 48, and 74 K for hydrogen, and 51, and 73 K for deuterium (Fig. 5.21). The main maximum, centered at 48 and 51 K for hydrogen and deuterium, respectively, is attributed to the interaction of gas molecules with the small 3.4 Å pore. A rather high desorption temperature indicates a strong interaction between the adsorbate and the adsorbent, since the small 3.4 Å pore is comparable to the kinetic diameter of the hydrogen molecule (2.89 Å). The total amount of gas desorbed corresponds to 1.14 wt.% H₂, and 2.72 wt.% D₂ (Table B-3). It is comparable to the maximum excess hydrogen uptake (1.1 wt.%) measured at 77 K and high pressure (20 bar) [174].

Mg-formate(1) adsorbs almost no nitrogen at 77 K, since the nitrogen kinetic diameter (3.64 Å) is greater than the size of the small 3.4 Å pore, which leads to a very low BET SSA of 16 m² g⁻¹. On the other hand, the hydrogen adsorption of 1.14 wt.% indicates a surface area of approximately 500 m² g⁻¹, according to Chahine's rule [193]. In the literature, selective adsorption of H₂ and CO₂ over Ar, N₂, or CH₄ was observed for the Mn-formate α -[Mn₃(O₂CH)₆] framework [194], isostructural to the Mg-formate reported in this work. The former may also be attributed to the smaller kinetic diameter, 2.8 and 3.3 Å for H₂ and CO₂, respectively, compared to 3.4, 3.64, and 3.8 Å for Ar, N₂, and CH₄, respectively. The inability of Mn-formate to adsorb N₂ was independently confirmed by Wang et al. [195]. This group of researchers also demonstrated that Co-formate [Co₃(O₂CH)₆] surprisingly displays significant N₂ sorption. Since the pore size of the Co framework is smaller than that of Mn-formate, the adsorbate kinetic diameter may not be the only reason for selective gas adsorption. Indeed, Mn-formate has shown the ability to accommodate nonpolar solvents such as benzene and hexane [196], which implies that small differences in the adsorption interactions exist between different adsorbates. Overall, it should be kept in mind that diffusion in the micropore, with a size comparable to the size of adsorbate molecules, is an activated process, and strongly depends on the adsorbate properties.

A special peculiarity of MOFs is the framework flexibility [197], which is not observed for rigid classical sorbents, porous carbons or zeolites. Structural changes may occur during the adsorption process without topological changes of the network, that is, the structure expands upon adsorption of adsorbate molecules, and shrinks again upon desorption. Indeed, apart from the major maxima (over 90% of the total gas desorption), a small desorption peak is observed at higher temperature, centered at about 74 K for hydrogen. A pronounced filling of the high temperature maximum is

observed only for increased gas loading (for 10 mbar gas loading and higher, Fig. 5.22). Since the high temperature peaks state about the strongest adsorbate/adsorbent interaction this maximum is expected to appear primarily. In comparison, the main maximum has reached the saturation uptake already for 5 mbar gas loading. This implies that possibly structural transformations, caused by the external triggers, occur within the Mg–formate(1) framework. The rather high desorption temperature of 74 K states about the strong H₂–MOF interaction, and might be assigned to adsorption at the metal centers, which become accessible due to pressure increase. Indeed, the hydrogen isosteric heat of adsorption was calculated to lie in the range of 7.0 – 9.5 kJ mol⁻¹ upon adsorption at Mg₃(O₂C–C₁₀H₆–CO₂)₃ framework with unsaturated Mg²⁺ centers and narrow pore dimensions [198].

Mg–formate(2)

Hydrogen and deuterium desorption spectra for Mg–formate(2) show many similarities to the TDS spectra observed for Mg–formate(1), as expected, since these are two isostructural compounds. The desorption maxima appear at 23, 51, and 76 K for hydrogen, and at 27, 54, and 71 K for deuterium. The sample structure details have not been disclosed prior to completion of this work, therefore, it is difficult to correlate different maxima to potential adsorption sites. The comparison can be made with Mg–formate(1) regarding the total gas uptake, which is 1.92 wt.% H₂ for Mg–formate(2) vs. 1.14 wt.% H₂ for Mg–formate(1), and 4.47 wt.% D₂ for Mg–formate(2) vs. 2.72 wt.% D₂ for Mg–formate(1), Table B–3 and –4. As mentioned in the previous section, the pore diameter, and the pore volume of Mg–formate(2) are tailored to be larger, compared to Mg–formate(1), which is in a good agreement with the higher gas uptake calculated for Mg–formate(2) framework. Commonly, Mg–MOFs exhibit rather low hydrogen storage capacity. The highest hydrogen storage capacity reported in the literature is only 0.78 wt.% at 77 K and 1 bar, as observed for Mg₃(NDC)₃ [199]. Therefore, targeted chemistry applied for Mg–formate(2) synthesis showed that MOF properties can be successfully tailored toward the specific application, and that higher storage capacity may be reached.

MOF–177

The MOF–177 was long time regarded as the material with the highest reported surface area (approaches 4750 m² g⁻¹), and as the benchmark for hydrogen adsorption, i.e., the MOF with the highest hydrogen adsorption capacity amongst all the hydrogen storing materials, either by physical or chemical adsorption. Chae et al. [101] reported the hydrogen adsorption capacity of 7.5 wt.% at 77 K and 80 bar for MOF–177 with a Langmuir surface area of 4500 m² g⁻¹. This result was later

reproduced by several research groups using different experimental techniques (Table D–1). The superiority of MOF–177 over other MOFs, in terms of high–pressure hydrogen storage, lies not only in its exceptionally high surface area. A structure with the higher porosity, and the BET surface area of $5200 \text{ m}^2 \text{ g}^{-1}$, UMCM–2, was shown to have an excess gravimetric hydrogen uptake of 6.9 wt.% [103], lower than the one reported for MOF–177. Indeed, MOF–177 was shown to be capable of absorbing inorganic and organic guest molecules such as H_2 [200], N_2 [201], CO_2 [202], C_{60} , and dyes [101].

Although MOF–177 exhibits excellent hydrogen storage characteristics at 77 K its performance at 298 K is poor. Hydrogen adsorption uptake at RT and 100 bar was measured to be 0.62 wt.% [201], owing to the weak interaction between H_2 and the MOF framework. The heat of hydrogen adsorption, less than 4 kJ mol^{-1} [203, 204], is the cause for the drastic fall of hydrogen adsorption capacity at ambient temperature. Indeed, as seen from the TDS spectra (Fig 6.27), already below the temperature of about 50 K hydrogen was mainly desorbed. The total amount of hydrogen desorbed corresponds to 1.7 wt.%, which is considerably lower than the maximum excess adsorption uptake reported in the literature. The small heat of adsorption (less than 4 kJ mol^{-1}) results in very weak interaction of hydrogen with the wide 11.17 Å pore. The gas does not adhere to the surface of MOF–177, even at temperature of 20 K, and is partially desorbed in vacuum before the heating ramp is applied. Indeed, a long desorption tail observed at lower temperature (Fig. 5.27 and – 6.28 for hydrogen and deuterium, respectively) indicates that already at 20 K a considerable gas desorption takes place.

Further, gas adsorption on atomic level was probed upon loading the sample with a hydrogen/deuterium gas mixture. In particular, the desorption trace derived from the m/Z signal of 1 amu (corresponding to atomic hydrogen) is found to be negligible, while the m/Z signal of 3 amu (corresponding to hydrogen deuteride) gives very small contribution, indicating that some exchange occurs, Fig. 5.29. Dominantly, m/Z signals of 2 amu and 4 amu, corresponding to molecular hydrogen and deuterium, respectively, were observed, while the intensity of the desorption signal is considerably higher for deuterium, and relates to quantum effects (further discussed in Chapter 7).

MFU–4

In the pressure range of 1 to 50 mbar the TDS spectra of hydrogen on MFU–4 show a small desorption shoulder at a temperature of about 30 K, and the major desorption peak at 74 K (Fig. 5.30, heating rate of 0.10 K s^{-1}). For deuterium desorption corresponding maxima are observed at 26 and 74 K. Gas desorption mainly occurs at temperatures above 60 K, which is considerably higher than the desorption temperatures observed for other MOFs investigated in this study, and

reported in the literature [205]. Indeed, a pronounced maximum observed at 74 K, which corresponds to more than 85% of the total amount of gas desorbed, is the highest desorption temperature ever measured for physisorbed hydrogen on MOFs. Furthermore, for higher gas loadings another desorption shoulder is observed, even at higher temperature, centered at about 109 and 105 K for hydrogen and deuterium, respectively (Fig. 5.31). Different desorption temperatures state about the two substantially different adsorption sites, and are attributed to adsorption at the small, and the large cavity. They are arranged in an alternate fashion, thus, gas molecules moving from one larger cavity to another must pass through a smaller cavity (Fig. 5.47).

The permanent porosity of MFU-4 was proven using hydrogen and water adsorption measurements. It was shown that hydrogen follows the Type I adsorption isotherm by the IUPAC classification, and yields a storage capacity of 1.62 wt.% at 77 K and 1 bar [177]. The maximum hydrogen uptake calculated from the TDS measurements corresponds to 0.81 wt.% (Table B-6), somewhat lower than the maximum excess adsorption uptake at 77 K and 20 bar [178]. The filling of the smaller cavity is prolonged as the access of adsorbate molecules is somewhat hindered, and the adsorption kinetics most probably diffusion limited, due to the narrow-sized joining aperture of 2.5 Å in diameter, between the small and the large cavity. A prolonged cooling procedure (70 min. vs. 30 min, commonly applied to cool the sample from RT to 20 K), and increased equilibration time at 20 K (80 min. vs. 30 min.), increased the maximum gas uptake by more than 0.30 wt.% H₂. This experimental result confirms the low mobility of adsorbate molecules, and a complex adsorption mechanism, due to the presence of narrow and wide pores. Molecules with larger kinetic diameter (Ar and N₂) are excluded from sorption in MFU-4 [177], which enables its application for gas separation.

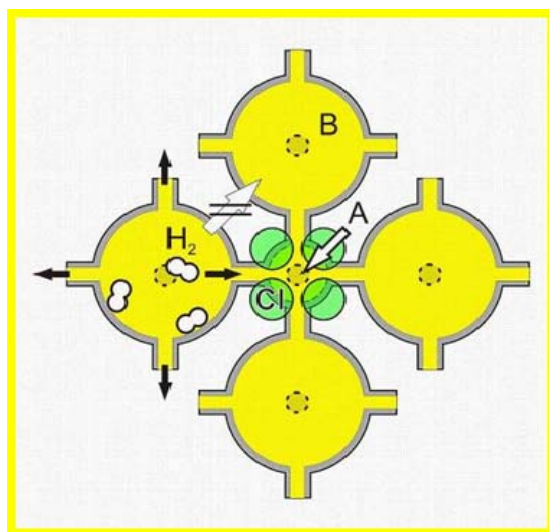


Fig. 5.47 The diffusion path of hydrogen molecules through the two structurally different types of cavities within MFU-4 framework, according to the ref. [178].

MFU-4l

The crystal structure of MFU-4l is similar to that of MFU-4 as it possesses a cubic six-connected net. Analogous to MFU-4, the MFU-4l framework has two different types of cavities, smaller and larger ones, arranged in an alternate fashion. MFU-4l exhibits two hydrogen maxima, one broad and large maximum centered at about 31 K, and a smaller maximum centered at 51 K (Fig. 5.32). For deuterium desorption a major maximum is centered at 32 K, and additional small maximum observed at 53 K. The major, the first desorption maximum is assigned to molecules adsorbed in the large 18.56 Å cavity, and the second maximum is attributed to adsorption in the small 11.97 Å cavity. While the area under the desorption peak corresponds to the number of occupied adsorption sites, due to the relative difference in the peak intensity among two maxima, we can conclude that the number of adsorption sites within the larger cavity is considerably greater than within the small one. About 80% of total gas desorption corresponds to desorption from large cavity, and 20% to desorption from the small cavity. The total amount of gas desorbed from MFU-4l corresponds to 2.2 wt.% H₂, and 4.88 wt.% D₂ (Table B-7).

Further discussion regarding the differences in the desorption mechanism from MFU-4 and MFU-4l is given in Chapter 6.2.1.

Al(OH)(ndc)

In Fig. 5.34 the desorption spectrum of hydrogen on Al(OH)(ndc) is shown. Three desorption maxima are observed, at 35 K, at about 43, and 55 K. The main adsorption sites for accommodation of gas molecules within Al(OH)(ndc) are rectangular pores of about 8.5 x 8.5 Å² in diameter. The structure of Al(OH)(ndc) represents the “open form” of aluminum naphthalate Al(OH)(ndc)(H₂O) (MIL-69) [206], synthesized using water as solvent. MIL-69 contains residual water molecules in channels, and exhibit low porosity after activation. The Al-Al-Al angle (α) in MIL-69 is 34° (Fig. 5.48), while the corresponding angle in Al(OH)(ndc) framework is considerably larger, Fig. 5.49.

The high opening degree of Al(OH)(ndc) framework gives rise to a very flexible structure. Therefore, it is very likely that desorption occurs from multiple adsorption sites with similar energetic barrier to desorption, which is why several desorption maxima are observed. Indeed, the trinuclear Al metal cluster was encountered as a building unit for the formation of the giant pore compounds of the mesoporous series MIL-100 [180], MIL-101 [98], and the flexible hybrid frameworks MIL-88 [207] with large swelling effects. The total amount of hydrogen desorbed corresponds to 0.82 wt.%.

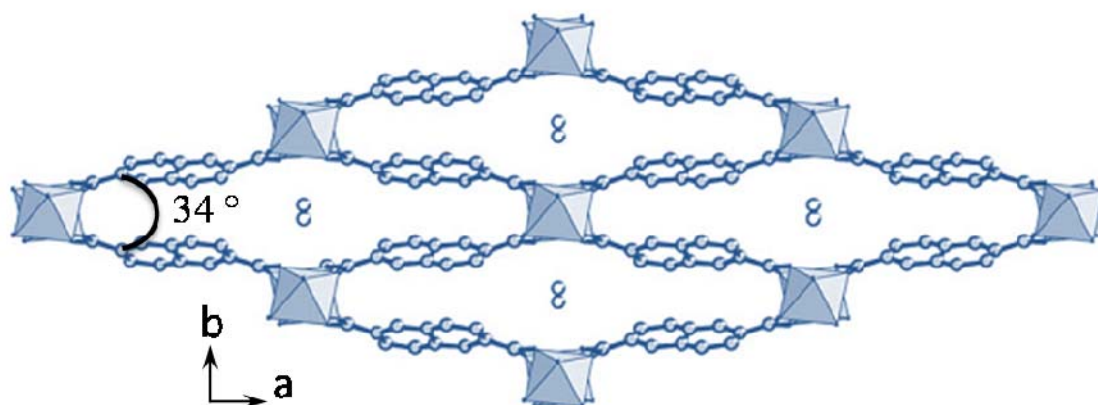


Fig. 5.48 A representation of the structure of $\text{Al}(\text{OH})(\text{O}_2\text{C}-\text{C}_{10}\text{H}_6-\text{CO}_2)\cdot\text{H}_2\text{O}\cdot(\text{MIL}-69)$ showing the channels running along the c -axis, and encapsulated water molecules (open circles). Representation comprises blue octahedra: $\text{AlO}_4(\text{OH})_2$, and the framework opening angle, according to the ref. [205].

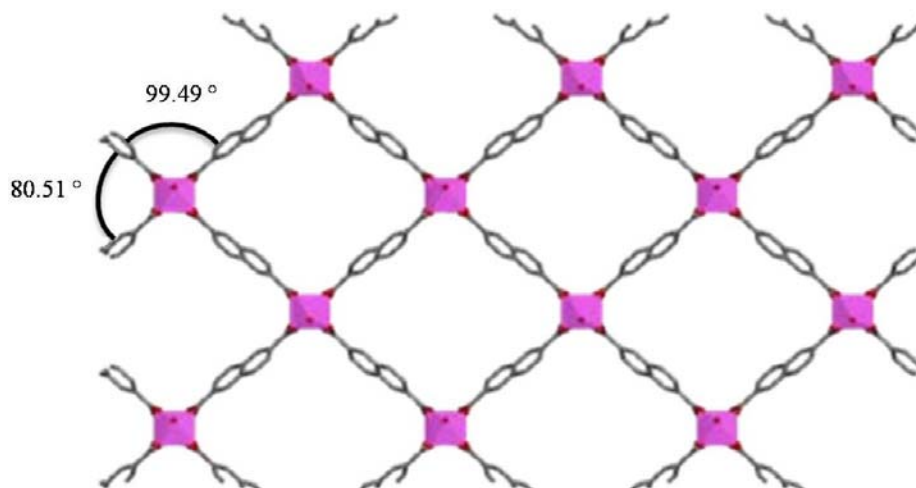


Fig. 5.49 The structure of $\text{Al}(\text{OH})(\text{ndc})$ viewed along the c -axis with indicated framework opening angles.⁸

Al(OH)(bpdc)

Analogous to $\text{Al}(\text{OH})(\text{ndc})$, the hydrogen desorption spectra of $\text{Al}(\text{OH})(\text{bpdc})$ shows a small desorption shoulder at 29 K, major maxima at about 33 K, and another desorption shoulder at 42 K (Fig. 5.35). $\text{Al}(\text{OH})(\text{bpdc})$ possess slightly larger pores of about $11.1 \times 11.1 \text{ \AA}^2$ in diameter, compared to $\text{Al}(\text{OH})(\text{ndc})$, and accordingly a higher sorption capacity, 2.41 wt.% for $\text{Al}(\text{OH})(\text{bpdc})$ vs. 0.82 wt.% for $\text{Al}(\text{OH})(\text{ndc})$. A comparative investigation between these two structures is further addressed in Chapter 6.2.1.

⁸ <http://www.metal-organic-frameworks.de>

MIL-100(Al, -V, -Cr, and -Fe)

A gas desorption from the MIL-100 series proceeds in four desorption steps. These compounds have removable terminal water molecules and, therefore, potentially unsaturated metal sites. The compounds exhibit a polymodal pore size distribution, and possess both micropores and mesopores, with small and large cages. A characteristic step adsorption isotherm, a rare phenomenon for classic porous materials, was determined by nitrogen physisorption at 77 K, and by water adsorption [208]. The same was previously observed for bimodal Cu-BTC structure [168]. Most interestingly, the TDS spectra show pronounced differences in the high temperature peak, assigned to adsorption at the unsaturated metal centers. A broad, pronounced desorption peak is observed for MIL-100(Cr), with the desorption in the range from 60 to 120 K, and with the maxima centered at 81 and 100 K for hydrogen and deuterium, respectively (Fig. 5.41, 1 mbar loading). The desorption peak observed for MIL-100(Fe) is rather long, but with slightly smaller intensity, and centered at 71 and 84 K for hydrogen and deuterium, respectively (Fig. 5.43, 1 mbar loading). A contribution of the high temperature maxima for MIL-100(V) is rather small, compared to the Cr compound and even smaller for MIL-100 (Al), Fig. 5.39 and Fig. 5.37, respectively. The number of metal sites is relatively small, and they are quickly saturated. Already for 3 mbar gas loading the intensity of peaks grows considerably, and new maxima appear, while adsorption proceeds in the pore system. The MIL-100 series exhibits a hierarchy of micro- ($\varnothing \approx 6.5 \text{ \AA}$) and mesopores ($\varnothing \approx 25\text{--}30 \text{ \AA}$), with a giant cubic cell, the volume of which is close to 368401, 387511 and 394481 \AA^3 , for MIL-100(Al, -Cr, and -Fe), respectively. The giant pore dimensions obtained for MIL-100 are commonly observed for mesoporous solids, which, in contrast to MIL-100 compounds, have amorphous walls. The structure comprises two types of mesoporous cages, a smaller and a large cage, with a free aperture close to about 25 and 29 \AA , respectively. The slight differences among the four investigated samples remain only in the window diameter. The free opening of the small pentagonal windows is 5.2 x 5.2, 4.7 x 5.7, and 4.7 x 5.5 \AA^2 for MIL-100(Al, -Cr, and -Fe), respectively. The aperture of the large hexagonal window is 8.8, 8.6, and 8.6 \AA^2 MIL-100(Al, -Cr, and -Fe), respectively. Following the occupancy of the micropores, the adsorption proceeds at the mesopores, i.e., from the small to the large cage, in consistence with the theory of micropore filling [209]. The maxima observed at 37, 48, 32, and 31 K for MIL-100(Al, -V, -Cr, and -Fe), respectively, are assigned to adsorption at the small 25 \AA cage (Fig. 5.44). Further, maxima at 32, 32, 24, and 26 K for MIL-100(Al, -V, -Cr, and -Fe), respectively, are assigned to adsorption in the large cage. In addition, another maximum is observed for MIL-100(Al), centered at 21 K (Fig. 5.37), which is assigned to liquid deuterium. This maximum appears for gas loadings higher than 4 mbar, after the large mesopore is completely saturated. The total amount of hydrogen desorbed corresponds to 2.85,

2.43, 1.91, and 1.36 wt.% for MIL-100(Al, -V, -Cr, and -Fe), respectively. The Langmuir surface area is calculated to be 2919, 2139, 3100, and 2800 m² g⁻¹ for MIL-100(Al, -V, -Cr, and -Fe), respectively. The lack of a linear correlation between the hydrogen adsorption capacity and the surface area indicates that low-pressure hydrogen adsorption is controlled by the other factors. Indeed, GCMC simulations done by Frost et al. [210], on a series of ten isoreticular MOFs, with the same framework topology and a surface chemistry, but different pore sizes, investigated the effects of surface area, the free volume, and the heat of adsorption on hydrogen uptake at 77 K, over a wide range of pressures. The authors found three adsorption regimes where the isosteric heat, the surface area, and the free volume each dominate the amount of hydrogen adsorbed. At low pressure (less than 1 bar), the hydrogen uptake correlates with the heat of adsorption. At intermediate pressure the uptake correlates with the surface area, while at high pressure the total gas uptake correlates best with the surface area and the free volume. Indeed, for a series of samples studied by the group of Yaghi, a saturation adsorption of hydrogen on various MOFs was found to scale the best with the Langmuir surface area [200], which appears to give reasonable values for an apparent surface area for MOFs [94]. Theoretically, a minimum surface area of about 1400 m² g⁻¹ is needed for a material to reach an excess adsorption of 6 wt.% (or 2100 m² g⁻¹ for 9 wt.%) [211].

The correlations made for absolute hydrogen adsorption at 77 K do not hold well for absolute hydrogen adsorption at 298 K [212]. At low loadings, the absolute excess amount of hydrogen adsorbed correlates with the heat of adsorption, while, at high loadings, the adsorption correlates better with the adsorbent surface area than with the free volume.

Further discussion about the influence of metal centers on the strength of interaction with hydrogen molecules is given in the Chapter 6.3.

5.2.3 Summary

The interaction of coordinatively unsaturated metal centers with hydrogen/deuterium molecules and a sequential filling of other adsorption sites within several MOF samples have been studied by the low-temperature thermal desorption spectroscopy.

Three maxima were observed for Cu-BTC, and could be assigned to different adsorption sites by comparison with the neutron diffraction studies from the literature. The maximum with the highest desorption temperature, which could be separated by either partial loading or interrupted desorption, is attributed to molecules adsorbed on the metal sites. The two maxima appearing on lower temperature, for higher gas loadings, have been assigned to successive filling of the side pockets and the large pore. The TDS measurements are shown to yield information that supplement finding obtained by the other, independent experimental methods.

The three desorption maxima were observed as well for hydrogen/deuterium adsorption on Fe–BTC framework. Analogous to Cu–BTC structure, Fe–BTC possesses open metal sites, and two types of mesoporous cages. One of the coordination positions of Fe^{3+} ions is occupied by solvent molecules in as-synthesized form and, therefore, is available to accommodate gas molecules after out-gassing the sample at elevated temperature, under HV. Apart from the high temperature maximum, assigned to adsorption at metal sites, two additional maxima were observed and assigned to adsorption in the small and the large pore. Overall, iron is an environmentally benign, cheap, and non-toxic component, which is why Fe–BTC might be suitable for an industrial application.

The utility of an s-block metal, Mg, and formic acid resulted in producing a light-weight MOF, Mg–formate(1). Although it is commonly believed that only the use of extended ligands results in a stable, porous structure, the use of formic acid, the smallest of the carboxylate linkers, yielded material with sustainable porosity. Small 3.4 Å pores lead to a strong interaction between the adsorbent and the adsorbate, and resulted in rather high hydrogen desorption maximum, centered at 48 K. A slightly changed synthesis procedure, and a formation of bigger pores within Mg–formate(2), resulted in increased H_2/D_2 total sorption capacity.

A unique desorption mechanism was observed for MFU–4, an unprecedented cubic framework constructed from BBTA²⁻ dianions and $\text{Zn}_5\text{Cl}_4^{6+}$ coordination units. Gas penetration is found to be diffusion limited, as the framework features a narrow-sized joining apertures of 2.5 Å, that allow a passage of sufficiently small molecules only. The high temperature hydrogen peaks observed for MFU–4, centered at 74 and 109 K, are the highest desorption temperatures yet measured for hydrogen desorption from MOFs.

The crystal lattice of MFU–4l resembles that of MFU–4 in terms of structural parameters, as both are cubic six-connected nets, and both possess two different types of cavities. However, considerably larger pore diameters, and the large pore apertures in MFU–4l allow adsorption, and a free diffusion of gas molecules. The MFU–4l framework adsorbs twice the amount of hydrogen, compared to MFU–4. However, the desorption occurs at a considerably lower temperatures, and the interaction with the hydrogen molecules is rather weak. More than 99% of hydrogen desorbed below 60 K, while the gas desorption for MFU–4 only begins at this temperature.

Two Al based MOFs have been investigated, Al(OH)(ndc), the open form of MIL–69, and a new isorecticular compound, Al(OH)(bpdc). A greater surface area and the pore volume within Al(OH)(bpdc) induced a greater storage capacity. As a light, and a cheap element aluminum yields frameworks with relatively low density and potentially high storage capacity, that can be produced at relatively low cost, at the industrial scale.

Four isostructural compounds from the MIL-100 series were used for a comparative investigation regarding the influence of open metal sites on the strength of the H₂-MOF interaction, and on the total storage capacity. The partial filling of different adsorption sites was observed upon changing the initial gas loading. The TDS measurements have shown that the coordinatively unsaturated metal sites induce strong H₂-MOF interaction, and have been identified as the most energetic sites within the MIL-100 structure. The interaction was found to exhibit maximum for MIL-100(Cr) compound, regarding the highest desorption temperatures.

Following adsorption at the coordinatively unsaturated metal centers, the micropores, and finally the mesopores are filled.

Chapter 6

TAILORING THE H₂-MOF INTERACTION

6.1 An Overview

The major advantage of MOFs over the more traditional porous materials, the activated carbons and the zeolites, is an almost endless variety of structures, and the possibility to tailor these materials toward a specific application. They can be synthesized in high crystallinity, a potentially large quantity, and at low cost. In comparison with four-connected zeolites, MOFs show a broader variety of net-topologies, such as 3-, 5-, 6-, 7-, and 8-connected 3D nets. Unlike zeolites, which usually require the use of inorganic or organic templates, the solvents utilized in the synthesis of porous MOFs can act as templates themselves.

Over the last decade a notable research has been conducted to design new structures, and to improve MOF performance in terms of an increased storage capacity, and enhanced adsorption enthalpy. A significant storage capacity has been reached, even surpassed the DoE targets (Chapter 1), albeit only under cryogenic conditions. The majority of investigated adsorbents exhibit hydrogen adsorption enthalpies in the range of 4.7 to 7.5 kJ mol⁻¹ [111, 213 – 215]. For a reversible H₂ storage at RT, and the fuel-cell operating pressures between 1.5 and 30 bar, the fundamentally weak physisorption interaction between the light-atom surfaces, and poorly polarizable H₂ molecule need to be enhanced. The required, theoretically estimated hydrogen adsorption enthalpy is 13 to 20 kJ mol⁻¹, whilst 15.1 kJ mol⁻¹ is commonly cited as an optimal value [61]. Several approaches have been proposed to enhance the strength of interaction of hydrogen with the MOF framework [176]. This chapter summarizes these approaches, and results published over the last decade, with the emphases on the most prominent results, and give a comparative study regarding the MOF structures investigated within this work.

6.2 The Pore Size Optimization

One way to increase the strength of interaction between the hydrogen and the MOF framework is to tailor the pore dimensions. Initially, the pore sizes within MOFs were too large for the effective hydrogen adsorption. In Fig. 6.1 a comparison is given between the large 15.2 Å pore within MOF-5 [176], and the size of the hydrogen molecule (kinetic diameter of 2.89 Å).

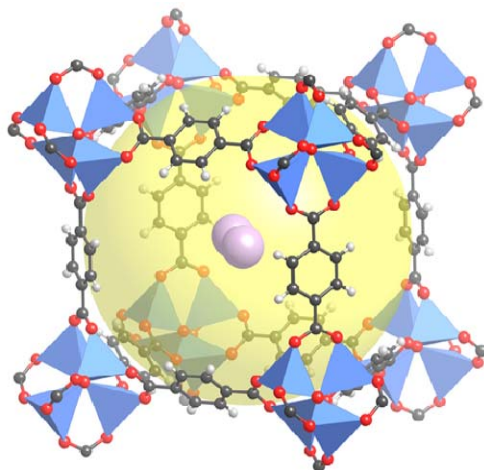


Fig. 6.1 The large spherical pore in MOF-5 (yellow sphere), compared to the size of a hydrogen molecule (lilac sphere). The framework comprises the following atoms: C (black), H (white), O (red), and Zn (blue tetrahedra). Representation is taken from the ref. [176].

The pore size can be optimized by changing organic linkers, by framework catenation, and/or by impregnation. As the pore size decreases, the interaction energy is enhanced, while the attractive potential field from the opposite pore walls overlap [216], thus, maximizing the total van der Waals force on the adsorbate. This approach has resulted in enhancement of the hydrogen adsorption enthalpy (in the range of 7.0 to 9.5 kJ mol⁻¹), as found for microporous Mg-MOF with small 3.5 Å pores [198].

The role of the pore size on the adsorbate-MOF interaction is illustrated in Fig. 6.2, for the three MOF samples investigated within this work. MOFs possessing different structure and composition, Cu-BTC, MOF-177, and Mg-formate(1) are studied under the same experimental conditions. The structure of all three samples is discussed in details in the Chapter 5.1.

In MOF-177 already below the temperature of about 50 K hydrogen was mainly desorbed, and corresponds to 1.28 wt.% (Table B-5). The gas does not adhere to the surface of MOF-177 even at temperatures close to 20 K, and is partially desorbed in vacuum before the TDS measurement starts. Under the same experimental conditions the hydrogen desorption spectra of Cu-BTC show two maxima, correlated to the sequential occupancy of the framework pore system. At first tetrahedral

side pockets are occupied, followed by adsorption in the large pores, which indicates a stronger interaction between the hydrogen and the smaller pore. Both the neutron powder diffraction, and the inelastic neutron scattering (INS) data support these findings [186, 187]. The total amount of hydrogen desorbed is determined to be 1.62 wt.%. The hydrogen desorption spectrum of Mg-formate(1) exhibits one broad maximum centered at 52 K, and another small maximum at 81 K. The amount of hydrogen desorbed is calculated at 1.00 wt.%. The maximum centered at 52 K is attributed to the interaction of hydrogen molecules with the small 3.4 Å pore. It is in the same temperature range as for the tetrahedral side pockets within the Cu-BTC structure.

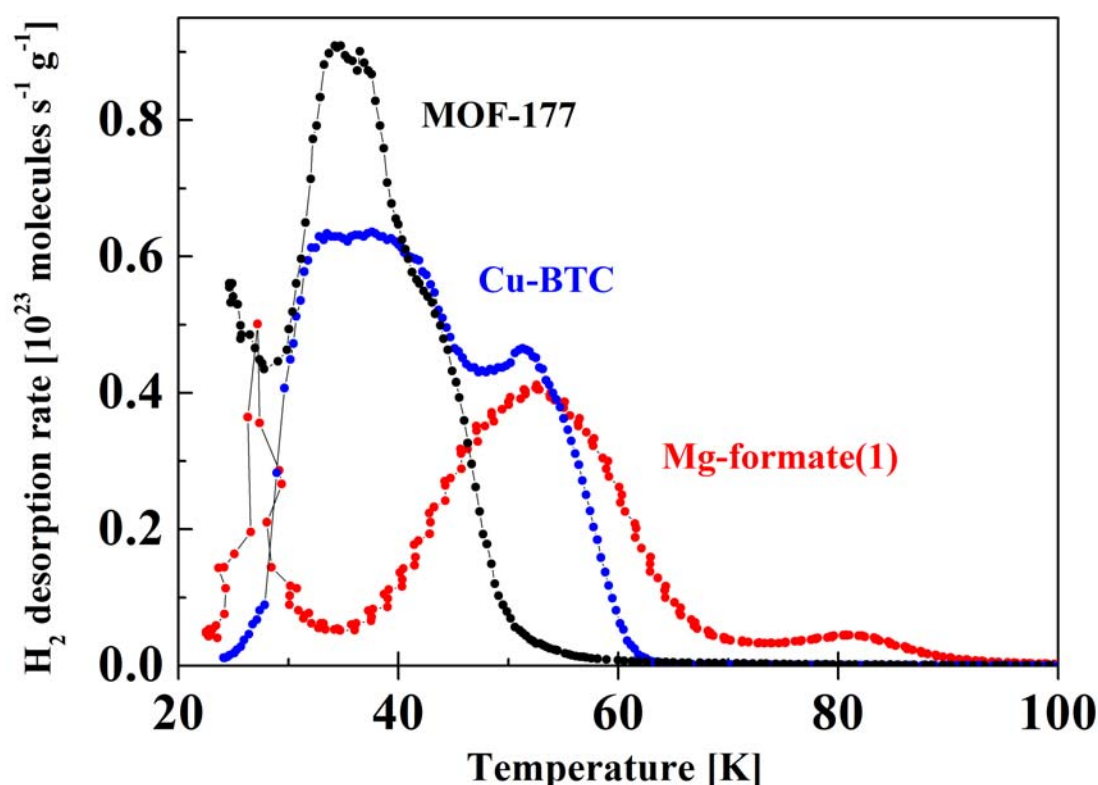


Fig. 6.2 The thermal desorption spectra for the three MOF samples, loaded at 25 mbar, and recorded with the heating rate of 0.10 K s⁻¹.

A further comparison among the three investigated samples is given in Fig. 6.3, where the hydrogen total coverage is reported versus the desorption temperature. It is assumed that for temperatures close to 20 K the maximum (saturation) coverage is attained, i.e., $\theta_{max} = 1$. Fig. 6.3 points out the salient differences in the desorption mechanism regarding the different pore structure. At about 30 K there is a crossover between the MOF-177 and the Mg-formate(1) curve. However, above 30 K the total coverage rapidly decreases for MOF-177, and already at 50 K the gas is mainly desorbed. Gas desorption from Mg-formate(1) proceeds at higher temperature, mainly in the temperature range from 40 to 90 K. Two pronounced regions are observed, pointing to two distinct desorption

maxima, i.e., two different adsorption sites. On the other hand, gas desorption from Cu-BTC mainly occurs in the temperature range from 40 to 60 K with two desorption regions, not that strongly pronounced, as they are correlated to the desorption from overlapping desorption maxima. The area under the desorption curve is proportional to the total storage capacity, and the maximum temperature correlates to the strength of interaction of hydrogen with the MOF framework. For 25 mbar gas loading the total storage capacity of the three investigated samples proceeds in the following manner: 1.00, 1.28, and 1.62 wt.% for Mg-formate(1), MOF-177, and Cu-BTC, respectively. The corresponding BET surface area is 16, 4239, and 1154 m² g⁻¹, and the Langmuir surface area 24, 5635, and 1958 m² g⁻¹ for Mg-formate(1), MOF-177, and Cu-BTC, respectively (determined by the N₂ adsorption at 77 K). While diffusion limitations disable an accurate determination of the Mg-formate(1) surface area (discussed in Chapter 5.2), and the weak interaction of hydrogen with the MOF-177 results in a storage capacity less than the one observed at 77 K and high pressure (Table D-1), a correlation between the total storage capacity and the surface area is not straightforward, and cannot be applied here.

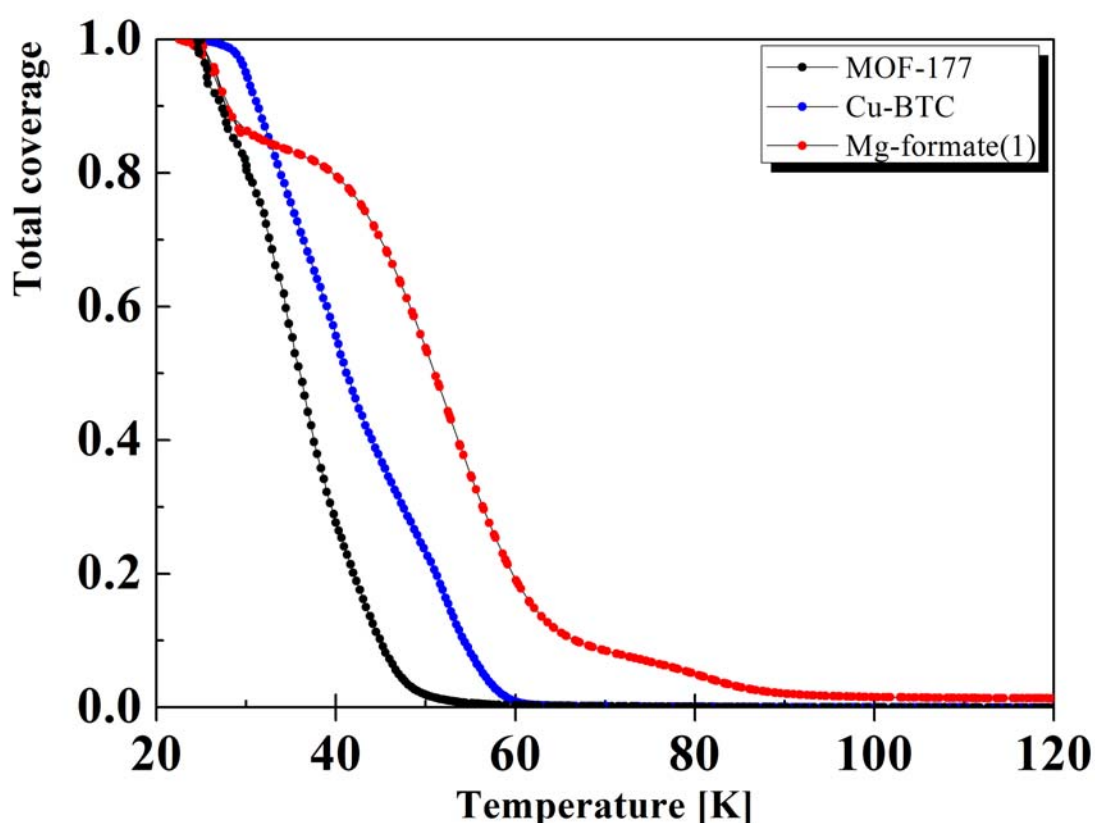


Fig. 6.3 Hydrogen surface coverage of MOF-177 (black), Cu-BTC (blue), and Mg-formate (1) (red) vs. the desorption temperature.

The low-temperature TDS measurements further allow a correlation between the desorption temperature, and the pore diameter to be established. Utilizing the small pores, comparable to the kinetic diameter of the hydrogen molecule, enhances the strength of the hydrogen-MOF interaction. Generally, it is observed that the desorption temperature is higher for materials with smaller pore size (Fig. 6.4), indicating that MOFs with smaller cavities lead to a higher heat of adsorption. For MOFs possessing a bimodal pore size distribution, the smaller pore is filled first, while hydrogen desorbs at lower temperature from the large pore.

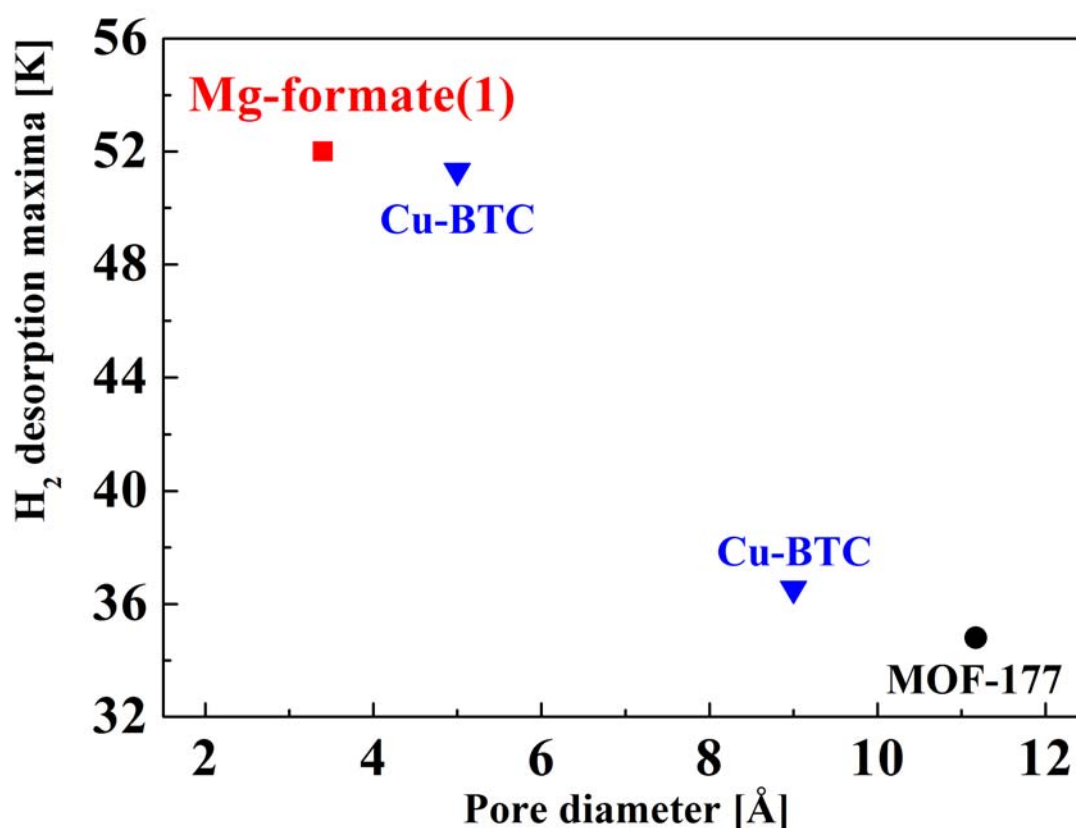


Fig. 6.4 The temperature of hydrogen desorption maxima vs. pore diameter for the three investigated MOF samples.

6.2.1 Functionalization of the Pore Size and the Pore Volume by Ligand Modification

Over the last decade a great progress has been achieved in predicting and designing new porous structures, predominantly by the group of Yaghi and co-workers, who introduced the concept of iso-reticular design [217]. They developed a strategy, based on the concept of SBUs, where a series of isoreticular MOF-structures (IRMOFs) were presented, Fig. 6.5. Using 16 different molecules, which act as organic linkers with different length and functionality, it has been successfully shown that one can enlarge the pore size, from 3.8 to 29 Å, in the so-called reticular synthesis [217].

Sagara et al. have used DFT *ab initio* calculations and second-order Møller–Plesset perturbation theory to approximate the binding energy of H₂ to IRMOF-1 [218]. It should be kept in mind that open-shell electronic configurations and negative charge considerations often make DFT calculations computationally demanding and unreliable, which is why the issue of modeling the H₂ interaction with coordinatively unsaturated metal centers within MOFs is still an unsolved problem [188].

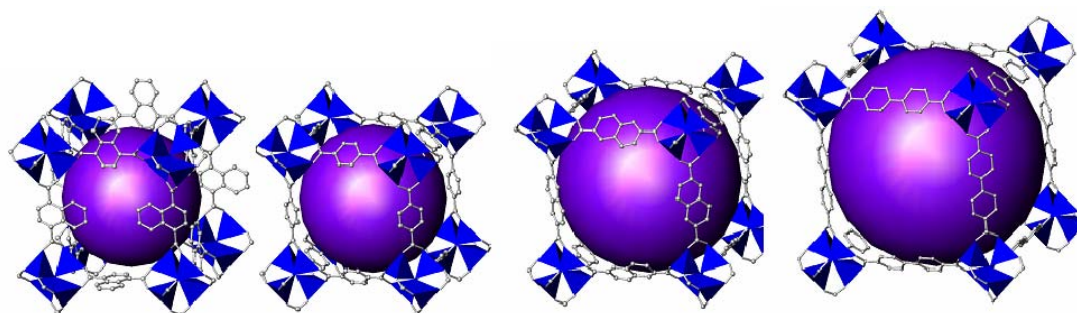


Fig. 6.5 A series of four isoreticular MOFs based upon an augmented simple cubic net, IRMOF-7, IRMOF-1 (MOF-5), IRMOF-8, and IRMOF-10. The large pore of each structure is represented with a violet sphere, with diameter defined by the distance between the van der Waals surfaces of the framework atoms. Representation comprises the following atoms: C (grey), and Zn (blue tetrahedra). H and O atoms are omitted. Further structure variations are possible. Representation is given according to the references [139, 217].

The reticular synthesis enables the construction of MOFs with the same topology, synthesized using the same metal ion or metal cluster as node of the framework, but different linkers. The influence of the ligand structure on hydrogen sorption capacity of MOFs can be traced back to the first reported hydrogen uptake in MOFs, in which the authors proposed that using larger aromatic ligands increases the hydrogen sorption capacity [219]. This idea was later supported by the theoretical studies [220, 221].

In the literature systematic investigation of the influence of the pore volume on the hydrogen sorption capacity was made for the three MOFs with NbO-type topology. Extension of biphenyl-3,3',5,5'-tetracarboxylate to terphenyl-3,3'',5,5'''-tetracarboxylate and quaterphenyl-3,3''',5,5''''-tetracarboxylate lead to a proportional increase in the pore sizes: 6.5, 7.3, and 8.3 Å [222]. The maximum amount of H₂ adsorbed increased with increasing the pore size, while the maximum adsorbate density proportionally decreased with increasing the pore size.

Prominent examples from this study will be discussed in this regard. A slight change in the synthesis procedure, and the usage of a longer linker, H₂-BTDD (for MFU-4l), instead of H₂-BBTA (for MFU-4), resulted in synthesis of the two analogous frameworks with the two different

types of cavities, arranged in an alternating fashion (Chapter 5.1). In Table 6.1 the relevant structural parameters are compared for both investigated structures.

TABLE 6.1

The relevant structural parameters and the porosity data for MFU-4 and MFU-4l.

Parameter	MFU-4	MFU-4l
Small cavity [Å]	3.88	11.97
Large cavity [Å]	11.94	18.56
Aperture [Å]	2.52	9.13
Volume [Å ³]	10114(9)	29955(4)
Surface area [m ² g ⁻¹]	1611	2746

Fig. 6.6 shows the thermal desorption spectra of hydrogen for MFU-4 and MFU-4l for two different heating rates, 0.10 and 0.01 K s⁻¹, in the temperature range between 15 and 120 K. At higher temperatures no hydrogen was desorbed. Additional comparison is shown in Fig. C-1 for deuterium desorption. The TDS spectra show distinct differences in the desorption range, and in the magnitude of the desorption signal between MFU-4 and MFU-4l. For MFU-4 the major hydrogen desorption begins at about 60 K, while for MFU-4l the majority of hydrogen molecules are already desorbed at this temperature. The intensity of the desorption signal shows the opposite behavior.

While water adsorption within MFU-4 shows a steep uptake at 298 K, N₂ is occluded from adsorption at 77 K and pressure up to 1 bar [177]. Hydrogen penetration is somewhat hindered as well, and results in low gas uptake in MFU-4. The intensity of the desorption signal is several orders of magnitude higher for MFU-4l, while the MFU-4l framework features large pore apertures of 9.13 Å, and allows adsorption and free diffusion of hydrogen molecules. The total amount of desorbed hydrogen corresponds to 0.23 and 2.29 wt.% for MFU-4 and MFU-4l, respectively. These values correlate well with the reported surface area, predicted by the Monte Carlo integration technique for MFU-4, and from N₂ adsorption at 77 K for MFU-4l, Table 6.1.

The increased pore diameter and the pore volume (Table 7.1) lead to an increase in the maximum sorption capacity for MFU-4l, whereas the interaction potential exhibits a reverse behavior. Since the strength of the H₂-MOF interaction is equally important as the total storage capacity, the MFU-4 might be regarded as a more suitable hydrogen adsorbent than the MFU-4l, regarding the constant aim to bring hydrogen adsorption in MOFs more close to RT application.

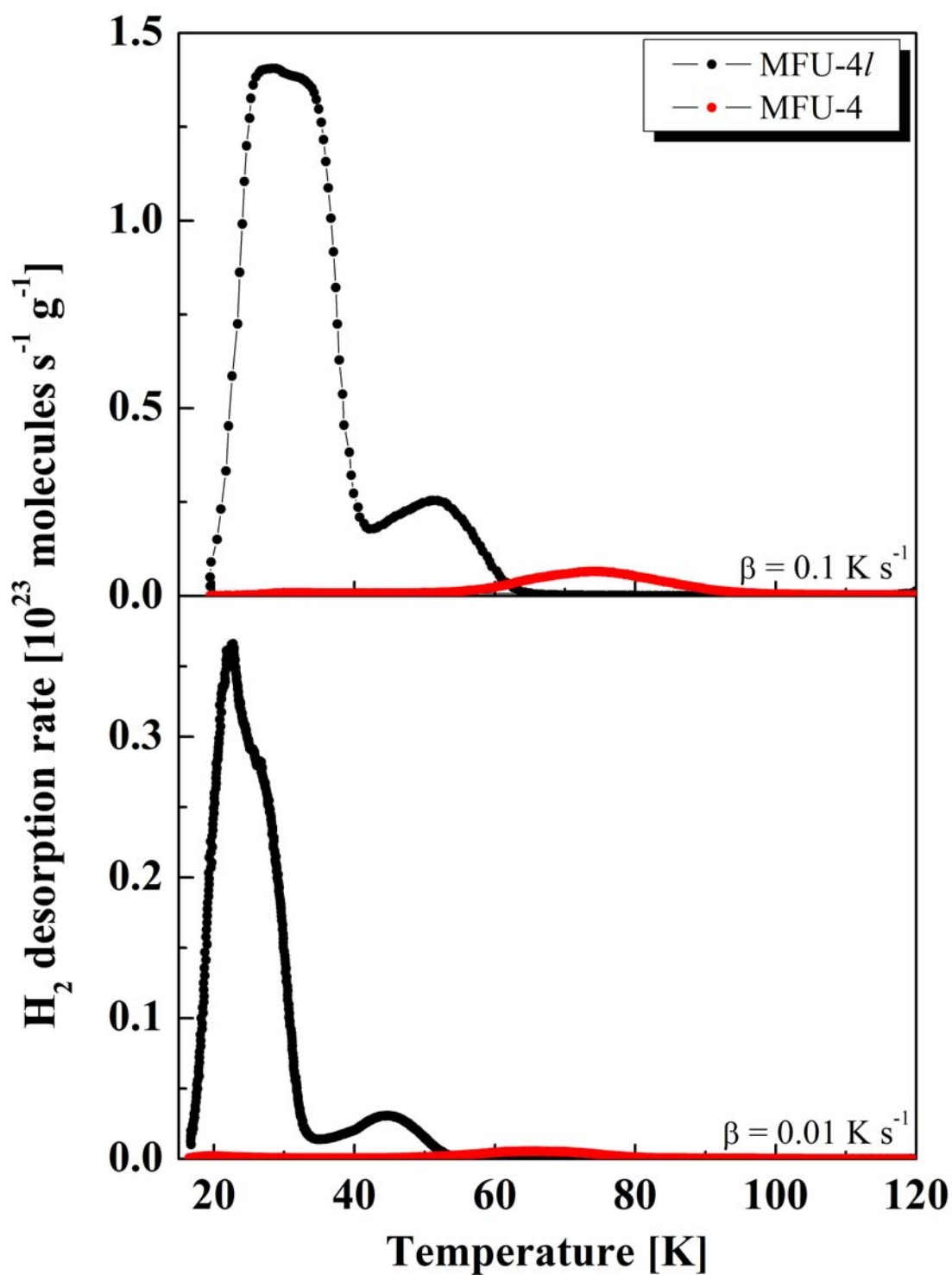


Fig. 6.6 The hydrogen thermal desorption spectra of MFU-4 and MFU-4l, loaded at 25 mbar, and recorded with the heating rate of 0.10 and 0.01 K s⁻¹.

The influence of ligand optimization on the pore dimensions and the sorption capacity is further discussed for Al-based MOFs, Al(OH)(ndc) and Al(OH)(bpdc). Both compounds are synthesized using N,N-dimethylformamide (DMF) as solvent and structure-directing agent. Al³⁺ was used as

metal center, and 2,6-naphthalene dicarboxylate (ndc), and 4,4'-biphenyl dicarboxylate (bpdc) as linkers, Fig. 6.7.

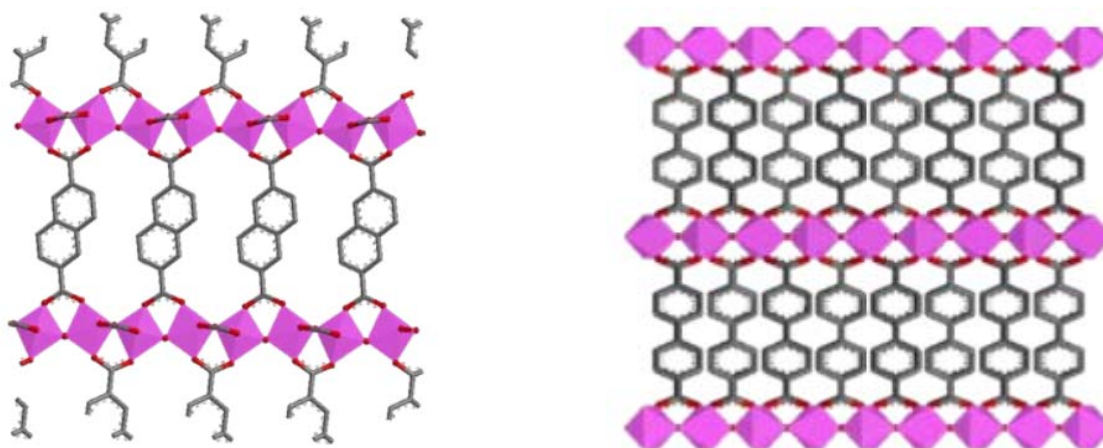


Fig. 6.7 Representation of Al(OH)(ndc) and Al(OH)(bpdc) structure, left and right, respectively.⁹

For both compounds the gas desorption mainly occurs in the same temperature range, from about 20 to 55 K (Fig. 6.8, heating rate of 0.10 K s^{-1}). Since there is only a slight difference in the pore diameter between the two structures, $8.5 \times 8.5 \text{ \AA}^2$ for Al(OH)(ndc) vs. $11.1 \times 11.1 \text{ \AA}^2$ for Al(OH)(bpdc), the desorption maxima occur at comparable temperatures for the two compounds. However, a notable difference is observed in the intensity of the desorption signal, and, therefore, in the total sorption capacity. The total amount of hydrogen desorbed is calculated to be 0.82 wt.% for Al(OH)(ndc) vs. 2.41 wt.% for Al(OH)(bpdc). These values are expected regarding the difference in the surface area, 1308 and $1613 \text{ m}^2 \text{ g}^{-1}$, and the cell volume $2159.3(9)$ and $2885.4(5) \text{ \AA}^3$, for Al(OH)(ndc) and Al(OH)(bpdc), respectively. Al(OH)(bpdc) has a greater pore volume and, therefore, the larger storage capacity. These observations illustrate the importance of tailored synthesis and a profound effect of the pore volume on the total storage capacity, which is larger for frameworks synthesized using the longer linkers.

⁹ <http://www.metal-organic-frameworks.de>

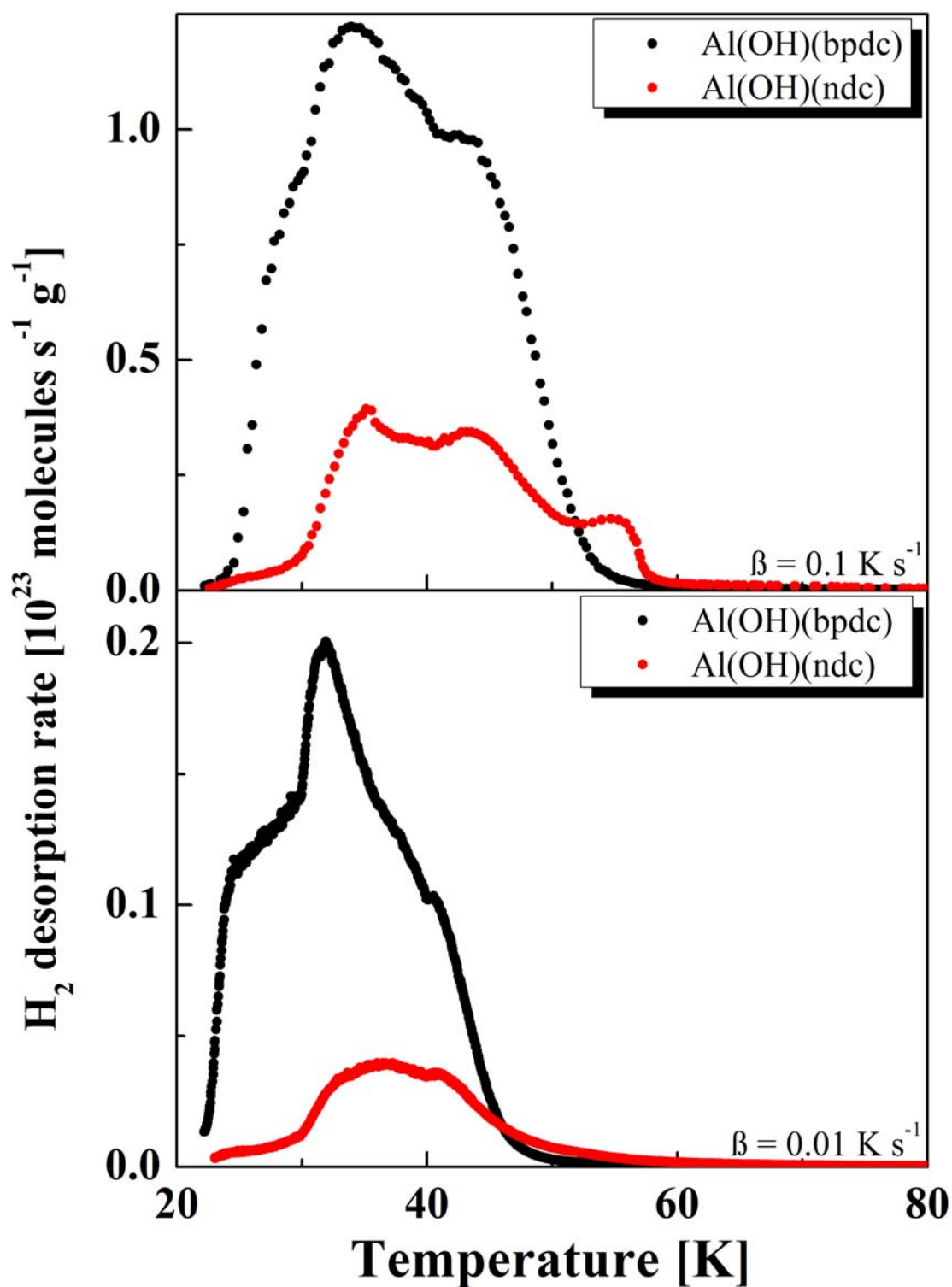


Fig. 6.8 The TDS spectra of hydrogen desorbed for Al(OH)(ndc) and Al(OH)(bpdC) loaded at 25 mbar, and recorded with the heating rate of 0.10 and 0.01 K s⁻¹.

The effects of framework self-catenation and impregnation, as an alternative approach to tailor the pore size, has not been investigated within this study. Nevertheless, they will be discussed briefly, regarding its overall importance in tailoring MOF properties.

6.2.2 Catenane Formation

Framework catenation, the intergrowth of two or more identical frameworks, is another effective way to tune the pore size of MOFs. The catenation can be achieved by interpenetration [223], and by interweaving [224], Fig. 6.9.

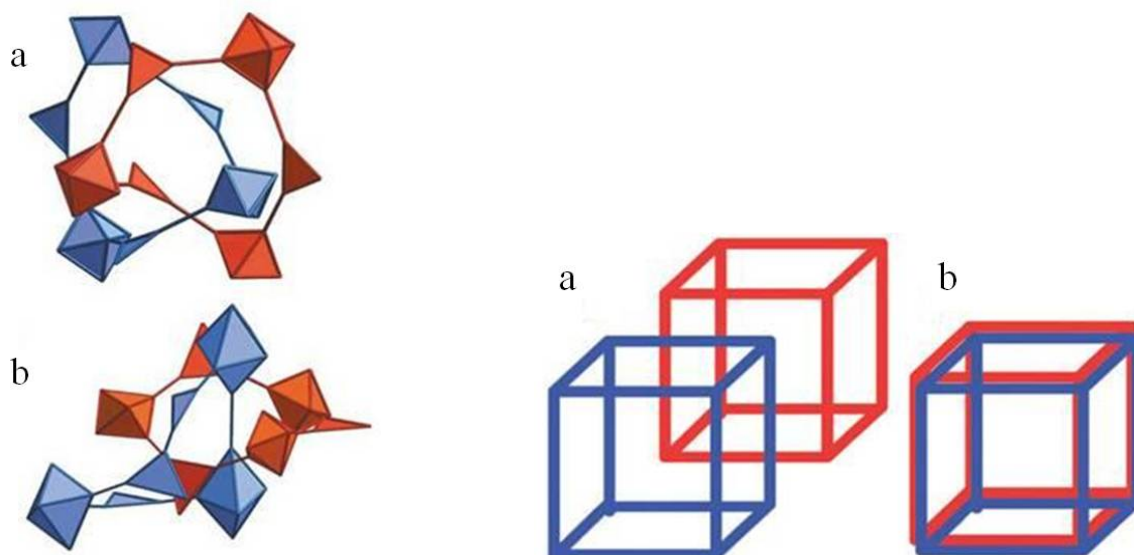


Fig. 6.9 (left) A catenation of rings in nets intergrown with their dual structures. The nets are shown augmented with triangles, at the three-coordinated vertices, and with octahedra at the six-coordinated vertices. Reproduced from the ref. [101].

Fig. 6.9 (right) Schematic representation of porous coordination polymers of cubic topology illustrating catenated frameworks: the interpenetration (a) and interweaving (b) of identical lattices. A SBUs are shown as cubes, and linkers depicted as rods. Reproduced from the ref. [225].

The interpenetrated structures give the best results when the second framework is shifted exactly in the middle of the first one, which keeps those frameworks maximally displaced from each other [226]. The reduction of the pore diameter due to catenane formation may as well be achieved by interweaving, where frameworks are minimally displaced from each other and exhibit many close contacts [94]. Interweaving improves the material's rigidity by mutual reinforcement, which is the source of further framework stabilization. However, the undesirable outcomes are thicker pore walls and blockage of potential adsorptive sites. Therefore, interpenetration rather than interweaving is a desirable approach to synthesize catenated MOF frameworks.

The effects of catenation on hydrogen sorption capacity was investigated for IRMOFs, and revealed that catenated IRMOF-9, -11, and -13 have a higher hydrogen adsorption capacities than the non-catenated IRMOF-11 [171]. Furthermore, the theoretical studies on IRMOFs [225, 227, 228], using GCMC simulations at 77 K, showed that the small pores generated by catenation play a role in

confining the hydrogen molecules more densely. At RT catenation does not improve the hydrogen uptake for the three IRMOFs studied. The gravimetric hydrogen uptake for catenated structures is approximately one half that of the non-catenated structures, while the volumetric hydrogen uptake is similar for catenated and non-catenated MOFs. Interpenetrated MOFs have a higher hydrogen uptake than the non-interpenetrated MOFs only at low pressure. At higher pressures, however, the non-catenated IRMOFs adsorb more hydrogen due to a greater free volume.

The group of H.-C. Zhou developed a templating strategy to control the catenation/noncatenation in porous MOFs, and made a comparative study where catenated and non-catenated forms of the same framework were directly compared for hydrogen storage. These studies revealed that the catenation yields a 41% increase in the apparent Langmuir surface area (3800 m² g⁻¹ for PCN-6 vs. 2700 m² g⁻¹ for PCN-6'), a 29% increase in the excess gravimetric hydrogen uptake at 77 K and 1 bar, and a 133% enhancement in volumetric hydrogen uptake [226, 229].

6.2.3 Impregnation

The pore size may be optimized by inserting a non-volatile guest molecule within the large-pore MOF by impregnation – experimentally proved by including large molecules such as C₆₀ and Reichardt's dye into MOF-177 [101, 225], Fig. 6.10. The framework must be well-anchored, and have a very low vapor pressure, to suppress its desorption along with the adsorbate. The impregnated guest molecules should not block the existing adsorptive sites within the framework. All aspects of this process are well studied in the excellent publication by Rowsell and Yaghi [176].

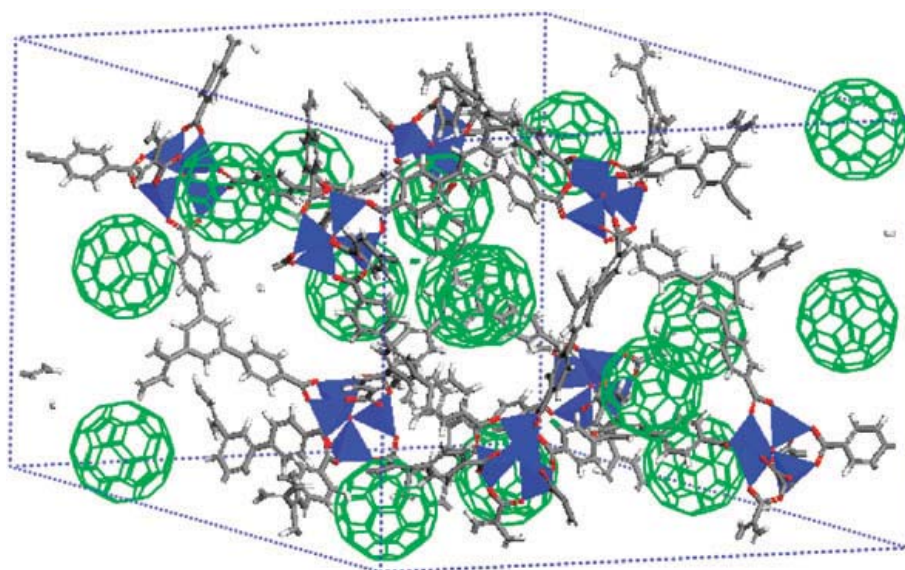


Fig. 6.10 A C₆₀-impregnated MOF-177 structure, reproduced from the ref. [225].

6.3 Influence of Coordinatively Unsaturated Metal Centers on the Strength of the H₂–MOF Interaction

The second strategy, regarded as the most effective one [176], proposed to further improve the hydrogen adsorption enthalpy in MOFs is through the introduction of coordinatively unsaturated metal centers, perhaps the most attractive structural feature of MOFs. The coordinatively unsaturated metal sites in MOFs are usually fully exposed, and can be liberated by the removal of solvent molecules coordinated to the metal center, while heating the sample under HV. Compared to the zeolites, the amount of metal sites in MOFs is by almost a factor of ten higher [165].

MOF-505 was shown to have an exceptionally high hydrogen capacity of 2.47 wt.% at 77 K and 1 bar, after removal of axial aqua ligands from the dicopper paddlewheel SBUs, via thermal activation [230]. The Long's group demonstrated the adsorption enthalpies of 9.5 and 10.1 kJ mol⁻¹, using unsaturated Cu²⁺ [231], Mn²⁺ [232], and Mg²⁺ [198] centers. The isosteric heat of hydrogen adsorption as high as 12.3(5) kJ mol⁻¹ [184] and 13.5 kJ mol⁻¹ [189, 233] were reported in the literature, which is close to the projected optimum of 15.1 kJ mol⁻¹ for RT application [61]. Among the series of isostructural MOFs investigated by Zhou et al., the Zn–MOF was shown to exhibit the lowest heat of adsorption (8.5 kJ mol⁻¹), while the Ni–MOF exhibits the highest heat of adsorption (12.9 kJ mol⁻¹) [234]. These values are considerably higher than for the hydrogen–carbon interaction [176]. The experimental data show that incorporation of transition metal cations in MOFs could lead to the materials with H₂ binding energies which fall in the desired 15–20 kJ mol⁻¹ range [188, 235].

The positive influence of unsaturated metal sites becomes easily evident after comparing the isostructural samples with and without the unsaturated metal sites [236]. MOFs containing unsaturated metal sites have a higher hydrogen uptake both at low pressure (2.87 wt.% vs. 2.07 wt.% at 77 K and 1 bar), and at high pressure (5.22 wt.% vs. 3.70 wt.% at 77 K and 50 bar). The presence of coordinatively unsaturated metal sites induces the higher zero-coverage isosteric heat of adsorption (11.60 kJ mol⁻¹ vs. 7.24 kJ mol⁻¹). The experimental H₂ uptake in MOFs with exposed metal sites was reviewed in details by Dincă and Long [188].

Four isostructural compounds from the MIL-100 series: MIL-100(Al, -V, -Cr, and -Fe) were the subject of a comparative investigation, regarding the influence of metal centers on the strength of interaction with hydrogen (deuterium) molecules, and on the total sorption capacity. The compounds are characterized with the large accessible and permanent porosity, and synthesized using the analogy with the zeolite architecture of MTN topology, where the tetrahedral unit (SiO₄) in the zeolite ZSM-39 corresponds to the hybrid super-tetrahedra in MIL-100 (Chapter 5.1). A

ligand-regulated synthesis enabled the formation of isostructural porous MOFs synthesized using the same ligand (BTC), but different metals centers, a p element (Al³⁺), and 3d transition metals (V³⁺, Cr³⁺, and Fe³⁺).

A comparison of the TDS spectra for hydrogen and deuterium is given in Fig. 6.11 and Fig. C-2, respectively, for three samples from the MIL-100 series, MIL-100(V, -Cr, and -Fe). The spectra are presented in the same temperature range, from 20 to 120 K, and for the same intensity range, thus, the relative contribution of the different maxima can be compared directly. The hydrogen desorption from the MIL-100(V) occurs mainly in the temperature range from 20 to 80 K, while the corresponding desorption range is slightly narrower, from about 24 to 55 K, for hydrogen desorption from the MIL-100(Cr, and -Fe).

A further comparison is given in Fig. 5.44 and E-3, for hydrogen and deuterium, respectively, for all four investigated compounds.

Gas adsorption on the MIL-100 series proceeds by adsorption at the coordinatively unsaturated metal sites at low gas loading, followed by adsorption in the pore system (Chapter 5.3). The TDS spectra show pronounced differences in the high temperature peak, corresponding to the partial filling of the first adsorption site. The high temperature maximum is centered at 81 and 70 K for MIL-100(Cr, and -Fe), respectively (Fig. 6.11, 1 mbar gas loading). In the same temperature range (50 to 100 K) the desorption peak is observed for the MIL-100(V), and centered at 61 K, while the intensity of the high temperature maximum for the MIL-100(Al) is rather small (Fig. 5.36, and Fig. 6.12). A rather high desorption temperature suggests that the coordinatively unsaturated metal sites induce a strong hydrogen-framework interaction, in particular for the MIL-100(Cr). The Cr(III) trimers are occupied by water molecules in their as-synthesized form. Both, free and coordinated water molecules can be removed without any collapse of the framework, while heating the sample under HV. By removing the terminal water molecules Cr³⁺ coordinatively unsaturated metal sites are provided in the structure. Depending on the activation temperature, MIL-100(Cr) exhibits either Brønsted or Lewis acidity, i.e., the framework has the ability to convert Lewis acid sites into Brønsted acid sites upon water adsorption. The number and the strength of accessible metal sites is close to 3 – 3.5 mmol g⁻¹ for the MIL-100(Cr, and -Fe). At the same time Lewis acidity of Cr is higher than the one of Fe, giving rise to the stronger interaction and the higher desorption temperature, 81 vs. 71 K. The high temperature maximum for MIL-100(V) is centered at 61 K, indicating even lower strength of interaction with hydrogen than for Cr and Fe compound. The particularity of the Al compound is the number of possible uncoordinated Al sites. Over the three sites of the AlO₆ trimeric unit only one should be the uncoordinated metal site.

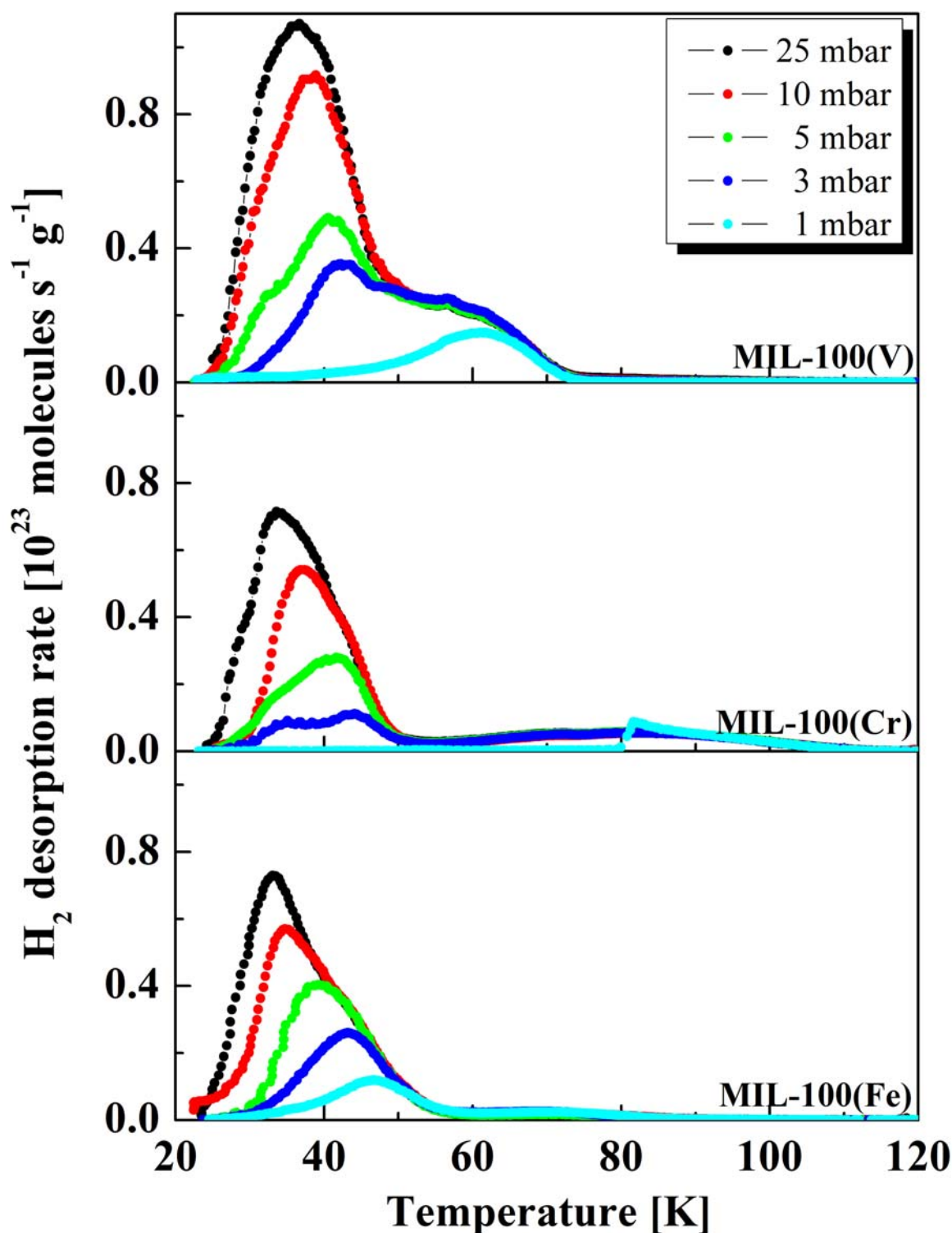


Fig. 6.11 A comparison of hydrogen thermal desorption spectra for MIL-100(V, -Cr, and -Fe), recorded for different initial gas loadings, and with the heating rate of 0.10 K s⁻¹.

In comparison, for the Cr compound the ratio is two sites per triplet of chromium. Indeed, the relative peak intensity for the MIL-100(V, and -Al) is low, while the number of accessible metal sites is close to 1 mmol g⁻¹. Slightly higher peak intensity for MIL-100(V), compared to MIL-100(Al), may be due to the partial filling of the second adsorption site. The Lewis acidity of Cr is

again higher than the one of Al, and, therefore, exhibits a maximum at higher temperature. Overall, the area under the high temperature peak for all four investigated samples is rather small, compared to the main desorption maxima. The biggest contribution is observed for the MIL-100(Cr, and -Fe), and corresponds to about 20% and 8%, respectively, of the total sorption capacity. Thus, the number of metal sites is relatively small, and they are quickly saturated. For higher gas loadings new desorption maxima appear (Fig. 6.11), while adsorption proceeds in the pore system (Chapter 5.3).

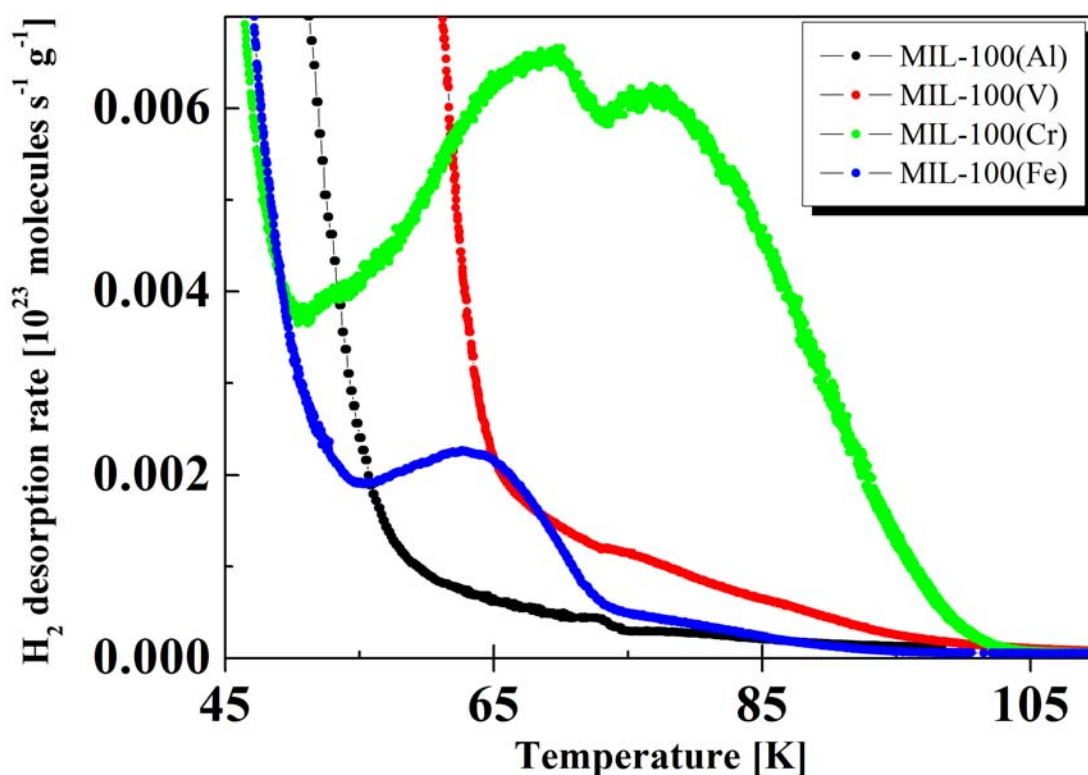


Fig. 6.12 A comparison of the hydrogen thermal desorption spectra for MIL-100(Al, -V, -Cr, and -Fe), presented in the limited temperature range, with the emphasis of the high desorption maxima. The spectra are recorded with the heating rate of 0.01 K s⁻¹.

A further comparison between the desorption behaviour of all four investigated samples is given in Fig. 6.13, which shows the relation between the hydrogen coverage, θ , and the desorption temperature, for measurements done with the heating rate of 0.01 K s⁻¹. It is assumed that for temperatures close to 20 K a complete coverage exists, i.e., $\theta_{max} = 1$. At temperatures below 40 K the desorption behaviour of hydrogen is similar for all four MIL-100 samples, while they all have the same pore system which gives rise to the desorption at low temperatures. The differences arise at temperatures above 40 K, when the coordinatively unsaturated metal sites induce a different

interaction with the hydrogen molecules. The strength of interaction proceeds from Cr^{3+} , over Fe^{3+} , and V^{3+} to Al^{3+} .

The theoretical studies based on DFT calculations by Sun et al. shown that the binding energy can be tuned from about 10 to 50 kJ mol^{-1} , by incorporating the transition metals into MOF frameworks [237].

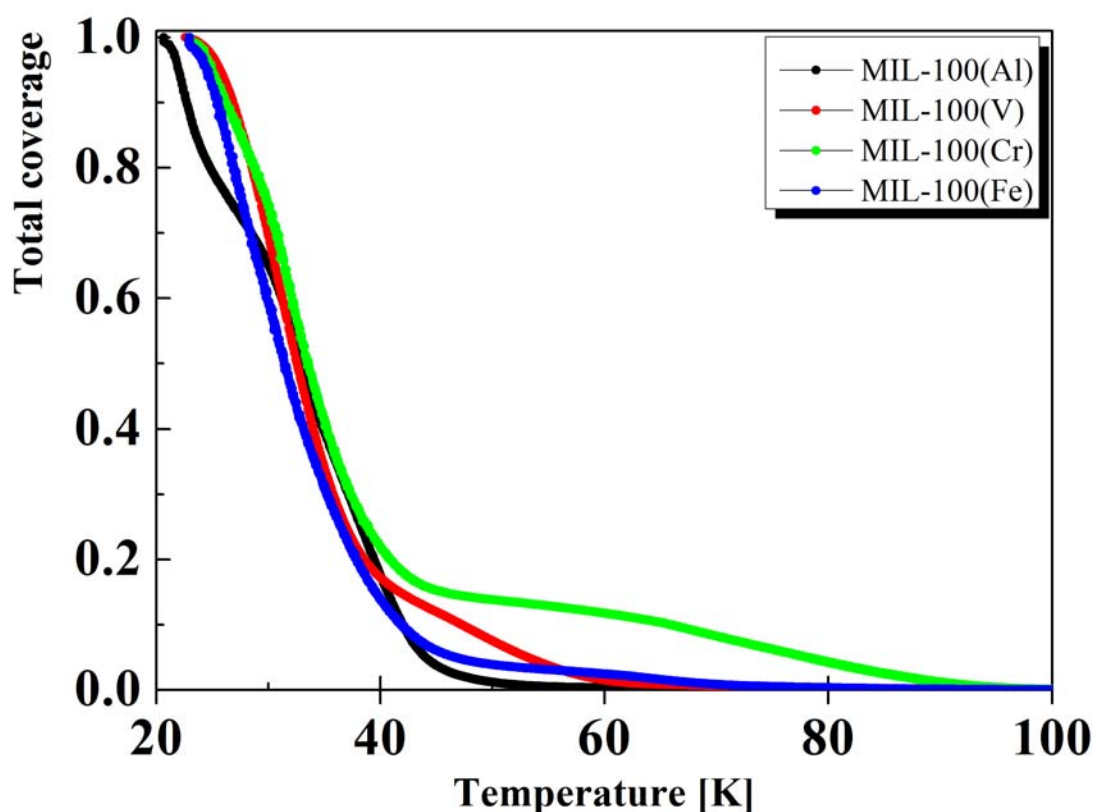


Fig. 6.12 Hydrogen total coverage vs. the desorption temperature for MIL-100(Al, -V, -Cr, and -Fe).

Although, the coordinatively unsaturated metal sites induce a strong interaction of hydrogen molecules with the MOF framework, their effect on the total hydrogen sorption capacity is limited due to the small number of metal sites which get saturated at low pressure, while at high pressure the surface area and the pore volume play the primary roles. The usage of light main group metal ions (Be^{2+} , Mg^{2+} , and Al^{3+}) was regarded as a good strategy for synthesis of the light weight materials with a high sorption capacity. Among the investigated MIL-100 samples the maximum storage capacity is calculated for MIL-100(Al), 2.85 wt.% H_2 . Of the few known magnesium frameworks, a H_2 uptake of 0.78 wt.% at 77 K and 1 bar was reported for $\text{Mg}_3(\text{NDC})_3$ [199]. Two other Mg-MOFs, investigated in this work (Chapter 5), showed a greater hydrogen capacity of 1.14 wt.% Mg-formate(1), and 1.92 wt.% Mg-formate(2). In principal, the introduction of heavy metals increases the weight of the host material, negatively affecting the gravimetric storage capacity. The

usage of the first row transition metals, V³⁺, Cr³⁺, and Fe³⁺ in MIL-100 samples investigated within this study, did not show the positive effect of increasing the overall hydrogen storage capacity.

Chapter 7

QUANTUM EFFECTS

The TDS measurements employed to investigate the physisorption phenomena on porous adsorbents comprised H₂, HD, and D₂ adsorption at 20 K, and subsequent measurements of gas desorption in the temperature range from 17 to 370 K, with the desorption mainly occurring in the temperature range from 17 to 120 K. Deuterium desorption measurements confirmed the desorption mechanism observed for hydrogen, and further enabled observation of quantum molecular effects by employing gas desorption measurements for the first time. The experimental observations are summarized in five salient points, discussed, and compared with the adsorption measurements and theoretical investigations published in the literature.

7.1 When an isotopic mixture (HD) is adsorbed on the surface, the heavier isotope (deuterium) is preferentially adsorbed, compared to lighter isotope (hydrogen).

Several experiments, done on different porous adsorbents, T3A (Fig. 4.8), MOF-177 (Fig. 5.29), Mg-formate(1) (Fig. E-1), Mg-formate(2) (Fig. E-2), MFU-4 (Fig. E-3), demonstrated that the heavier isotope is adsorbed to a greater extent, compared to the lighter one, when a H₂/D₂ gas mixture is used for adsorption/desorption measurements. The difference observed is related to the closer spacing of the discrete negative energy states and smaller zero-point energy of D₂ molecules compared to H₂ molecules, giving rise to significant differences in the adsorption characteristics (Chapter 2.4.1). The lower energies of quantum states of the heavier isotopologue in the adsorbed phase make its adsorption more favorable [239].

The separation of hydrogen isotopes by selective adsorption of heavier isotope on a solid has been observed in several experiments already, and reported in the literature. Basmadjian has reported an

experimental investigation where adsorption isotherms of hydrogen and deuterium have been measured at temperatures of 75 and 90 K on six different adsorbents: charcoal, silica gel, and Linde molecular sieves type 411, 5A, and 13X [240]. Binary adsorption isotherms were determined on the same adsorbents in the range 10–90% D₂ at temperatures of 75 and 90 K, and a total pressure of 1 and 0.267 bar. The analyses were performed by the thermal conductivity method using thermistor sensing elements in a static system at atmospheric pressure. Deuterium was found to be adsorbed to a greater extent than hydrogen in all cases investigated, and both gases yield type I adsorption isotherms. A little variation in the separation factors measured on chemically identical adsorbents of different origin has been found. Type 13X sieves with a nominal pore diameter of 13 Å give similar enrichment as type 4A, the pore size of which is close to the van der Waals diameter of hydrogen (2.4 Å). Furthermore, binary separation factors were found to be constant over the concentration range investigated due to differences in chemical composition of adsorbents rather than the pore size, surface area, or origin of the materials. It was concluded that the relatively high separation factors (particularly on type T4A molecular sieves) does not appear to be due to any screening effect of the pores, and that greater chemical heterogeneity tend to yield increased enrichment [240]. Further investigation of the fundamental factors which determine isotope separation factors on adsorbents, based on hydrogen and deuterium isotherms have been given by the same author [241]. Separation of isotopes by selective adsorption at low temperature has been theoretically predicted by Katorsji et al. [242]. Experimentally 16% difference in the amount of H₂ and D₂ taken up by the adsorbent (designated SU-60) at liquid oxygen temperature has been observed by Freeman [243]. Later-on, a theoretical treatment of experimental results of isotopic substitution in the adsorption of H₂, D₂, CH₄, and CD₄ on a graphitized carbon Black P33 has been made by Yaris [244]. A reasonable correspondence between experimental separation factors and heats of adsorption derived from chromatographic experiments, and those computed from the theory of adsorption of the isotopic hydrogen molecules were found in the work of Katorski et al. [245]. A comprehensive investigation has been made by Maienschei et al. [246] where selective isotope adsorption on a solid at 20 K, observed for several solids published in the literature, has been used to construct adsorption isotherms, calculate separation factors, and develop a computational model to calculate column operation. Model results show that column diameter and length, particle diameter, choice of the solid, and the fractional void space of the packed solid are all key parameters which determine the total purification capacity of a column. Furthermore, measurements have been made both with chromatographic separation and with equilibration of pure hydrogen isotope mixtures. Separation factors for hydrogen isotopes on zeolites 4A, 5A, 13X, and on alumina showed that zeolite 4A has the highest separation factors, zeolites 5A, and 13X are about the same

but lower, and alumina has the lowest separation capability at 77 K. From the isotherm and separation factor data zeolite 13X was shown to be the optimal adsorbent which has the highest adsorption capacity, while zeolite 4A has the highest estimated separation factor [246].

In the gas phase, both H₂ and D₂ have the bond lengths of 0.7416 Å [247], thus, separation on the basis of size alone is not possible. However, the different zero-point energies give rise to differences in the vibrational and the rotational frequencies of the molecules, which depend on the reduced mass and on the moments of inertia, respectively. All kind of mass effects, like zero-point energy effects and tunneling, are highly expressed for hydrogen isotopes, in particular for muonium (Mu), an elementary particle with a mass of approximately 1/9th the proton mass [248]. The difference in physical properties of hydrogen and deuterium may be illustrated by the melting points and boiling points of hydrogen, deuterium, and hydrogen deuteride (Appendix F). Owing to their relative mass differences, physical properties which depend on the mass are expected to exhibit large isotope effects.

The origin of the differences between H- and D-atoms lies in their nuclei, which is a single proton for the H-atom, and a proton plus a neutron for the D-atom. The neutron has the same weight as the proton, but has no electric charge. This has several consequences. First, the two nuclei have accordingly a different mass: the mass of the deuteron is twice that of the proton. Second, the spin of the deuteron made of two particles, a neutron and a proton that have each a spin 1/2, has a spin 1, different from the spin 1/2 of a proton. Conversely, the electric charge of a deuteron is identical to that of the proton, which implies that the electronic structure of the D-atom, sensitive to the charge of the D-nucleus but not to its spin, is identical to that of the H-atom. This further implies that the chemical properties of hydrogen and deuterium, and the corresponding compounds of hydrogen and deuterium are qualitatively the same, while the electronic structure of a D-bond is identical to the electronic structure of its equivalent H-bond, though quantitatively there are marked differences.

Due to the fact that nucleons of H₂ (and D₂) are identical, special symmetry restrictions are placed upon the wave functions. The molecular wave function for any isolated homonuclear diatomic molecule must be symmetric or antisymmetric under nuclear exchange. A hydrogen molecule is a homonuclear diatomic molecule composed of two indistinguishable fermions. As such, the total wave function must be antisymmetric upon exchange of the nuclei, which leads to two distinct types of hydrogen: *ortho* and *para*, with a total spin of 1 and 0. With *ortho*-hydrogen (parallel proton spins, nuclear spin degeneracy 3, odd rotational quantum number J) or with *para*-hydrogen (proton spins antiparallel, spin multiplicity 1, even rotational quantum number J) different rotational energy levels are populated. With D₂, on the other hand, the total wave function must be symmetric, because the deuterons have spin 1 and are bosons, where *ortho*-D₂ has even and *para*-D₂ odd J

numbers. For the HD molecule the nuclei are not identical, and the above explained degeneracy is removed, with the consequence that no *ortho*- and *para*-HD modifications are distinguishable.

Ordinarily, transitions between *ortho* and *para* levels are relatively rare, so that the gas can be considered as a mixture of two distinct components. The high temperature equilibrium mixture of the two forms is called the normal mixture, and the more abundant component of the normal mixture is called the *ortho* component. The equilibrium *ortho*-hydrogen concentration is easily calculated by using the rotational energy of a diatomic simple rotator $E_{\text{rot}} = BJ(J + 1)$, where $B = 59.3 \text{ cm}^{-1}$ is the rotational constant for hydrogen, and assuming a Boltzmann distribution. In thermal equilibrium (at temperatures $> 100 \text{ K}$) the ratio *o*-H₂:*p*-H₂ is 3 (75% *ortho*-hydrogen and 25% *para*-hydrogen). As the temperature decreases, however, the ratio of *para*-hydrogen increases to the point where at liquid hydrogen level ($T = 20.27 \text{ K}$) the percentage of *para*-hydrogen reaches almost 100% (as *para*-hydrogen is energetically more favorable).

While *ortho-para* conversion is strictly forbidden for isolated molecules, conversion does occur in the solid. The theory of *ortho-para* conversion in solid hydrogen has been treated for the first time by Motizuki and Nagamiya [249]. Conversion of an *ortho*-molecule into a *para*-molecule requires a simultaneous change of angular momentum and a nuclear spin flip, i.e., the rotational state of this molecule changes between triplet and singlet states (from $J = 1$ to $J = 0$), and the difference of the energies of these states must be taken up by the lattice vibrations. The interaction comprises nuclear spin transition, which requires a magnetic field gradient. The perturbation that causes the transition arises from interaction of the magnetic moments of the nuclei of an *ortho*-molecule with the inhomogeneous magnetic field. This field can arise both from the interaction between the nuclear spin magnetic moment of one molecule, and due to the rotational and spin magnetic moments of its neighbours. After the temperature variation of the sample, the *ortho-para* conversion starts, until thermodynamic equilibrium is reached again. At ambient pressure *ortho-para* conversion in the solid is very slow, taking weeks for a sample to equilibrate [250]. Natural *ortho-para* conversion rates in H₂, in a wide range of fluid states: in the liquid at temperatures 17–32 K and pressures up to 500 bar, and in the gas at temperatures 40–120 K and pressures from 20 to 700 bar, have been measured by Milenko et al. [251]. It has been found that the interconversion of *ortho*-H₂ to the more stable *para* form is very slow even in the liquid state. A small inter-conversion rate constant of $1.9\% \text{ h}^{-1}$ is observed at low temperature [250], while faster interconversion can be promoted by spin catalytic conversion of one species into the other [252]. The rate of conversion is enhanced by introducing paramagnetic ions or molecules. *Ortho*-molecules in the neighborhood of an oxygen molecule will change to *para* in a short time, so that the initial increase of *para*-concentration will be great [249].

At high temperatures normal deuterium consists of 2/3 *ortho*-D₂ and 1/3 *para*-D₂ (*o*-D₂:*p*-D₂ = 2), and at low temperatures, opposite to H₂, *ortho*-D₂ represents the more stable species. In D₂ the change of rotational energy is going from the $J = 1$ to the $J = 0$ state, thus, conversion is more difficult and 32 times slower compared to H₂ [250], which explains why earlier investigations reported 100% *para*-H₂ but only 97% *ortho*-D₂ ($J = 0$) [253, 254]. The small rate of self conversion of D₂, compared to H₂, is the result of the smaller magnetic moment of the deuteron compared to the proton (the ratio of nuclear magnetic moments D/H is 0.26).

The difference in the ground-state energies of *ortho*- and *para*-H₂ contribute significantly to the selectivity of *ortho/para*-H₂ adsorption. The investigation performed by Sandler has shown that *ortho*-H₂ is more strongly adsorbed than *para*-H₂ when physically adsorbed on TiO₂ or charcoals. A separation factor of about 1.6 is observed with TiO₂ at 90 K [255]. A theoretical investigation by White et al. predicts that *ortho*-H₂ is more strongly adsorbed than *para*-H₂ at all barrier heights, and that *para*-D₂ is more strongly adsorbed than *ortho*-D₂ [256].

The differences in physical and chemical properties of hydrogen isotopes are greater than in the case of other isotopes, and enable their separation by adsorption. The hydrogen molecule and its isotopes, confined in a very narrow space, can be no longer treated as classical particles, as quantum effects are significant and lead to the equilibrium *quantum molecular sieving*, the effect first theoretically proposed by Beenakker *et al.* [257, 258], while investigating quantum effects for adsorption of hard-sphere molecule (with a hard-core diameter σ) in a cylindrical pores (with a pore diameter d). The authors proposed that when the molecule is restricted in its transverse motion in a space given by $d-\sigma$, which is a small quantity comparable to the de Broglie wavelength λ ($\lambda = h/mv_r$, where h is Planck's constant, m is mass, and v_r is the radial velocity), both the zero-point energy, E_0 , and the separation of discrete negative energy states (E_1-E_0 , where E_1 is the first excited energy level) turn out to be greater for the lighter isotope. With decreasing d and m , E_0 increases, thus, in the narrow channels quantization of the transverse motion for lighter isotope cannot be neglected. There are two parameters characterizing the quantum effects: (1) the excitation energy for the first excited energy level, compared to the thermal energy of the molecule $(E_1-E_0)/k_B T$, where k_B is the Boltzmann constant, and T is the absolute temperature, and (2) the relative importance of the zero-point energy with respect to the potential energy, originating from the molecule-wall interaction, E_0/ϵ .

The separation of isotopes in nanopores, by the preferential adsorption of the heavier isotope from an isotopic mixture, was named *quantum molecular sieving* because the separation is caused by the differences in the quantum energy levels of the isotopes being separated. This aspect is illustrated in Fig. 7.1, where the well depth is sketched as a function of the pore diameter, d . Even before the pore

diameter becomes comparable to the size of adsorbate molecule ($d = \sigma$), the binding energy, ε , becomes negative, and the process of molecule entrance into the pore becomes a thermally activated process.

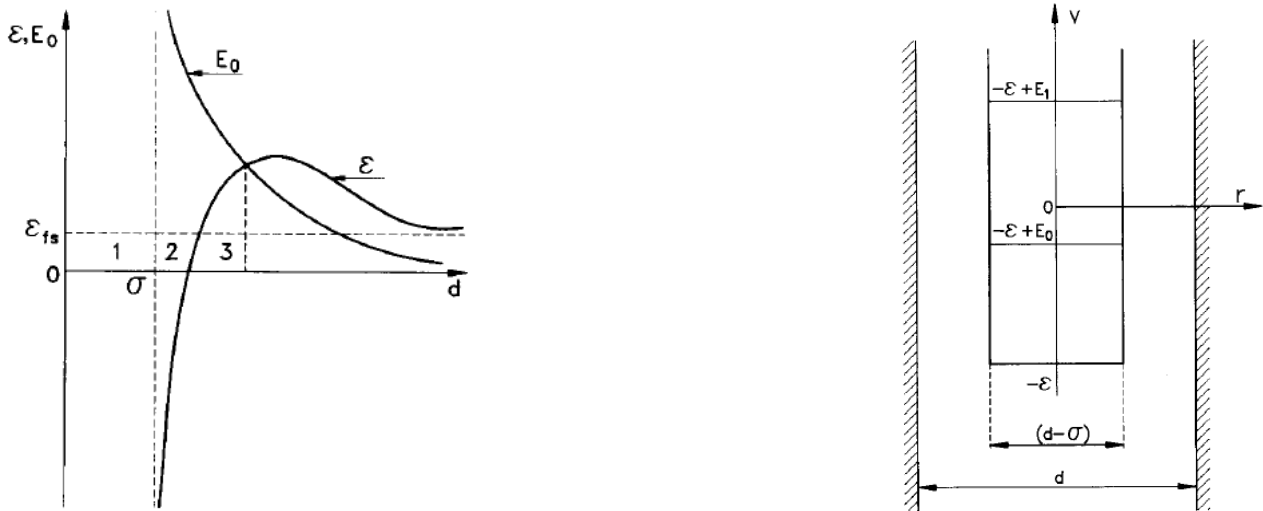


Fig. 7.1 The behaviour of the well depth, ε , and zero-point energy, E_0 , as a function of the channel diameter, d , (qualitative picture). Regions (1), (2), and (3) can be attributed to classical geometrical, potential, and quantum sieving, respectively.

Fig. 7.2 Potential energy, V , and transverse motion energy levels, E_i , for a molecule in a channel with $(d - \sigma) \sim \lambda$ (qualitative picture). Zero energy corresponds to that of the molecule in the free space. Representations are taken from the ref. [258].

While decreasing the pore diameter, d , further, the repulsive forces give an opposite contribution which finally prevails. With decreasing d and m , the level splitting in the well occurs, $(E_1 - E_0)/kT \gg 1$, and becomes so large that the first and the upper excited levels are not populated, and all particles in the pore are in the ground state. The system will behave as 1D gas, where two degrees of freedom are frozen and only one – the axial translational motion – remains. In the case when $E_0 > V$, Fig. 7.2, the zero-point motion overcompensates the attraction of the pore walls (the molecule-surface interaction), and the binding energy ($V - E_0$) of the molecule in the pores become negative. This implies a further effect on the molecular transport while the molecule faces an energy barrier at the pore entrance that can be overcome *via* thermal activation or by *quantum tunneling* (discussed in the last segment of this chapter).

Several subsequent investigations have confirmed and elaborated quantum effects in greater detail, and further extended these ideas using more realistic models to treat the effects of confinement. The theoretical basis for the phenomenon of quantum sieving, detailed for confined 1D systems, was given by Johnson and co-workers, which used analytical methods in conjunction with theory and

GCMC simulations to calculate zero–pressure selectivities due to quantum sieving inside the Carbon Nanotubes (CNTs) and their interstitial channels [259 – 263]. A low pressure binary mixture, composed of the same binary components, in equilibrium with an adsorbed phase has been considered. If the adsorbent has unidimensional micropores, on the order of the size of the adsorbate molecules, then the adsorbate molecules will act as a 1D gas, with unhindered translational motion of adsorbed particles along the axial direction (regarding the low density of adsorbate in the pore). However, across the pore, adsorbate molecules are strongly localized by the pore wall and, therefore, the transverse (radial) degrees of freedom are quantized.

At low temperatures adsorbate molecules will reside mostly in their ground states, thus, the chemical potential of the adsorbed species can be expressed in terms of the ground–state energy of its transverse wave function, Eq. (7.1):

$$\mu_i^{ads} = E_i + k_B T \ln \left(\frac{\rho_i \lambda_i}{q_i} \right) \quad (7.1)$$

where E_i is the transverse ground state energy of species i , ρ_i is the number density of component i in the pore, λ_i is the de Broglie thermal wavelength, q^i is the internal partition function, k_B is the Boltzmann constant, and T is the absolute temperature. The uncertainty in the location of the transferred particle may be estimated from the particle's de Broglie wavelength, Eq. (7.2):

$$\lambda_i = \frac{h}{\sqrt{2m_i E}} \quad (7.2)$$

where m_i is the mass of the particle i , and E is its energy. This wavelength for a hydrogen with an energy of 10 kJ mol^{-1} is thereby calculated to be 0.5 \AA for ^1H (protium, H), 0.31 \AA for ^2H (deuterium, D), and 0.25 \AA for ^3H (tritium, T).

The bulk gas is considered to be in an ideal state at very low pressure, thus, the chemical potential of the gas phase, μ_i^{gas} , is given by Eq. (7.3):

$$\mu_i^{gas} = k_B T \ln \left(\frac{n_i \lambda_i^3}{q_i} \right) \quad (7.3)$$

where n_i is the gas phase density of the component i . At equilibrium conditions the chemical potential of the adsorbed species can be equated to the chemical potential of the gas component, $\mu_i^{ads} = \mu_i^{gas}$. Thus, assuming that q_i is the same in the gas phase and in the adsorbed phase, the adsorbate density is given by Eq. (7.4):

$$\rho_i = n_i \lambda_i^2 e^{-\frac{E_i}{k_B T}} \quad (7.4)$$

By equating the chemical potentials of adsorbate molecule and that in the gas phase, the selectivity can be defined. When the coadsorption of two distinct species occurs (e.g. a mixture of hydrogen isotopes), the component which is preferentially adsorbed will lead to enrichment in the adsorbed phase, and depletion in the gaseous phase. For a binary gas mixture in static equilibrium with an adsorbent, the separation factor for the component 1 over 2 is defined by Eq. (7.5):

$$S = \frac{x_1 / x_2}{y_1 / y_2} \quad (7.5)$$

where x_i and y_i are the isotopic concentrations of species 1 and 2 , and refer to the mole fractions in the gas-phase, x , and in the adsorbed-phase, y . The value of the separation factor indicates the degree of separation, with a higher value giving rise to a greater separation of two components.

In the limit of zero pressure, when the adsorbate-adsorbent interactions can be neglected, the selectivity (S_0) depends only on the energy levels of the adsorbed molecules, and not on the gas phase composition, Eq. (7.6):

$$S_0 = \frac{(\rho_1 / \rho_2)}{(n_1 / n_2)} = \frac{m_2}{m_1} \exp \left[-\frac{E_1 - E_2}{k_B T} \right] \quad (7.6)$$

where m_i is the molecular mass of the component i . The Eq. (7.6) is only valid at extremely low temperatures and pressures when all molecules are in their ground state.

In case of a cylindrical pore where the adsorbate-pore potential is well approximated by a 2D radially symmetric harmonic potential, $V(r) = kr^2/2$, the ground-state energy for isotopes of mass m_1 and m_2 are given by Eq. (7.7):

$$E_i = \hbar \sqrt{\frac{k}{m_i}} \quad (7.7)$$

Since two isotopes of the adsorbed species with mass m_1 and m_2 are subject to the same potential, the low-pressure selectivity of component 2 over component 1 is given by Eq. (7.8):

$$S_0 = \frac{m_2}{m_1} \exp \left[-\frac{\hbar \sqrt{k}}{k_B T} \left(\frac{1}{\sqrt{m_1}} - \frac{1}{\sqrt{m_2}} \right) \right] \quad (7.8)$$

In the case of isotopic mixtures, both isotopes (having equal values of σ , but different m) are the subject to the same adsorption potential, so the preferential adsorption of the heavier isotope is

purely due to dependence of the zero-point energy, E_0 , on m . For a proton and deuteron ($m_p = 1.6726 \cdot 10^{-27}$ kg, $m_d = 3.3436 \cdot 10^{-27}$ kg), confined in a 1D square well the size of an atom ($a = 10^{-10}$ m), the zero-point energy amounts to 20.4 meV and 10.23 meV, respectively (Chapter 2.4.1, Eq. (2.26)). That is, if $m_1 < m_2$, then $S_0 > 1$ at low temperatures, thus, the pores selectively adsorb the heavier isotope over the lighter one.

When gas containing two isotopes of hydrogen is equilibrated with an adsorbent, the adsorbed phase is enriched in the preferentially adsorbed isotope, and the gas phase is, therefore, enriched in the lighter isotope [246]. If the enriched gas is then equilibrated with fresh adsorbent, further enrichment takes place, and the preferentially adsorbed isotope is gradually removed. The selectivities observed for adsorption of hydrogen isotopes on common sorbents such as activated carbons, zeolites, and alumina are typically in the range of 1.1–3 [261].

In contrast, theoretical and simulation studies showed that various Carbon nanotubes and interstices of nanotubes act as highly effective quantum sieves for hydrogen isotopes and show a strong preference for adsorption of the heavier isotope (T_2), compared to the lighter isotope (H_2), in the limit of zero pressures. Certain nanotubes show selectivities on the order of 100 000 for T_2 over H_2 at 20 K, and the selectivity of this process increases dramatically as the nanotube diameter is reduced [259].

Using the rigorous analytical calculations of quantum sieving, carbon nanotubes of various sizes and helicities have been investigated for their ability to separate light-isotope mixtures of H_2 – T_2 , H_2 –HD, ^3He – ^4He , and CH_4 – CD_4 [260]. Adsorption isotherms of mixtures of H_2 – T_2 and H_2 – D_2 in nanotubes and interstices at 20 and 77 K, calculated by the modified Path Integral Grand Canonical Monte Carlo (PI-GCMC) simulations, showed that the D_2/H_2 selectivity is almost 20 times lower than the T_2/H_2 selectivity, and that the selectivity increases with pressure until the nanotube is saturated [261].

PI-GCMC simulations used to investigate the separation of H_2 and HD, as well as H_2 and D_2 , in slit-like carbon nanoporous materials of various sizes showed, as expected, that the selectivity of HD over H_2 is lower than that of D_2 over H_2 at the same conditions, due to the smaller mass of HD molecules, and, hence, larger quantum effects. The calculations show that lower temperatures and narrow pore sizes, with the optimal pore widths of 0.56 and 0.57 nm for HD/ H_2 separations, are favorable to high selectivities. A comparison of simulation results, based on ideal adsorption solution theory (IAST), an approximate method that predicts multicomponent adsorption from single component isotherms, shows good agreement with the adsorption isotherms of binary mixtures of HD/ H_2 and D_2/H_2 at all investigated temperatures and pressures [264].

When the excited states are also populated the chemical potential of the adsorbed component is given by Eq. (7.9):

$$\mu_i^{ads} = -k_B T \ln \left(\sum_l e^{-\frac{E_l^i}{k_B T}} \right) + k_B T \ln \left(\frac{\rho_i \lambda_i}{q_i} \right) \quad (7.9)$$

where E_l is the l^{th} energy level for the quantized transverse motion. The Eq. (7.9) reduces to Eq. (7.1) when only the ground state is populated. Considering the population of excited states, Eq. (7.9) is combined with Eq. (7.3) to give the selectivity S_0 , Eq. (7.10):

$$S_0 = \frac{m_2}{m_1} \exp \left[\frac{\sum_l \exp \left(-\frac{E_l^1}{k_B T} \right)}{\sum_l \exp \left(-\frac{E_l^2}{k_B T} \right)} \right] \quad (7.10)$$

The contribution from excited states becomes more important as the temperature increases. However, the quantum sieving effects decrease rapidly with the temperature increase.

Additional contributions to the selectivity arise when the rotational degrees of freedom of the adsorbed isotopomers are affected by the confinement in a nanotube. The rotational eigenvalues of isotopically substituted hydrogen molecules adsorbed into single-walled CNs, calculated using a semiclassical method in the work of Hathorn et al. [265], indicated that rotational effects enhance the overall selectivity of the heavier isotope confined in CNTs. Assuming that translational and rotational degrees of freedom are uncoupled (which is an excellent approximation for H_2 in the gas, liquid, and even low-pressure solid phases [262]), their findings imply that taking rotations into account would increase the total selectivity by a factor of the order of 100, over the translational selectivity in CNTs with diameters of 8 Å or less at 20 K. Thus, in addition to the radial confinement, the hindered molecular rotation of molecules confined in CNTs ought to contribute to quantum sieving. The effects of including both translation and rotation are discussed in more details in the publication by Lu et al. [266, 267].

Theoretical calculations by Garberoglio et al. [262], using a simple approximate theory for several different potential models, showed that the rotational degrees of freedom have a significant effect on the overall selectivity in CNTs, while the contribution of the rotational states of the adsorbed species to the overall selectivity is less and less important as the geometrical tube radius grows. The quantum states of molecular hydrogen isotopes, confined in carbon slit pores of varying width, showed that the role of the rotational degrees of freedom is far from negligible, resulting in values of the isotopic separation 8 to 50 times higher than those calculated using spherically symmetric

models for the hydrogen molecule [268]. The expected selectivity depends on the temperature and the dimension of the pores, which is in qualitative agreement with the results already known for carbon nanotubes [266]. The effect of the quantized rotational degrees of freedom of *para*-T₂/*para*-H₂ selectivity in various carbon nanotubes at 20 K, studied using computer simulations, showed that the quantized nature of rotational degrees of freedom dramatically affect adsorption and selectivity for hydrogen isotopes adsorbed in very narrow nanotubes. The isotopic selectivity is found to increase with pressure, tending to a constant value at saturation [263].

The effects of vibrational motions of solid atoms around their mean positions are commonly neglected, regarding the low temperatures at which the simulations are conducted (30–160 K).

Several publications pointed out the importance of the topology and the pore size for efficient quantum sieving of hydrogen isotopes. The smaller the pore size, the larger is quantum effect on adsorption of hydrogen isotopes, which is why the reduction in the pore size increases the D₂/H₂ equilibrium separation factor. Theoretical investigation by Challa et al. showed that very large potential gradients can be realized in carbon pores with a diameter below 7 Å [260]. For tubes with diameters greater than 7 Å molecules preferentially adsorb near the pore walls, rather than in the pore center, leading to the type of 1D quantum confinement. Adsorption isotherms of hydrogen isotopes obtained by molecular simulations in CNTs showed that the selectivity due to quantum sieving is a strong function of the pore diameter. Differences in zero-point energies of adsorbed species are more pronounced when molecules are confined in narrow pores, comparable in size to the size of adsorbate molecule [261, 264].

Theoretical investigation by Lu et al. showed that smaller tubes bind hydrogen more strongly than the larger ones. The low-pressure quantum sieving selectivity factors, S_0 , was found to be primarily a function of the nanotube diameter and not its shape. S_0 decreases with the tube diameter until the transition between 1D and 2D confinement is reached, after which it increases significantly [266].

The quasi-1D cylindrical pores of single-walled boron nitride (BNs) and CNTs have been shown to efficiently differentiate adsorbed hydrogen isotopes at 33 K. Extensive PI-GCMC simulations revealed that the mechanisms of quantum sieving for both types of nanotubes are quantitatively similar. The variation of the D₂/H₂ equilibrium selectivity upon the pore filling consists of three stages. At the first stage (i.e. in the Henry's region) the equilibrium selectivity of D₂ over H₂ is constant, and its value is governed by the difference between the enthalpy of hydrogen and deuterium adsorption. At the second stage the D₂/H₂ equilibrium selectivity drops to the minimum value. The position and the value of the minimal D₂/H₂ equilibrium selectivity are strongly related to the nanotube pore diameter. Finally, after the initial drop to the minimum, further increase of the D₂/H₂ equilibrium selectivity has been predicted. However, both calculations at zero coverage, as

well as at finite pressures revealed that BNs are more efficient for separation of hydrogen isotopes under the assumed thermodynamics equilibrium. The stronger and heterogeneous external solid–fluid potential, generated from single–walled BNs, enhanced the selectivity of deuterium over hydrogen, both at zero coverage and at finite pressures. This enhancement of the D_2/H_2 equilibrium selectivity results from larger localization of hydrogen isotopes in the interior space of single–walled BNs, in comparison to that of equivalent single–walled CNs. Thus, the operating pressures for efficient quantum sieving of hydrogen isotopes are strongly dependent on both the type, as well as the size of the nanotube [269].

The square–shaped carbon pores enhance the selectivity of deuterium over hydrogen in comparison to equivalent slit–shaped carbon pores at zero coverage, as well as at finite pressures (i.e. quantum sieving of hydrogen isotopes is pore–topology–dependent). The enhancement of the D_2/H_2 equilibrium selectivity results from larger localization of hydrogen isotopes in square–shaped pores in comparison to equivalent slit–shaped carbon pores [270].

7.2 For all investigated samples the total amount of D_2 desorbed exceeds that of H_2 . The difference in the total storage capacity between hydrogen and deuterium increases for higher pressure loadings.

For the three investigated CMS samples, the total amount of deuterium desorbed exceeds that of hydrogen, especially for higher gas loadings (500 and 700 mbar). For T3A a comparison can be made for 50 mbar gas loading and higher (Table A–3 and –4), where a slightly higher amount of deuterium was desorbed. For the sample loaded at 50 mbar the total amount of deuterium desorbed exceeds that of hydrogen by 25%, and for the sample loaded at 700 mbar the total amount of deuterium desorbed exceeds that of hydrogen by 38%. The difference in the amount of gas desorbed tends to increase upon increasing the pressure.

For the T4A loaded at pressures in the range of 1 to 5 mbar the total amount of hydrogen and deuterium desorbed is comparable. However, already for 15 mbar gas loading a considerable difference is observed, and expresses the maximum for 700 mbar gas loading, when the total amount of deuterium desorbed exceeds that of hydrogen by 32%. For the T5A loaded at 25 mbar the total amount of deuterium desorbed exceeds that of hydrogen by 28%.

The same trend as for carbon samples is commonly observed for MOF samples. For Cu–BTC a comparison can be made for the sample loaded at 25 mbar, where, under the same experimental condition, the total amount of hydrogen and deuterium desorbed corresponds to 117 and 197 molecules per unit cell (Chapter 5.2.1 and –5.3). For Fe–BTC, however, such a difference has not

been observed (Table B-2), while the total amount of hydrogen desorbed exceeds that of deuterium for all measurements done in the pressure range from 1 to 700 mbar.

A common trend is again observed for Mg-formate(1) where the total amount of deuterium desorbed exceeds that of hydrogen, Table B-3. In particular, for the sample loaded at 1 to 7 mbar the total amount of hydrogen and deuterium desorbed are comparable. However, in the range of 10 to 700 mbar the total amount of deuterium desorbed exceeds that of hydrogen. For the sample loaded at 700 mbar the total amount of deuterium desorbed is 16% higher than that of hydrogen. As expected, the difference in the total amount of hydrogen and deuterium desorbed is more pronounced for Mg-formate(2), the sample isostructural to Mg-formate(1), but comprising a bigger pore volume (Chapter 5.1). Already, for the sample loaded at 1 mbar the total amount of deuterium desorbed exceeds that of hydrogen by 50%. The difference is not that pronounced for the sample loaded at 700 mbar, where the total amount of deuterium desorbed exceeds that of hydrogen by 10%, Table B-4.

For MOF-177 a comparison can be made for the sample loaded at 25 and 700 mbar. A slightly higher amount of deuterium desorbed was observed for both measurements, Table B-6.

Both for MFU-4 and MFU-4l the total amount of deuterium desorbed exceeds that of hydrogen only slightly, Table B-6 and -7. In the case of MFU-4, for all pressures applied, the total amount of hydrogen and deuterium desorbed might be regarded as comparable. As for Mg-formate(1) and Mg-formate(2) a greater difference is observed within the sample with a greater pore volume, i.e., MFU-4l, especially for the sample loaded at 700 mbar where the total amount of deuterium desorbed exceeds that of hydrogen by 14%.

For the samples from MIL-100 series a direct comparison can be made for MIL-100(V, -Cr, and -Fe), Table B-9 and -10. The greatest difference in the total amount of hydrogen and deuterium desorbed is observed for MIL-100(Cr). For the sample loaded at 25 mbar the total amount of deuterium desorbed exceeds that of hydrogen by 25%. In the case of MIL-100(V) this difference is smaller, and corresponds to 16%.

For MIL-100(Fe) a common trend of a greater amount of deuterium desorbed is not observed, as for Fe-BTC. Both samples have the polymodal pore size distribution and two pores of comparable size, Table 5.1. The bimodal pore size distribution is reported for the other samples from the MIL-100 series and Cu-BTC (Chapter 5.1) where the opposite trend is found, and the total amount of deuterium desorbed exceeds that of hydrogen. On the other hand, both Fe-BTC and MIL-100(Fe) are synthesized using Fe^{3+} as a metal center, which is a core point that differentiates those two samples from all the others.

A greater amount of deuterium desorbed, as commonly observed, might be explained if the de Broglie wavelength is regarded as a measure of a molecular diameter. The hydrogen molecules occupy more volume than the deuterium molecules, regarding their larger wavelength, Eq. (7.2). Consequently, fewer H₂ than D₂ molecules are adsorbed at saturation in the pore or interstice, and a lower saturation density is reached.

A quantum sieving effect, based on the equilibrium adsorption, and larger amount of D₂ adsorbed, compared to H₂, has been observed for activated carbon fibers (ACFs) and their fluorides at 20 K within both cylindrical pores and slit pores, where the quantum confinement of the adsorbate is 2D and 1D, respectively [271]. The D₂/H₂ selectivity of ACFs, evaluated by ideal adsorption solution theory, was larger than that of the fluorinated ACFs.

The GCMC simulations of hydrogen and deuterium adsorption in the zeolite Rho, having the narrow 0.543 nm pore opening, showed that heavier deuterium is adsorbed more strongly than lighter hydrogen in the temperature range studied [272]. The higher amount of D₂ adsorbed, compared to H₂, was experimentally observed within gravimetric adsorption studies for mixed-MOF Zn₃(BDC)₃[Cu(Pyen)] (DMF)₅(H₂O)₅ [184], which was attributed to the higher molar density of liquid D₂ (41.9 mol L⁻¹ at 22.24 K) than H₂ (35.12 mol L⁻¹ at 20.2 K).

7.3 The activation energy of deuterium desorption is greater than the activation energy of hydrogen desorption in the temperature range studied, as concluded from the position of the corresponding desorption maxima.

For CMS samples the desorption maxima appear at higher temperature for deuterium than for hydrogen desorption, Chapter 4.4.3. The same trend is observed for MOF samples, Chapter 5.2.1. The temperature at which the maximum occurs is directly proportional to the activation energy for desorption (Eq. (2.20), Chapter 2.2), which is why the greater activation energy for deuterium desorption is expected due to the difference in the zero-point energy.

A given set of experimental conditions, in particular the adsorbate used and the pressure applied, mainly determine the interaction potential. In the case of a pure diatomic gas the intermolecular interactions (attractive and repulsive) with other gas molecules perturb the intramolecular potential, thus, affecting the stretching frequency of the molecule. Intermolecular forces of hydrogen and deuterium differ because the mean internuclear separations of H₂ and D₂ molecules are different (Table F-1), as a result of the different zero-point vibrations of their nuclei.

7.4 There is a greater shift in the position of the desorption maxima toward lower temperatures for D₂ than for H₂ desorption, upon increasing the surface coverage.

The multiple TDS spectra recorded for different surface coverages enabled the possible shift in the peak maxima to be observed. For the CMS T4A loaded at 1 mbar the hydrogen high temperature maximum, centered at 70 K, shows a shift in the position toward lower temperature, and it is centered at 66 K for the sample loaded at 700 mbar. In the case of deuterium desorption a shift from 75 to 65 K, for the sample loaded at the same pressure is observed, Fig. 4.9.

For the T5A the position of the hydrogen high temperature maximum shifts from 66 to 47 K, for the sample loaded at 1 and 25 mbar, respectively. For the deuterium desorption the corresponding maximum shifts from 70 to 51 K, Fig. 4.11.

The high temperature maximum for T3A is an exception of this trend, for the reasons explained within the point 5 of this Chapter.

Regarding the MOF samples a direct comparison can be made for the Fe–BTC where the hydrogen high temperature maximum shifts from 47 to 42 K for the sample loaded at 1 and 5 mbar, respectively, while for deuterium the shift from 55 to 44 K is observed, Fig. 5.19.

For Mg–formate(1) the main hydrogen desorption maximum observed at 51 K does not show a shift upon partial sample loading, while for deuterium desorption the position of the corresponding maximum is shifted from 56 to 51 K for the sample loaded at 1 and 700 mbar, respectively, Fig. 5.21. For Mg–formate(2) the main hydrogen desorption maximum is shifted from 55 to 51 K for the sample loaded at 1 and 700 mbar, respectively, while for deuterium desorption the corresponding maximum is centered at 57 and 54 K, respectively, Fig. 5.24.

For MFU–4 there is no shift in the position of the main desorption maximum upon partial sample loading, Fig. 5.31. For MFU–4l the hydrogen desorption maximum centered at 33 K (for the sample loaded at 5 mbar) is shifted to 32 K (for the sample loaded at 10 mbar). A shift from 36 to 35 K is observed for deuterium desorption under the same experimental conditions, Fig. 5.33. In principle, for the MFU–4l a greater number of measurements was done, and a comparison could be made for higher pressure loadings. However, the peak gets rather broad and it is difficult to read the position of the maximum.

For the samples from the MIL–100 series the peak position is particularly well defined for MIL–100(Cr, and –Fe), and will be used for a comparison. While increasing the pressure in the range of 1 to 25 mbar the peak position shifts from 44 to 34 K for hydrogen, and from 47 to 34 K for deuterium, for the MIL–100(Cr), Fig. 5.41. For the MIL–100(Fe) the hydrogen peak position shifts from 47 to 33 K, while the deuterium peak position is shifted from 54 to 33 K, for the sample loaded at 1 and 25 mbar, respectively, Fig. 5.43.

The variation in the desorption temperature for a particular adsorbate, while changing the surface coverage, is commonly assigned to the surface heterogeneity, where favorable adsorption sites are occupied primarily, following adsorption at the less favorable adsorption sites. Commonly, the highest adsorption energies are obtained at small adsorbate coverages where adsorbate–adsorbent interactions have the dominant role. For increased surface coverage a shift in the position of the desorption maxima toward lower temperatures is observed (Chapter 5.2.2), while the lateral interactions of molecules in the adsorbed layer (adsorbate–adsorbate interactions) are pronounced, and the desorption spectra are shifted toward lower temperature for increased gas loadings. From the TDS spectra a greater shift of the desorption maxima was observed toward lower temperature for D₂ than for H₂, since D₂–D₂ repulsive interactions are weaker than H₂–H₂ interaction.

Early investigations published in the literature gave experimental verification of these predictions. Studies of H₂ and D₂ adsorption on Carbox charcoal gave values in the range of approximately 7–1.5 kJ mol⁻¹ for the enthalpies of adsorption, which decreased with increasing surface coverage [273].

The heat of adsorption for deuterium was found to exceed that of hydrogen on six investigated adsorbents (charcoal, silica gel, and Linde molecular sieves type 411, 5A, and 13X), the difference tending to increase toward lower coverages [240].

Slightly higher enthalpies of D₂ adsorption, 5.4 and 5.6 kJ mol⁻¹ for H₂ and D₂, respectively, were obtained for the isosteric enthalpies of adsorption at zero surface coverage on graphitized carbon black, over the temperature range of 90 to 138 K [274].

H₂ and D₂ adsorption on single–wall carbon nanohorns (SWNHs) measured at 77 K, coupled with GCMC simulations, showed that the heat of hydrogen adsorption was always smaller than the values obtained for deuterium. At zero coverage, the difference in the heat of adsorption between H₂ and D₂ amounts to 0.35 kJ mol⁻¹ [275].

A virial analysis of the isotherms for H₂ and D₂ adsorbed on CMS T3A and nanoporous carbon at 77 K showed that the adsorbate–adsorbent interactions are slightly stronger for D₂, while adsorbate–adsorbate repulsive interactions are weaker for D₂ than for H₂ [127].

The analysis of H₂/D₂ adsorption isotherms for mixed–MOF Zn₃(BDC)₃[Cu(Pyen)] (DMF)₅(H₂O)₅ also indicated slightly greater D₂–surface than H₂–surface interactions, while D₂–D₂ interactions were lower than H₂–H₂ interactions. The decrease in H₂– and D₂–surface interactions was shown by the decrease in enthalpies of adsorption with increasing the amount adsorbed [184].

7.5 The heavier deuterium diffuses faster than the lighter hydrogen when the pore dimensions of the microporous material are sufficiently small, i.e., comparable to the size of adsorbate molecules.

Ordinarily, the rate of H₂ desorption is faster than the corresponding rate for D₂, as concluded from the position of the desorption maxima, and the point where the intensity gets to zero. This behavior is observed for CMS samples T4A (Fig. 4.9) and T5A (Fig. 4.11), and for the following MOF samples: Cu–BTC, Fe–BTC, MFU–4l, MIL–100(V), MIL–100(Cr), and MIL–100(Fe), shown in Fig. 5.14, 5.19, 5.33, 5.39, 5.41, and 5.43, respectively. On the other hand, D₂ desorption is found to be faster, compared to the corresponding profiles for H₂, for the high temperature desorption maximum within CMS T3A, Mg–formate(1), and –(2), and MFU–4. In particular, the desorption maxima for T3A appear in the following sequence 33, 44, and 122 K for hydrogen desorption, and 35, 45, and 119 K for deuterium desorption (Chapter 4.4.3). For Mg–formate(1) the maxima are observed at 19, 48, and 78 K for hydrogen, and at 26, 51, and 74 K for deuterium, and for Mg–formate(2) at 23, 51, and 76 K for hydrogen, and at 27, 54, and 71 K for deuterium (Chapter 5.2.1). Finally, for MFU–4 the desorption maxima appear at 30, 74, and 109 K for hydrogen, and 25, 74, and 105 K for deuterium desorption (Chapter 5.2.1). All the values are summarized within Table 7.1. Overall, D₂ desorption is slower, i.e., desorption maxima appear on higher temperature for low temperature peaks, however, for the high temperature desorption maxima, assigned to adsorption at strong (more favorable) adsorption sites, commonly within narrow pores with the pore diameter commensurate to the size of the adsorbate molecules, a reversed behavior (named *quantum effect – induced kinetic molecular sieving*, or *reverse kinetic molecular sieving*) is observed.

Contrary to the expected trend, based on mass, the size effect owns the main role for this reversed behavior. Since the molecular sizes of H₂ and D₂ are the same in the gas phase, and the latter is heavier, diffusion of D₂ along the pores is expected to be slower than that of H₂ ($1/\sqrt{2}$ H₂ rate for Knudsen diffusion). At sufficiently low temperature, when adsorption occurs in microporous adsorbents with confined pores, the length characterizing the interaction of the molecules with the pore walls is no longer negligibly small and deviations from Knudsen flow appear. In essence, the lower zero–point energy of deuterium implies a smaller vibration amplitude and hence a smaller effective radius (van der Waals radius) than that of protium, which is why deuterium faces less steric hindrance for the cage–to–cage migration, and lower energy barrier at the pore entrance.

The higher effective collision cross section of H₂ than D₂ produces a higher barrier to diffusion into the porous structures and slower adsorption/desorption kinetics. The system can overcome a barrier *via* a thermally activated process or by *quantum tunneling*. The phenomenon of a particle tunneling through a barrier results from the wave/particle duality of matter. Tunneling is promoted by a low

mass, and a narrow and not too high barrier [248]. It is important in the kinetics of light particles (e^- , Mu , H , D , ...), and sensitive to isotopic substitution. The smaller the particle, the less well its location is defined, and the higher is its zero-point energy. For very narrow pore size materials the de Broglie wavelength, as a measure of the particle size, exceeds the barrier width. This quantum mechanical effect is denoted as tunneling because the particle seems to 'dig a tunnel through the barrier'. The Fig. 7.3 demonstrates how this increases the diffusion rate for H compared to D and T , while the zero-point energy level puts a "false bottom" in the potential energy well, i.e., the heavier isotope exhibit a deeper potential energy well.

TABLE 7.1

The position of the desorption maxima within four investigated samples, pointing to the reverse kinetic molecular sieving effect.

Sample	T [K]	T [K]	T [K]
CMS T3A			
H_2	33	44	122
D_2	35	45	119
Mg-formate(1)			
H_2	19	48	78
D_2	26	51	74
Mg-formate(2)			
H_2	23	51	76
D_2	27	54	71
MFU-4			
H_2	30	74	109
D_2	25	74	105

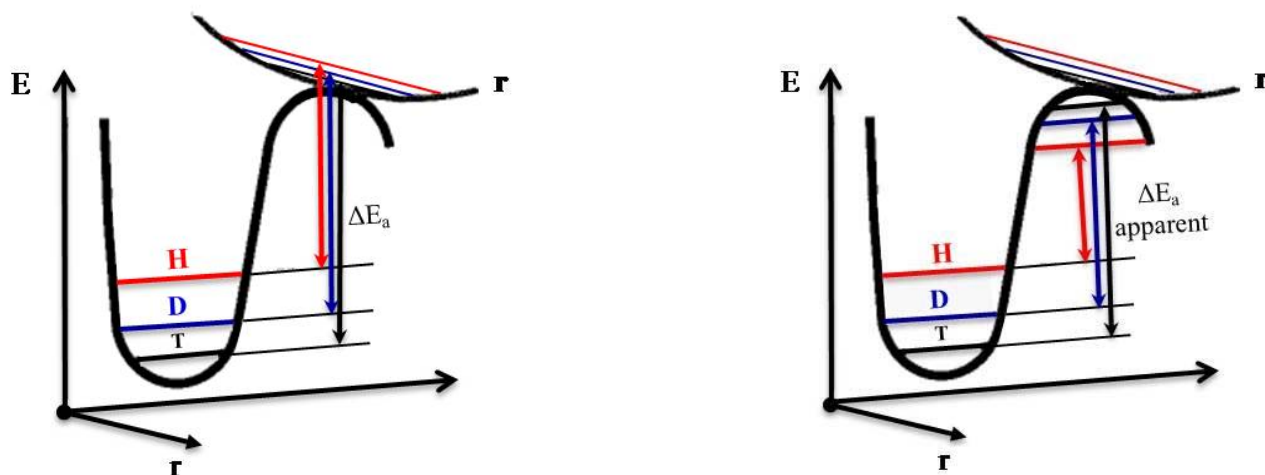


Fig. 7.3 left Different energies of activation, ΔE_a , for H (red), D (blue), and T (black), along the reaction coordinate, r , resulting from their different zero-point energies. A semiclassical model for quantum mechanical zero-point energy with no tunneling.

Fig. 7.3 right Tunneling correction for a Transition State Theory (TST) type of model. The color code and coordinates are the same. In addition to its higher zero-point energy, the lighter isotope tunnels at a lower energy under the top of the barrier, resulting in smaller ΔE_a (relative to that of the heavier isotope), than in the semiclassical model. Representation is adopted from the ref. [276].

A considerable deviation from behavior expected from Arrhenius Eq. (7.11), which relates the rate of a reaction to an energy barrier, is indicative of tunneling,

$$\ln k = \ln A - \frac{\Delta E_a}{RT} \quad (7.11)$$

where A is the Arrhenius pre-exponential factor, ΔE_a is the activation energy, and R is the gas constant. Notably, only the height of the activation barrier plays a role in determining the reaction rate, regardless of the shape of the potential surface. At very high temperature, as excess thermal energy is available, quantum effects are negligible and the temperature dependence of the reaction presents a linear behavior on an Arrhenius plot, $\ln k$ vs. the reciprocal of temperature $1/T$. At very low temperatures the contribution of thermal activation is lost (the plot curves upwards as its slope changes from $-\Delta E_a/R$ to zero), and tunneling contributes to the reaction rate. Plotting $\ln k$ vs. $1/T$ for two isotopes (H and D, Fig. 7.3) shows the expected trend. As the tunneling rate is temperature independent, the Arrhenius plot in the high temperature region is flat. At low temperatures, as tunneling becomes more dominant, there is a decrease in the slope. As a lighter particle is more affected by the tunneling, than the heavier isotope, this curvature takes place at a higher temperature (lower $1/T$) for the light isotope.

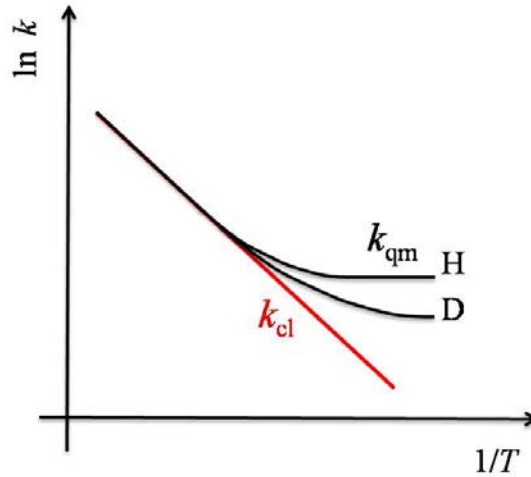


Fig. 7.3 The Arrhenius plots of $\ln(\text{rate constant})$ vs. reciprocal absolute temperature ($1/T$) for a light isotope (H), and a heavier isotope (D), for classical (cl) and quantum (qm) model.

One property of an adsorbed molecule that is intimately related to the desorption kinetics is the *surface residence time* – which is the average time that a molecule spends on the surface under a given set of conditions (in particular for a specified surface temperature), before it desorbs into the gas phase. Surface diffusion is a very important process which influences especially the kinetics of the adsorption and desorption reaction, and it is strongly dependent on the surface coverage. The residence time may be defined by the Frenkel Eq. (7.12):

$$\tau = \tau_0 \exp\left(\frac{E_a}{RT}\right) \quad (7.12)$$

By introducing the diffusion coefficient D the following expression may be written, Eq. (7.13):

$$D = D_0 \exp\left(\frac{E_a}{RT}\right) \quad (7.13)$$

The diffusivity ratio between H_2 and D_2 , and conditions which lead to the faster diffusion of D_2 may be calculated using TST, Eq. (7.14):

$$\frac{D(D_2)}{D(H_2)} = \sqrt{\frac{m_{H_2}}{m_{D_2}}} \exp\left(\frac{E_a^{H_2} - E_a^{D_2}}{k_B T}\right) = \frac{1}{\sqrt{2}} \exp\left(\frac{E_a^{H_2} - E_a^{D_2}}{k_B T}\right) \quad (7.14)$$

Induced reverse kinetic molecular sieving for H_2/D_2 mixtures in zeolite Rho has been theoretically predicted using the atomistic molecular dynamics simulations incorporating quantum effects via the Feynman–Hibbs approach, by Bhatia and co-workers [272, 277], and experimentally verified for

the first time by Zhao et al. [127] in gravimetric adsorption studies of H₂ and D₂ adsorbed in porous CMSs with micropore dimensions of 0.546 and 0.566 nm. Adsorption and desorption of H₂ and D₂ from porous carbon materials at 77 K were found to be fully reversible, with very rapid adsorption/desorption kinetics, while the rate constants for adsorption of heavier deuterium on CMS T3A were found to be faster than for lighter hydrogen [127]. The CMS 5A was shown to exhibit very modest selectivity and capacity to the preferential adsorption of hydrogen isotopes at ambient temperature [278].

Further theoretical investigations, using Monte Carlo and molecular dynamics (MD) simulations, and quasi-elastic neutron scattering experiments, employed to study the adsorption and diffusion of H₂ and D₂ in zeolite Rho, in the temperature range of 30–150 K, points toward the importance of the pore dimension in achieving the reverse kinetic selectivity [279]. The MD simulations results on two different structures of zeolite Rho, with quantum effects incorporated via the Feynman and Hibbs formalism, clearly demonstrate that the quantum effect is very sensitive to pore dimensions and under suitable conditions can lead to a reverse kinetic molecular sieving, with deuterium diffusing faster than hydrogen. A difference of 0.05 nm in the pore dimensions results in vastly different dynamic behavior between the zeolite Rho I and Rho II. The reversal of kinetic selectivity in the zeolite Rho II, where the pore opening is 0.596 nm, was not observed [272], while quantum mediated reverse kinetic selectivity for D₂ for the zeolit Rho I, where the pore opening is 0.543 nm, was theoretically predicted [277].

Later-on, the same group of researchers applied TST and MD simulations to study the quantum effects on diffusion of hydrogen isotopes in 1D channels of microporous aluminophosphate AlPO₄-25 at low temperatures [280]. It was demonstrated that the diffusivities of hydrogen and deuterium decrease from their classical values when quantum corrections are incorporated. The ratio between the classical and quantum diffusivity was higher for H₂ than for D₂, thus, the lighter molecule feels the quantum effects more than the heavier molecule, which is why the decrease in diffusivity is larger for H₂. Furthermore, quantum-effect-induced kinetic molecular sieving, in which the heavier isotope (deuterium) diffuses faster than the lighter hydrogen, was observed at low temperature, showing that at sufficiently low temperature the free energy barrier for diffusion is smaller for deuterium than for hydrogen, and exhibits inverse temperature dependence [280].

The first microscopic observation of faster diffusion of D₂ compared to H₂, obtained using quasielastic neutron scattering, has been observed in nanoporous CMS T3A [281]. The temperature variation of self diffusivity of H₂ and D₂ in the CMSs, over the temperature range 30 to 140 K, revealed a crossover of diffusivity at 100 K, with D₂ diffusing faster than H₂ below this temperature.

Chu et al. have investigated equilibrium and dynamical adsorption of hydrogen and deuterium in various mesoporous and microporous materials at 77 K, and reported that, although, the rate of adsorption for hydrogen is larger than that of deuterium in mesoporous materials, this order reverses in small micropores. The ratio of rate of adsorption of deuterium to that of hydrogen was found to have a maximum at a pore dimension of about 0.5 nm [282].

The first experimental observation of kinetic isotope quantum molecular sieving in MOFs was reported by Chen et al. [184]. Mixed zinc/copper MOF $Zn_3(BDC)_3[Cu(Pyen)](DMF)_5(H_2O)_5$, having a 3D structure with planar open copper centers and bimodal pore size distribution, shows two independent quantum effects for diffusion. A slower kinetic process for 1D diffusion in very narrow ultramicropores in the *b* axis direction (forming an approximately 2D array of pores), and the other for curved narrow pores ($5.6 \times 12.0 \text{ \AA}$) in the *c* axis direction, where 2D diffusion occurs. The rate constants for heavier D_2 were faster, and the activation energies slightly lower, than the corresponding values for H_2 kinetics, for both components. This is attributed to quantum effects with the higher zero-point energy for H_2 , giving a higher effective collision cross-section than D_2 , producing a higher barrier to diffusion along the pores.

Full quantum mechanical calculations for the isotopic selectivity of T_2/H_2 and D_2/H_2 mixtures in MOFs, covalent organic frameworks (COFs), and zeolitic imidazolate frameworks (ZIF), using path integral Monte Carlo simulations, showed that the most efficient materials for isotope separation are those with the narrowest pores [283]. However, the isotopic selectivities are found to be orders of magnitude smaller than the extraordinary values predicted for narrow nanotubes [259 – 261].

Chapter 8

CONCLUSIONS

Stimulated by the interest to move further toward the development of hydrogen-powered fuel cell vehicles, an intensive research effort has been made over the last decade to explore the existing and look for new light-weight, and cost effective high surface area adsorbents that can be used for on-board hydrogen storage. Storage by physisorption remains at the forefront of this research field regarding the pronounced advantages of complete reversibility, the fast refueling time, the low heat evolution, and above all increased safety.

Simultaneously with the development of light-weight materials with the high storage capacity, a considerable effort has been made to understand the nature of hydrogen-adsorbent interaction, as a result of coupled experimental and theoretical approaches. The complex experimental set-up required for the low-temperature conditions of gas physisorption on porous adsorbents put constraints on the available experimental techniques. Thermal Desorption Spectroscopy (TDS) holds pronounced advantages over the volumetric and gravimetric measurements, commonly applied for the characterization of porous adsorbents (Chapter 3.1), and it has been extensively applied within this study to obtain an overview on the number and the relative strength of energetically different adsorption sites. The in-house designed experimental apparatus, developed and optimized for *in situ* measurements, has been further upgraded, and for the first time the measurements have been performed with deuterium, which improved the sensitivity of the TDS method by reducing the background disturbance from water, and showed an excellent correspondence to hydrogen measurements. In addition, hydrogen/deuterium gas mixtures have been used, aiming to investigate the desorption mechanism on an atomic level. The analysis of the desorbing gases showed dominantly m/Z signals of 2 amu and 4 amu, corresponding to molecular

hydrogen and deuterium, respectively, whereas the desorption traces derived from the m/Z signals of 1 amu (corresponding to atomic hydrogen) and 3 amu (corresponding to hydrogen deuteride) gave a rather small contribution.

A series of measurements on the different microporous materials has been performed and showed a good repeatability. The amount of gas desorbed for each particular loading was determined after calibration with Pd powder, and found to be in a good agreement with the amount of gas stored within the high pressure measurements at 77 K, reported in the literature. This means that the sample coverage is in the technologically relevant range, and can be observed by TDS. Furthermore, only a few mg of sample are required to obtain a quick overview of the energetically different adsorption sites, owing to the high sensitivity of the method.

The TDS technique provided detailed information about the various binding sites that hydrogen/deuterium molecules occupy during the different loading regimes, and the approximate order in which these are filled. A sequential filling of the different adsorption sites has been identified by interrupted desorption and stepwise loading. For both hydrogen and deuterium desorption a *multistage adsorption/desorption model* has been established, as follows: an initial adsorption occurs at the coordinatively unsaturated metal centers (*stage I*), followed by the adsorption within the micropores (*stage II*), then at the mesopores (*stage III*), and finally the macropores are filled (*stage IV*), i.e., for adsorbents possessing a bimodal pore size distribution the small pores are filled primarily, and then the large pores.

Both commercially available samples, and completely novel materials, produced on a laboratory scale, were employed for this study. The carbon-based materials are the most exploited adsorbents, but rarely a systematic investigation on the influence of the pore size on the hydrogen adsorption potential was experimentally addressed. Three comparable, yet distinctively different, commercially available Carbon Molecular Sieves, T3A, T4A, and T5A, were used for a systematic study of the effect of the pore size distribution on the adsorption/desorption of hydrogen. The study includes porosity characterization by N_2 adsorption at 77 K, CO_2 adsorption at 273 K, the low pressure H_2 adsorption data at 77 K, GCMC calculations of the pore size distribution, and the TDS measurements of hydrogen, deuterium, and hydrogen deuteride desorption mechanism. A detailed TDS investigation, made by comparing three narrow sized samples with ultramicropores, showed the salient effect that just a slight change in the pore size (the pore opening diameter) has on the desorption profile, the differences that cannot be observed from the adsorption isotherms, nor time consuming GCMC runs. A linear correlation has been found between the total amount of hydrogen desorbed, from all three investigated samples, and the apparent specific surface area calculated from the CO_2 adsorption data. The total amount of hydrogen desorbed from T4A and T5A correlates well

with the N₂-derived BET surface area as well. This approximation does not apply to the desorption behavior of T3A where diffusion limitations disable hydrogen penetration at 20 K. Indeed, a tremendous difference of hydrogen diffusivities between T3A and the other two samples was evident from H₂ adsorption measurements at 77 K, slow N₂ diffusion at 77 K, but considerable CO₂ adsorption at 273 K. Possible diffusion limitations due to microporosity within T3A have been observed from the TDS data as well. Prolonged filling of the high temperature maximum, without attaining the saturation value, and the shift in the position of this maximum by nearly 17 K, when applying a slower heating rate of 0.01 K s⁻¹, are the first experimental observations of that kind made by TDS measurements on porous adsorbents. Furthermore, only for T3A two clearly separated desorption regimes are observed, and an enhancement of the interaction potential in narrow micropores, with a size comparable to the kinetic diameter of the hydrogen molecule (0.28 nm). The overlap of the potential field from the pore wall gives rise to a TDS maximum centered on 122 K, the highest desorption temperature ever measured for the desorption of physisorbed hydrogen.

The low storage capacity of conventional adsorbents has brought porous coordination polymers, known as Metal Organic Frameworks (MOFs), into the focus of investigation all over the world, during the last decade. The TDS measurements have been extensively employed to investigate topical compounds from the MOF family, as they stand at the forefront of the hydrogen storage field. A systematic study enabled observation of sites with stronger H₂-adsorbent interaction, and the influence of particular structural features (the coordinatively unsaturated metal centers, the pore size, the pore shape, and the pore opening diameter) on the adsorption potential. The TDS measurements have shown to yield information complementary to the results obtained by the other independent experimental methods, as shown by the direct comparison of the TDS data with neutron powder diffraction measurements on Cu-BTC. A detailed study of interrupted desorption and a partial sample loading was shown to be an asset in resolving the desorption from multiple adsorption sites with similar energetic barriers to desorption. The careful data collection with very small dosing steps, compared to the other experimental techniques where frequently only the discrete snapshots of the loading behavior can be seen, enabled overlapping desorption maxima to be separated, and the adsorbed amount to be quantified for each maximum.

Maintaining cryogenic temperature in an on-board storage system is a limiting step for the practical application of MOFs, and most of the research conducted over the last decade was directed on designing materials that can reversibly store and release hydrogen at temperatures close to ambient. Various strategies have been developed to increase the strength of the H₂-MOF interaction, and bring adsorption closer to RT conditions. In this work two main strategies, an introduction of the

open metal sites, and optimization of the pore size by ligand modification, have been closely examined.

The influence of the *open metal centers* on the strength of interaction with hydrogen has been investigated by directly comparing the TDS spectra of four isostructural compounds from the MIL-100 series. The copious amount of data, collected down to very low gas loadings, revealed salient differences among the four investigated samples, regarding the position of the peak maxima, and the relative peak intensity, which can be correlated to the strength of interaction of H₂ with a particular metal center. The TDS results indicate that open metal centers improve the strength of the H₂-MOF interaction, which can be further tuned by variation of the metal centers. Within investigated MIL-100 samples it was observed that the strength of interaction proceeds from Cr³⁺, over Fe³⁺, and V³⁺ to Al³⁺ compound. However, the overall number of the coordinatively unsaturated metal centers is relatively small, compared to the available surface area. These sites get quickly saturated, and, therefore, their contribution to the total storage capacity is small (Chapter 5.3, -6.2).

A comparative investigation has been conducted to address the effect that alteration of *the length of organic ligands* have on the pore size, the pore volume, and, therefore, on the total hydrogen storage capacity, by directly comparing MFU-4 and MFU-4l, Al(OH)(ndc) and Al(OH)(bpdc), and Mg-formate(1) and Mg-formate(2) structures, synthesized using the same metal ions as framework nodes, but different organic ligands. Two analogous frameworks with two different types of cavities, arranged in an alternating fashion, MFU-4 and MFU-4l, have been directly compared, and showed that by decreasing the pore diameter the strength of the H₂-MOF interaction can be considerably increased. Indeed, MFU-4, possessing very small pores, shows desorption maxima only at high temperatures, at 75 and 109 K, which are the highest desorption temperatures ever measured for hydrogen adsorbed at MOF structures. Again, another valuable observation has been made by the TDS measurements, the diffusion limited hydrogen adsorption/desorption kinetics due to the narrow-size pore opening diameter, as for CMS T3A. MFU-4l, on the other hand, exhibits rather weak interaction with the hydrogen molecules. However, the total storage capacity exhibits the reverse behavior, and shows its maximum for the MFU-4l structure (Chapter 5.3 and -6.1.1). Indeed, for ligands with a greater number of phenyl rings the total amount of hydrogen desorbed is bigger, due to the greater pore volume. The same trend has been observed for Al(OH)(ndc) and Al(OH)(bpdc), and Mg-formate(1) and Mg-formate(2) structures. These observations show the importance of targeted synthesis, and the profound effect of the length and functionality of organic linkers on the pore volume, the pore size, and, thus, on the hydrogen-MOF interaction potential.

Although lower binding energies are realized, compared to the interaction with coordinatively unsaturated metal centers, bigger surface areas and hydrogen storage capacities are reached.

As for carbon materials, MOFs with small pores show higher desorption temperatures and, therefore, tend to possess the stronger adsorbent–adsorbate interaction. Almost a linear correlation between the desorption temperature, and the pore size has been established for the three MOF samples, MOF–177, Cu–BTC, and Mg–formate(1) (Chapter 6.1). The H₂–MOF interaction potential is especially enhanced in materials with a pore size comparable to the kinetic diameter of the hydrogen molecule. However, smaller pores prevent hydrogen penetration and induce diffusion limitations. Furthermore, the molecular transport in confined pores at low temperatures may be significantly affected by quantum effects. By making use of differences in the zero–point energy of two isotopes, confined in very narrow pores, the isotopic mixtures can be efficiently separated. The separation is not based on the size, the shape, nor on the chemical affinity, but on the differences in the quantum energy levels of molecules confined in a very narrow space, comparable to the de Broglie wavelength. The preferential adsorption of the heavier isotope from the isotopic mixture, the higher amounts of deuterium adsorbed, compared to hydrogen, and the stronger D₂–surface interaction, observed from the TDS measurements, have been discussed in terms of quantum effects. The selectivity due to quantum sieving has shown to be a strong function of the pore diameter. Two independent quantum effects for diffusion have been observed in the same material. Both for carbon and MOF samples, a *reverse kinetic molecular sieving* has been observed for CMS T3A, Mg–formate(1), Mg–formate(2), and MFU–4, whereby the deuterium diffuses faster than hydrogen in nanoporous material with sufficiently small pore dimension, at low temperatures (Chapter 7). The kinetic molecular sieving mediated by quantum effects, highly sensitive to changes in the pore dimension, enables application of porous adsorbents for new isotope separation processes.

Although thousands of different structures have been published, and the remarkable values for specific surface areas attained, exceeding that of traditional adsorbents, the RT application is not a reality yet, and still awaits a breakthrough material. However, a comparative investigation performed within this research, and a broad overview of hydrogen storage within porous adsorbents, given through a great number of citations, clearly show that a considerable improvement has been made in increasing the strength of hydrogen–adsorbent interaction, and that the research field did go a step further. Both for the carbon materials and for MOF samples, the highest desorption maxima ever recorded for physisorbed hydrogen were observed within this work.

APPENDICES

APPENDIX A

TABLE A-1

Surface area and pore volume properties of the three CMS samples.

Sample	N ₂							CO ₂		
	S _{BET} [m ² g ⁻¹]	S _{DR} [m ² g ⁻¹]	V _t [cm ³ g ⁻¹]	V _{micro} [cm ³ g ⁻¹]	V _{micro} (DR) [cm ³ g ⁻¹]	V _{meso} * [cm ³ g ⁻¹]	V _{macro} # [cm ³ g ⁻¹]	S _{DR} [m ² g ⁻¹]	V _{micro} (DR) [cm ³ g ⁻¹]	V _{micro} (MC) [cm ³ g ⁻¹]
T3A	–	–	–	–	–	–	0.08	465	0.17	0.18
T4A	428	465	0.20	0.17	0.16	0.03	0.05	695	0.23	0.22
T5A	560	600	0.25	0.20	0.21	0.05	0.01	720	0.24	0.23

S_{BET} : BET surface area, S_{DR} : DR surface area, V_t : total pore volume (at $p/p_0 = 0.95$), V_{micro} : Micropore volume deduced from t-method (t), Dubinin–Radushkevich approach (DR) and Monte Carlo simulations (MC), V_{meso} : Mesopore volume, V_{macro} : Macropore volume, * $V_t - V_{micro}$ (t-method), # Volume at $p/p_0 = 0.995 - V_t$.

TABLE A–2**Summary of relevant porosity and structure data on Takeda samples published in the literature.**

Sample	V_{micro} [cm ³ g ⁻¹]	V_{meso} [cm ³ g ⁻¹]	V_{macro} [cm ³ g ⁻¹]	Micropore diameter [Å]	Macropore diameter [μm]	Effective aperture width [Å]
T3A	0.2 [a, b], 0.21 [c], 0.224 [d]	Negligible [152]		5 Å [130]	0.27 μm [130]	3.2 [e, f]
T4A	0.17 [285] – 0.22 [160]	Negligible [160]	0.31 [285]		0.30 [285]	4.1 [286]
T5A	0.24 – 0.3 [g] 0.26 [h] 0.33 [160]	Negligible [160]	0.28 [131]			4.3 [130]

Acronyms:

The data are obtained from N₂ adsorption measurements, except where indicated differently.

[a] CO₂ adsorption at 298 K [284].

[b] CO₂ adsorption at 273 K [20, 21].

[c] CO₂ adsorption at 273 K upon prolonged equilibration time above 300 s, when the activated diffusion overcomes [284].

[d] CO₂ adsorption at 273 K [127].

[e] The value is obtained from the activation energy for methane adsorption into T3A, estimated by kinetic measurement [150].

[f] The pore opening half-width was estimated to fall in the range from 0.3 to 3.1 Å [70].

[g] The micropore volume obtained from N₂ adsorption at 77 K is calculated to be 0.27 cm³ g⁻¹, from CO₂ adsorption at 273 K and high pressures 0.24 cm³ g⁻¹, and from CO₂ adsorption at 273 K and subatmospheric pressures 0.3 cm³ g⁻¹ [21].

[h] CO₂ adsorption at 273 K [284].

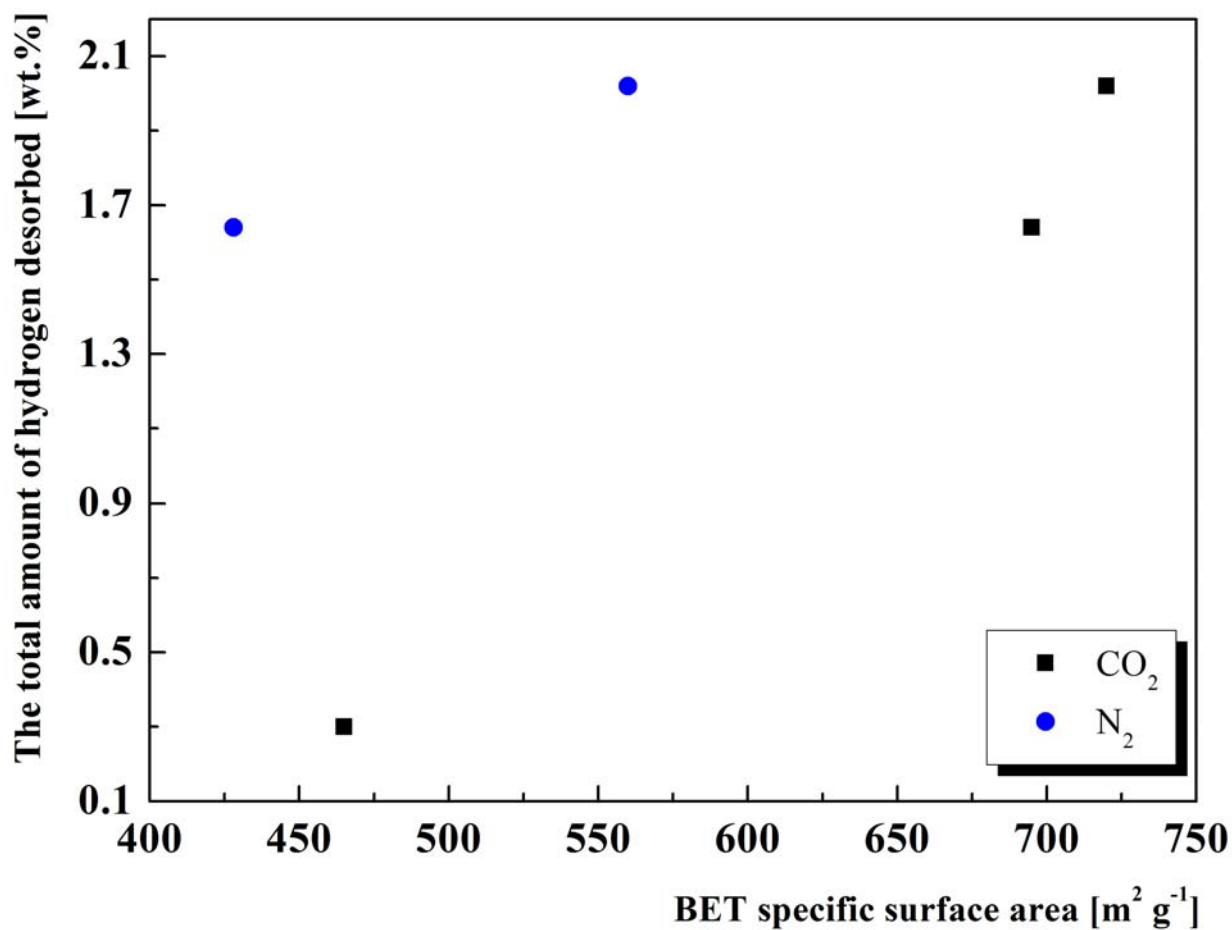


Fig. A-1 The total amount of hydrogen desorbed from CMS samples vs. the BET SSA calculated from the N₂ adsorption data at 77 K (blue), and the CO₂ adsorption data at 273 K (black).

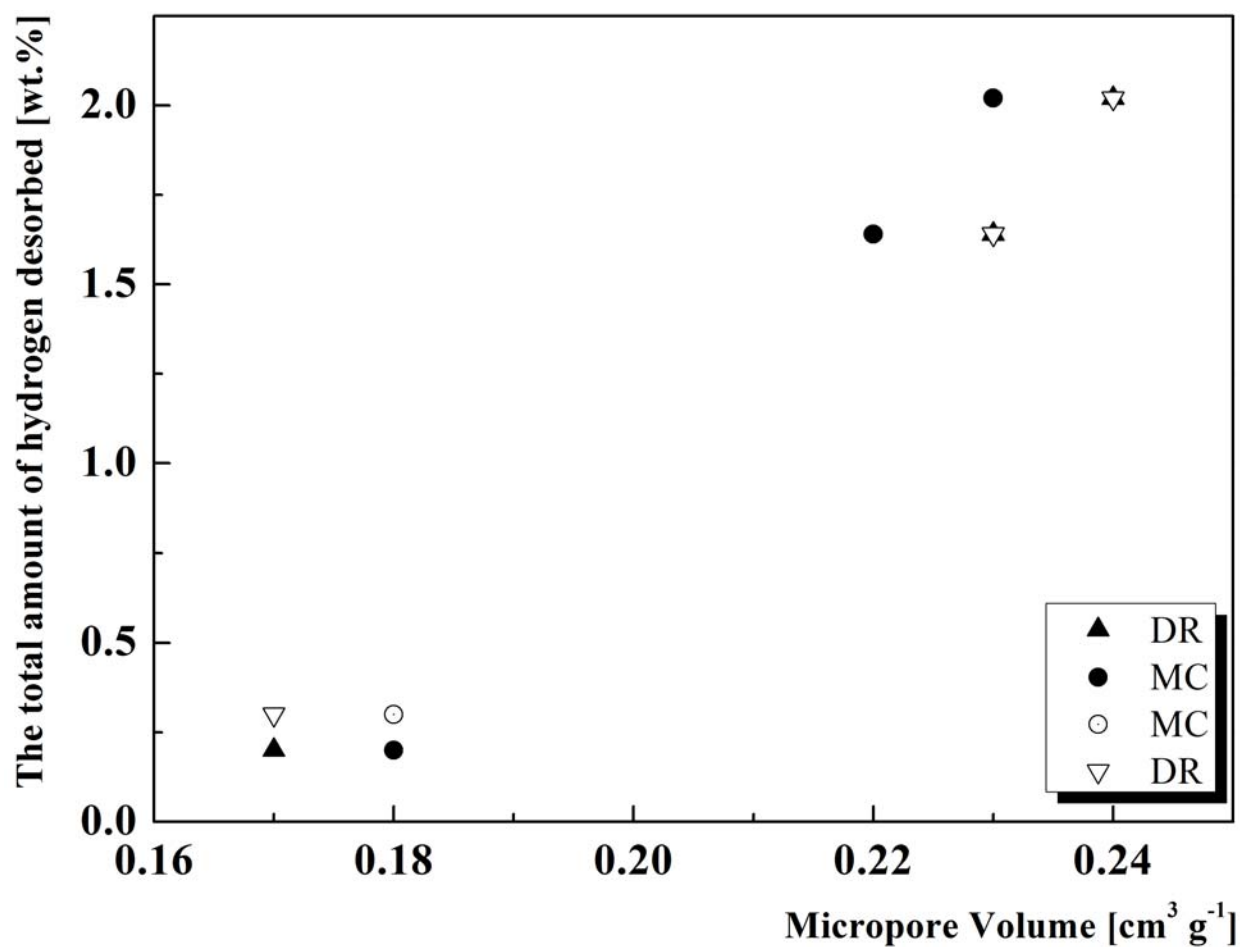


Fig. A-2 The total amount of hydrogen desorbed from CMSs vs. micropore volume calculated from the CO₂ adsorption data at 273 K by DR approach (triangles), and MC approach (circles). The total amount of gas desorbed for all three samples (open symbols), is compared to the total amount of gas desorbed from T4A and T5A, and considering the micropores only within T3A (filled symbols).

TABLE A-3

The Total Amount of H₂ desorbed [wt.%].

P [mbar]	Takeda 3A	Takeda 4A	Takeda 5A
1	—	0.21	0.16
3	—	0.62	0.48
5	—	1.04	0.81
7	—	—	1.06
9	—	—	1.36

15	–	1.46	1.84
20	–	–	1.92
25	0.10	1.44	1.74
50	0.12	–	–
100	0.13	–	–
200	0.19	–	–
250	–	–	1.99
500	0.25	–	1.98
700	0.30	1.64	2.02

TABLE A-4**The Total Amount of D₂ desorbed [wt.%].**

P [mbar]	Takeda 3A	Takeda 4A	Takeda 5A
1	–	0.34	0.23
3	–	1.27	–
5	–	2.66	–
7	–	–	2.86
15	–	4.42	–
25	–	4.48	4.83
50	0.32	–	–
300	0.70	–	–
500	0.82	–	–
700	0.97	4.82	–

Appendix B

The amount of hydrogen/deuterium desorbed corresponding to different initial gas loadings for all investigated MOF samples. The values are calculated after subtracting the amount of gas desorbed below 27 and 30.3 K for hydrogen and deuterium, respectively.

TABLE B-1

The Total Amount of D₂ Desorbed from Cu-BTC.

P [mbar]	wt.% D₂	D₂ /unit cell
1	0.30	7
2	0.48	12
3	1.33	32
4	1.13	27
5	1.19	29
6	1.45	35
7	1.70	41
10	2.21	53
15	3.61	87
25	8.19	197
200	9.06	217

TABLE B-2

The Total Amount of Gas Desorbed from Fe-BTC.

P [mbar]	wt.% H₂	wt.% D₂
1	0.34	0.51
3	0.83	0.75
5	1.03	1.69
7	1.76	1.46
10	2.14	2.27
15	1.54	3.02
25	2.20	3.06

700

1.62

2.97

TABLE B-3**The Total Amount of Gas Desorbed from Mg-formate(1).**

P [mbar]	wt.% H₂	wt.% D₂
1	0.28	0.26
2	0.48	0.82
3	0.64	1.07
4	0.62	1.25
5	0.72	1.31
7	0.72	1.44
10	0.75	1.69
15	0.76	1.66
25	0.81	1.68
100	0.90	2.16
700	1.14	2.72

TABLE B-4**The Total Amount of Gas Desorbed from Mg-formate(2).**

P [mbar]	wt.% H₂	wt.% D₂
1	0.18	0.71
2	0.52	1.30
3	0.86	2.10
4	1.03	2.48
5	1.31	3.01
7	1.59	3.70
10	1.68	4.47
15	1.66	4.22
25	1.78	4.32

100	1.92	4.47
700	1.92	4.26

TABLE B-5**The Total Amount of Gas Desorbed from MOF-177.**

P [mbar]	wt.% H₂	wt.% D₂
1	0.08	
5	0.23	
25	1.28	2.85
250	1.33	
700	1.52	3.26
900		3.32

TABLE B-6**The Total Amount of Gas Desorbed from MFU-4.**

P [mbar]	wt.% H₂	wt.% D₂
1	0.04	0.06
5	0.09	0.14
15	0.18	0.30
25	0.23	0.36
50	0.30	0.61
150	0.53	1.03
250	0.56	1.17
500	0.81	1.69
700	0.79	1.81

TABLE B-7**The Total Amount of Gas Desorbed from MFU-4l.**

P [mbar]	wt.% H₂	wt.% D₂
1	0.21	0.28
5	0.90	1.24
10	1.83	2.72
15	2.27	3.96
25	2.29	4.73
250	2.27	4.52
700	2.12	4.88

TABLE B-8**The Total Amount of Gas Desorbed from MIL-100(Al).**

P [mbar]	wt.% D₂
1	3.41
2	5.71
3	9.33
4	10.95
5	11.50
6	11.69

TABLE B-9**The Total Amount of H₂ Desorbed [wt.%] for three samples from MIL-100 series.**

P [mbar]	MIL-100(V)	MIL-100(Cr)	MIL-100(Fe)
1	0.36	0.14	0.25
3	1.07	0.42	0.45
5	1.34	0.68	0.65

10	2.16	0.96	0.97
25	2.57	1.34	1.24

TABLE B-10**The Total Amount of D₂ Desorbed [wt. %] for three samples from MIL-100 series.**

P [mbar]	MIL-100(V)	MIL-100(Cr)	MIL-100(Fe)
1	0.58	0.21	0.38
3	1.71	1.16	1.13
5	2.25	1.69	1.57
10	4.32	2.72	3.32
25	6.11	3.56	2.45

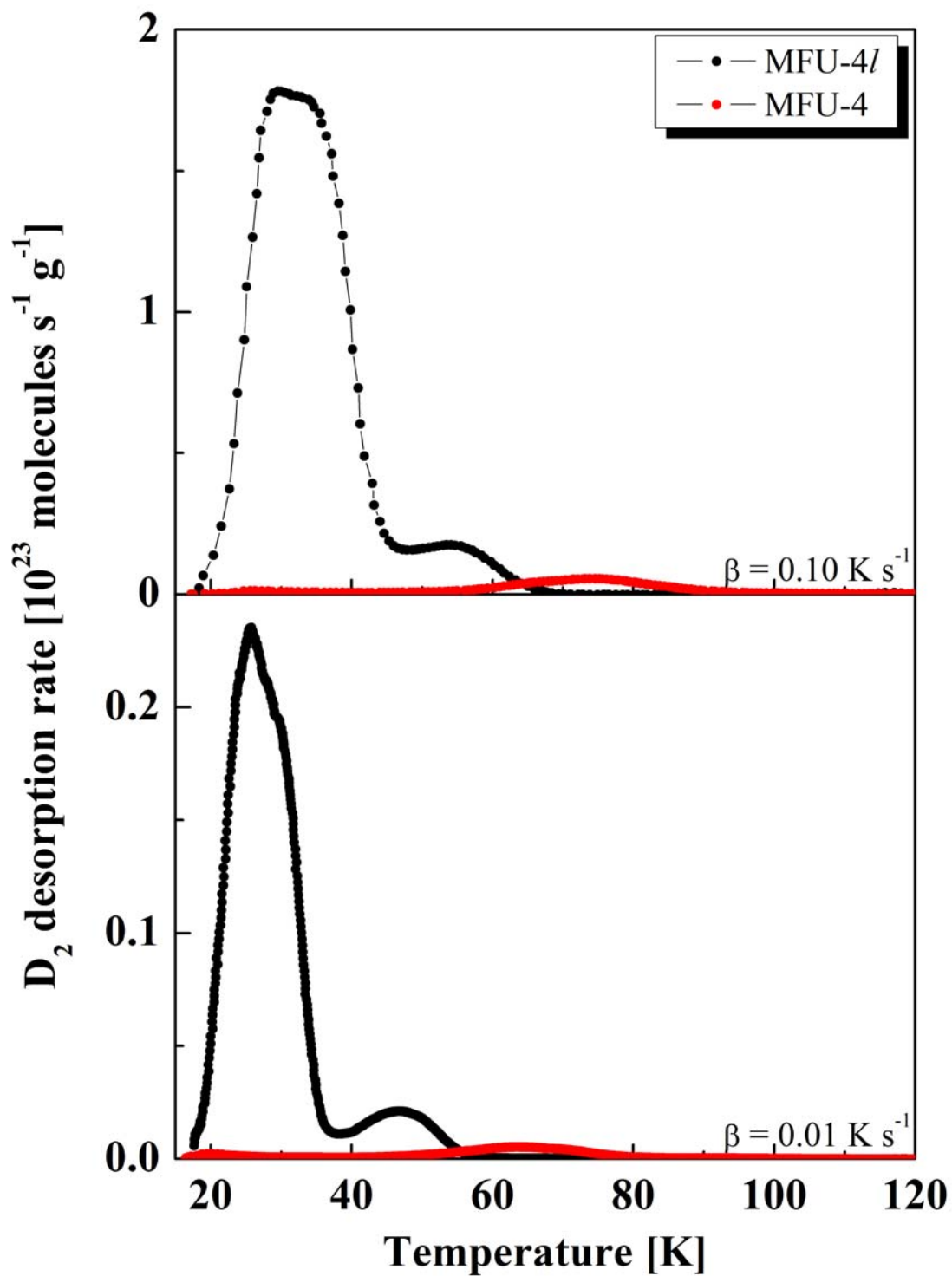
Appendix C

Fig. C-1. Deuterium thermal desorption spectra of MFU-4 and MFU-4/ recorded with the heating rate of 0.10 and 0.01 K s⁻¹.

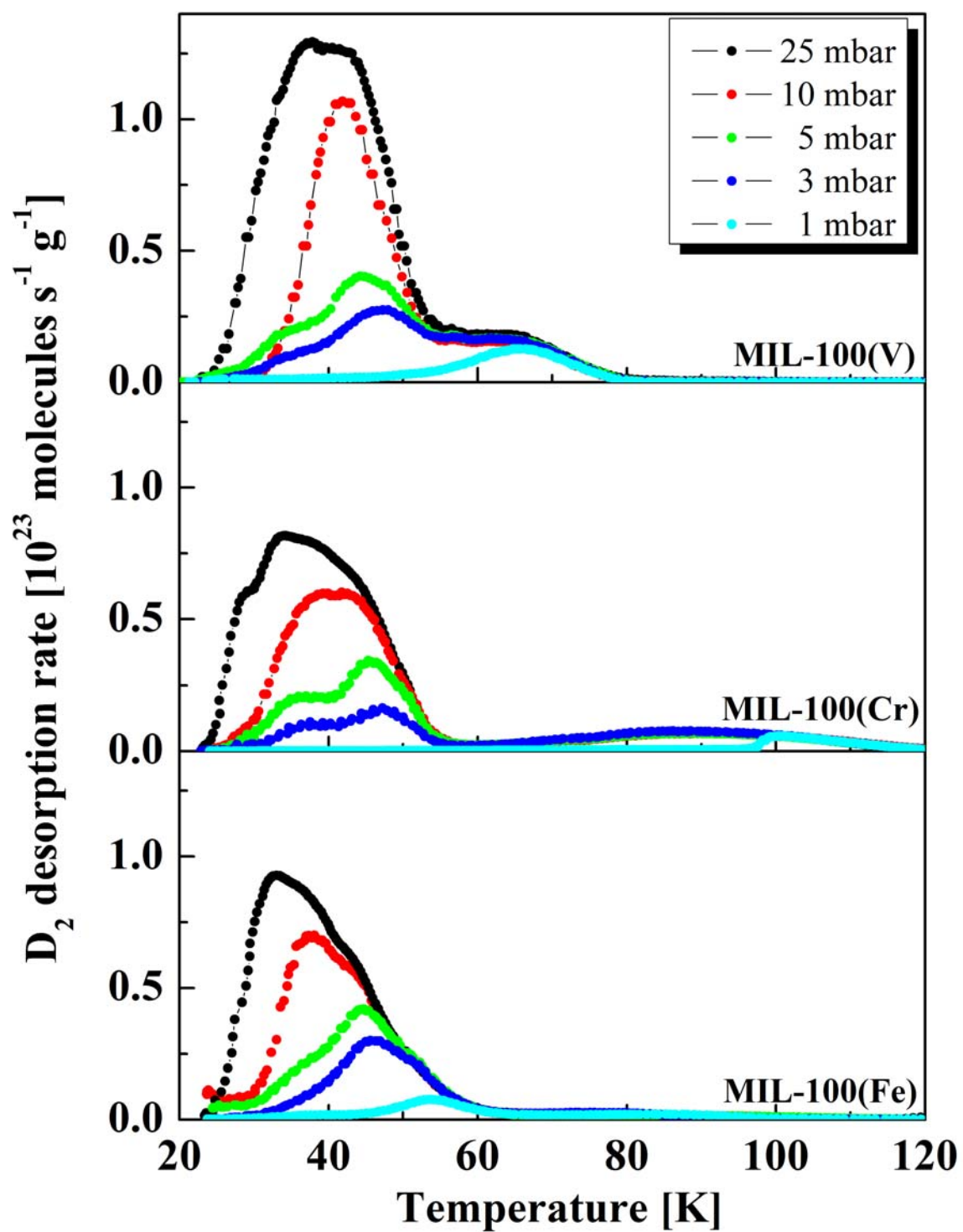


Fig. C-2. A comparison of deuterium thermal desorption spectra for MIL-100(V, -Cr, and -Fe). The spectra are recorded for different initial gas loadings, and recorded with the heating rate of 0.10 K s^{-1} .

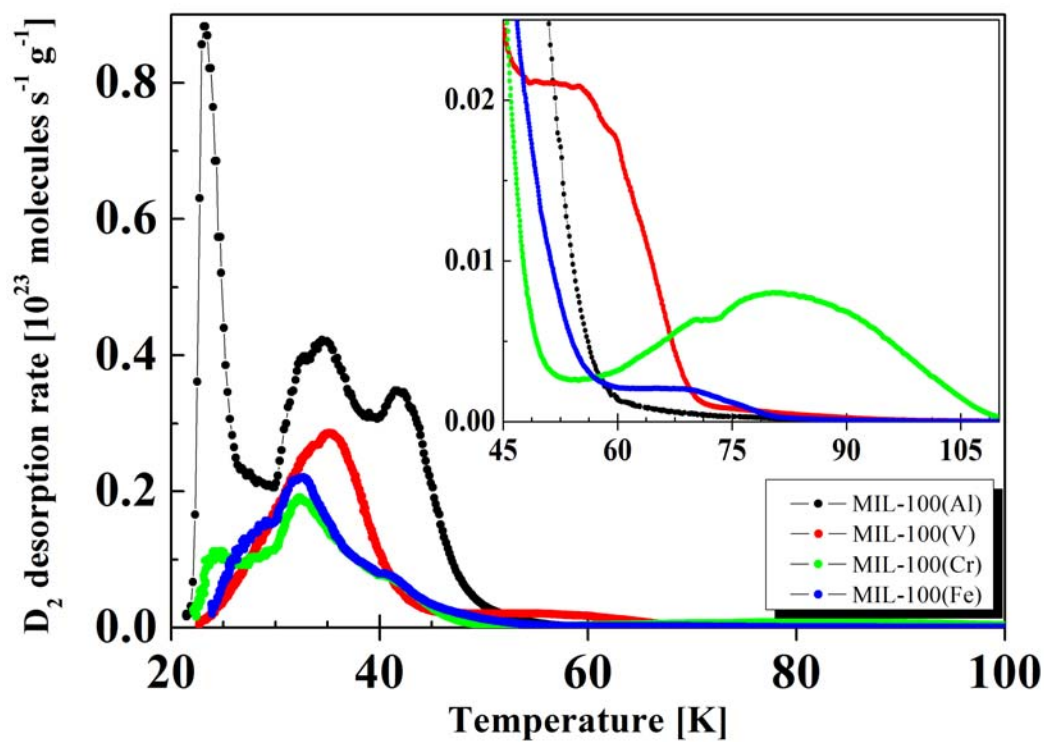


Fig. C-3. A comparison of deuterium thermal desorption spectra for MIL-100(Al, -V, -Cr, and -Fe). The spectra are recorded with the heating rate of 0.01 K s⁻¹.

Appendix D**TABLE D-1**

Summary of Porosity Data, the Total Hydrogen Adsorption Capacity at 77 K, and Calculated Binding Energy of the H₂ Molecules by Various Sites in MOFs published in the Literature.

Sample	S_{BET} [m ² g ⁻¹]	S_{Langmuir} [m ² g ⁻¹]	H₂ uptake [wt.%]	Pressure [bar]	Heat of adsorption [kJ mol ⁻¹]	Ref.
Cu-BTC	1154	1958	3.60	50	4.5	[287]
			2.50	1		[287]
			0.35	65 [a]		[287]
			1	60 [b]		[287]
	1482		4.10	26	[288]	
			2.90	1	[288]	
			0.66	1	[289]	
	1239		2.18	1	6.1 [c]	[168]
	1507	2175	2.54 [d]	1	5.8 – 6.6 [e]	[171]
			1.44	1	6.0 – 7.0	[291]
2.27			1	[291]		

			3.60	10		[291]
	1944	2260	3.26 [d]	77		[200]
		872	1.38	0.92		[169]
MOF-177		4526	1.25 [d]	1		[292]
	4746	5640	7.50 [d]	70		[200]
	4750	5640	7.60	66		[59]
			11.40	78		[59]
	3100	4300	0.62 [a]	100	5.8 – 11.3 [f]	[201]
	3275	5994	11	120		[203]
Al(OH)(ndc)			2.10	30		[179]
Al(OH)(bpdc)			3.30	40		[179]
MIL-100(Cr)		2800	3.28	27		[293]
		2700	0.15 [a]	73.3	5.6 – 6.3	[293]

Acronyms:

The apparent surface area is calculated from N₂ adsorption at 77 K using the Langmuir model, except where indicated differently.

[a] Hydrogen adsorption isotherm measured at 298 K.

[b] Hydrogen adsorption isotherm measured at 200 K.

[c] Values obtained from adsorption experiments at different temperatures.

[d] Gravimetric uptake of hydrogen (wt.%).

[e] The adsorption enthalpy at an isolated Cu^{2+} center is estimated to be $10.1(7) \text{ kJ mol}^{-1}$ [189].

[f] BET surface area from O_2 adsorption at 77 K.

Appendix E

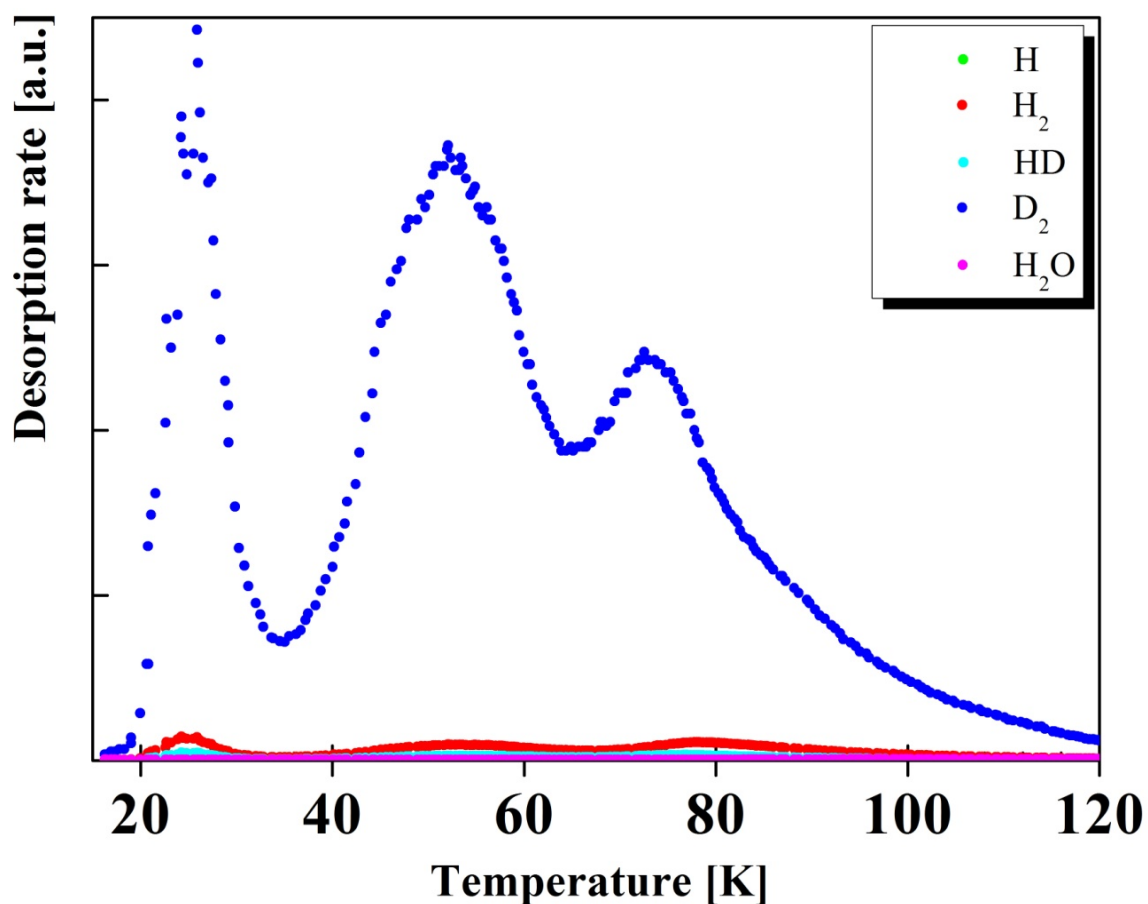


Fig. E-1 The desorption from Mg-formate(1) surface with respect to atomic and molecular hydrogen, atomic and molecular deuterium, hydrogen deuteride and water. The spectra are recorded after exposing the sample to H_2/D_2 gas mixture, and recorded with heating rate of 0.10 K s^{-1} .

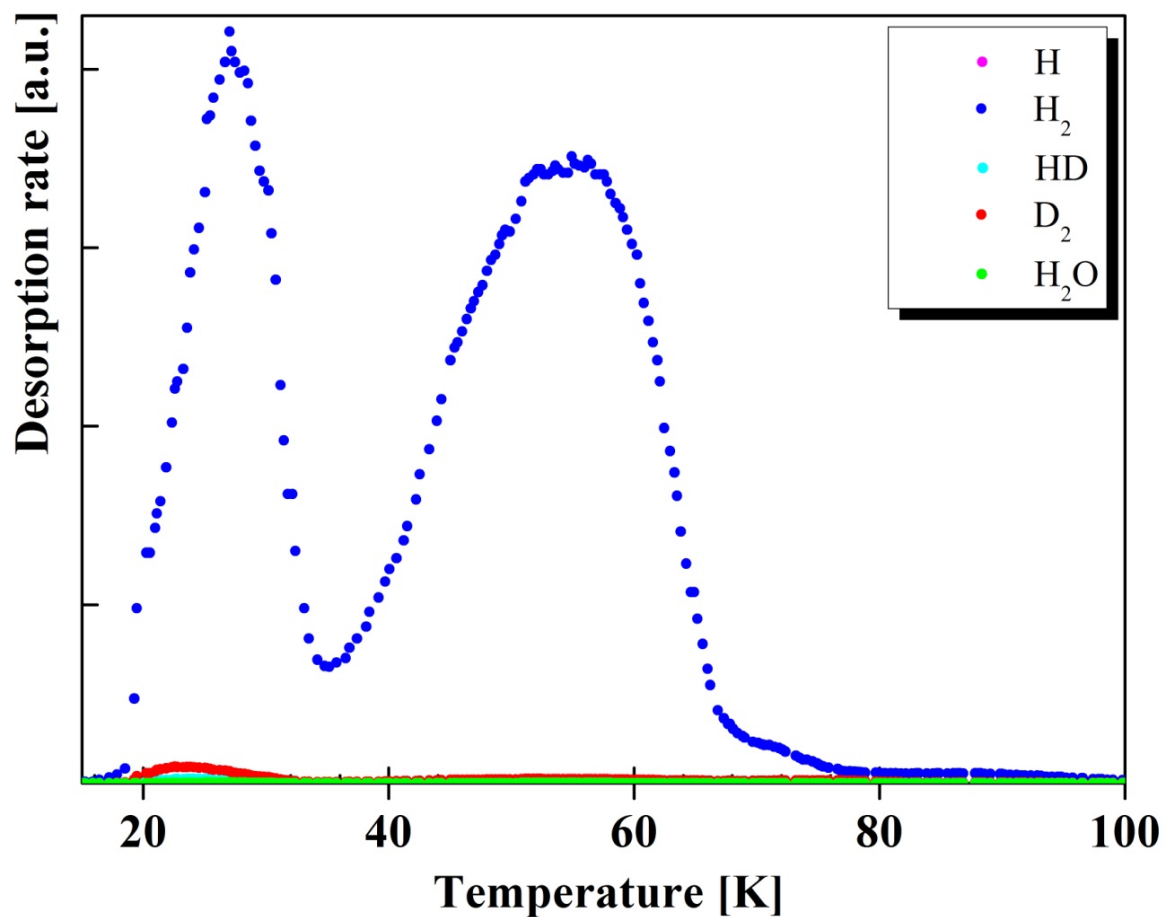


Fig. E-2 The desorption from Mg-formate(2) surface with respect to atomic and molecular hydrogen, atomic and molecular deuterium, hydrogen deuteride and water. The spectra are recorded after exposing the sample to H₂/D₂ gas mixture, and recorded with heating rate of 0.10 K s⁻¹.

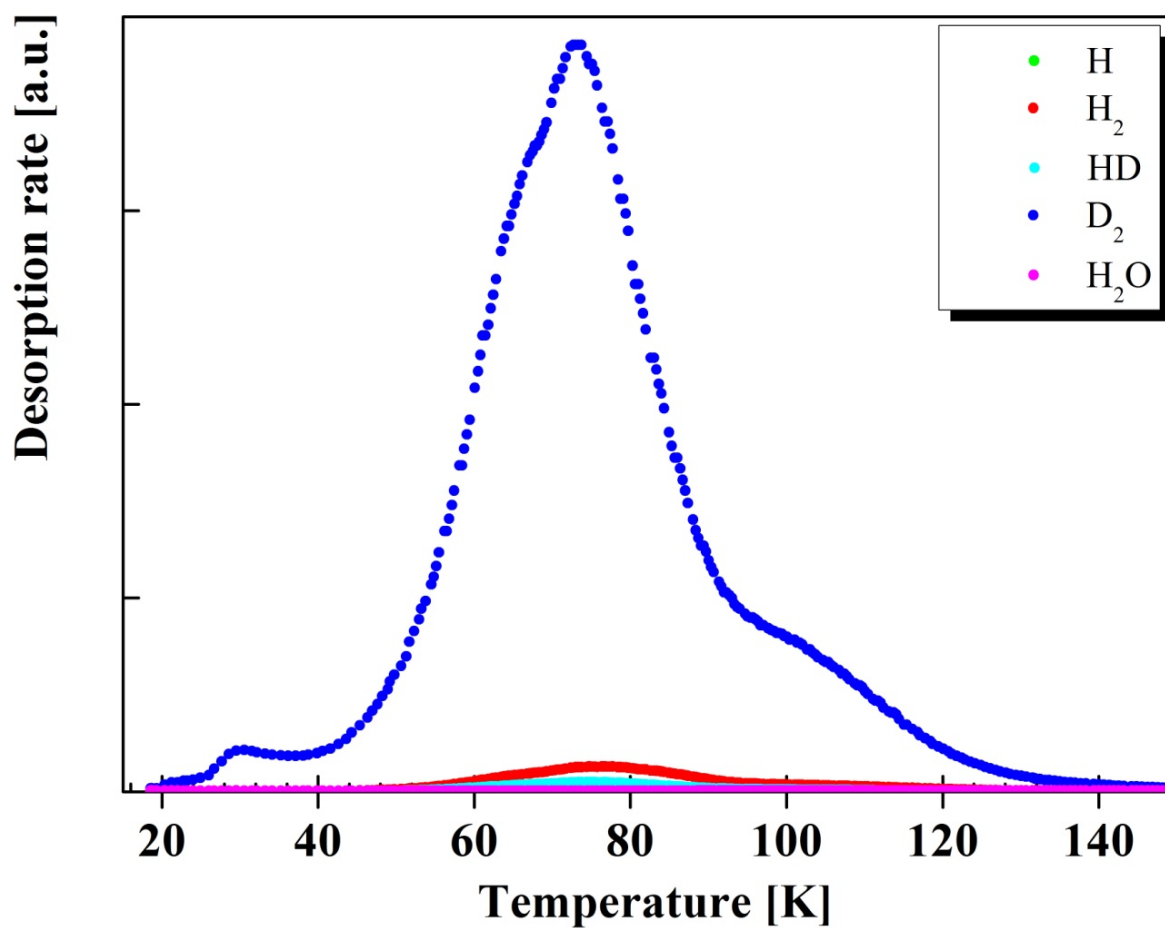


Fig. E-3 Desorption from MFU-4 surface with respect to atomic and molecular hydrogen, atomic and molecular deuterium, hydrogen deuteride and water. The spectra are recorded after exposing the sample to H₂/D₂ gas mixture, and recorded with heating rate of 0.10 K s⁻¹.

*Appendix F***TABLE F-1****Selected physical and thermodynamic properties of molecular hydrogen.**

Property [unit]	H₂	D₂	HD
Molecular mass [g mol ⁻¹]	2.1059	4.0282	6.0322
Absolute mass [kg]	3.497·10 ⁻²⁷	6.6847·10 ⁻²⁷	/
Natural abundance [%]	99.985	0.015	/
Binding energy [eV mol ⁻¹]	4.4763	4.553	4.511
Internuclear distance [m]	0.7416·10 ⁻¹⁰	0.7417·10 ⁻¹⁰	0.4713·10 ⁻¹⁰
Ionisation potential [eV]	15.427	15.46	/
Moment of inertia [kg m ²]	0.460 10 ⁻⁴⁷	0.919 10 ⁻⁴⁷	0.611·10 ⁻⁴⁷
Rotational constant B ₀ [cm ⁻¹]	60.809	30.4	/
Ground state vibrational frequency [cm ⁻¹]	4395.2	3118.4	3817
Triple point [K]	13.95		/
Melting point [K]	14.025	18.65	/
Boiling point [K]	20.39	23.6	/

THE REFERENCE LIST

- [1] A.W.C. van den Berg, C.O. Arean, *Chem. Commun.* 6 (2008) 668–681.
- [2] D.A.J. Rand, R.M. Dell, *Hydrogen Energy: Challenges and Prospects*, The Royal Society of Chemistry, Cambridge, UK 2008.
- [3] L. Schlapbach and A. Züttel, *Nature* 414 (2001) 353–358.
- [4] J. Wolf, *MRS Bulletin* 27, 9 (2002) 684–687.
- [5] K.L. Lim, H. Kazemian, Z. Yaakob, W.R. Wan Daud, *Chem. Eng. Technol.* 33, 2 (2010) 213–226.
- [6] P.A. Redhead, *J. Vac. Sci. Technol. A* 13, 2 (1995) 467–475.
- [7] H. Margenau, *Rev. Mod. Phys.* 11, 1 (1939) 1–35.
- [8] F. London, *Z. Phys.* 63 (1930) 245–279.
- [9] K.S.W. Sing, D.H. Everett, R.A.W. Haul, L. Moscou, R.A. Pierotti, J. Rouquerol, T. Siemieniowska, *Pure Appl. Chem.* 57, 4 (1985) 603–619.
- [10] S. Brunauer, L.S. Deming, W.S. Deming, E. Teller, *J. Amer. Chem. Soc.* 62 (1940) 1723–1732.
- [11] P.H. Emmett and S. Brunauer, *J. Am. Chem. Soc.* 59, 1 (1937) 1553–1564.
- [12] A. Zsigmondy, *Zeitschrift für Anorganische Chemie* 77, 4 (1911) 356–377.
- [13] W.T. Thomson, *Phil. Mag.* 42, 1 (1871) 448.
- [14] I. Langmuir, *J. Am. Chem. Soc.* 40 (1918) 1361–1403.
- [15] S. Brunauer, P.H. Emmet, and E. Teller, *J. Am. Chem. Soc.* 60 (1938) 309–319.
- [16] S. Brunauer and P.H. Emmet, *J. Am. Chem. Soc.* 57 (1935) 1754–1755.
- [17] F. Rouquerol, J. Rouquerol, and K.S.W. Sing, Chapter 2.5.2 in the *Handbook of Porous Solids*, Wiley–VCH, 2002.
- [18] J.R. Goates and C.V. Hatch, *Soil. Sci.* 75, 4 (1953) 275–278.
- [19] J. Garrido, A. Linares–Solano, J.M. Martín–Martínez, M. Molina–Sabio, F. Rodríguez–Reinoso, and R. Torregrosa, *Langmuir* 3, 1 (1987) 76–81.
- [20] D. Lozano–Castelló, D. Cazorla–Amorós, A. Linares–Solano, *Carbon* 42, 7 (2004) 1233–1242.
- [21] D. Cazorla–Amorós, J. Alcañiz–Monge, M.A. de la Casa–Lillo, and A. Linares–Solano, *Langmuir* 14, 16 (1998) 4589–4596.
- [22] D. Lozano–Castelló, D. Cazorla–Amorós, and A. Linares–Solano, *Chem. Eng. Tech.* 26, 8 (2003) 852–857.

- [23] J. Milewska–Duda, J.T. Duda, G. Jodlowski, M. Kwiatkowski, *Langmuir* 16, 18 (2000) 7294–7303.
- [24] K.S.W. Sing, R.T. Williams, *Adsorpt. Sci. Technol.* 23, 10 (2005) 839–853.
- [25] Y. Amenomiya and R.J. Cvetanović, *J. Phys. Chem.* 67, 1 (1963) 144–147.
- [26] L. Apker, *Ind. Eng. Chem.* 40, 5 (1948) 846–847.
- [27] R.J. Cvetanović and Y. Amenomiya, in: D.D. Eley, H. Pines and P.B. Weisz (Eds.), *Advances in Catalysis Vol. 17*, second ed., Academic Press, New York, 1967, p. 103–149.
- [28] R.J. Cvetanović and Y. Amenomiya, *Catal. Rev.* 6 (1972) 21–48.
- [29] D.A. King, *Surf. Sci.* 47, 1 (1975) 384–402.
- [30] J.L. Falconer, J.A. Schwarz, *Catal. Rev.–Sci. Eng.* 25, 2 (1983) 141–227.
- [31] A.V. Sklyarov, *Russ. Chem. Rev.* 55, 3 (1986) 214–221.
- [32] S. Bhatia, I. Beltramini, D. Do, *Catal. Today* 7, 3 (1990) 309–438.
- [33] A.W. Smith and S. Aranoff, *J. Phys. Chem.* 62, 6 (1958) 684–686.
- [34] P.A. Redhead, *Vacuum* 12 (1962) 203.
- [35] G. Carter, *Vacuum* 12 (1962) 245–254.
- [36] W.A. Grant and G. Carter, *Vacuum* 15, 1 (1965) 13.
- [37] G. Ehrlich, *Adv. Catal.* 14 (1963) 255–427.
- [38] V.I. Yakerson, V.V. Rozanov, and A.M. Rubinshtein, *Surf. Sci.* 12, 2 (1968) 221–246.
- [39] M. Polanyi, E. Wigner, *Z. Phys. Chem.* 139 (1928) 439–452.
- [40] J. Joly and A. Perrard, *Langmuir* 17 (2001) 1538–1542.
- [41] J.A. Konvalinka and J.J.F. Scholten, *J. Catal.* 52 (1978) 547.
- [42] C.M. Chan, R. Aris and W.H. Weinberg, *Appl. Surf. Sci.* 1, 3 (1978) 360–376.
- [43] J.L. Falconer, R.J. Madix, *Surf. Sci.* 49 (1975) 393–405.
- [44] R.J. Gorte, *J. Catal.* 75, 1 (1982) 164–174.
- [45] A. M. de Jong, J.W. Niemantsverdriet, *Surf. Sci.* 233 (1990) 355.
- [46] D.H. Parker, M.E. Jones, B.E. Koel, *Surf. Sci.* 233, 1–2 (1990) 65–74.
- [47] R. Zacharia, H. Ulbricht, and T. Hertel, *Phys. Rev. B* 69, 15 (2004) 155406–1–155406–7.
- [48] P.A. Redhead, *Transfaraday Soc.* 57, 4 (1961) 641–656.
- [49] K.C. Waugh, *Appl. Catal.* 43, 2 (1988) 315–337.
- [50] F.M. Lord and J.S. Kittelberger, *Surface Sci.* 43, 1 (1974) 173–182.
- [51] E. Habenschaden and J. Küppers, *Surf. Sci.* 138 (1984) L147.
- [52] L. Spenadel and M. Boudart, *J. Phys. Chem.* 64, 2 (1960) 204–207.
- [53] S.D. Robertson, B.D. McNicol, J.H. De Baas, S.C. Kloet, J.W. Jenkins, *J. Catal.* 37, 3 (1975) 424–431.

- [54] M.J. Benham and D.K. Ross, *Z. Phys. Chem. Neue Folge* 163 (1989) 25–32.
- [55] T.P. Blach, E.M. Gray, *J. Alloys. Compd.* 446–447 (2006) 692–697.
- [56] D.P. Broom, *Int. J. Hydrogen Energy* 32, 18 (2007) 4871–4888.
- [57] D.P. Broom and P. Moretto, *J. Alloys Compd.* 446 (2007) 687–691.
- [58] A. Anson, M. Benham, J. Jagiello, M.A. Callejas, A.M. Benito, W.K. Maser, A. Züttel, P. Sudan and M.T. Martinez, *Nanotechnology* 15, 11 (2004) 1503–1508.
- [59] H. Furukawa, M.A. Miller and O.M. Yaghi, *J. Mater. Chem.* 17, 30 (2007) 3197–3204.
- [60] A.Z. Panagiotopoulos, *Mol. Phys.* 62, 3 (1987) 701–719.
- [61] N. Metropolis, A.W. Rosenbluth, M.N. Rosenbluth, A.N. Teller and E. Teller, *J. Chem. Phys.* 21 (1953) 1087.
- [62] A.Z. Panagiotopoulos, N. Quirke, M. Stapleton, D.J. Tildesley, *Mol. Phys.* 63, 4 (1988) 527–545.
- [63] S.K. Bhatia and A.L. Myers, *Langmuir* 22, 4 (2006) 1688–1700.
- [64] T. Kawakami, S. Takamizawa, Y. Kitagawa, T. Maruta, W. Mori, K. Yamaguchi, *Polyhedron* 20 (2001) 1197–1206.
- [65] A.I. Skoulidas, *J. Am. Chem. Soc.* 126, 5 (2004) 1356–1357.
- [66] D. Dubbeldam and R.Q. Snurr, *Mol. Simul.* 33, 4–5 (2007) 305–325.
- [67] E. Roduner, Aspects of muon chemistry. In: R. Cywinski, S.L. Lee, S.H. Kilcoyne, editors, *Muon science – muons in physics, chemistry and materials*, pages 173–209. Institute of Physics Publishing, London/Philadelphia, 1999.
- [68] M.S. Kane, J.F. Goellner, H.C. Foley, R. DiFrancesco, S.J.L. Billinge, L.F. Allard, *Chem. Mater.* 8, 8 (1996) 2159–2171.
- [69] T.J. Barton, L.M. Bull, W.G. Klemperer, D.A. Loy, B. McEnaney, M. Misono, P.A. Monson, G. Pez, G.W. Scherer, J.C. Vartuli, and O.M. Yaghi, *Chem. Mater.* 11, 10 (1999) 2633–2656.
- [70] C. Nguyen and D.D. Do, *Langmuir* 16, 4 (2000) 1868–1873.
- [71] J. Biscoe and B.E. Warren, *J. Appl. Phys.* 13, 6 (1942) 364–371.
- [72] M. Suzuki, *Adsorption Engineering*, Kodansha Ltd., Tokyo and Elsevier Science Publishers, Amsterdam, 1990.
- [73] Z. Hu and E.F. Vansant, *Carbon* 33, 5 (1995) 561–567.
- [74] C. Nguyen, D.D. Do, *Carbon* 33, 12 (1995) 1717–1725.
- [75] C. Nguyen, A. Ahmadpour, D.D. Do, *Adsorption Sci. & Technol.* 12, 3 (1995) 247–258.
- [76] Z. Hu and E.F. Vansant, *Microporous Mater.* 3, 6 (1995) 603–612.
- [77] R.F.P.M. Moreira and A.E. Rodrigues, *Lat. Am. Appl. Res.* 31, 5 (2001) 391–396.
- [78] J.E. Metcalfe, M. Kawahata, P.L. Walker, *Fuel* 42, 3 (1963) 233–238.

- [79] T.G. Lamond, J.E. Metcalfe, III, P.L. Walker, *Carbon* 3 (1965) 59–63.
- [80] S.P. Nandi, P.L. Walker, *Fuel* 54, 3 (1975) 169–178.
- [81] H. Munzer, H. Heimbach, W. Korbacher, W. Peters, H. Jüntgen, K. Knoblauch, D. Zundorf, US Patent 3,801,513, 1974.
- [82] H. Jüntgen, *Carbon* 15, 5 (1977) 273–283.
- [83] H. Jüntgen, K. Knoblauch, and K. Harder, *Fuel* 60, 9 (1981) 817–822.
- [84] A.L. Cabrera, J.E. Zehner, C.G. Coe, T.R. Gaffney, T.S. Farris, J.N. Armor, *Carbon* 31, 6 (1993) 969–976.
- [85] Y. Kinoshita, I. Matsubara, T. Hibuchi, and Y. Saito, *Bull. Chem. Soc. Jpn.* 32 (1959) 1221–1226.
- [86] E.A. Tomic, *J. Appl. Polym. Sci.* 9, 11 (1965) 3745–3752.
- [87] B.F. Hoskins, and R. Robson, *J. Am. Chem. Soc.* 111, 15 (1989) 5962–5964.
- [88] B.F. Abrahams, B.F. Hoskins, J.L. Liu, R. Robson, *J. Am. Chem. Soc.* 113, 8 (1991) 3045–3051.
- [89] B.F. Hoskins and R. Robson, *J. Am. Chem. Soc.* 112 (1990) 1546–1554.
- [90] O.M. Yaghi, G. Li and H. Li, *Nature* 378, 6558 (1995) 703–706.
- [91] M. Kondo, T. Yoshitomi, K. Seki, H. Matsuzaka and S. Kitagawa, *Angew. Chem. – Int. Ed.* 36, 16 (1997) 1725–1727.
- [92] O.M. Yaghi, D.A. Richardson, G. Li, E. Davis and T.L. Groy, *Mater. Res. Soc. Symp. Proc.* 371 (1995) 15–19.
- [93] O.M. Yaghi and H. Li, *J. Am. Chem. Soc.* 117, 41 (1995) 10401–10402.
- [94] J.L.C. Rowsell and O.M. Yaghi, *Micropor. Mesopor. Mater.* 73, 1–2 (2004) 3–14.
- [95] M. O’Keeffe, M.A. Peskov, S.J. Ramsden and O.M. Yaghi, *Acc. Chem. Res.* 41, 12 (2008) 1782–1789.
- [96] O.M. Yaghi, M. O’Keeffe, N.W. Ockwig, H.K. Chae, M. Eddaoudi, J. Kim, *Nature* 423 (2003) 705.
- [97] S. Kitagawa, R. Kitaura, and S. Noro, *Angew. Chem. – Int. Ed.* 43, 18 (2004) 2334–2375.
- [98] G. Férey, C. Mellot-Draznieks, C. Serre, F. Millange, J. Dutour, S. Surblé, I. Margiolaki, *Science* 309, 5743 (2005) 2040–2042.
- [99] C. Volkringer, D. Popov, T. Loiseau, G. Férey, M. Burghammer, C. Riekkel, M. Haouas, and F. Taulelle, *Chem. Mater* 21, 24 (2009) 5695–5697.
- [100] C. Serre, F. Millange, C. Thouvenot, M. Nogues, G. Marsolier, D. Louer, and G. Férey, *J. Am. Chem. Soc.* 124, 45 (2002) 13519–13526.

- [101] H.K. Chae, D.Y. Siberio-Pérez, J. Kim, Y. Go, M. Eddaoudi, A.J. Matzger, M. O’Keeffe and O.M. Yaghi, *Nature* 427, 6974 (2004) 523–527.
- [102] Q.R. Fang, G.S. Zhu, Z. Jin, M. Xue, X. Wei, D.J. Wang, S.L. Qiu, *Cryst. Growth Des.* 7 (2007) 1035–1037.
- [103] K. Koh, A.G. Wong-Foy, A.J. Matzger, *J. Am. Chem. Soc.* 131, 12 (2009) 4184 – 4185.
- [104] H. Furukawa, N. Ko, Y.B. Go, N. Aratani, S.B. Choi, E. Choi, A.Ö. Yazaydin, R.Q. Snurr, M. O’Keeffe, J. Kim, O.M. Yaghi, *Science* 329, 5990 (2010) 424–428.
- [105] A.W. Chester, P. Clement, S. Han, U.S. Patent 2000/6, 136, 291A.
- [106] A. Züttel, P. Sudan, P. Mauron and P. Wenger, *Appl. Phys. A* 78, 7 (2004) 941–946.
- [107] N.L. Rosi, J. Eckert, M. Eddaoudi, D.T. Vodak, J. Kim, M. O’Keeffe, O. Yaghi, *Science* 300, 5622 (2003) 1127–1129.
- [108] S. Takamizawa and E. Nakata, *Cryst. Eng. Comm.* 7 (2005) 476–479.
- [109] Y. Kubota, M. Takata, R. Matsuda, R. Kitaura, S. Kitagawa, K. Kato, M. Sakata and T.C. Kobayashi, *Angew. Chem. – Int. Ed.* 44, 6 (2005) 920–923.
- [110] F.M. Mulder, T.J. Dingemans, M. Wagemaker, G.J. Kearley, *Chem. Phys.* 317, 2–3 (2005) 113–118.
- [111] S. Bordiga, J.G. Vitillo, G. Ricchiardi, L. Regli, D. Cocina, A. Zecchina, B. Arstad, M. Bjorgen, J. Hafizovic, K.P. Lillerud, *J. Phys. Chem. B* 109, 39 (2005) 18237–18242.
- [112] A. Centrone, D.Y. Siberio-Perez, A.R. Millward, O.M. Yaghi, A.J. Matzger and G. Zerbi, *Chem. Phys. Lett.* 411, 4–6 (2005) 516–519.
- [113] A. Centrone, L. Brambilla and G. Zerbi, *Phys. Rev. B: Condens. Matter Mater. Phys.* 71, 24 (2005) 245406–1–7.
- [114] C.M. Lastoskie, K.E. Gubbins, N. Quirke, *J. Phys. Chem.* 97, 18 (1993) 4786–4796.
- [115] P.I. Ravikovitch, G.L. Haller, A.V. Neimark, *Stud. Surf. Sci. Catal.* 117 (1998) 77–84.
- [116] S. Keskin, D.S. Sholl, *Langmuir* 25, 19 (2009) 11786–11795.
- [117] D.G. Samsonenko, H. Kim, Y.Y. Sun, G.H. Kim, H.S. Lee, K. Kim, *Chem.–Asian J.* 2, 4 (2007) 484–488.
- [118] A.C. Sudik, A.R. Millward, N.W. Ockwig, A.P. Cote, J. Kim, O.M. Yaghi, *J. Am. Chem. Soc.* 127, 19 (2005) 7110–7118.
- [119] L.Q. Ma, C. Abney and W.B. Lin, *Chem. Soc. Rev.* 38, 5 (2009) 1248–1256.
- [120] J.Y. Lee, O.K. Farha, J. Roberts, K.A. Scheidt, S.T. Nguyen and J.T. Hupp, *Chem. Soc. Rev.* 38, 5 (2009) 1450–1459.
- [121] R. Kitaura, K. Seki, G. Akiyama, S. Kitagawa, *Angew. Chem. – Int. Ed.* 42, 4 (2003) 428–431.

- [122] J.-R. Li, R.J. Kuppler and H.-C. Zhou, *Chem. Soc. Rev.*, 38, 5 (2009) 1477–1504.
- [123] P. Horcajada, C. Serre, M. Vallet–Regí, M. Sebban, F. Taulelle, G. Férey, *Angew. Chem. – Int. Ed.* 45, 36 (2006) 5974–5978.
- [124] W. Rudzinski, T. Borowiecki, T. Panczyk, and A. Dominko, *J. Phys. Chem. B* 104, 9 (2000) 1984–1997.
- [125] E. Wicke and G.H. Nernst, *Berich Bunsen Gesell* 68, 3 (1964) 224–235.
- [126] A. Stern, A. Resnik, and D. Shaltiel, *J. Phys. F Met. Phys.* 14, 7 (1984) 1625–1639.
- [127] X. Zhao, S. Villar–Rodil, A.J. Fletcher, and K. Mark Thomas, *J. Phys. Chem. B.* 110, 20 (2006) 9947–9955.
- [128] K. Chihara, M. Suzuki, *Carbon* 17, 4 (1979) 339–343.
- [129] G. Onyestyák, Z. Ötvös, K. Papp, *Micropor. Mesopor. Mat.* 110, 1 (2008) 86–91.
- [130] S.W. Rutherford and D.D. Do, *Langmuir* 16, 18 (2000) 7245–7254.
- [131] S.W. Rutherford, D.D. Do, *Carbon* 38, 9 (2000) 1339–1350.
- [132] A. Konstantakou, T.A. Steriotis, G.K. Papadopoulos, M. Kainourgiakis, E.S. Kikkinides, and A.K. Stubos, *Appl. Surf. Sci.* 253, 13 (2007) 5715–2570.
- [133] V. Fierro, A. Szczurek, C. Zlotea, J.F. Marêché, M.T. Izquierdo, A. Albinia, M. Latroche, G. Furdin, A. Celzard, *Carbon* 48, 7 (2010) 1902–1911.
- [134] E.G. Derouane, *Micropor. Mesopor. Mat.* 104, 1–3 (2007) 46–51.
- [135] P. Kowalczyk, H. Tanaka, R. Holyst, K. Kaneko, T. Ohmori, J. Miyamoto, *J. Phys. Chem. B* 109, 36 (2005) 17174–17183.
- [136] Y. Gogotsi, R.K. Dash, G. Yushin, T. Yildirim, G. Laudisio, *J. Am. Chem. Soc.* 127, 46 (2005) 16006–16007.
- [137] G. Yushin, R. Dash, J. Jagiello, J.E. Fischer, Y. Gogotsi, *Adv. Funct. Mater.* 16, 17 (2006) 2288–2293.
- [138] J.T. Culp, S. Natesakhawat, M.R. Smith, E. Bittner, C. Matranga, B. Bockrath, *J. Phys. Chem. C* 112, 17 (2008) 7079–7083.
- [139] M.G. Nijkamp, J.E.M.J. Raaymakers, A.J. van Dillen and K.P. de Jong, *Appl. Phys. A: Mater. Sci. Process.* 72, 5 (2001) 619–623.
- [140] N. Texier–Mandoki, J. Dentzer, T. Piquero, S. Saadallah, P. David and C. Vix–Guterl, *Carbon* 42, 12–13 (2004) 2744–2747.
- [141] M. Hirscher and B. Panella, *J. Alloys Compd.* 404 (2005) 399–401.
- [142] B. Panella, M. Hirscher and S. Roth, *Carbon* 43 (2005) 2209–2214.
- [143] R. Zacharia, K.Y. Kim, S.W. Hwang and K.S. Nahm, *Catal. Today* 120, 3–4 (2007) 426–431.
- [144] H. Jin, Y.S. Lee and I. Hong, *Catal. Today* 120, 3–4 (2007) 399–406

- [145] H.C. Foley, *Microporous Mater.* 4, 6 (1995) 407–433.
- [146] D.K. Mackay, P.V. Roberts, *Carbon* 20 (1982) 95–104.
- [147] J.R. Fryer, *Carbon* 19 (1981) 431–439.
- [148] H. Marsh, D. Crawford, T.M. O’Grady, A. Wennenberg, *Carbon* 20 (1982) 419–436.
- [149] M. Jordá–Beneyto, F. Suárez–García, D. Lozano–Castelló, D. Cazorla–Amorós and A. Linares–Solano, *Carbon* 45, 2 (2007) 293–303.
- [150] S.W. Rutherford, C. Nguyen, J.E. Coons, and D.D. Do, *Langmuir* 19, 20 (2003) 8335–8342.
- [151] Q.Y. Wang, J.K. Johnson, *J. Chem. Phys.* 110 (1999) 577–586.
- [152] S.W. Rutherford, J.E. Coons, *J. Colloid Interf. Sci.* 284, 2 (2005) 432–439.
- [153] D.G. Schalles, R.P. Danner, *AIChE Symp. Ser.* 84, 264 (1988) 83–88.
- [154] S.W. Rutherford and J.E. Coons, *Carbon* 41 (2003) 405–411.
- [155] A.L. Cabrera, J.N. Armor, U.S. Patent 5,071,450 (1991).
- [156] J.N. Armor, C.G. Coe, T.S. Farris, J.M. Schork, U.S. Patent 5,164,355, (1992).
- [157] T.C. Golden, P.J. Battavio, Y.C. Chen, J.N. Armor, T.S. Farris, U.S. Patent 5,135,548 (1992).
- [158] T.R. Gaffney, T.S. Farris, A.L. Cabrera, J.N. Armor, U.S. Patent 5,098,880 (1992).
- [159] E. David, A. Talaie, V. Stanciu, A.C. Nicolae, *J. Mater. Process. Tech.* 157 (2004) 290–296.
- [160] M. Krutyeva, F. Grinberg, F. Furtado, P. Galvosas, J. Kärger, A. Silvestre–Albero, A. Sepulveda–Escribano, J. Silvestre–Albero, F. Rodríguez–Reinoso, *Micropor. Mesopor. Mat.* 120, 1–2 (2009) 91–97.
- [161] P. Bénard and R. Chahine, *Scr. Mater.* 56, 10 (2007) 803–808.
- [162] Q.M. Wang, D. Shen, M. Bülow, M.L. Lau, S. Deng, F.R. Fitch, N.O. Lemcoff, J. Semancin, *Micropor. Mesopor. Mat.* 55, 2 (2002) 217–230.
- [163] S.S.Y. Chui, S.M.F. Lo, J.P.H. Charmant, A.G. Orpen, I.D. Williams, *Science* 283, 5405 (1999) 1148–1150.
- [164] K. Schlichte, T. Kratzke, S. Kaskel, *Micropor. Mesopor. Mat.* 73, 1–2 (2004) 81–88.
- [165] U. Müller, M. Schubert, F. Teich, H. Puetter, K. Schierle–Arndt, J. Pastre, *J. Mater. Chem.* 16, 7 (2006) 626–636.
- [166] Z.–Q. Li, L.–G. Qui, T. Xu, Y. Wu, W. Wang, Z.–Y. Wu, X. Jiang, *Mater. Lett.* 63 (2009) 78–80.
- [167] A. Vishnyakov, P.I. Ravikovitch, A.V. Neimark, M. Bulow, Q.M. Wang, *Nano Lett.* 3, 6 (2003) 713–718.
- [168] P. Krawiec, M. Kramer, M. Sabo, R. Kunschke, H. Fröde, and S. Kaskel, *Adv. Eng. Mater.* 8, 4 (2006) 293–296.

- [169] C. Prestipino, L. Regli, J.G. Vitillo, F. Bonino, A. Damin, C. Lamberti, A. Zecchina, P.L. Solari, K.O. Kongshaug, S. Bordiga, *Chem. Mater.* 18, 5 (2006) 1337–1346.
- [170] B. Xiao, Q. Yuan, *Particuology* 7, 2 (2009) 129–140.
- [171] J.L.C. Rowsell, O.M. Yaghi, *J. Am. Chem. Soc.* 128, 4 (2006) 1304–1315.
- [172] P. Chowdhury, C. Bikkina, D. Meister, F. Dreisbach, S. Gumma, *Micropor. Mesop. Mat.* 117, 1–2 (2009) 406–413.
- [173] A. Dhakshinamoorthy, M. Alvaro, H. Garcia, *J. Catal.* 267, 1 (2009) 1–4.
- [174] J.A. Rood, B.C. Noll, and K.W. Henderson, *Inorg. Chem.* 45, 14 (2006) 5521–5528.
- [175] B. Schmitz, I. Krkljus, E. Leung, H.W. Höffken, U. Müller, and M. Hirscher, *ChemSusChem* 3, 6 (2010) 758 – 761.
- [176] J.L.C. Rowsell and O.M. Yaghi, *Angew. Chem. – Int. Ed.* 44, 30 (2005) 4670 –4679.
- [177] S. Biswas, M. Grzywa, H.P. Nayek, S. Dehnen, I. Senkovska, S. Kaskel and D. Volkmer, *Dalton. Trans.* 33 (2009) 6487–6495.
- [178] D. Denysenko, M. Grzywa, M. Tonigold, B. Schmitz, I. Krkljus, M. Hirscher, E. Mugnaioli, U. Kolb, J. Hanss, and D. Volkmer, *ChemistryJEur*, DOI: 10.1002/chem.201001872.
- [179] I. Senkovska, F. Hoffmann, M. Fröba, J. Getzschmann, W. Böhlmann, S. Kaskel, *Micropor. Mesopor. Mat.* 122, 1–3 (2009) 93–98.
- [180] G. Férey, C. Serre, C. Mellot–Draznieks, F. Millange, S. Surblé, J. Dutour, I. Margiolaki, *Angew. Chem. – Int. Ed.* 43, 46 (2004) 6296 –6301.
- [181] P. Horcajada, S. Surblé, C. Serre, D.–Y. Hong, Y.–K. Seo, J.–S Chang, J.–M. Grenèche, I. Margiolaki and G. Férey, *Chem. Commun.* 27 (2007) 2820–2822.
- [182] S.I. Nicholl, J.W. Talley, *Chemosphere* 63, 1 (2006) 132–141.
- [183] J.W. Talley, U. Ghosh, S.G. Tucker, J.S. Furey, R.G. Luthy, *Environ. Eng. Sci.* 21, 6 (2004) 647–660.
- [184] B. Chen, X. Zhao, A. Putkham, K. Hong, E.B. Lobkovsky, E.J. Hurtado, A.J. Fletcher, and K.M. Thomas, *J. Am. Chem. Soc.* 130, 20 (2008) 6411–6423.
- [185] W.E. Farneth, R.J. Gorte, *Chem. Rev.* 95, 3 (1995) 615–635.
- [186] V.K. Peterson, Y. Liu, C.M. Brown and C.J. Kepert, *J. Am. Chem. Soc.* 128, 49 (2006) 15578–15579.
- [187] Y. Liu, C.M. Brown, D.A. Neumann, V.K. Peterson and C.J. Kepert *J. Alloys Compounds* 446 (2007) 385–388.
- [188] M. Dincă and J.R. Long, *Angew. Chem. – Int. Ed.* 47, 36 (2008) 6766–6779.
- [189] S. Bordiga, L. Regli, F. Bonino, E. Groppo, C. Lamberti, B. Xiao, P.S. Wheatley, R.E. Morris, A. Zecchina, *Phys. Chem. Chem. Phys.* 9, 21 (2007) 2676–2685.

- [190] Y. Liu, C.M. Brown, D.A. Neumann, V.K. Peterson and C.J. Kepert, *J. Alloys Compd.* 446–447 (2007) 385–388.
- [191] J.H. Luo, H.W. Xu, Y. Liu, Y.S. Zhao, L.L. Daemen, C. Brown, T.V. Timofeeva, S.Q. Ma, H.C. Zhou, *J. Am. Chem. Soc.* 130, 30 (2008) 9626–9627.
- [192] A.J. Ramirez–Cuesta, M.O. Jones and W.I.F. David, *Materials Today* 12, 11 (2009) 54–61.
- [193] R. Chahine, T.K. Bose, *Hydrogen Energy*, Prog. XI Proc. World Hydrogen Energy Conf. 1–3 (1996) 1259–1263.
- [194] D.N. Dybtsev, H. Chun, S.H. Yoon, D. Kim, K. Kim, *J. Am. Chem. Soc.* 126, 1 (2004) 32–33.
- [195] Z.–M. Wang, B. Zhang, M. Kurmoo, M.A. Green, H. Fujiwara, T. Otsuka, H. Kobayashi, *Inorg. Chem.* 44, 5 (2005) 1230–1237.
- [196] Z.–M. Wang, B. Zhang, H. Fujiwara, H. Kobayashi, M. Kurmoo, *Chem. Commun.* 4 (2004) 416–417.
- [197] A.J. Fletcher, K.M. Thomas, M.J. Rosseinsky, *J. Solid State Chem.* 178, 8 (2005) 2491–2510.
- [198] M. Dincá and J.R. Long, *J. Am. Chem. Soc.* 127, 26 (2005) 9376–9377.
- [199] I. Senkowska and S. Kaskel, *Eur. J. Inorg. Chem.* 22 (2006) 4564–4569.
- [200] A.G. Wong–Foy, A.J. Matzger and O.M. Yaghi, *J. Am. Chem. Soc.* 128, 11 (2006) 3494–3495.
- [201] Y. Li and R.T. Yang, *Langmuir* 23, 26 (2007) 12937–12944.
- [202] A.R. Millward and O.M. Yaghi, *J. Am. Chem. Soc.* 127, 51 (2005) 17998–17999.
- [203] D. Saha, Z. Wei, S. Deng, *Int. J. Hydrogen Energ.* 33, 24 (2008) 7479–7488.
- [204] M. Schlichtenmayer, B. Streppel, M. Hirscher, *International Journal of Hydrogen Energy* (2010), DOI:10.1016/j.ijhydene.2010.09.057
- [205] B. Panella, K. Hönes, U. Müller, N. Trukhan, M. Schubert, H. Pütter, and M. Hirscher, *Angew. Chem. – Int. Ed.* 47, 11 (2008) 2138–2142.
- [206] T. Loiseau, C. Mellot–Draznieks, H. Muguerra, G. Férey, M. Haouas, F. Taulelle, C. R. Chimie 8, 3–4 (2005) 765–772.
- [207] C. Serre, C. Mellot–Draznieks, S. Surblé, N. Audebrand, Y. Filinchuk, G. Férey, *Science* 315, 5820 (2007) 1828–1831.
- [208] P. Küsgens, M. Rose, I. Senkowska, H. Fröde, A. Henschel, S. Siegle, S. Kaskel, *Micropor. Mesopor. Mater.* 120, 3 (2009) 325–330.
- [209] S.J. Gregg, K.S.W. Sing: *Adsorption, Surface Area and Porosity*, Academic Press, London 1982.
- [210] H. Frost, T. Düren and R.Q. Snurr, *J. Phys. Chem. B* 110, 19 (2006) 9565–9570.

- [211] Y. Liu, H. Kabbour, C.M. Brown, D.A. Neumann and C.C. Ahn, *Langmuir* 24, 9 (2008) 4772–4777.
- [212] H. Frost and R. Q. Snurr, *J. Phys. Chem. C* 111, 50 (2007) 18794–18803.
- [213] E. Poirier, R. Chahine, P. Benard, L. Lafi, G. Dorval–Douville, P. A. Chandonia, *Langmuir* 22, 21 (2006) 8784–8789.
- [214] C.O. Arean, O.V. Manoilova, B. Bonelli, M.R. Delgado, G.T. Palomino, E. Garrone, *Chem. Phys. Lett.* 370, 5–6 (2003) 631–635.
- [215] B. Schmitz, U. Müller, N. Trukhan, M. Schubert, G. Férey, M. Hirscher, *ChemPhysChem* 9, 15 (2008) 2181–2184.
- [216] D.H. Everett, J.C. Powl, *J. Chem. Soc. Farady Trans. I* 72 (1976) 619–636.
- [217] M. Eddaoudi, J. Kim, N. Rosi, D. Vodak, J. Wachter, M. O’Keeffe, O.M. Yaghi, *Science* 295 (2002) 469 – 472.
- [218] T. Sagara, J. Klassen, E. Ganz, *J. Chem. Phys.* 121, 24 (2004) 12543–12547.
- [219] N.L. Rosi, J. Eckert, M. Eddaoudi, D.T. Vodak, J. Kim, M. O’Keeffe and O.M. Yaghi, *Science* 300, 5622 (2003) 1127–1129.
- [220] S.S. Han, W.Q. Deng and W.A. Goddard III, *Angew. Chem. – Int. Ed.* 46, 33 (2007) 6289–6292.
- [221] T. Sagara, J. Ortony and E. Ganz, *J. Chem. Phys.* 123, 21 (2005) 214707–1–6.
- [222] X. Lin, J. Jia, X.K. Zhao, M. Thomas, A.J. Blake, G.S. Walker, N.R. Champness, P. Hubberstey, M. Schröder, *Angew. Chem. – Int. Ed.* 45, 44 (2006) 7358–7364.
- [223] T.K. Maji, R. Matsuda and S. Kitagawa, *Nat. Mater.* 6, 2 (2007) 142–148.
- [224] B. Chen, M. Eddaoudi, S.T. Hyde, M. O’Keeffe and O.M. Yaghi, *Science* 291, 5506 (2001) 1021–1023.
- [225] S.S. Han, J.L. Mendoza–Cortés and W.A. Goddard III, *Chem. Soc. Rev.* 38, 5 (2009) 1460–1476.
- [226] S.Q. Ma, D.F. Sun, M. Ambrogio, J.A. Fillinger, S. Parkin, H.–C. Zhou, *J. Am. Chem. Soc.* 129, 7 (2007) 1858–1859.
- [227] D.H. Jung, D. Kim, T.B. Lee, S.B. Choi, J.H. Yoon, J. Kim, K. Choi and S.–H. Choi, *J. Phys. Chem. B* 110 (2006) 22987–22990.
- [228] P. Ryan, L.J. Broadbelt and R.Q. Snurr, *Chem. Commun.* 35 (2008) 4132–4134.
- [229] D. Sun, S. Ma, Y. Ke, D.J. Collins and H.–C. Zhou, *J. Am. Chem. Soc.* 128, 12 (2006) 3896–3897.
- [230] B. Chen, N.W. Ockwig, A.R. Millward, D.S. Contreras, and O.M. Yaghi, *Angew. Chem. – Int. Ed.* 44, 30 (2005) 4745–4749.

- [231] M. Dincă, W.S. Han, Y. Liu, A. Dailly, C.M. Brown, J.R. Long, *Angew. Chem. – Int. Ed.* 46, 9 (2007) 1419–1422.
- [232] M. Dincă, A. Dailly, Y. Liu, C.M. Brown, D.A. Neumann, J.R. Long, *J. Am. Chem. Soc.* 128 (2006) 16876–16883.
- [233] J.G. Vitillo, L. Regli, S. Chavan, G. Ricchiardi, G. Spoto, P.D.C. Dietzel, S. Bordiga, A. Zecchina, *J. Am. Chem. Soc.* 130, 26 (2008) 8386–8396.
- [234] W. Zhou, H. Wu, T. Yildirim, *J. Am. Chem. Soc.* 130, 46 (2008) 15268–15269.
- [235] S.S. Kaye, and J.R. Long, *J. Am. Chem. Soc.* 127, 18 (2005) 6506–6507.
- [236] Y.G. Lee, H.R. Moon, Y.E. Cheon, M.P. Suh, *Angew. Chem. – Int. Ed. Engl.* 47, 40 (2008) 7741–7745.
- [237] Y.Y. Sun, Y.H. Kim, S.B. Zhang, *J. Am. Chem. Soc.* 129, 42 (2007) 12606–12607.
- [238] D. Phanon, P.L. Llewellyn, I. Krkljus, M. Hirscher, D. Fairen-Jimenez, T. Düren, C. Serre, G. Férey, and A. Vimont. To be submitted to *Langmuir*.
- [239] H.W. Woolley, R.B. Scott, F.G. Brickwedde, *J. Res. Nat. Bur. Stand.* 41, 5 (1948) 379–475.
- [240] D. Basmadjian, *Can. J. Chem.* Vol. 38, 1 (1960) 141–148.
- [241] D. Basmadjian, *Can. J. Chem.* Vol. 38, 1 (1960) 149–156.
- [242] A. Katorski, J.G. Eberhart, and D. White, *J. Chem. Phys.* 34, 6 (1961) 2189–2190.
- [243] M.P. Freeman, *J. Phys. Chem.* 64, 1 (1960) 32–37.
- [244] R. Yaris and J.R. Sams, *J. Chem. Phys.* 37, 3 (1962) 571–576.
- [245] A. Katorski and D. White, *J. Chem. Phys.* 40, 11 (1964) 3183–3194.
- [246] J.L. Maienschein, R.S. Hudson, R.T. Tsugawa, E.M. Fearon, P.S. Souers, and G.W. Collins, *J. Vac. Sci. Technol. A* 10, 3 (1992) 556–569.
- [247] B.P. Stoicheff, *Can. J. Phys.* 35 (1957) 730–741.
- [248] E. Roduner, Muonium – an ultra-light isotope of hydrogen, in: A. Kohen and H.–H. Limbach, editors. *Isotope Effects in Chemistry and Biology*. Taylor & Francis, Boca Raton, 2005 (invited).
- [249] K. Motizuki and T. Nagamiya, *J. Phys. Soc. Jpn.* 11 (1956) 93–104.
- [250] I.F. Silvera, *Rev. Mod. Phys.* 52 (1980) 393–452.
- [251] Y.Y. Milenko, R.M. Sibileva, and M.A. Strzhemechny, *J. Low Temp. Phys.* 107 (1997) 77–92.
- [252] B.F. Minaev, H. Agren, *J. Phys. Chem.* 99 (1995) 8936–8940.
- [253] H.P. Gush, W.F.J. Hare, E.J. Allin, and H.L. Welsh, *Can. J. Phys.* 38 (1960) 176.
- [254] A. Crane and H.P. Gush, *Can. J. Phys.* 44 (1966) 373.
- [255] Y.L. Sandler, *J. Phys. Chem.* 58, 1 (1954) 58–61.
- [256] D. White and E.N. Lassettre, *J. Chem. Phys.* 32, 1 (1960) 72–84.

- [257] J.J.M. Beenakker, V.D. Borman and S.Y. Krylov, *Phys. Rev. Lett.* 72, 4 (1994) 514–517.
- [258] J.J.M. Beenakker, V.D. Borman and S.Y. Krylov, *Chem. Phys. Lett.* 232, 4 (1995) 379–382.
- [259] Q.Y. Wang; S.R. Challa, D.S. Sholl, and J.K. Johnson, *Phys. Rev. Lett.* 82 (1999) 956–959.
- [260] S.R. Challa, D.S. Sholl, and J.K. Johnson, *Phys. Rev. B* 63 (2001) 245419–1–9.
- [261] S.R. Challa, D.S. Sholl, and J.K. Johnson, *J. Chem. Phys.* 116, 2 (2002) 814–824.
- [262] G. Garberoglio, M.M. DeKlavon, and J.K. Johnson, *J. Phys. Chem. B* 110 (2006) 1733–1741.
- [263] G. Garberoglio and J.K. Johnson, *ACS Nano* 4, 3 (2010) 1703–1715.
- [264] Y. Wang and S.K. Bhatia, *J. Phys. Chem. C* 113, 33 (2009) 14953–14962.
- [265] B.C. Hathorn, B.G. Sumpter, and D.W. Noid, *Phys. Rev. A* 64 (2001) 22903.
- [266] T. Lu, E.M. Goldfield, and S.K. Gray, *J. Phys. Chem. B* 107, 47 (2003) 17457–17465.
- [267] T. Lu, E.M. Goldfield, and S.K. Gray, *J. Phys. Chem. B* 110, 4 (2006) 1742–1751.
- [268] G. Garberoglio, *Eur. Phys. J. D* 51, 2 (2009) 185–191.
- [269] P. Kowalczyk, P.A. Gauden, and A.P. Terzyk, *J. Phys. Chem. B* 112, 28 (2008) 8275–8284.
- [270] P. Kowalczyk, P.A. Gauden, A.P. Terzyk and S. Furmaniak, *J. Phys. Condens. Matter* 21 (2009) 144210.
- [271] Y. Hattori, H. Tanaka, F. Okino, H. Touhara, Y. Nakahigashi, S. Utsumi, H. Kanoh, and K. Kaneko, *J. Phys. Chem. B*, 110, 20 (2006) 9764–9767.
- [272] A.V.A. Kumar, H. Jobic, and S.K. Bhatia, *J. Phys. Chem. B* 110, 33 (2006) 16666–16671.
- [273] W. van Dingenen, A. van Itterbeek, *Physica (The Hague)* 6 (1939) 49.
- [274] G. Constabaris, J.R. Sams, G.D. Halsey, *J. Phys. Chem.* 65, 2 (1961) 367–369.
- [275] H. Tanaka, H. Kanoh, M.J. Yudasaka, S. Iilima, and K. Kaneko, *J. Am. Chem. Soc.* 127, 20 (2005) 7511–7516.
- [276] A. Kohen and J.P. Klinman, *Acc. Chem. Res.* 31 (1998) 397–404.
- [277] A.V.A. Kumar and S.K. Bhatia, *Phys. Rev. Lett.* 95 (2005) 245901(1) – 245901(4).
- [278] Z. Donghui, Z. Li, S. Wei and S. Yan, *Chinese J. Chem. Eng.* 14, 4 (2006) 526–531.
- [279] A.V.A. Kumar, H. Jobic, and S.K. Bhatia, *Adsorption* 13 (2007) 501–508.
- [280] A.V.A. Kumar and S.K. Bhatia, *J. Phys. Chem. C* 112 (2008) 11421–11426.
- [281] T.X. Nguyen, H. Jobic, S.K. Bhatia, *Phys. Rev. Lett.* 105, 8 (2010) 085901–1–4.
- [282] X.Z. Chu, Y.P. Zhou, Y.Z. Zhang, W. Su, Y. Sun and L. Zhou, *J. Phys. Chem. B* 110 (2006) 22596–22600.
- [283] G. Garberoglio, *Chem. Phys. Lett.* 467, 4–6 (2009) 270–275.
- [284] R.V.R.A. Rios, J. Silvestre–Albero, A. Seplveda–Escribano, M. Molina–Sabio, and F. Rodriguez–Reinoso, *J. Phys. Chem. C*. 111, 10 (2007) 3803–3805.
- [285] C.A. Grande, V.M.T.M. Silva, C. Gigola, A.E. Rodrigues, *Carbon* 41 (2003) 2533–45.

- [286] P.J.M. Carrott, M.M.L. Ribeiro Carrott, I.P.P. Cansado, J.M.V. Nabais, *Carbon* 38 (2000) 465–474.
- [287] B. Panella, M. Hirscher, H. Pütter and U. Müller, *Adv. Funct. Mater.* 16, 4 (2006) 520–524.
- [288] J.C. Liu, J.T. Culp, S. Natesakhawat, B.C. Bockrath, B. Zande, S.G. Sankar, G. Garberoglio, J.K. Johnson, *J. Phys. Chem. C* 111, 26 (2007) 9305–9313.
- [289] M. Dincã, A.F. Yu, J.R. Long, *J. Am. Chem. Soc.* 128, 27 (2006) 8904–8913.
- [290] J.Y. Lee, J. Li and J. Jagiello, *J. Solid State Chem.* 178, 8 (2005) 2527–2532.
- [291] B. Xiao, P.S. Wheatley, X.B. Zhao, A.J. Fletcher, S. Fox, A.G. Rossi, I.L. Megson, S. Bordiga, L. Regli, K.M. Thomas and R.E. Morris, *J. Am. Chem. Soc.* 129, 5 (2007) 1203–1209.
- [292] J.L.C. Rowsell, A.R. Millward, K.S. Park, O.M. Yaghi, *J. Am. Chem. Soc.* 126, 18 (2004) 5666–5667.
- [293] M. Latroche, S. Surblé, C. Serre, C. Mellot-Draznieks, P.L. Llewellyn, J.-H. Lee, J.-S. Chang, S.H. Jung, C. Férey, *Angew. Chem. – Int. Ed.* 45 (2006) 8227–8231.

ACKNOWLEDGMENTS

The experimental part of this thesis was mainly carried out in the Department for Modern Magnetic Materials at the Max Planck Institute for Intelligent Systems, in the context of activities of the Hydrogen Storage Group, and within the framework of the European Integrated Project NESSHY (Novel and Efficient Solid State HYdrogen storage systems). Hereby, I would like to particularly thank *Prof. Dr. Gisela Schütz* for accepting me as a member of her department. Further acknowledgment goes to *Dr. Michael Hirscher* for opportunity to partake in NESSHY project and perform interesting research in a dynamic research field. Special thanks for the freedom to explore the measurements with deuterium and gas mixtures, and connect them to quantum effects, without whom this work would have been intellectually poorer. I would further like to thank *Prof. Dr. Emil Roduner* for giving me the possibility to partake in his department seminar. Very special thanks for his time and effort in careful reading of the manuscript, and for proficient suggestions for the preparation of the final draft. My kind acknowledgment also goes to *Prof. Dr.-Ing. Elias Klemm* for accepting to take the chair of the examination board.

Bernd Ludescher is thanked for technical support and *Knut Richter* for *He* supply.

Within the scope of this research neutron diffraction studies were carried out. I appreciate the association and collaboration with *Dr. Theodore Steriotis*, *Dr. Georgia Charalambopoulou*, and *Dr. Jorge Hernandez-Velasco*. *Dr. Dirk Walacher*, Deputy Head of the Department Sample Environment, is thanked for facilitating the neutron diffraction research performed at Helmholtz-Zentrum Berlin für Materialien und Energie GmbH, and the Institute management for the allocation of the beam time in the year 2009 and 2010.

An appreciation is extended to the following individuals for provision of samples utilized for this study: *Dr. G. Charalambopoulou* and *Dr. T. Steriotis* for the Takeda samples, *Dr. U. Müller* and *E. Leung* for provision of the Cu-BTC, Fe-BTC, Mg-MOF samples, and the MOF-177, *Prof. Dr. D. Volkmer* and *D. Denysenko* for the MFU-4(l), *Prof. Dr. S. Kaskel*, *Dr. I. Senkovska*, and *N. Klein* for DUT-4/5, *Prof. Dr. G. Ferey*, *Dr. T. Loiseau*, and *Dr. C. Serre* for the MIL-100 series.

I would like to acknowledge with thanks to *Dr. Theodore Steriotis* and his group for additional pore size characterization of the Takeda samples.

A partial funding by the European Commission DG Research (contract SES6-2006-518271/NESSHY), and an additional funding provided by the IMPRS-AM are gratefully acknowledged.

It goes without saying that homage is to be paid to the people that every day work for us and we but rarely say Thank You – the personnel that maintains our offices and laboratories, the library personnel for the archived publications retrieval, and the MPI guardians. I thankfully remember numerous e-mails sent by Frau *Ursula Habel* to international doctoral students at Uni. Stuttgart.

A very special thanks goes to the following people:

Dr. Aleksandar Tucić (†) – Hvala ti što si me ohrabrio na ovaj korak, na podršci i nesebičnoj želji da pomogneš. Nadam se da si otišao putem svetlosti i da počivaš u miru. Poslednji pozdrav dragom kolegi.

Posebno hvala *Dr. Čedomiru Jovalekiću* za mudre i iskrene reči podrške i ohrabrenja.

Đurđi, Ana–Mariji i Milanu(†) *Pandža* hvala na pomoći prilikom selidbe, pronalaženja i opremanja stana.

I can't forget to thank to people who made my days in Germany more enjoyable and memorable. I wish you all the best for the future.

Frau *Edmute Seibert* danke für den Deutschunterricht und die Korrekturen meiner Übersetzung der Zusammenfassung.

Finally, I wish to express my most sincere appreciation to people who supported me on a journey leading to completion of this quest, the people who left indelible mark, and meant to me in a special, more profound way:

У Господу Богу, љубљени мој духовни оче *Бранивоје* – неизмерно поштовање, захвалност и љубав исказујем ти. За јуче, за данас, за сутра. За све!

My warm thanks go to few very special friends for their friendship and regard. It has been a pleasure knowing you.

Изнад свега моју најискренију љубав и захвалност исказујем мојим највољенијима, Биљани и Петру. Сазнање да сте ту, дишете и постојите, ваше охрабрење и љубав дали су ми снагу.

Хвала вам што сте били уз мене – тако далеко, а тако близу. Нека вам је на благослов душе и тела, љубљени моји.

Хвала Господе што си ми се смиловао, успокојио, умирио ме и помиловао ме грешну. Што си ме довео до краја овог пута.

Ваша у Господу

Ивана (Биљана) Кркљуш

REFEREED PUBLICATIONS

1. **I. Krkljus** and M. Hirscher, *Characterization of hydrogen/deuterium adsorption sites in nanoporous Cu–BTC by low-temperature Thermal–Desorption Mass Spectroscopy*, Micropor. Mesopor. Mater. 142 (2011) 725–729.
2. D. Denysenko, M. Grzywa, M. Tonigold, B. Schmitz, **I. Krkljus**, M. Hirscher, E. Mugnaioli, U. Kolb, J. Hanss, and D. Volkmer, *Elucidating Gating Effects for Hydrogen Sorption in MFU–4 Type Triazolate-based MOFs Featuring Different Pore Sizes*, Chemistry J. Eur. 17, 6 (2011) 1837–1848.
3. B. Schmitz, **I. Krkljus**, E. Leung, H.W. Höffken, U. Müller, and M. Hirscher, *High heat of adsorption for hydrogen in magnesium formate*, ChemSusChem 3, 6 (2010) 758 – 761.
4. **I. Krkljus**, T. Steriotis, G. Charalambopoulou, A. Gotzias and M. Hirscher, *H₂/D₂ adsorption and desorption studies of carbon molecular sieves with different pore structure*, to be submitted to Carbon.
5. D. Phanon, P.L. Llewellyn, **I. Krkljus**, M. Hirscher, D. Fairen–Jiminez, T. Düren, C. Serre, G. Férey, and A. Vimont, *Sorption properties of hydrogen at 77 K of various MIL–100 metal organic frameworks (M = Al, V, Cr, Fe) as characterised by microcalorimetry, thermodesorption and molecular simulation*, to be submitted to Langmuir.
6. E. Maccallini, G. Kalantzopoulos, A. Policicchio, G. Golemme, M.G. Buonomenna, **I. Krkljus**, M. Hirscher, and R.G. Agostino, *Gas solubility and mobility in modified and unmodified zeolites at low and high pressures by PcT kinetic and equilibrium sorption*, to be submitted.

CURRICULUM VITAE

IVANA B. KRKLJUŠ

Date and place of Birth: **05. October, 1980**. Belgrade (Serbia).

EDUCATION AND ACADEMIC POSITIONS

- 2008 – 2011 **Dissertation at the Max Planck Institute for Intelligent Systems (MPI-IS).**
- 2006 – 2008 **Research Assistant** on the Project “*Advanced metal oxide electroceramics and thin films*“, financed by the Ministry of Science and Technology of the Republic of Serbia (2006 – 2010). Institute for Multidisciplinary Research, Materials Science Department, Belgrade, Serbia.
- 1999 – 2005 **Faculty of Physical Chemistry, University of Belgrade.**
Title of Diploma Thesis: “Kinetics of (E)-4-(4-Methoxyphenyl)-4-oxo-2-Butenoic Acid Release, immobilised on Poly(Acrylic Acid) Hydrogel“, done at the Department for Material Science (Material Dynamics and Structure).
- 1995 – 1999 **IV Belgrade Gymnasium**
Major field: Nature–mathematics.
Matriculation: “Structure and significance of DNA”.
- 1987 – 1994 **Primary School:** “Filip Filipović”.

PUBLICATIONS

I. Krkljus, et al. The Electrophoretic Deposition of Lanthanum Manganite Powders for a Cathode-Supported Solid Oxide Fuel Cell in Planar and Tubular Configurations, *Int. J. Appl. Ceram. Tec.* 5, 6 (2008) 548 – 556.

B. Adnadjevic, J. Jovanovic, **I. Krkljus**, Isothermal Kinetics of (E)-4-(4-Methoxyphenyl)-4-oxo-2-butenic Acid Release from a Poly(acrylic acid-co-methacrylic acid) Hydrogel, *J. Appl. Polym. Sci.* 107, 5 (2008) 2768–2775.

SCHOLARSHIPS, HONOURS AND AWARDS

Scholarship holder and a member of the **International Max Planck Research School for Advanced Materials (IMPRS-AM)**, class 2008.

„Design of SOFC by means of EPD” – **Invited lecture** at the Annual meeting of the Serbian Chemical Society, Ceramic Section, November 2007, Belgrade, Serbia.

1st Price of the Student Lecture Competition, held at Xth Conference and exhibition of the European Ceramic Society, 17th – 21st June 2007, Berlin, Germany.

1st Price of the Contest of Young Researchers of Ceramic Section, held at 45th Meeting of the Serbian Chemical Society, 25th – 26th January 2007, Novi Sad, Serbia.

A **scholarship for Postgraduate studies** granted by the Faculty of Physical Chemistry, University of Belgrade.

LIVE CURIOUS

If you are you breathe.

If you breathe you talk.

If you talk you ask.

If you ask you think.

If you think you search.

If you search you experience.

If you experience you learn.

If you learn you grow.

If you grow you wish.

If you wish you find.

And if you find you doubt.

If you doubt you question.

If you question you understand and if you understand you know.

If you know you want to know more.

If you want to know more you are alive.

Ivana B. Krkljuš

CORRELATION BETWEEN THE MICROSTRUCTURE OF POROUS MATERIALS AND THE
ADSORPTION PROPERTIES OF H₂ AND D₂

Max Planck Institute for Intelligent Systems (formerly Max Planck Institute for Metals Research).
Abteilungen Prof. Dr. G. Schütz
Faculty of Chemistry, University of Stuttgart, Institute for Physical Chemistry, Prof. Dr. E. Roduner.